Lecture Notes on

Stellar Structure and Evolution

Jørgen Christensen-Dalsgaard
Institut for Fysik og Astronomi, Aarhus Universitet

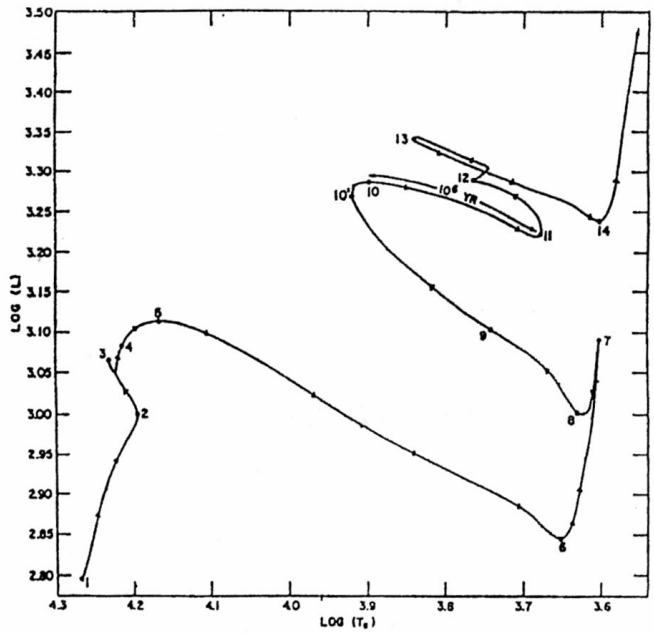

Eighth Edition

August 2023

Preface

The present notes grew out of an introductory course in stellar evolution which I gave for several years to third-year undergraduate students in physics at the Aarhus University The goal of the course and the notes is to show how many aspects of stellar evolution can be understood relatively simply in terms of basic physics. Apart from the intrinsic interest of the topic, the value of such a course is that it provides an illustration (within the syllabus in Aarhus, almost the first illustration) of the application of physics to "the real world" outside the laboratory.

I am grateful to the students who have followed the course over the years, and to my colleague J. Madsen who has taken part in giving it, for their comments and advice; indeed, their insistent urging that I replace by a more coherent set of notes the textbook, supplemented by extensive commentary and additional notes, which was originally used in the course, is directly responsible for the existence of these notes. Additional input was provided by the students who suffered through the first edition of the notes in the Autumn of 1990. I hope that this will be a continuing process; further comments, corrections and suggestions for improvements are most welcome. I thank N. Grevesse for providing the data in Figure 14.1, and P. E. Nissen for helpful suggestions for other figures, as well as for reading and commenting on an early version of the manuscript. I also thank Bent Christensen-Dalsgaard and T. M. Brown for their assistance in locating the Bradbury reference in Chapter 2. The High Altitude Observatory, Boulder, Colorado is thanked for hospitality during the Summer of 1990, where a substantial part of the notes were written.

Aarhus, August 1991

Jørgen Christensen-Dalsgaard

Preface to 4th edition

Relative to earlier editions a number of mistakes have been corrected and some of the figures have been revised. I am grateful to all of those who have provided comments and corrections, in particular N. H. Andersen and H. Jørgensen, who provided extensive lists of errors and suggestions for improvements. A revised description of the origin of the "hook" in the evolution tracks for moderate- and large-mass stars at the end of central hydrogen burning resulted from work by E. Michel, and I am very grateful to him for discussions and computations leading to this correction. The computations on which some of the figures

are based were supported by the Danish Natural Science Research Council. Once again I thank the High Altitude Observatory for Summer hospitality during the revisions.

Boulder, August 23, 1995

Jørgen Christensen-Dalsgaard

Preface to 5th edition

The notes have been significantly revised and updated in this edition, including new results on the solar neutrino problem and from helioseismology, as well as an update of the discussion of supernova explosions and nucleosynthesis. In addition, Chapter 16 on compact objects is new; I am very grateful to Jes Madsen for his permission to include it, and to Karlheinz Langanke for translating it from the Danish original ('Stjerneudviklingens slutstadier'). I also thank Langanke for very substantial contributions to the revised Chapters 14 and 15. Discussions with A. V. Sweigart and J. Lattanzio were very helpful in bringing my ideas about late stellar evolution more up to date, and I thank the former for providing the data used in Figure 12.8. Further corrections and suggestions received from the students who have followed the course are also gratefully acknowledged.

Aarhus, September 6, 2000

Jørgen Christensen-Dalsgaard

Preface to 6th edition

The only substantial change in this edition is an update of Section 11.5.3, including the spectacular results on neutrino oscillations from the Sudbury Neutrino Observatory. In addition, a number of minor corrections have been incorporated.

Second printing: In this reprinting a few minor changes have been made, including a replacement of Figure 2.6 and an update of a few references.

Third printing: In this reprinting some generally minor changes have been made, particularly in Chapter 14, and a few references have been added.

Fourth printing: This reprinting is essentially identical in content to the third printing, but the text has been reset in LaTeX, and the figures have been included in the output file. Thus this version is being made available on the internet.

Aarhus, 9 March, 2008

Jørgen Christensen-Dalsgaard

Preface to 7th edition

In the present edition some updates have been made, to bring it a little more in line with recent developments. Section 10.3 is new, and there are some updates to Sections 2.2, 2.8, 11.5.2, 11.5.3 and 15.2. In addition, a few pictures have been included, and an index has been provided. I am grateful to Mia Lundkvist and Hans Kjeldsen for the inspiration for this update and to Mia for help with establishing the index.

Aarhus, 27 August 2022

Jørgen Christensen-Dalsgaard

Preface to 8th edition

The present edition includes further updates. Section 6.4 and Chapter 10 have been somewhat reorganized, and Section 13.4 is new. Figures 10.4, 12.4, 12.5, 12.9, 12.11 and 12.12 have been replaced by Figures 10.6, 12.5, 12.6, 12.12, 12.13 and 12.14, based on more recent stellar evolution calculations. I am grateful to Mia Sloth Lundkvist for extensive comments and suggestions that have inspired this revision, to Johannes Holm Jørgensen, Mark Lykke Winther and Jakob Lysgaard Rørsted for stellar model calculations used for the revised figures and help in producing them, to Yixiao Zhang for an important contribution to Section 6.4.4, to Rasmus Sloth Lundkvist for comments on solar neutrinos and to Karsten Brogaard for providing Section 13.4.

Aarhus, 22 August 2023

Jørgen Christensen-Dalsgaard

Contents

Chapter 1

Introduction

The purpose of the present notes is to provide an introduction to the structure and evolution of stars, as we have come to understand it in terms of their physical properties. The goal has been to keep the description as simple as possible, while maintaining the principal ingredients, and presenting the most important results. It has *not* been a goal to provide a "cookery book" for prospective stellar model builders; there already exist a substantial number of such books, some of which are described in the bibliography in section 1.5. Thus, after going through the notes the reader will not be able to sit down and write yet another computer programme for calculating stellar models. But it is hoped that the notes will provide a basic understanding about what "makes a star tick", and how the ticking relates to the underlying physics.

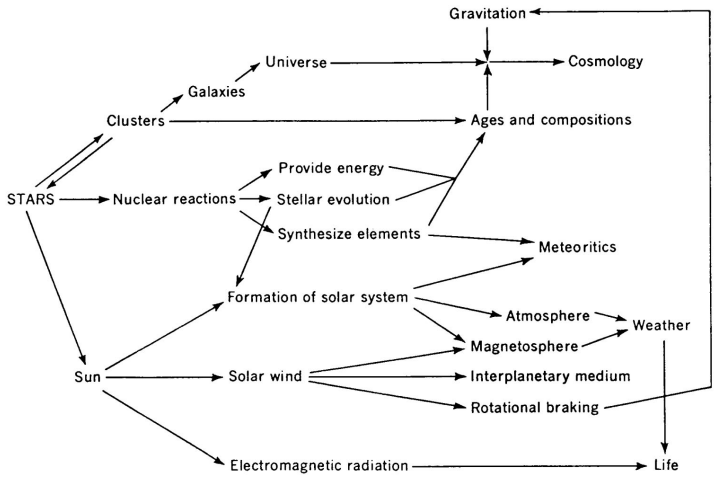

Figure 1.1: The role of the star in astrophysics. Almost every subject in astrophysics is influenced by our ideas about the structure and evolution of the stars. (From Clayton 1968).

The study of stellar structure and evolution plays a central role in modern astrophysics.[1] This is illustrated graphically in Figure 1.1. For example, the study of distances

[1] A very useful phrase when writing grant applications.

and ages of stars, which are crucial to our understanding of the structure and history of our Galaxy, depends on stellar evolution calculations. Furthermore, since the synthesis of almost all chemical elements is supposed to take place inside stars, an understanding of the chemical history of the Universe (and of our own origins) requires that one understands stellar evolution. However, there is another side to the importance of stellar evolution calculations, to which we return in section 1.4: the calculations depend on knowledge of the physical properties of the matter in the stars; hence by testing the computed models against observations we are effectively testing the physics that was used to compute the models, often under conditions where it is impossible to carry out tests in the laboratory.

This chapter provides an introduction to some of the terminology and concepts which will be discussed later. Also it gives a sketch of the life histories of typical stars. In this way it is hoped to establish a framework for organizing the details which follow in the subsequent chapters.

1.1 Stellar time scales

1.1.1 The dynamical time scale

Changes in a star may occur on a range of different time scales. The shortest relevant time scale is the *dynamical* timescale $t_{\rm dyn}$. Consider a star of mass M and radius R. The gravitational acceleration at the surface of the star is

$$g_{\rm s} = \frac{GM}{R^2} \ , \tag{1.1}$$

where G is the gravitational constant. Hence the time required for a particle to fall the distance ℓ in the gravitational field of the star is

$$t = \left(\frac{2\ell}{g_{\rm s}}\right)^{1/2} = \left(\frac{2\ell R^2}{GM}\right)^{1/2} .$$

If we take ℓ to be $R/2$ we obtain a time scale that is characteristic for motions over stellar scales in the gravitational field:

$$t_{\rm dyn} = \left(\frac{R^3}{GM}\right)^{1/2} . \tag{1.2}$$

It is obvious that there is a great deal of arbitrariness in this definition; after all, we could have chosen a distance of R, or $R/10$, instead of $R/2$. However, the point of arguments like this is not to obtain *precise* values for the quantities that are being estimated; rather, the purpose is to get a feel for the magnitude of the quantity, and its dependence on basic stellar parameters. Hence we shall use equation (1.2) as a reasonable estimate for dynamical changes to a star. Using the solar values $\rm M_\odot$ and $\rm R_\odot$ for M and R, we may write the equation as[2]

$$t_{\rm dyn} = 30\,{\rm min}\left(\frac{R}{\rm R_\odot}\right)^{3/2}\left(\frac{M}{\rm M_\odot}\right)^{-1/2} . \tag{1.3}$$

[2]The precise value of $t_{\rm dyn}$, as defined in equation (1.2), for the Sun is 26.5642 min; however, given the philosophy behind the estimate it is clearly meaningless to give the result with that many significant figures.

Stellar radii vary over a range from roughly $0.01\,\mathrm{R}_\odot$ to roughly $1000\,\mathrm{R}_\odot$, whereas the mass ranges from $0.1\,\mathrm{M}_\odot$ to $100\,\mathrm{M}_\odot$. Hence the dynamical time scale ranges from seconds to years. However, in most cases we see no evidence for motion with such time scales on the stars. This indicates that the forces on the star are very nearly balanced; we describe this situation by saying that the star is in *hydrostatic equilibrium*.

1.1.2 The time scale for release of gravitational energy (or the thermal time scale)

If a star has no internal sources of energy, it can still radiate energy by contracting. In this way it gets gravitationally more tightly bound; its gravitational potential energy decreases (*i.e.*, becomes of larger negative magnitude), and the star has to get rid of the excess energy somehow. As discussed in section 4.4, half of the energy released goes to heat up the star, and the other half is radiated away.

An estimate for the time scale of this process can be obtained by calculating the time a star could radiate at a given rate on the energy released through gravitational contraction to a given radius. Let L_s be the *surface luminosity* of the star, *i.e.*, the amount of energy it radiates per unit time. The gravitational potential on the surface of the star is $-GM/R$, and so an estimate of the gravitational binding energy is

$$\Omega = -\frac{GM^2}{R}\ , \tag{1.4}$$

calculated as the gravitational potential energy of the stellar mass in the surface gravitational potential. Hence the relevant time scale, known as the *Kelvin-Helmholtz time scale*, is

$$t_\mathrm{KH} = \frac{GM^2}{RL_\mathrm{s}}\ . \tag{1.5}$$

In terms of solar values, the result is

$$t_\mathrm{KH} = 30\,\mathrm{million\ years}\left(\frac{M}{\mathrm{M}_\odot}\right)^2\left(\frac{R}{\mathrm{R}_\odot}\right)^{-1}\left(\frac{L_\mathrm{s}}{\mathrm{L}_\odot}\right)^{-1}\ . \tag{1.6}$$

This value gave rise to some controversy in the 19th century, at a time when the origin of the solar energy output was unknown. Gravitational contraction was considered as a viable hypothesis, but this clearly limited the age of the Sun, and hence presumably of the Earth, to be of order t_KH. On the other hand it was becoming clear from geological evidence, and from the time required for the evolution of the species, that the Earth had to be much older. An interesting description of this discussion was given by Badash (1989). As we now know the resolution of the problem came with the realization that the solar energy derives from nuclear reactions in the solar core.

It will be shown in section 4.4 that the gravitational binding energy and the total thermal energy of a star have the same magnitude. Hence t_KH also gives the time it would take for a star to radiate its thermal energy at a given luminosity, whence the name *thermal time scale*.

1.1.3 The nuclear time scale

During most of the life of a star the energy it radiates comes from the fusion of hydrogen into helium. The total amount of energy that is available from this reaction may be

estimated as $\Delta E = \Delta m\, \tilde{c}^2$, where Δm is the difference in mass between the original hydrogen and the resulting helium, and $\tilde{c}$ is the speed of light. In the fusion of hydrogen to helium about 0.7 per cent of the mass is lost. The reaction occurs only in the inner about 10 per cent of the mass of the star. Hence the total amount of energy available is approximately $7 \times 10^{-4} M\tilde{c}^2$, and the corresponding timescale is

$$t_{\rm nuc} = 7 \times 10^{-4} \frac{M\tilde{c}^2}{L_{\rm s}} \ , \tag{1.7}$$

or

$$t_{\rm nuc} = 10^{10}\,{\rm years} \quad \left(\frac{M}{{\rm M}_\odot}\right) \left(\frac{L_{\rm s}}{{\rm L}_\odot}\right)^{-1} \ . \tag{1.8}$$

Since a star spends by far the largest part of its life in the hydrogen burning phase, $t_{\rm nuc}$ provides a measure of the total lifetime of a star. It is shown in Chapter 7 that the luminosity is a steeply increasing function of stellar mass. Hence, the dependence on $L_{\rm s}$ is dominant in equation (1.8), and the nuclear time scale decreases rapidly with increasing mass. For a $30\,{\rm M}_\odot$ star the entire evolution, from birth to death, only lasts about 5 million years, whereas a star of $0.5\,{\rm M}_\odot$ has barely had time to begin evolving over the age of the Universe.

1.2 The life of stars

The evolution of a star is largely a fight between gravity and nuclear reactions. In addition to providing the energy output of stars, the nuclear reactions also cause the build-up of gradually heavier elements, starting from hydrogen and helium. In fact, essentially all other elements than hydrogen and helium are believed to have been formed in stellar interiors. The details of the fight depends critically on the mass of the star. Gravity is nearly always victorious in the end: when all the accessible nuclear fuel has been used up, the star ends as a tightly bound body, gradually cooling down. However, in the course of evolution parts of the star are often ejected; this enriches the interstellar gas with material that has undergone nuclear reactions and hence has an increased abundance of elements heavier than hydrogen and helium.

It is instructive to illustrate the evolution of stars in terms of observable properties. These are discussed in more detail in Chapter 2. Here it is enough to note that one can determine the luminosity $L_{\rm s}$ of a star if the amount of energy reaching Earth, as given by the apparent brightness of the star, and its distance are measured. Also, the temperature of the stellar atmosphere can be estimated from the distribution of energy in the spectrum of the star; it is often specified in terms of the *effective temperature* $T_{\rm eff}$, defined such that

$$L_{\rm s} = 4\pi\sigma T_{\rm eff}^4 R^2 \ , \tag{1.9}$$

where σ is the Stefan-Boltzmann constant.[3] The evolution of a star can then be illustrated in a diagram plotting luminosity against effective temperature, a so-called *Hertzsprung-Russell* (or HR) diagram, as shown in Figure 1.2; it is a convention that $T_{\rm eff}$ increases

[3] $T_{\rm eff}$ is the temperature that the star would have if it were radiating as a black body; although the stellar spectrum is in general rather different from a black-body spectrum, $T_{\rm eff}$ is nonetheless representative of the temperature in the surface layers of the star.

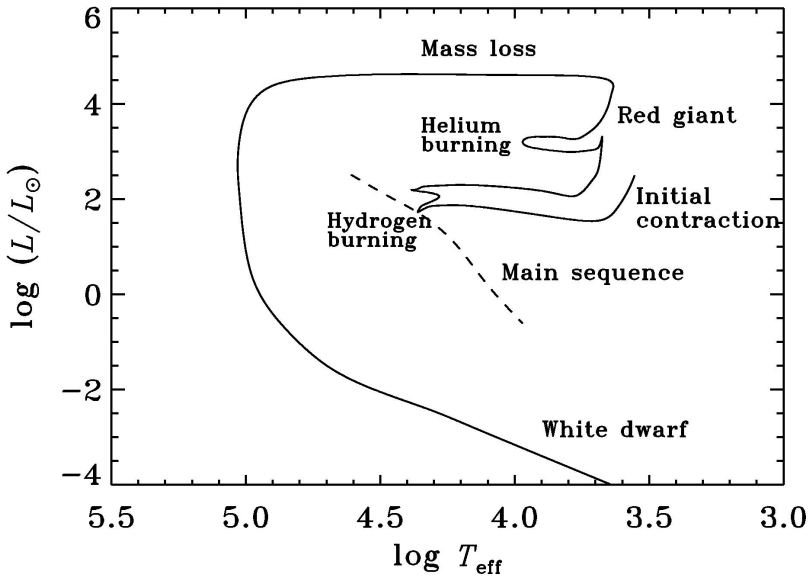

Figure 1.2: Schematic illustration of the evolution of a moderate-mass star. The effective temperature $T_{\rm eff}$ is in K, and the luminosity $L_{\rm s}$ is measured in units of the solar luminosity $\rm L_\odot$. The dashed line indicates the zero-age main sequence, corresponding to the onset of hydrogen burning.

towards the left. The schematic evolution track in this diagram has been roughly modelled on the results of detailed calculations for a $5\,\rm M_\odot$ star.

Stars are born from a contracting cloud of interstellar matter. As the cloud contracts, gravitational potential energy is released. Part of this energy is used to heat up the gas; in this way the cloud becomes hotter than its surroundings and starts to radiate energy away.[4] As long as there are no other sources of energy in the cloud, the energy that is lost through radiation must be compensated by further release of gravitational potential energy, *i.e.*, through further contraction. The rate of contraction is determined by the rate of energy loss. It is obvious that this phase occurs on something like the Kelvin-Helmholtz time scale discussed above. Due to the contraction the surface radius of the star decreases; since the luminosity is roughly constant during this phase, it follows from equation (1.9) that $T_{\rm eff}$ must increase, *i.e.*, the star moves to the left in the HR diagram.

This contraction continues up to the point where the temperature in the core of the star gets sufficiently high that nuclear reactions can take place, at a rate where the energy generated balances the radiation from the stellar surface. The temperature required is determined by the energy needed to penetrate the potential barrier established by the Coulomb repulsion between different nuclei. Hence the first nuclei to react are those with the lowest charge, *i.e.*, hydrogen, starting when the temperature reaches a few million degrees. At this point a number of reactions set in, the net effect of which is to fuse

[4]It is shown in section 4.4 that approximately half the energy liberated in the contraction goes to heating the gas, the remainder being radiated away.

hydrogen into helium,

$$4\,{}^1\mathrm{H} \rightarrow {}^4\mathrm{He} + 2\mathrm{e}^+ + 2\nu_\mathrm{e}\ . \tag{1.10}$$

It is worthwhile to consider this reaction in a little more detail. Because of charge conservation, two of the four protons on the left-hand side have to be converted into neutrons and positrons; the positrons are immediately annihilated by two electrons, so that the reaction can be thought of as a reaction where four hydrogen *atoms* fuse into one helium atom (although at the temperature in the stellar core the atoms are fully ionized, *i.e.*, separated into nuclei and free electrons). The reaction furthermore has to conserve the number of *leptons*, *i.e.*, light elementary particles; since two anti-leptons (the positrons) are created, this must be balanced by the creation of two leptons, the neutrinos. Thus, regardless of the path the reactions take, the fusion of four hydrogen atoms into one helium atom leads to the production of two neutrinos.

Once hydrogen burning in the core has been established, the contraction of the stars stops. Stars in this phase of their evolution are said to be on the *main sequence*. The duration of the phase is given by the nuclear time scale determined above; since this is the longest active phase of the life of the star, most of the "normal" stars that we observe within a given volume of space are main-sequence stars.[5] During main-sequence evolution the structure of a star gradually changes as hydrogen is used up in the core. The result is a contraction of the core and an expansion of the outer layers, accompanied by an increase in the luminosity. For example, the luminosity of the Sun has increased by about 30 per cent since it started the core hydrogen burning phase.[6]

The onset of nuclear burning puts a temporary halt on the tendency of gravity to make the star contract; but it is obvious that this is only effective until the time when hydrogen is exhausted in the core. At that point hydrogen burning stops in the core, although it continues in a shell around it. The core contracts, again releasing gravitational energy and heating up, while the outer parts of the star expand drastically and cool, until the star becomes a *red giant*, with a radius that may be as large as the distance between the Sun and the Earth. As in the case of the initial contraction, the contraction of the core may be halted when its temperature becomes high enough for helium to react, to produce carbon:

$$3\,{}^4\mathrm{He} \rightarrow {}^{12}\mathrm{C}\ , \tag{1.11}$$

possibly followed by

$${}^4\mathrm{He} + {}^{12}\mathrm{C} \rightarrow {}^{16}\mathrm{O}\ . \tag{1.12}$$

The result of this is to revert the previous evolution: the core expands somewhat, the outer layers contract and heat up, and the star settles down on the *helium-burning main sequence*, while still maintaining a hydrogen-burning shell.

When helium is exhausted in the core, the history to some extent repeats itself: gravity again gets the upper hand, and the core, which now consists mainly of carbon and oxygen, contracts and heats up, surrounded by a helium-burning shell and, further out, possibly still a hydrogen-burning shell. The subsequent evolution depends crucially on the mass of the star. If the mass is less than about $10\,\mathrm{M}_\odot$, the core never becomes hot enough for the next nuclear reaction (between two carbon nuclei) to start; this is the case illustrated in

[5] After the end of nuclear burning most stars survive essentially forever as cooling white dwarfs; see below.

[6] A fact which has caused some embarrassment for modellers of the Earth's climate; see section 11.4.3.

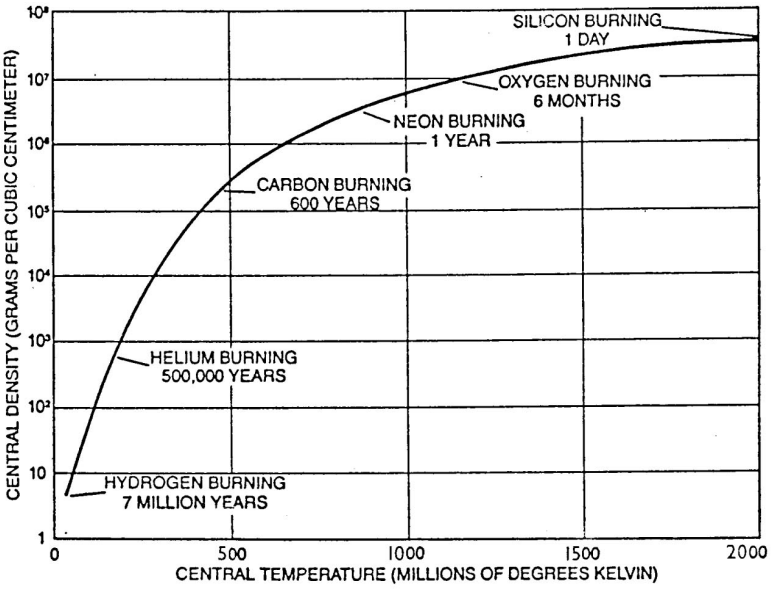

Figure 1.3: Evolution of a massive star is a steadily accelerating process toward higher temperature and density in the core. For the most of the star's lifetime the primary energy source is the fusion of hydrogen nuclei to form helium. When the hydrogen in the core is exhausted, the core contracts, which heats it enough to ignite the fusion of helium into carbon. This cycle then repeats, at a steadily increasing pace, through the burning of carbon, neon, oxygen and silicon. The final stage of silicon fusion yields a core of iron, from which no further energy can be extracted by nuclear reactions. Hence the iron core cannot resist gravitational collapse, leading to a supernova explosion. The sequence shown is for a $25\,M_\odot$ star. (From Bethe & Brown 1985).

Figure 1.2. The core continues to contract and the outer layers expand until the star enters a second red giant phase. At this point an instability develops between the hydrogen- and helium-burning shells. It is thought that this instability leads to the loss of large amounts of mass from the star, undoubtedly aided by the large luminosity and radius of the star. The mass that is lost ends up as a *planetary nebula* and is later dispersed into the interstellar medium; this leaves behind the carbon-oxygen core which at that point has contracted to a radius comparable with the radius of the Earth, but is still extremely hot; such an object is observed as a *white dwarf*. It continues to radiate by losing its internal thermal energy, a process that lasts essentially forever. The oldest observed "white" dwarfs (which in fact have effective temperatures of about 4600 K and hence appear quite red) have ages of about 10^{10} years, roughly corresponding to the age of the Galaxy.

For more massive stars, the carbon-oxygen core heats up sufficiently to start the next type of nuclear reactions. The star continues through a sequence of nuclear burning phases of gradually heavier elements, interspersed by phases of gravitational contraction. The evolution of a $25\,M_\odot$ star is summarized in Figure 1.3; it is particularly striking that the phases of the evolution following carbon burning last only about a year.

The burning of heavier and heavier elements has to end when the material of the core has been transformed into elements in the iron group: the nuclear binding energy per nucleon is at its largest for these elements, and hence fusion into even heavier elements *requires* energy instead of releasing it. At that point gravity has won in the core; the core continues to contract and heat up, until the temperature gets so high that the iron nuclei are dissociated into protons and neutrons. The drastic increase in density forces the electrons and protons in the gas to recombine to neutrons, and the density gets so high that the neutrons essentially touch each other. At that point the core can contract no further; the result is a bounce which propagates out through the outer parts of the star as a shock-wave, expelling them in a *supernova explosion*, in which the star for a few days becomes as luminous as all the stars in a normal galaxy combined. The energy derives from the gravitational energy released by the collapse of the core. In the reactions taking place during the explosion many neutron-rich nuclei are formed.

The fate of the core depends on its mass. If the core mass is less than about $2\,M_\odot$ a stable configuration is formed consisting almost entirely of neutrons; this has a radius of only about 10 km. Observational evidence for such *neutron stars* has been found in the *pulsars* which are rapidly spinning neutron stars emitting radio pulses with a very precisely defined period. If the core mass is greater, even the pressure of neutrons cannot withstand gravity, and the core collapses into a black hole, where matter is essentially crushed out of existence. The ultimate victory of gravity!

An excellent and somewhat more detailed description of stellar evolution, with special emphasis on supernova explosions, was given by Woosley & Weaver (1989).

The overall theme of this picture of stellar evolution is the fusion of lighter elements into heavier. If there had been no loss of mass from the stars the creation of heavy elements would have had no further consequences: the elements formed would remain locked into the stellar interiors. However, this is evidently not the case: mass-loss in less massive stars, or supernova explosions of massive stars, enrich the interstellar matter by material that has undergone nuclear burning. This adds elements heavier than hydrogen and helium to the gas out of which new stars are formed. It is believed that essentially all elements other than hydrogen and helium have been created and distributed in this way. There is in fact observational evidence that the abundance of heavy elements has increased during the evolution of our Galaxy.

1.3 The physics of stellar interiors

The evolution sketched in the previous section is based on a large number of very complex numerical calculations. These, in turn, depend on knowledge and assumptions about the properties of stellar interiors.

To make the computations even possible, drastic simplifications are required, relative to the complex phenomena that might occur in real stars. The stars are assumed to be spherically symmetric; thus effects of rotation, which probably takes place in all stars at some level and which must lead to departures from spherical symmetry, are neglected. The same is true for large-scale magnetic fields, which could also have an effect on the structure of the stars. Convective motions (to be discussed below), which probably take place in almost all stars, are treated very crudely. Other instabilities which may develop in the star and which could cause mixing between the core, where nuclear burning is taking

place, and the outer parts of the star, are generally ignored. Mass-loss from the star is normally either ignored or treated very approximately.

These complicating effects have been studied under other simplifying assumptions, but in most calculations of stellar evolution, including those described in these notes, they are ignored. One reason for this is that to include them all would make the computations completely intractable. A more fundamental difficulty is that we simply do not know how to handle them consistently; these problems are still very much at the frontier of current work on stellar evolution. And finally, it is probably wise to try to understand simplified stellar evolution theory, and to test it against observations, before trying to incorporate the complications.

Given these simplifications, the main features which determine the structure and evolution of stars are the *microscopic properties* of stellar matter, more specifically its equation of state, the transport of radiation through it and the nuclear reactions. The equation of state determines the relations between the various thermodynamic properties, such as the temperature, density and pressure, of the gas that stars are made of. At the most elementary level (which is adequate for much of these notes) this is very simple: due to the high temperature the gas is fully ionized and behaves essentially as an ideal gas. To carry out realistic calculations of stellar models, however, complicating effects have to be included. Near the stellar surface the gas is only partially ionized, and hence its properties depend on the degree of ionization, which in turn is determined by the interaction between the various components in the gas. At even lower temperature, in the atmospheres of cool stars, the formation of molecules also affects the equation of state. On the other hand, in the cores of massive stars in advanced stages of evolution the temperature may get so high that the formation of electron-positron pairs has to be taken into account, as well as processes involving the production of, and energy loss through, neutrinos. Also, at high densities quantum-mechanical effects set in, leading to the properties of the gas being dominated by *degenerate electrons*.

The energy transport is carried out by radiation under many circumstances, and hence is determined by the interaction between radiation and matter, as specified by the *absorption coefficient* or *opacity* of the matter. This depends on the detailed distribution of the atoms in the gas on energy levels, and hence on the equation of state of the gas, on the cross-section for absorption in each level in the atoms, and on the interaction between the atoms. Thus the calculation of opacities is a major undertaking. As an example it may be mentioned that for some years a large number of scientists in several countries have been engaged in collecting the atomic data and recomputing the equation of state with the goal of setting up new tables of opacities; even so, the resulting tables are restricted to relatively low densities where the interactions between the atoms can be ignored (for an overview of issues related to the equation of state and opacity see, for example, Däppen & Guzik 2000).

When the opacity or the amount of energy to be transported gets too high, energy transport by radiation can no longer be achieved in a stable manner. It is replaced by transport through motions in the gas, the so-called *convection*, which is quite similar to the motions in a pot of water being heated. Even convection in a pot of water gives rise to complex hydrodynamical phenomena which are far from understood; hence it is not surprising that convection in stars is still an area of considerable uncertainty in studies of stellar structure. Besides its effect on the energy transport, convection also affects the evolution of a star by mixing material; in stars with convective cores, for example, the

composition is homogenized in regions of nuclear burning, with visible consequences on the evolution of the stars.[7]

The rates of nuclear reactions are determined by the speed with which the nuclei move relative to each other which in turn depends on the temperature, and by the cross-sections for the reactions which again are functions of the relative energy of the nuclei. The cross-sections can in principle be measured experimentally; a problem is, however, that reactions under stellar conditions often occur at such low energies that the corresponding rate of reactions under laboratory conditions is almost unmeasurably small. Hence a considerable amount of theoretical extrapolation is required to determine the stellar rates. Furthermore, the reactions are also affected by the presence of other particles in the gas, which may partly shield the charges of the nuclei and hence increase the reaction rates; this again depends on the thermodynamic state of the gas.

It is obvious that the description of the physical state of stellar interiors gives rise to a number of difficult problems, which are still being investigated. Fortunately, it is possible to obtain a basic understanding of the evolution of stars without going into such detail. Thus, in the following we shall consider only the simplest possible physics, while occasionally hinting at some of the complications.

1.4 Tests of stellar evolution calculations

Except for the Sun and a few other stars, it is difficult to observe detailed properties of individual stars. Hence much of the testing of the results of stellar evolution calculations is of a statistical nature, from observation of the properties of stars in *stellar clusters*. Stars in a given cluster can be assumed to have the same age and chemical composition and hence, at least within the framework of the simplified description discussed in the previous section, differ only in their mass. From comparisons between the observations and the properties of stellar models of different masses evolved to the same age it is possible to identify many of the phases of stellar evolution found in the calculations.

Information about the structure of individual stars can be obtained in the cases where the stars are observed to pulsate, since the pulsation periods depend on the structure of the star. If only a single period of pulsation is observed, this essentially provides a measure of the dynamical time scale $t_{\rm dyn}$ of the star (*cf.* equation (1.2)). For example, some red giants are observed to pulsate with periods of more than a year, thus confirming their very large radii. The amount of information increases with the number of individual pulsation periods observed. In the case of the Sun many thousands of periods have been determined, and this has made it possible to measure properties of the solar interior in considerable detail, thus providing a very good test of calculations of solar structure and evolution.

Finally, the neutrinos produced in nuclear reactions (such as the fusion of hydrogen to helium; *cf.* equation (1.10)) escape from the star essentially without being absorbed, because of the extremely small cross-sections of neutrino reactions. Hence, by observing the flux of neutrinos from the Sun we may get a direct measure of the rate of reactions in the solar core. A complication is that the so-called electron neutrinos produced in the Sun may be changed, through interaction with matter in the Sun, into other types of neutrinos; this interaction depends on the detailed properties of the neutrinos. Observations

[7] As discussed in Chapter 12, the small leftward excursion, or "hook", visible in Figure 1.2 at the end of hydrogen burning is a result of the presence of a convective core.

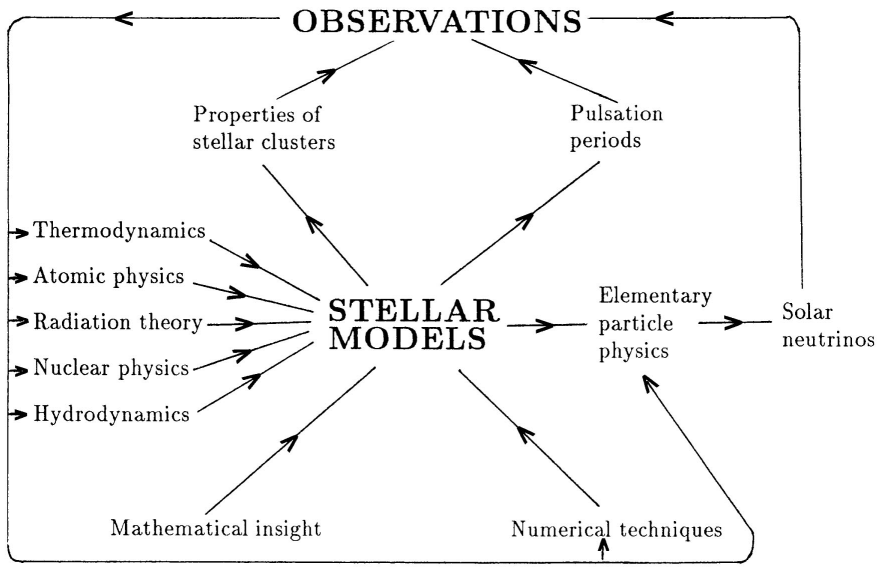

Figure 1.4: Schematic illustration of the relation between physics, stellar models and observations. The physics is used as input to stellar model calculations. The stellar models can be used to predict observable quantities, such as properties of stellar clusters, pulsation periods or the flux of neutrinos from the Sun; the latter prediction requires additional physical information about the properties of the neutrino. When these predictions are compared with the observations, corrections may be required to the input physics, the description of the neutrino or (in the case of programming errors) to the numerical techniques. One may hope that this iteration process will eventually converge!

of these neutrino types became possible around 2000; when combined with the information obtained from the analysis of the observed oscillation periods of the Sun stringent constraints on the neutrino interactions have been obtained.

The computed stellar models evidently depend on the assumed physical properties of matter, and on the assumptions about stellar structure, that went into the calculations. Thus by comparing the results of the calculations with the different kinds of observations we are effectively testing the underlying physics. Among many examples may be mentioned that the observed solar pulsation periods are very sensitive to the details of the equation of state and opacities used in the computation of solar models and hence offer a way of inferring properties of plasmas under quite extreme conditions; and that the interaction of neutrinos with matter can probably *only* be studied experimentally by comparing the observed number of neutrinos with the number of neutrinos generated in the solar core, assuming that conditions in the core can be determined from the pulsation periods. From the point of view of basic physics this is probably the most important aspect of stellar evolution theory; it is illustrated schematically in Figure 1.4.

1.5 Bibliographical notes

There are four "classical" books in the theory of stellar structure and evolution. The first comprehensive description of the properties of stars, on the basis of thermodynamics and hydrostatic equilibrium, was given by Emden (1907). A much more detailed treatment was given by Eddington (1930), who included discussions of quantum mechanical effects in the transfer of radiation, and showed how one could predict the luminosities of stars on this basis. In terms of physical insight, and certainly in terms of sheer quality of writing, this book has hardly been surpassed. However, at the time when it was written the sources of stellar energy production had not been identified. Chandrasekhar (1939) goes into considerably more mathematical detail, and presents a comprehensive treatment of the thermodynamics of stellar matter, including one of the first discussions of electron degeneracy. Finally, the book by Schwarzschild (1958) summarizes the physics of stellar interiors, including the nuclear reactions, and discusses results of numerical calculations which up to that point had been done with simple calculators. It is interesting that in all these cases a great deal of emphasis is put on understanding the properties of stars in simple terms. This is of course partly a result of necessity, given that large-scale computations were not feasible; the result, however, is to convey a level of insight which has to some extent been lost in later work.

Schwarzschild's book came at the time when electronic computers were just beginning to be used for stellar evolution calculations. Over the next decade this completely revolutionized the field, resulting in large-scale calculations of realistic stellar models to late stages of evolution, and including very detailed physics. A substantial number of books have been written based on these efforts. A general trend, however, has been to describe the physics of the calculations, and the computational techniques, in a great deal of detail, whereas the *results* of the calculations have been dealt with relatively briefly, and little attempt has been made to understand them. Among these books may be mentioned Clayton (1968), who in particular gives a good introduction to the treatment of nuclear reactions and the synthesis of elements in stars; and the two-volume work by Cox & Giuli (1968), who treat the physics in almost overwhelming detail.

Kippenhahn, Weigert & Weiss (2012) give a good combination of treatment of the physics, although not in great detail, with descriptions of the numerical models including attempts to understand them in terms of simple approximations. This marks a tendency away from the fascination with numerical details and towards an understanding of the broader principles, in the tradition of the earlier works.

The technical literature on stellar structure and evolution is very extensive, and I make no attempt to give reasonably comprehensive references to it. However, in the following I quite often refer to articles in *Scientific American* which expand on some of the subjects treated here. While these articles are at a considerably lower technical level than the present notes, they very often provide good overviews of particular subjects, usually with suggestions for further reading. Detailed reviews of the subjects treated here, as well as all other branches of astrophysics, can be found in the series *Annual Review of Astronomy and Astrophysics*.

The best way to gain a deeper understanding of stellar structure and evolution is to carry out stellar modelling and analyse the results. A very flexible and reasonably user-friendly tool for this is the `MESA` package (see Paxton *et al.*, 2019, and references therein), the result of a decade of development by a substantial group of developers. Details on the

code and instructions for installing and running it are available at `http://mesa.sourceforge.net/`.

Chapter 2

Observable properties of stars

2.1 Introduction

No theoretical investigation is of much interest if its results cannot be compared with experiments or observations. The same is certainly true for calculations of stellar evolution. Thus it is important to consider the data that may be used to test the results of the calculations.

It is obvious that we cannot perform experiments on stars, or take surface samples from them.[1] Thus we are restricted to studying them through the radiation they emit, or possibly through the effect of their gravitational field. The radiation that we can detect is, with a few exceptions discussed below, *electromagnetic*. A further restriction is that almost all stars can be observed only as points of light. The most obvious exception is the Sun, where very detailed observations are possible. This enables us to investigate in detail phenomena on the Sun that can be inferred only indirectly in other stars; furthermore it has allowed us to obtain seismic measurements of the structure and motions of the solar interior. However, the Sun is only one star, caught at a particular moment in its evolution. It has been possible to measure the diameter directly for some stars, and in a few cases also to observe very large-scale features on the stellar surface, although the interpretation of these observations is somewhat questionable. In all other cases we have determinations only of the position of the star in the sky, and of the properties of the emitted radiation, integrated over the surface of the star. As we shall see, even these limited data allow us to learn a great deal about the stars, and hence to test computations of stellar evolution.

2.2 Stellar positions and distances

Stellar positions have been measured since antiquity. The most basic quantity is the *angular distance* between two stars, *i.e.*, the angle between the lines-of-sight to the stars. This is traditionally measured in degrees ($^\circ$) or its subdivisions arcminutes ($'$) or arcseconds ($''$), defined by

$$1^\circ = 60' = 3600'' \tag{2.1}$$

(note also that 1 radian = $206265''$). Under the best conditions an optical telescope on the surface of the Earth can separate two stars that are at a distance of about $0.1''$, although

[1] However, in a nice combination of the Icaros and Prometheus myths, Bradbury (1953) wrote a short story about a mission to return a sample of the Sun.

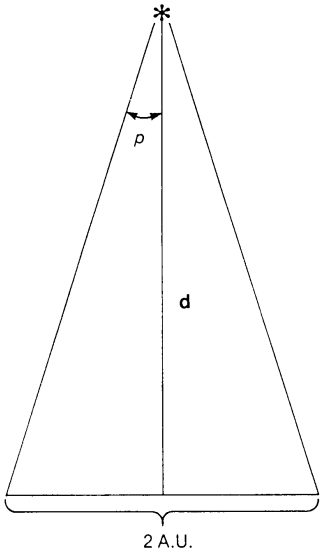

Figure 2.1: Parallax p of a star at a distance d from the Earth.

with care angular separations can be measured with somewhat better precision.[2]

From the point of view of investigating stellar structure and evolution, the positions of stars are in themselves of little interest; however, measurements of the change in apparent position as the Earth moves in its orbit around the Sun provide our only direct determinations of distances to stars other than the Sun.[3] The change in direction to the star, as measured relative to very distant stars, as the Earth moves from a point in its orbit to the opposite point is defined to be $2p$, where p is the *parallax* of the star. Hence p is the angle subtended by the radius of the Earth's orbit as seen from the star (*cf.* Figure 2.1), so that

$$\tan p = \frac{1\,\mathrm{A.U.}}{d} \ , \tag{2.2}$$

where d is the distance to the star, and $1\,\mathrm{A.U.} = 1.496 \times 10^{13}$ cm is the radius of the Earth's orbit. Since p is a very small angle equation (2.2) gives

$$d \simeq \frac{1\,\mathrm{A.U.}}{p\ (\mathrm{radian})} = \frac{1\,\mathrm{pc}}{p''} \ , \tag{2.3}$$

where p'' is the parallax measured in arcsec, and we have introduced the distance measure *parsec* (or pc), where $1\,\mathrm{pc} = 206265\,\mathrm{A.U.} = 3.086 \times 10^{18}$ cm.

The closest star other than the Sun has a parallax of $0.76''$, and hence a distance of 1.32 pc. The best terrestrial observations yield parallaxes with a precision of about $0.002 - 0.01''$, although the best results are typically only available for a limited number of stars (*e.g.* Harrington *et al.* 1993). This allows determination of distances of a few thousand stars in the solar neighbourhood. Much better observations and more extensive results

[2]The magnitude of $1''$ is illustrated by the fact that it corresponds to the angular extent of a Danish 25 øre (roughly corresponding in size to a British or US penny) seen at a distance of 3.4 km.

[3]Distances within the solar system are known very accurately from radar measurements and from the motion of space-probes. This allows a determination of the distance from the Earth to the Sun.

have been obtained from the satellite Hipparcos, which was launched by the European Space Agency (ESA) in 1989. Hipparcos has determined parallaxes for about 10^5 stars with a precision of better than $0.001''$ in some cases. An extensive overview of the mission was provided by van Leeuwen (1997), while summaries of the observations and applications of the results to a variety of astrophysical problems have been given by Kovalevsky (1998), Reid (1999) and Lebreton (2000). Hipparcos was followed by the much more ambitious *Gaia* mission, launched by ESA in 2013 (for a review, see Brown 2021). Here a precision down to of order $10^{-5}\,''$ is reached, and more than one billion (10^9) stars are observed for parallax and proper motion, as well as in two-colour photometry and, for stars brighter than Gaia magnitude 14, detailed spectroscopy and radial-velocity determination. These data, from the third release in June 2022, are playing a huge role towards the understanding of the structure and evolution of the Milky Way Galaxy.

2.3 Stellar brightness

In early star catalogues stars were classified according to their *magnitude*, the brightest stars having magnitude 0 and the faintest stars visible to the naked eye having magnitude 6. This scheme for describing the brightness of stars has essentially been maintained, but has been made precise.

What is measured on the Earth is the *apparent luminosity* of a star, characterized by the local flux l, *i.e.*, the energy from the star that passes through a unit area (orthogonal to the direction to the star) in unit time. Hence the unit for l is $\mathrm{erg\,cm^{-2}\,sec^{-1}}$. It was found that this precisely defined quantity could be related to the loosely defined magnitude scale by *defining* the apparent magnitude m of a star as

$$m = -2.5 \log l + K_1 \ , \tag{2.4}$$

where K_1 is a constant which is determined by specifying the magnitude of a given star, say; also "log" is the logarithm to base 10. The reason for the "–" in the definition of m is evidently that the magnitude of stars, according to the old definition, increases as the stars get fainter.[4] Since the magnitude is defined only to within a constant, a more convenient form of equation (2.4) is

$$m_1 - m_2 = -2.5 \log \left(\frac{l_1}{l_2} \right) \ , \tag{2.5}$$

where l_1 and l_2 are the apparent luminosities of two stars, and m_1 and m_2 are the corresponding magnitudes.

For the purpose of comparing with stellar evolution calculations a much more interesting quantity is the *absolute luminosity* L_s, *i.e.*, the total amount of energy radiated by the star per unit time. If we assume that the radiation is emitted isotropically,[5] that there is no absorption between the star and us, and that all the energy reaching the detector is measured, then

$$l = \frac{L_\mathrm{s}}{4\pi d^2} \ , \tag{2.6}$$

[4] For a discussion of the origins of the magnitude scale, see Hearnshaw (1992).

[5] *i.e.*, equally in all directions.

where d is the distance to the star. Corresponding to the apparent magnitude m we introduce the *absolute magnitude* M, by

$$M = -2.5 \log L_{\rm s} + K_2 \ , \tag{2.7}$$

where K_2 is another constant. From equations (2.4), (2.6) and (2.7) we then obtain a relation between m and M. It is conventional to choose the constant K_2 such that this relation has the form

$$m = M + 5 \log d - 5 \ , \tag{2.8}$$

when d is measured in parsec. Thus M corresponds to the apparent magnitude the star would have had if it had been at a distance of 10 pc.

Exercise 2.1:

Show that one can obtain a relation of the form (2.8) by suitable choice of K_2.

It is obvious that the description of a star's brightness in terms of its magnitude is entirely conventional, and for the uninitiated somewhat awkward. However, it does reflect one important feature of observations of stellar brightness, namely that it is quite difficult to determine the amount of energy received from a given star, since this requires an absolute calibration of the measuring device. It is far easier to measure the ratio between the luminosities of two stars, and hence their magnitude difference. Once the zero-point of the magnitude scale has been established by arbitrarily assigning a given magnitude to a given star, one can then determine the magnitudes of other stars.

In equation (2.6) it was assumed that all the energy emitted by the star in the direction of the detector was measured. In fact, we must take into account absorption of the light from the star, not only in interstellar space but also through the Earth's atmosphere and in the instrument used to measure the light. Also, the absorption and the sensitivity of the detector depend on the wavelength of the light. Finally, we are interested in measuring not only the total amount of energy coming from the star, but also its distribution with wavelength. Thus the description of stellar magnitudes given above has to be generalized.

We can characterize the distribution of energy with the wavelength λ or frequency ν of the radiation by the apparent specific luminosity l_λ or l_ν defined such that, in the absence of atmospheric and instrumental absorption, the energy per unit area and time received in the wavelength interval $\mathrm{d}\lambda$ (or the frequency interval $\mathrm{d}\nu$) is $l_\lambda \mathrm{d}\lambda$ (or $l_\nu \mathrm{d}\nu$). The total apparent luminosity (also called the bolometric luminosity) is

$$l_{\rm bol} = \int_0^\infty l_\lambda \mathrm{d}\lambda = \int_0^\infty l_\nu \mathrm{d}\nu \ ; \tag{2.9}$$

in the absence of interstellar absorption $l_{\rm bol}$ is related to the absolute luminosity of the star through equation (2.6).

Exercise 2.2:

Find the relation between l_λ and l_ν, by using $\lambda\nu = \tilde{c}$, where $\tilde{c}$ is the speed of light.

The measured luminosity can now be characterized by a *sensitivity function* S_λ which depends on the absorption in the atmosphere and instrument and on the sensitivity of the detector. For a given S_λ we measure the luminosity

$$l_S = \int_0^\infty S_\lambda l_\lambda \mathrm{d}\lambda \ , \tag{2.10}$$

and hence the magnitude

$$m_S = -2.5 \log l_S + K_S \ . \tag{2.11}$$

Note in particular that the constant depends on S_λ and hence on the particular instrument which is being used. As before, K_S is determined by assigning a given magnitude to a given star. To m_S corresponds the absolute magnitude M_S, given as in equation (2.8) by

$$m_S = M_S + 5 \log d - 5 \ . \tag{2.12}$$

Some indication of the distribution of luminosity with wavelength can be obtained by observing the star through differently-coloured filters. To enable comparisons between results obtained at different observatories, standard sets of filters are used. A commonly used system is the so-called UBV system. This is characterized by sensitivity functions $S_{U,\lambda}$, $S_{B,\lambda}$ and $S_{V,\lambda}$, where the ranges in sensitivity are roughly

Ultraviolet	(U)	3000 – 4000 Å
Blue	(B)	3500 – 5500 Å
Visual	(V)	4800 – 6500 Å

Here U, B and V are used to denote the apparent magnitudes corresponding to these filters, and the corresponding apparent luminosities and absolute magnitudes are denoted l_U, l_B and l_V, and M_U, M_B and M_V.

To characterize the distribution of energy with wavelength, one introduces the *colour indices* $U - B$ and $B - V$, so that, for example,

$$U - B = 2.5 \log \left(\frac{l_B}{l_U} \right) + K_U - K_B \ , \tag{2.13}$$

where K_U and K_B are the constants in the definition of the U and B magnitudes. In the UBV system the constants are chosen such that $U - B = B - V = 0$ for a particular type of star (the so-called A0 dwarf stars; see section 2.5.2). For the Sun the colour indices are then

$$U - B = 0.13 \ , \qquad B - V = 0.65 \ . \tag{2.14}$$

Since the filters defining the UBV magnitudes let through light over fairly broad wavelength ranges, the magnitudes and colour indices can be measured even for very faint stars or galaxies. Furthermore, in the absence of interstellar absorption the colour indices are independent of the distance to the star, which is most often not known. Hence they can be used to characterize the intrinsic properties of a star.

Exercise 2.3:

Show that the colour indices are independent of distance.

The colour index is predominantly determined by the surface temperature of the star. Hotter stars radiate more of the energy at short wavelengths; hence their U magnitude tends to be low (recall that the magnitude decreases as the luminosity increases), relative to their B magnitude, and so they have a low colour index $U - B$, relative to cooler stars; the same is true for the index $B - V$. To describe the relation between temperature and colour indices more precisely we assume, as a first rough approximation, that the star radiates as a black body with a temperature T. Then the emission from the stellar surface is given by the Planck function, and it may be shown that the apparent luminosity of the star is

$$l_\lambda = \frac{2\pi h\tilde{c}^2}{\lambda^5} \frac{1}{\exp\left(\dfrac{h\tilde{c}}{\lambda k_{\rm B} T}\right) - 1} \left(\frac{R}{d}\right)^2 \; ; \tag{2.15}$$

here h is Planck's constant, $k_{\rm B}$ is Boltzmann's constant, and R is the radius of the star. A convenient approximation to this expression (the so-called Wien's approximation) is obtained for relatively short wavelengths where the exponential term dominates in the denominator in equation (2.15):

$$l_\lambda = \frac{2\pi h\tilde{c}^2}{\lambda^5} \exp\left(-\frac{h\tilde{c}}{\lambda k_{\rm B} T}\right) \left(\frac{R}{d}\right)^2 \; . \tag{2.16}$$

Exercise 2.4:

Show that the location $\lambda_{\rm max}$ of the maximum of l_λ as a function of λ satisfies

$$\lambda_{\rm max} T = \textit{constant} \; . \tag{2.17}$$

Find the value of the constant for Wien's approximation (easy) and for the full expression (more difficult). The answer to the last question is

$$\lambda_{\rm max} = \frac{2.8978 \times 10^7 \, \text{Å K}}{T} \; . \tag{2.18}$$

Equation (2.17) is known as *Wien's displacement law*.

Exercise 2.5:

Show that total apparent luminosity of the star, integrated over wavelength, may be written as

$$l_{\rm bol} = \sigma T^4 \left(\frac{R}{d}\right)^2 \; , \tag{2.19}$$

where σ is a constant (σ is the so-called *Stefan-Boltzmann constant*).

Equation (2.19) is known as the *Stefan-Boltzmann law*.

Even though real stars do not radiate as black bodies, it is conventional to describe their total energy emission by means of equation (2.19), by defining the *effective temperature* $T_{\rm eff}$ of the star such that

$$L_{\rm s} = 4\pi\sigma T_{\rm eff}^4 R^2 \,, \tag{2.20}$$

and

$$l_{\rm bol} = \sigma T_{\rm eff}^4 \left(\frac{R}{d}\right)^2 \,, \tag{2.21}$$

are exactly satisfied.

We can now use the black-body approximation to find the relation between stellar temperature and colour indices. In principle this requires that we know the sensitivity functions $S_{U,\lambda}$, $S_{B,\lambda}$ and $S_{V,\lambda}$. To simplify the problem, we approximate the sensitivity functions by delta-functions, so that the colour indices correspond to the luminosity at a single wavelength; this case is discussed in the following exercise.

Exercise 2.6:

Assume that the luminosity can be described by Wien's approximation, equation (2.16). Assume furthermore that the sensitivity functions can be approximated by delta-functions,

$$S_{i,\lambda} = \delta(\lambda - \lambda_i) \,,$$

where $i = U, B$ and V, and where

$$\lambda_U = 3700\,\text{Å} \,, \quad \lambda_B = 4450\,\text{Å} \,, \quad \lambda_V = 5500\,\text{Å} \,.$$

Finally use the solar colour indices given in equation (2.14) and take the surface temperature of the Sun to be 5778 K. Under these assumptions find and plot

i) $U - B$ and $B - V$ as functions of T.

ii) $U - B$ as a function of $B - V$.

From the results of this exercise it follows that the measurement of colour indices can be used to obtain an estimate of the surface temperature of a star, the so-called *colour temperature*. Since stars do not radiate like black bodies, the colour temperature is in general different from the effective temperature, although they are normally quite similar.

To get a measure of the total luminosity one introduces *the apparent bolometric magnitude*

$$m_{\rm bol} = -2.5 \log l_{\rm bol} + K_{\rm bol} \,. \tag{2.22}$$

This is related to the corresponding absolute bolometric magnitude $M_{\rm bol}$ by

$$m_{\rm bol} = M_{\rm bol} + 5 \log d - 5 \,; \tag{2.23}$$

$M_{\rm bol}$ is evidently directly determined by the total luminosity $L_{\rm s}$ of the star. Given the absorption in the atmosphere and instrument we obviously cannot measure the total apparent luminosity $l_{\rm bol}$ of a star directly.[6] Instead one introduces the *bolometric correction* B.C. such that

$$m_{\rm bol} = V + \text{B.C.} \; . \tag{2.24}$$

The bolometric correction depends on the sensitivity function $S_{V,\lambda}$ as well as on the distribution of luminosity with wavelength for the star, and hence on the stellar type. The constant in the definition of $m_{\rm bol}$ is chosen such that the maximum of B.C. over all stars is 0.

2.4 Interstellar absorption

The interstellar space contains matter, in the form of gas and dust, which affects the light on the way from a star to the observer. Thus, except for the nearest stars, we cannot immediately measure the intrinsic properties of the stars.

The interstellar absorption depends on the wavelength of the light, being strongest at short wavelengths.[7] Thus it changes not only the luminosity, and hence the magnitude of the star, but also its colour index. As a result of interstellar absorption, the relation between, for example, the apparent and absolute V-magnitude becomes

$$V = M_V + 5 \log d - 5 + A_V \; , \tag{2.25}$$

rather than equation (2.12), where A_V is the contribution from interstellar absorption (note that as absorption reduces the luminosity, it increases the magnitude; hence A_V is a positive quantity). Similarly the observed colour index $B - V$, for example, is related to the intrinsic colour index $(B - V)_0$ of the star by

$$B - V = (B - V)_0 + E(B - V) \; , \tag{2.26}$$

where $E(B-V) \equiv A_B - A_V$ is the so-called *colour excess*, which determines the interstellar reddening of the star.

The absorption A_V, A_B and A_U, and hence the colour excesses $E(B-V)$ and $E(U-B)$, obviously depend on the distance to the star and on the properties of the intervening stellar material. Since this is not known *a priori*, correcting for interstellar absorption may seem an impossible task. However, it has been found that although the amount of matter along the line of sight to the stars varies widely, the absorption per unit mass of the matter, and the variation of absorption with wavelength, are approximately independent of direction. As a result it may be shown that *ratios* between the absorption at different wavelength, and hence between the absorption and the colour excess, are largely independent of which star is observed. Typical values are

$$\frac{A_V}{E(B-V)} \simeq 3 \; , \qquad \frac{E(U-B)}{E(B-V)} \simeq 0.72 \; . \tag{2.27}$$

[6] The only exception is the case of the Sun, where it has been possible to measure the wavelength-integrated luminosity by means of a *radiometer*, which captures essentially all the radiant energy that falls on it. It was flown on the Solar Maximum Mission (SMM) satellite.

[7] The same is the case of scattering in the Earth's atmosphere; scattering of blue light is stronger than scattering of red light. This explains why the Sun looks red when it is about to set.

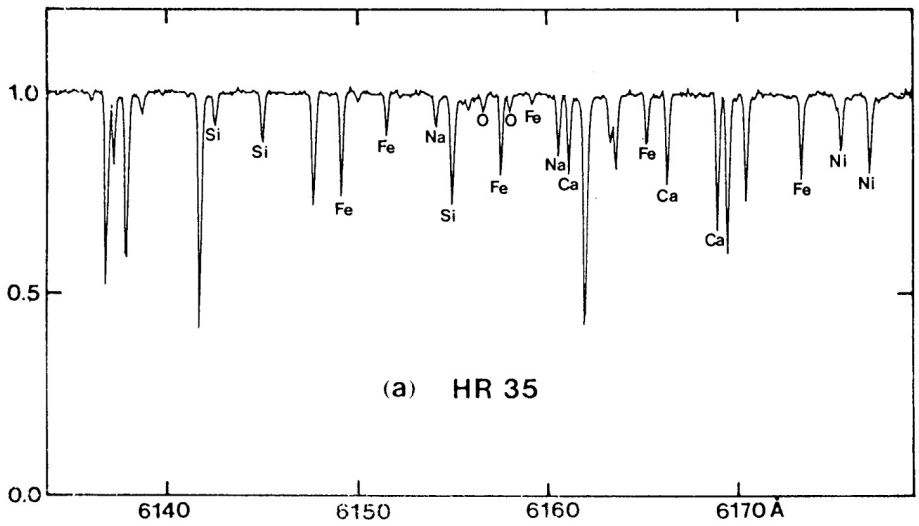

Figure 2.2: Representative high-resolution spectrum of a solar-type star, HR35. The plot shows specific luminosity l_λ plotted against wavelength; most of the lines in the spectrum are labelled with the corresponding element.

Hence, if we observe a star whose intrinsic colour index $(B-V)_0$ is known (*e.g.* because we have determined its spectral type, *cf.* section 2.5.2), we may use equation (2.26) to determine the colour excess. Then the interstellar absorption can be obtained from equation (2.27) as $A_V \simeq 3E(B-V)$. In this way it is possible to correct observed apparent magnitudes for interstellar absorption.

2.5 Spectral analysis

Luminosity measurements through coloured filters give only a rough indication of the distribution of energy with wavelength. To make a more detailed investigation the light of the star is dispersed according to wavelength in a *spectrograph*, to allow measurement of the intensity of the light as a function of wavelength. For the Sun, or observing bright stars with a large telescope, this can be done with a resolution of a small fraction of an Ångstrom. The resulting spectra contain a wealth of information about the star.

2.5.1 Spectral lines

Figure 2.2 shows a small segment of a typical stellar spectrum. It is dominated by *spectral lines* where the intensity is lower than in the surrounding *continuum*. The lines correspond to absorption in the stellar atmosphere, caused by excitation from one bound state to another, higher-lying state in one of the types of atoms which make up the atmosphere. In the line the absorption of radiation is stronger than in the surrounding continuum, and hence the stellar atmosphere is more opaque; as a result the light comes from a higher level in the atmosphere. Since the temperature normally decreases with increasing height in a stellar atmosphere, the emission of radiation is weaker in the line, which therefore

appears dark compared with the continuum.[8]

As seen on the star, the wavelength λ_{12} where the absorption takes place is determined by the difference between the energies E_1 and E_2 of the two levels in the atom responsible for the line:

$$\lambda_{12}^{-1} = \frac{E_2 - E_1}{h\tilde{c}} \ . \tag{2.28}$$

Thus, apart from possible line shifts (which are discussed in section 2.5.4 – 2.5.6 below), measurement of λ_{12} can be used to identify the element which causes the absorption, by comparison with tables of energy levels. In this way it has been possible to identify many, but not all, of the lines observed in stellar spectra; the identification is complicated by the fact that the atoms may be in states of ionization or excitation which are difficult to reproduce in the laboratory.

The *strength* of a line obviously depends on the number of atoms in the lower state from which the absorption takes place, as well as on the probability of absorption of a photon. The latter quantity can be measured, although often with difficulty. The number of atoms depends both on the total abundance of the given element in the stellar atmosphere, and on the fraction of the atoms which are in the right state. This fraction in turn depends on conditions in the stellar atmosphere, in particular the temperature; with increasing temperature the atoms are excited to higher states, or ionized. Thus lines corresponding to weakly bound electrons, which are typical of metals, disappear. Finally, it is possible to measure the *width* of the lines. This contains a contribution from the natural width of the line (corresponding to the quantum-mechanical indeterminacy of the energy levels); but the dominant contribution to the width comes from Doppler shift due to the motion of the atoms (*cf.* section 2.5.4) and from the disturbances of the atom from neighbouring atoms. The strength of the disturbances, and hence the linewidths, depend on the density of atoms in the stellar atmosphere; as discussed in Chapter 5, the density increases with increasing surface gravity

$$g = \frac{GM}{R^2} \ , \tag{2.29}$$

where G is the gravitational constant, and M is the mass of the star.[9] Hence the width of spectral lines provides some measure of the surface gravity.

2.5.2 Spectral classification

It is obvious that the interpretation of stellar spectra is a complicated problem. However, it is simplified by the fact that for many stars the chemical composition is roughly the same. Hence the spectrum is predominantly determined by the temperature and surface gravity of the stellar atmosphere. This justifies the *spectral classification* of stars, based on the appearance of their spectra. The temperature has the dominant effect on the spectrum; this is used to order the stars in a sequence of decreasing temperature, on the basis of which lines are found in the spectrum. The classification is described in Box 2.1, and illustrated schematically in Figure 2.3. For historical reason the different classes have

[8] This is obviously a very rough sketch of the line-forming process. Also it should be noticed that there are cases where the temperature, or at least the emission of radiation, increases with height in the atmosphere; in such cases the line may appear as an *emission line*, which is brighter than the continuum, or as an emission feature in the centre of an absorption line.

[9] It is unfortunate that the same symbol is traditionally used for absolute magnitude and stellar mass.

Box 2.1

Stellar spectral types

O	Hot stars; strong uv continuum; HeII absorption; lines of highly ionized atoms; H lines appear weakly; $T_{\rm eff} \gtrsim 25{,}000$ K.
B	HeI reaches maximum strength at B2; HeII vanishes beyond B0; H lines develop in late types; $12{,}000 \lesssim T_{\rm eff} \lesssim 30{,}000$ K.
A	H lines maximum at A0; CaII increases; weak neutral metal lines appear; $7{,}500 \lesssim T_{\rm eff} \lesssim 11{,}000$ K.
F	H lines weaken, but conspicious; CaII becomes stronger; metal lines increase in strength (both ions and neutrals); $6{,}000 \lesssim T_{\rm eff} \lesssim 7{,}500$ K.
G	CaII (H and K lines) become strong; solar types; Fe and metals strong; H lines weak; CH bands strengthen; $5{,}000 \lesssim T_{\rm eff} \lesssim 6{,}000$ K.
K	Metallic lines dominate; continuum becomes weak in the blue; molecular bands (CN, CH) develop; $3{,}500 \lesssim T_{\rm eff} \lesssim 5{,}000$ K.
M	TiO bands dominate; strong neutral metal lines; $T_{\rm eff} \lesssim 3{,}500$ K.

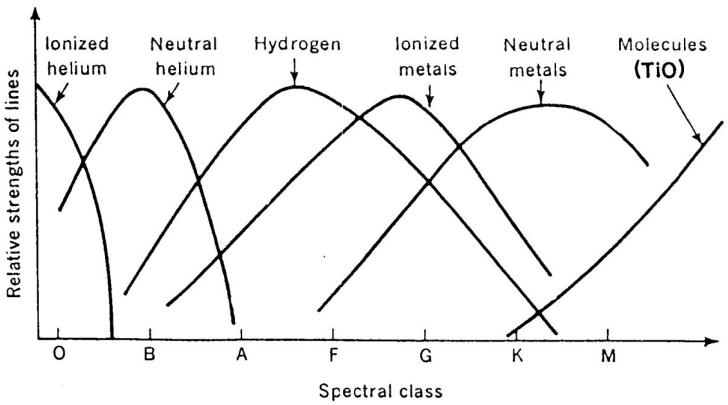

Figure 2.3: Schematic illustration of the relative strengths of spectral lines, as a function of spectral type. (From Abell 1964).

been assigned the letters O, B, A, F, G, K and M.[10] Each of these classes are subdivided into 10 sub-groups, labelled, for example, A0, A1, $\cdots$, A9. The first classes in the sequence (O and B) are referred to as *early* spectral types, whereas the last classes are referred to as *late* spectral types.

On the basis of the width of the lines the star is also assigned to one of five *luminosity classes*, labelled I – V. The classes are I (supergiants); II (bright giants); III (giants); IV (subgiants); and V (main sequence, or dwarf, stars). This sequence corresponds to increasing linewidth and hence increasing surface gravity. The reason that the classes are called luminosity classes (rather than gravity classes) is that stellar masses fall into a fairly narrow range, such that the dominant variation in g is caused by the variation in the stellar radius R; from equation (2.19) it follows that at a given temperature stars with large radius, and hence small g, have a high luminosity. Thus the star is given a combined labelling, called the *spectral type*, as *e.g.* an A0III star. The Sun is of spectral type G2V.

Spectral classification is normally carried out by visual inspection of relatively low-resolution photographic spectra. It provides a quick and convenient way of determining the overall properties of a large number of stars, and is commonly used to characterize a star; on the other hand it is essentially qualitative in nature. For more precise analyses it has been supplemented by accurate measurements of carefully chosen colour indices and spectral line strengths.

2.5.3 Stellar abundances

If conditions in the stellar atmosphere are known, the observed strengths of spectral lines can be used to determine the abundances of the elements in the atmosphere. In practice this requires the construction of a detailed theoretical model of the atmosphere, and the computation of the distribution of radiated intensity as a function of wavelength; the assumed abundances are varied until a satisfactory fit to the observations is achieved. Figure 2.4 shows an example of such a fit.

For almost all stars it is found that the composition is predominantly made up of hydrogen and helium, with all other elements making only a minor contribution. This motivates characterizing the composition by the abundances by mass X of hydrogen, Y of helium, and Z of all other (often, a little misleading, called *heavy*) elements. Obviously

$$X + Y + Z = 1 \, . \tag{2.30}$$

Furthermore, for most "normal" stars X appears to be in the range $0.70 - 0.73$.[11] On the other hand the total abundance of heavy elements varies widely, from $Z = 10^{-6}$ to about $Z = 0.04$.

This fact has important consequences for our understanding of the chemical evolution of the Universe. It is believed that hydrogen and helium, but essentially no other elements, were formed in the initial "Big Bang". This would account for the relative constancy of the hydrogen and helium abundances. All the heavy elements have been formed by

[10] This sequence is obviously difficult to remember; it helps to use the following attractive, if somewhat sexist, mnemonic:

Oh, Be A Fine Girl, Kiss Me .

[11] In fact, helium lines are only observed in the spectra of hot stars (*cf.* Box 2.1), and in some interstellar nebulae. Therefore the hydrogen and helium abundances of most stars, including the Sun, are somewhat uncertain.

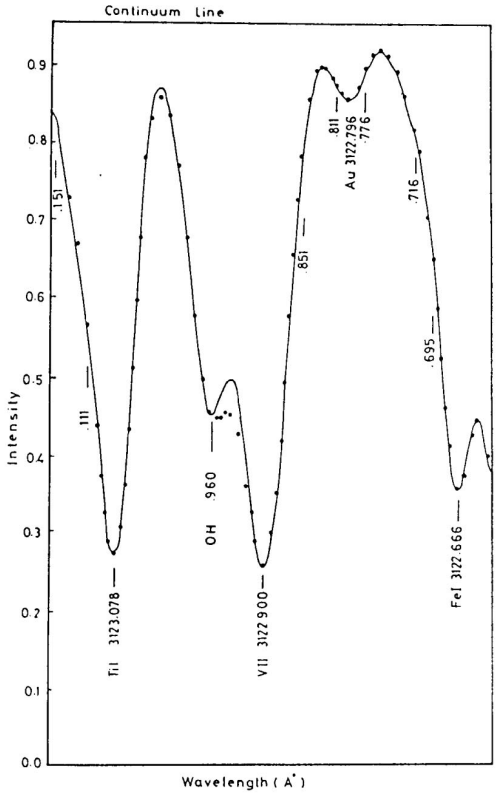

Figure 2.4: Observations (solid line) and numerical calculations (dots) for a very small segment of the solar spectrum. The abundance of gold in the calculations was adjusted to match the weak spectral line marked "Au 3122.796". This required a gold/hydrogen ratio of 9.0×10^{-12}. (From Youssef 1986).

nuclear reactions in stellar interiors; when the stars have lost large fractions of their mass, possibly through supernova explosions, the interstellar matter has been enriched by the heavy elements, which have therefore been incorporated into stars formed later. Thus the wide range of observed heavy element abundance can be interpreted as a result of widely differing stellar ages, the stars with very low Z having been formed before there had been a significant production of heavy elements.

The relative composition amongst the heavy elements is as a first rough approximation the same for all stars, which justifies that it is characterized by a single parameter; however, a more careful analysis reveals a systematic dependence of the relative composition on the total heavy element abundance. This must reveal properties of the processes that formed the heavy elements and mixed them into the interstellar medium; the details are still far from understood, however.

In some cases the observed abundances differ drastically from what is observed in most stars, with certain elements (for example rare earths) being enhanced by large factors relative to the remaining heavy elements. In some stars this can be understood in terms of *diffusion*, which selectively pushes certain elements towards the surface of the star, while other elements sink. In highly evolved stars it is also possible that elements produced by

nuclear reactions can be mixed to the surface. A particularly important example is the detection of the radioactively unstable element technetium in the atmospheres of some red giants. Such observations provide direct evidence for the occurrence of nuclear reactions in the stars, and are therefore of very great importance for our understanding of the synthesis of elements.

Stars in the Galaxy are divided into *populations* according to their heavy element abundance and their location and motion in the Galaxy. *Population I* stars are relatively rich in heavy elements; they are concentrated towards the disk of the Galaxy, and their motion is dominated by the common rotation of the Galaxy. *Population II* stars, on the other hand, are very poor in heavy elements; they are found at large distances from the disk of the Galaxy and have large random velocities. The interpretation of this division is that Population II stars were formed before the matter in the Galaxy collapsed into a disk, and that the Population I stars were formed in this disk. The detailed evolution of the Galaxy is still a matter of debate, however.

2.5.4 The Doppler shift

If the star moves relative to the observer in the direction of the line of sight the stellar spectral lines are shifted relative to the positions expected on the basis of the laboratory energy levels. The shift $\Delta\lambda_{\rm D}$ is approximately given by

$$\frac{\Delta\lambda_{\rm D}}{\lambda} = \frac{v_{\rm r}}{\tilde{c}} \, , \tag{2.31}$$

where $v_{\rm r}$ is the *radial velocity*, *i.e.*, the velocity in the direction of the line of sight, measured positive in the direction away from the observer. This effect allows the measurement of the motion of the star as a whole, or of the stellar surface as in the case of a pulsating star. Furthermore, the Doppler shift due to the random motion of atoms in a stellar atmosphere (caused by thermal motion, and possibly by large-scale motion due to convection; *cf.* Chapter 6) contributes to the width of the spectral lines. A further contribution from the Doppler shift may come from stellar rotation: since one side of a rotating star is moving towards the observer and the other away from the observer, the result is again a contribution to the line width which, in the case of rapidly rotating stars, may be dominant.

Exercise 2.7:

The average kinetic energy of an atom in a gas of temperature T is $\frac{3}{2}\, k_{\rm B} T$. Find the root-mean-square velocity of a hydrogen atom and an iron atom in a gas of temperature 5778 K (the effective temperature for the solar atmosphere). What are the corresponding Doppler shifts, for a spectral line at 5000 Å?

2.5.5 The gravitational redshift

It follows from the theory of General Relativity that photons undergo a redshift when they move out through a gravitational field; naively this can be thought of as a decrease in the

energy of the photon, corresponding to the work required to escape from the gravitational field. The result is a change in wavelength $\Delta\lambda_{\rm G}$, given by

$$\frac{\Delta\lambda_{\rm G}}{\lambda} = \frac{GM}{R\tilde{c}^2} \ . \tag{2.32}$$

This effect has been measured on the Sun, and for a few very compact stars, the so-called *white dwarfs*.

Exercise 2.8:

What is $\Delta\lambda_{\rm G}$ for the Sun, at a wavelength of 5000 Å? Which radial velocity is required to cause a corresponding Doppler shift? (Since wavelength shifts are often quite small, it is common to give them in *Doppler units*, by measuring them in terms of the speed required to produce the corresponding Doppler shift).
Answer the same questions for a white dwarf with a mass of $0.6\,{\rm M}_\odot$ and a radius of 10^9 cm.

2.5.6 The Zeeman effect

When the atom is in a magnetic field, the energy levels are shifted by the *Zeeman effect*. As a result the spectral lines are shifted or split. The shift $\Delta\lambda_B$ is given by

$$\frac{\Delta\lambda_B}{\lambda} = \frac{e}{4\pi\tilde{c}^2\, m_{\rm e}} g_{12}\lambda B \ , \tag{2.33}$$

where e and $m_{\rm e}$ are the charge and mass of an electron, g_{12} is the so-called Landé factor of the transition, and B is the magnetic field strength. If λ is measured in Ångstrom, and B is measured in gauss, this may also be written

$$\frac{\Delta\lambda_B}{\lambda} = 4.67 \times 10^{-13} g_{12}\lambda B \ . \tag{2.34}$$

Exercise 2.9:

What is the Zeeman splitting for a spectral line with a wavelength of 5000 Å, in a magnetic field of 3000 gauss (a typical value for a sunspot)? Assume that $g_{12} = 1$. What is the splitting in Doppler units?

The results of exercise 2.7 and 2.9 indicate that the Zeeman splitting, in the solar case, is comparable with the broadening of the spectral lines caused by the thermal motion of the atoms, and hence quite difficult to measure. However, more sensitive measurements of stellar magnetic fields can be obtained on the basis of observation of the polarization of the light in spectral lines. In this way it is possible to measure magnetic fields on the Sun with a precision of a few gauss.

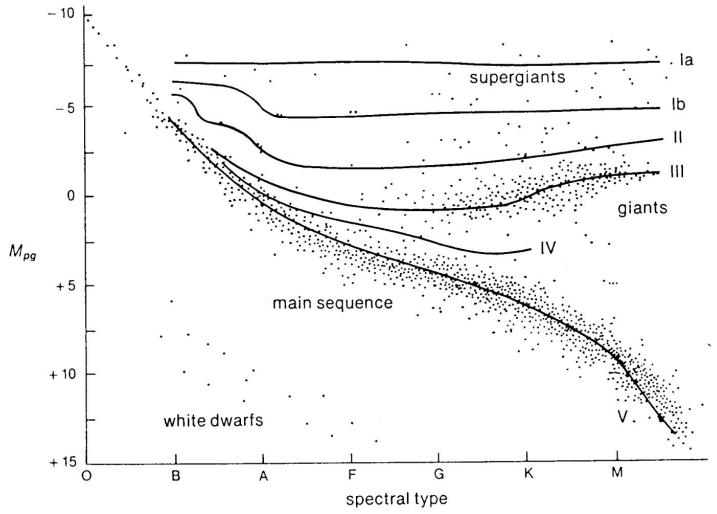

Figure 2.5: Hertzsprung-Russell diagram for stars in the solar vicinity, showing absolute photographic magnitude versus spectral type. Solid lines indicate the approximate definition of the luminosity classes.

2.6 Colour-magnitude diagrams

Given measurements of the brightness and surface temperature of a group of stars, as determined by their magnitudes and colour indices or spectral types, it is natural to plot these quantities against each other, to look for systematic correlations. This was first done independently by the Danish astronomer E. Hertzsprung and the American astronomer H. N. Russell. Hence such diagrams are collectively known as *Hertzsprung-Russell*, or HR, diagrams; the term colour-magnitude diagrams is also commonly used. Figure 2.5 shows an example of such a plot, for stars that are near enough to make possible a determination of their distance, and hence their absolute magnitude.[12] It is obvious that the distribution of stars is far from random. Most of the stars are concentrated in the *main sequence*, a fairly narrow band of stars with steeply increasing luminosities with increasing temperature.[13] These stars correspond to luminosity class V. In addition there is a number of stars concentrated in the subgiant and giant branch, of luminosity classes IV and III, and far fewer stars with even higher luminosities. Below the main sequence there is a small number of very faint and relatively hot stars, the *white dwarfs*. The appropriateness of this name follows immediately from equation (2.20): if hot stars are very faint, compared with main-sequence stars of the same temperature, their radii must be very small. The understanding of the distribution of stars in this diagram, and its relation to stellar evolution, is a major goal of these notes. We return to this in Chapter 13.

In view of the wide range of stellar distances, HR diagrams based on apparent magnitudes of stars are clearly in general meaningless. A very important exception is when

[12]The magnitude shown is the *photographic magnitude* $M_{\rm pg}$, based on measurements on photographic plates.

[13]It is an unfortunate historical accident that such diagrams are always plotted with the temperature increasing *to the left*.

(a)

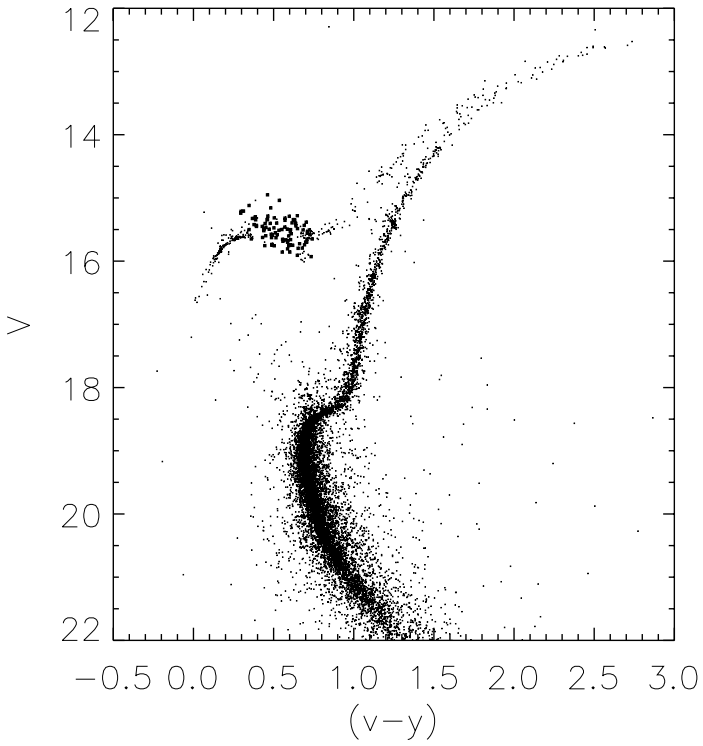

(b)

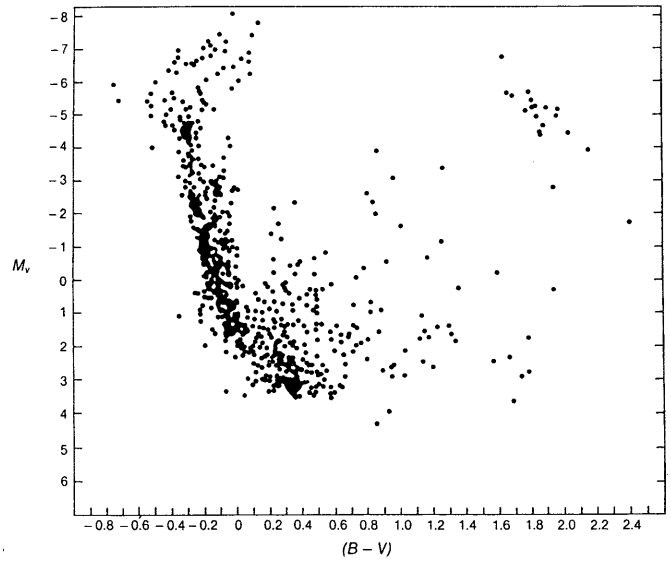

Figure 2.6: Colour-magnitude diagrams for (a): a typical globular cluster, Messier 3 in the constellation Canes Venatici, consisting of Population II stars (*cf.* Grundahl 1999); and (b) a typical galactic cluster, $h+\chi$ Persei (consisting of Population I stars). In panel a) the larger symbols mark the positions of the so-called *RR Lyrae* stars, a special class of pulsating stars.

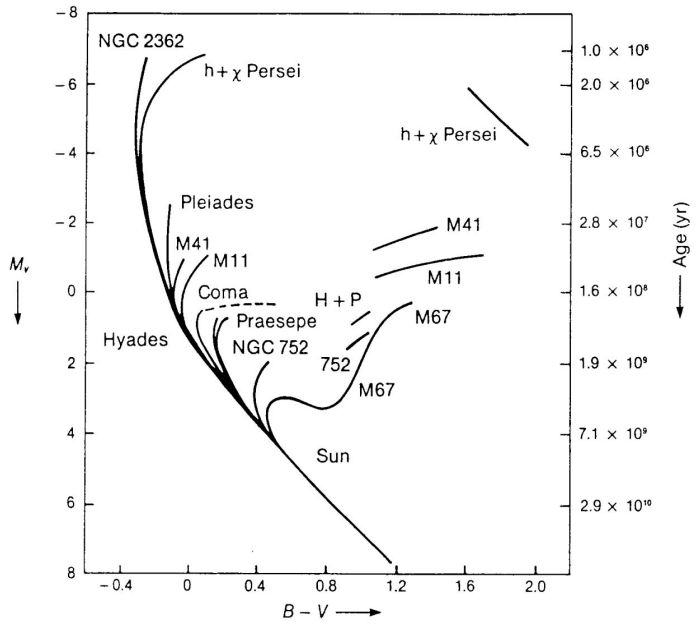

Figure 2.7: A schematic composite colour-magnitude diagram for several galactic clusters. As discussed in Chapter 13, the age scale on the right hand side of the diagram is based on stellar evolution calculations and indicates the age of a cluster for which the curve turns away from the main sequence at this luminosity. Thus, for example, the cluster M67 is estimated to have an age of about 5×10^9 years on the basis of this diagram (adapted from Sandage 1957).

groups of stars can be found which are at approximately the same distance. This is the case for *stellar clusters*, which are concentrations of stars in the sky which are so close together that they can be identified as being physically related. There are two basic types of stellar clusters: One class, the *galactic* or *open* clusters, consists of Population I stars and are concentrated to the disk of the Galaxy; they typically contain a few hundred stars. The second class are the *globular* clusters, consisting of Population II stars, which are found at large distances from the Galactic plane; they may contain millions of stars. In a given cluster all stars can be assumed to be at approximately the same distance; hence the difference between absolute and apparent magnitude is the same (*cf.* equation (2.8)), and a plot of apparent magnitude versus colour should show the same structure as a plot of absolute magnitude versus colour.

Figure 2.6 shows typical colour-magnitude diagrams for a globular and an open cluster. In both cases the main sequence can be clearly identified, although for the globular cluster it is quite short and concentrated at relatively late spectral types. Furthermore, Figure 2.7 shows schematic representations of the colour-magnitude diagrams for several open clusters. These have been shifted to a common scale of absolute magnitude by superposing their main sequences. It is evident that these diagrams show a great deal of regularity; as discussed in Chapter 13 this can be understood in detail on the basis of calculations of stellar evolution. Indeed, this agreement between observations and theory constitutes one

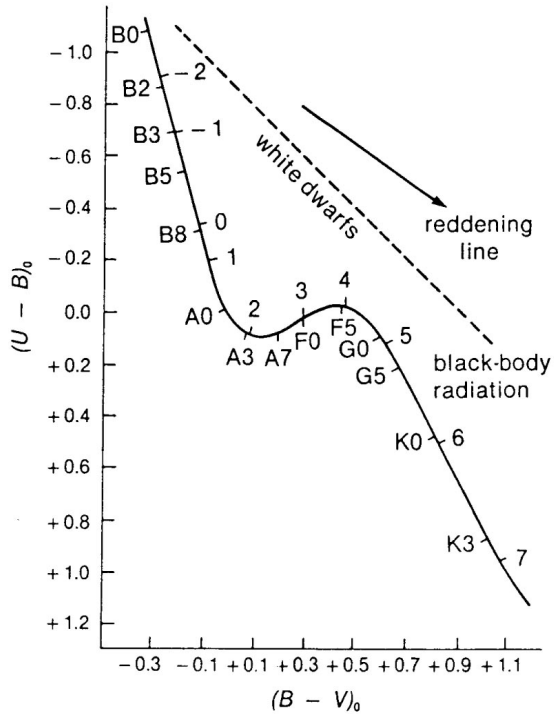

Figure 2.8: Colour-colour diagram for main-sequence stars. On the left side of the curve are indicated the spectral types of the stars, on the right hand side their absolute magnitudes. Also shown is the black-body curve (dashed) which marks the approximate location of the white dwarfs; the arrow indicates the direction in which the colour indices are shifted by interstellar absorption.

of the best tests of stellar evolution theory.

The results of stellar evolution calculations are most conveniently shown in a $(\log T_{\rm eff}, \log L_{\rm s})$ diagram. Several examples of such diagrams are presented in Chapters 10 – 12. To compare with the observations, we must be able to relate the observed quantities, for example V and $B-V$ to the computed quantities. This requires a determination of the bolometric correction (*cf.* equation (2.24)) and of the relation between colour index and effective temperature; these are non-trivial problems, which introduce elements of uncertainty into detailed quantitative comparisons.

It is also of interest to consider *colour-colour diagrams* where two colour indices are plotted against each other. As an example, Figure 2.8 shows a schematic diagram of (reddening-corrected) $U-B$ against $B-V$, for main-sequence stars. Also shown with an arrow is the direction in which stars are moved by interstellar reddening (*cf.* equation (2.27)) and the relation between $U-B$ and $B-V$ that would result if the stars were radiating as black bodies (*cf.* exercise 2.6).

Table 2.1

Parameters for stars of various spectral types. Columns give: spectral type; absolute visual magnitude, M_V; color index, $B - V$; bolometric correction, B.C.; bolometric magnitude, M_{bol}; effective surface temperature, T_{eff}; mass, radius, and luminosity in solar units; and average density in g/cm^3.

Sp	M_V	B-V	B.C.	M_{bol}	T_{eff}	$\log \frac{M}{M_\odot}$	$\log \frac{R}{R_\odot}$	$\log \frac{L}{L_\odot}$	$\log\bar{\rho}$
Main sequence (V):									
O5	−5.8	−0.35	−4.0	−10	40,000	1.6	1.25	5.7	−2.0
B0	−4.1	−0.31	−2.8	− 6.8	28,000	1.25	0.87	4.3	−1.2
B5	−1.1	−0.16	−1.5	− 2.6	15,500	0.81	0.58	2.9	−0.78
A0	0.7	0.0	−0.4	0.1	9,900	0.51	0.40	1.9	−0.55
A5	2.0	0.13	−0.12	1.7	8,500	0.32	0.24	1.3	−0.26
F0	2.6	0.27	−0.06	2.6	7,400	0.23	0.13	0.8	−0.01
F5	3.4	0.42	0.0	3.4	6,580	0.11	0.08	0.4	0.03
G0	4.4	0.58	−0.03	4.3	6,030	0.04	0.02	0.1	0.13
G5	5.1	0.70	−0.07	5.0	5,520	−0.03	−0.03	−0.1	0.20
K0	5.9	0.89	−0.19	5.8	4,900	−0.11	−0.07	−0.4	0.25
K5	7.3	1.18	−0.60	6.7	4,130	−0.16	−0.13	−0.8	0.38
M0	9.0	1.45	−1.19	7.8	3,480	−0.33	−0.20	−1.2	0.4
M5	11.8	1.63	−2.3	9.6	2,800	−0.67	−0.5	−2.1	1.0
M8	16	1.8			2,400	−1.0	−0.9	−3.1	1.8
Giants (III):									
G0	1.1	0.65	−0.03	1.1	5,600	0.4	0.8	1.5	−1.8
G5	0.7	0.85	−0.2	0.5	5,000	0.5	1.0	1.7	−2.4
K0	0.5	1.07	−0.5	0.2	4,500	0.6	1.2	1.9	−2.9
K5	−0.2	1.41	−0.9	−1.0	3,800	0.7	1.4	2.3	−3.4
M0	−0.4	1.60	−1.6	−1.8	3,200	0.8		2.6	−4.0
M5	−0.8	1.85	−2.8	−3				3.0	
Supergiants (I):									
B0	−6.4	−0.25	−3	−9	30,000	1.7	1.3	5.4	−2.1
A0	−6.2	0.0	−0.5	−7	12,000	1.2	1.6	4.3	−3.5
F0	−6	0.25	−0.1	−6	7,000	1.1	1.8	3.9	−4.2
G0	−6	0.70	−0.1	−5.2	5,700	1.0	2.0	3.8	−4.9
G5	−6	1.06	−0.3	−5.2	4,850	1.1	2.1	3.8	−5.2
K0	−5	1.39	−0.7	−5.4	4,100	1.1	2.3	3.9	−5.7
K5	−5	1.70	−1.2	−6	3,500	1.2	2.6	4.2	−6.4
M0	−5	1.94	−1.9	−7		1.2	2.7	4.5	−6.7
M5		2.14	−3.2						

SOURCE: Adapted from C. W. Allen, *Astrophysical Quantities*, 3rd ed. (London: The Athlone Press, 1973).

Exercise 2.10:

Discuss possible reasons for the deviation of the colour-colour curve from the black-body line.

A summary of some properties of various types of stars is given in Table 2.1. In view of the calibration uncertainties discussed above it should be taken only as indicative. Also, precise masses are difficult to assign, in particular for the stars away from the main sequence. Nevertheless, the table gives an idea about the typical parameters for the stars.

2.7 Stellar masses

The mass of a star is extremely important for its structure and evolution. Unfortunately direct determination of stellar masses has been possible only in a limited number of cases.

In the case of the Sun the product GM is known with extreme (about 10^{-9}) precision from the motion of planets and space probes. Hence the limiting factor is the accuracy

of the gravitational constant, which is comparatively poorly known. For other stars the situation is far worse. A relatively small number of stars are members of well-observed binary systems, where two stars orbit around each other.[14] When the orbit of the binary system can be observed, the masses of the stars can be determined from *Kepler's third law*, which may be written

$$M_1 + M_2 = \frac{a^3}{P^2} \, , \tag{2.35}$$

where M_1 and M_2 are the masses of the stars, measured in units of the solar mass, a is the semi-major axis of the orbit in astronomical units and P is the period in years. To determine a from measurements of the angular separation of the stars one clearly has to know the distance, and hence the parallax, of the stars. The periods of binary stars are often many years; hence a very extended observing program, in some cases spanning more than a century, is required to determine an accurate orbit.

2.8 Stellar pulsations

A number of different types of stars are observed to pulsate with one or more periods. The oscillation periods are determined by the structure of the stellar interior, and hence the periods, which can be determined observationally with very high precision, offer additional information about stellar structure. A schematic overview of these different types of pulsating stars is provided in Fig. 2.9. For a comprehensive discussion of stellar pulsations, see Aerts *et al.* (2010).

The "classical" pulsating stars were discovered as a result of the variation in their brightness which is often about 1 magnitude, and may exceed 5 magnitudes (in V; the variation in bolometric magnitude is considerably smaller). A very important class of pulsating stars are the Cepheids, which occupy a narrow region in the HR diagram. For these stars there is a well-defined relation between the period and the absolute luminosity; hence from measurements of the period it is possible to determine the absolute magnitude, and, given the apparent magnitude, the distance can be found from equation (2.8). This is the most important method for determining the distances of nearby galaxies.

The oscillations of these stars can be measured both in brightness and in radial velocity. The variations are caused by *radial pulsations*, where the star alternately expands and contracts. The periods of such oscillation are approximately given by the *dynamical time scale* of the star,

$$t_{\rm dyn} = \left(R^3/GM \right)^{1/2} = \left(\frac{4}{3} \pi G \, \overline{\rho} \right)^{-1/2} \, , \tag{2.36}$$

where $\overline{\rho} = M/(4\!/\!_3 \, \pi R^3)$ is the mean density of the star (*cf.* equation (1.2)). Hence measurement of their period gives information about the mean density of the star.

Exercise 2.11:

Some red giants have periods of a year. Estimate their mean density and compare it with the mean density in the Earth's atmosphere. Assuming that their mass is $1 \, {\rm M}_\odot$, estimate their radius.

---

[14] On the other hand it is estimated that a very large fraction of all stars, perhaps as many as half, are members of binary systems; but detailed observation of such systems is very difficult.

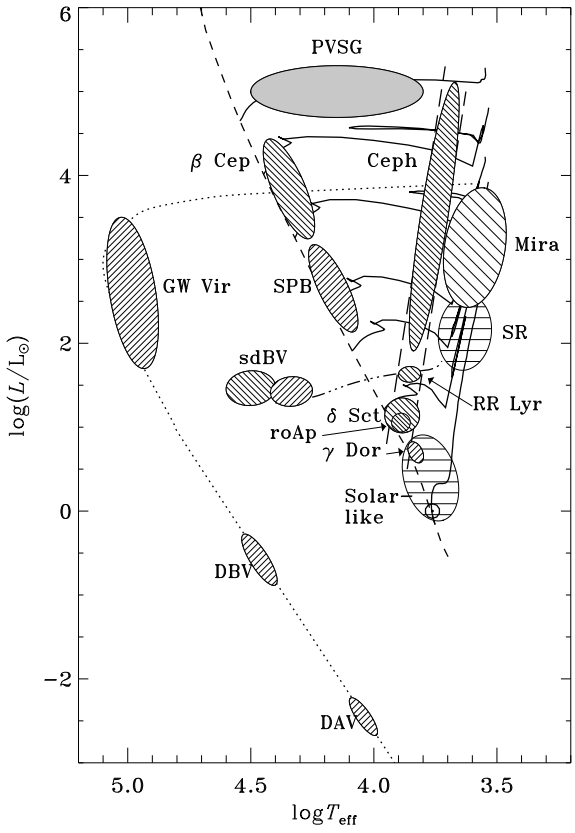

Figure 2.9: Schematic overview of various classes of pulsating stars. The hatching indicates the dominant modes of oscillations and excitation mechanism. Solar-like oscillations, excited by near-surface turbulent convection, are marked by horizontal lines.

Much more interesting are stars where several periods of oscillation are observed simultaneously, since this gives more information about their structure. An extreme case of this is the Sun, which is known to pulsate with tens of thousands of individual periods, many of which have been determined with very high precision. The oscillations have been observed both in radial velocity, by measuring the Doppler shift, and in intensity. To isolate the individual periods the observations are Fourier analyzed. Figure 2.10 shows a typical *oscillation spectrum* resulting from such an analysis. It is found that the solar oscillations have periods in the vicinity of five minutes; the amplitudes for each oscillation are less than 20 cm/sec for the Doppler velocity and less than a few times 10^{-6} in relative brightness. They range in scale on the solar surface from radial oscillations to oscillations with a wavelength of a few thousand kilometers.

The interpretation of these oscillations has led to the development of *helioseismology* which is in many ways analogous to seismic investigations of the Earth. It has been

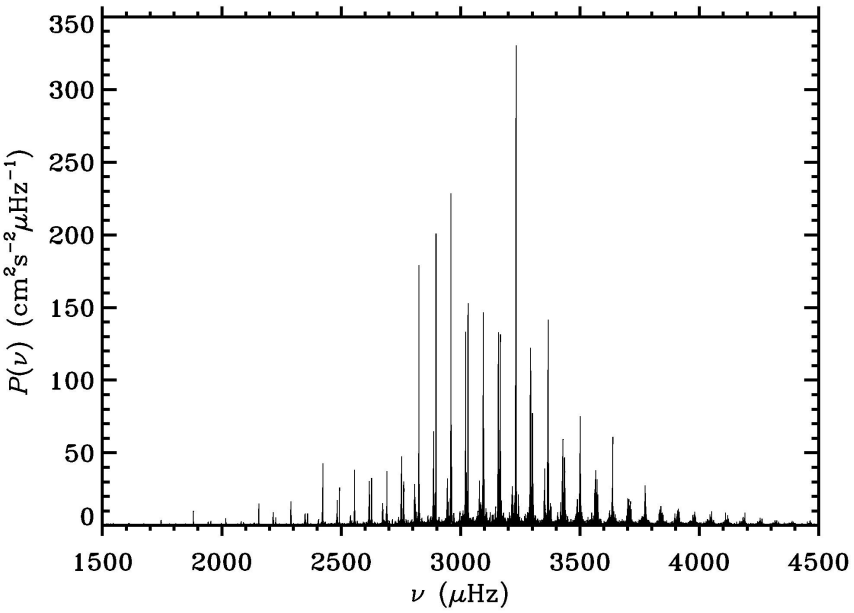

Figure 2.10: Observed spectrum of solar oscillations. The abscissa is oscillation frequency $\nu = 1/P$, where P is the oscillation period; a frequency of 3000 μHz corresponds to a period of about five minutes. The ordinate shows oscillation power at each frequency; each of the narrow lines corresponds to an individual oscillation. Only oscillations of very large horizontal scale were included in these observations. (See Elsworth *et al.* 1995.)

possible from the observed periods to determine the variation of sound speed and density throughout most of the Sun; such measurements are evidently very valuable as a test of stellar model computations. Furthermore, the observed periods may be used to determine the variation of rotation in the solar interior. Overviews of helioseismology were given by, for example, Leibacher *et al.* (1985), Libbrecht & Woodard (1991), Christensen-Dalsgaard *et al.* (2000) and Christensen-Dalsgaard (2002).

The last couple of decades have seen a dramatic evolution in studies of other types of pulsating stars, thanks to development of ground-based observing techniques and in particular space-based photometric missions, with the joint goals of searching for planets around other stars and studying stellar pulsations. These include the French/ESA CoRoT mission, and the NASA *Kepler* and TESS missions. As a result, we now have detailed data on essentially all the classes of pulsating stars that are shown in Fig. 2.9. For reviews on this development, see Chaplin & Miglio (2013) and Kurtz (2022). The resulting data allow tests of stellar models over a wide range of parameters, in what is called *asteroseismology*.

A large number of stars have been found with solar-like oscillations, from the main sequence to high up the red-giant branch. Such oscillations are excited by the acoustic noise from near-surface convection and hence are expected in all stars with outer convection zones (althugh the amplitude may be so low that they cannot at present be detected).

In other stars, the excitation is caused by a conversion of thermal to oscillation energy, the star effectively acting as a heat engine. An interesting case are the pulsating compact

stars, *i.e.* white dwarfs (see Chapter 16) and the so-called subdwarf B stars, which generally pulsate in several periods simultaneously. Particularly interesting are cases of white dwarfs where it has been possible to measure the *change* in oscillation period with time, as a result of the evolution of the stars.

2.9 Stellar activity

A wide range of phenomena are observed on the solar surface. The dominant ones are the *sunspots*; these are areas of concentrated magnetic field, somewhat cooler than the surrounding solar surface, which therefore appear darker. In connection with sunspots violent explosions are sometimes observed in the solar atmosphere, the so-called *flares*. Furthermore the Sun is observed to have a very hot (more than 10^6 K) and extended outer atmosphere, the *corona*; this extends into the *solar wind* which streams out through the solar system. A striking feature of these phenomena is their time-dependence: the number of sunspots varies roughly periodically with an 11-year period, in the so-called *solar cycle*.[15]

Although similarly detailed observations cannot be made for other stars, there are strong indications that the same phenomena occur, often on a much larger scale. The presence of starspots is indicated by periodic variations in stellar brightness with periods of days (and hence, for main-sequence stars, much longer than the plausible pulsation periods); these are probably caused by the rotation of dark areas over the stellar surface. Furthermore, the presence of features in certain spectral lines has been correlated with the solar magnetically active regions, and similar features are found in other stellar spectra; in some cases it has even been possible to find cycles of activity similar to the solar cycle (see Wilson, Vaughan & Mihalas 1981). Some late-type stars show sudden sharp increases in brightness which are interpreted as the results of very large flares. Finally the presence of hot coronae has been inferred for a variety of stars from X-ray observations. These various indices of activity appear to be systematically correlated with the overall properties of the stars, such as their luminosity, effective temperature and rotation rate.

The mechanisms responsible for this solar and stellar activity are so far not fully understood, although it is generally thought that the generation of the solar magnetic field is somehow related to an interaction between rotation and the motions in the solar convection zone (*cf.* Chapter 6). Our understanding of these processes is too incomplete to make it possible to use observations of activity to get information about basic stellar structure. On the other hand, there is little doubt that our quest for an understanding of solar activity will be helped greatly by the observation of similar phenomena in other stars.

2.10 Other types of emission

All the observational data discussed so far have been based on observation of electromagnetic radiation. However, there are a few other types of data which may be used to study stars, namely the neutrinos, and the solar wind particles.[16]

[15] It might be noted that the polarity of the solar magnetic solar field changes sign between each maximum in the number of sunspots; thus, strictly speaking, the period of the solar cycle is 22 years.

[16] There are other types of particles coming from space in *the cosmic rays*. However, since these particles are electrically charged, they are deflected by the interstellar magnetic fields. Hence they cannot be directly

2.10.1 Observations of neutrinos

Many of the nuclear reactions in stellar interiors generate neutrinos. Because neutrinos have very small cross-sections for interaction with matter, they escape from the stars essentially unhindered. Hence if detected they may provide information about the nuclear processes.

Because of the small cross-section detection of the neutrinos is very difficult. However, the neutrinos produced by the fusion of hydrogen to helium in the solar core have been measured by several experiments. In the first such experiment, the neutrinos were detected through the reaction

$$\nu_{\rm e} + {}^{37}{\rm Cl} \rightarrow {\rm e}^- + {}^{37}{\rm Ar} \ . \tag{2.37}$$

The detector consisted of a tank containing about 380 000 liter of C_2Cl_4 (which is a common cleaning fluid). Even with this large amount of detector material a solar neutrino event was recorded on average only every second day. This was substantially lower than the rate predicted by solar models. This discrepancy constituted the *solar neutrino problem* and was for a long time regarded as a potentially serious concern for stellar modelling.

A second experiment measured the scattering of neutrinos on electrons, in a tank containing 50,000 tons of water. Unlike the Cl experiment, the electron scattering experiment records the direction of the neutrinos, confirming that they do indeed come from the Sun. As in the case in the Cl experiment, the observed rate of neutrino events was substantially lower than theoretical predictions.

The Cl and electron scattering experiments are sensitive only to a small fraction of high-energy neutrinos, out of the total neutrino production of the Sun. Two independent experiments, sensitive to most of the neutrinos produced in the Sun, which use a reaction between the neutrino and ^{71}Ga yielded results closer to the model prediction, thus supporting the assumption that most of the Sun's energy output derives from nuclear reactions.

Around the turn of the century an experiment utilizing heavy water demonstrated that the origin of the original neutrino discrepancy arose from the fact that the earlier experiments were sensitive only, or predominantly, to the electron neutrinos. In contrast, the heavy-water experiment was also sensitive to the so-called muon and tau neutrinos. The results show that the *combined* flux of neutrinos is essentially consistent with solar models; however, a substantial fraction of the electron neutrinos generated in the solar core are converted to other types of neutrinos before reaching the detectors. Further experiments have provided more detailed information about these processes, and about the nuclear reactions in the solar core.

Observations of solar neutrinos and their interpretation are discussed in more detail in Chapter 11, section 11.5.3. An exhaustive treatment of early neutrino observations and the perceived solar neutrino problem was given by Bahcall (1989), and a more recent review was provided by Haxton *et al.* (2013).

Given the difficulty in detecting the neutrinos from the Sun, it is obvious that we cannot hope to detect neutrinos from other ordinary stars. On the other hand, a very intense flux of neutrinos is produced in supernova explosions. Such events are rare. However, about 20 neutrinos were recorded from the supernova (referred to as SN1987A) which was observed in the Large Magellanic Cloud in February 1987. This provides an extremely important

associated with any given star, or other object.

test of the complex and uncertain computations of the last phases of stellar evolution. It is remarkable that there is in fact good agreement between the observed number and energy of the neutrinos and the predictions of the models.

2.10.2 Solar wind particles

It was stated in the introduction that it is not possible directly to sample the material that stars are made of. The solar wind provides an interesting exception. Solar wind particles were trapped in foil which was hung on the Moon during the Apollo lunar landings. By analyzing these foils it has been possible to determine the relative abundances of a few isotopes in the solar wind (see Geiss *et al.* 1970). More extensive determination of the composition of the solar wind was carried out by the *Genesis* spacecraft (*e.g.* Heber *et al.* 2021). Unfortunately, the acceleration of particles in the solar wind is not the same from element to element, so that the composition of the solar wind is not directly representative of the solar surface composition. Nevertheless, this provides an interesting supplement to spectroscopic measurements of the solar abundances.

2.10.3 Meteoritic abundances

Meteorites constitute another example of stellar material that may, at least in principle, be investigated on Earth, by providing information about the composition of the matter from which the solar system was formed. In most cases the material in the meteorites has been melted and reprocessed, thus locally changing the initial relative abundances of elements and isotopes, just as is the case of rocks on Earth. However, in the so-called *primitive* meteorites grains are found, including very small diamonds (*e.g.*, Andersen *et al.* 1998), which apparently have originated in the atmospheres of red-giant stars and hence provide direct information about their composition. These therefore allow investigations of the processes leading to nucleosynthesis in stellar interiors. An interesting example, discussed by Nittler (2004), is the detection of decay products of the radioactive element technetium which is formed by neutron capture in the so-called asymptotic-giant-branch stars (see also Chapter 15).

Chapter 3

The equation of state

3.1 Introduction

The description of stellar structure requires knowledge about the properties of the matter in the stars. The present chapter deals with the thermodynamic properties of the gas. As is generally true in these notes, the level of detail is essentially kept to the bare minimum of what is required to understand how stars evolve. A complete description of the thermodynamic state of stellar matter is a very complex undertaking, which is still at the frontier of current research.

A fundamental assumption is that at any given point in the star the gas is in *thermodynamic equilibrium*. No better description of this assumption can be found than in the quote from Eddington's book *The Internal Constitution of the Stars* which is given in Box 3.1. The outcome is that we do not have to consider the detailed reactions between the particles (atoms, electrons, ions, photons) which make up the gas. Instead, the average properties of the gas can be described in terms of local state variables, and the relations between them. For example, given the values of the temperature T, the density ρ and the chemical composition it is possible to calculate all other state variables, including the pressure P and the internal energy per unit volume u. The specification of these relations constitutes the definition of the *equation of state* satisfied by the gas.

Implicit in the assumption of equilibrium is that the conditions in the gas change negligibly with distance over the mean-free-path of a particle in the gas, and negligibly with time over the mean time between collisions between the particles; in this condition "particle" must be taken to mean not only material particles such as atoms or electrons, but also photons. This condition is abundantly satisfied in stellar interiors, where the density is high; however, in the upper parts of stellar atmospheres it becomes questionable. Here a more detailed description of the statistical properties of the gas is required.

A considerable simplification results from the high temperature in stellar interiors, which means that in most of the star the gas can be assumed to be *fully ionized*, *i.e.*, decomposed into bare nuclei and free electrons. Therefore the gas consists of particles with no internal degrees of freedom. Also, as a first approximation one can neglect the interactions between the particles. Such a gas is described as being an *ideal gas*. As described in the following exercise it is possible to derive general relations between the pressure and internal energy for such a gas, with very few restrictions.

Exercise 3.1:

Relations between the pressure and internal energy of a gas. We consider a very simple model of the gas: assume that the gas consists of particles all with the same kinetic energy and with no internal degrees of freedom; assume that the direction of motion of the particles is isotropically distributed. The pressure in the gas is given by the normal component of the momentum transport through a plane in the gas, and the internal energy is the sum over the kinetic energies of the particles.
Show under these assumptions that the internal energy u per unit volume, in the case when the motion of the particles is nonrelativistic, is related to the pressure P by

$$u = \frac{3}{2}P \ , \qquad \text{nonrelativistic} \ . \tag{3.1}$$

Show that the corresponding relation in the extremely relativistic case is

$$u = 3P \ , \qquad \text{extremely relativistic} \ . \tag{3.2}$$

Relax the assumption that the kinetic energy is the same for all particles and show that equations (3.1) and (3.2) still apply.

3.2 The ideal gas

3.2.1 Simple gas

We first consider an ideal gas consisting of a single type of non-relativistic particles. The ideal-gas law for the gas contained in a volume V is commonly written

$$PV = Nk_{\rm B}T \ , \tag{3.3}$$

where N is the number of particles in V and $k_{\rm B}$ is Boltzmann's constant.

In the stellar case we are not concerned with a given volume of gas, and hence it is more convenient to write equation (3.3) as

$$P = nk_{\rm B}T \ , \tag{3.4}$$

where $n = N/V$ is the number of particles per unit volume. Introducing the mass density ρ and the (dimensionless) atomic mass μ of the particles, we have

$$n = \frac{\rho}{\mu m_{\rm u}} \ , \tag{3.5}$$

where $m_{\rm u}$ is the atomic mass unit, and hence

$$P = \frac{\rho k_{\rm B}T}{\mu m_{\rm u}} \ . \tag{3.6}$$

Equation (3.6), with a small extension discussed in section 3.2.2 below, is the most commonly used form of the ideal gas law.

Box 3.1

The Inside of a Star.

17. The inside of a star is a hurly-burly of atoms, electrons and aether waves. We have to call to aid the most recent discoveries of atomic physics to follow the intricacies of the dance. We started to explore the inside of a star; we soon find ourselves exploring the inside of an atom. Try to picture the tumult! Dishevelled atoms tear along at 50 miles a second with only a few tatters left of their elaborate cloaks of electrons torn from them in the scrimmage. The lost electrons are speeding a hundred times faster to find new resting-places. Look out! there is nearly a collision as an electron approaches an atomic nucleus; but putting on speed it sweeps round it in a sharp curve. A thousand narrow shaves happen to the electron in 10^{-10} of a second; sometimes there is a side-slip at the curve, but the electron still goes on with increased or decreased energy. Then comes a worse slip than usual; the electron is fairly caught and attached to the atom, and its career of freedom is at an end. But only for an instant. Barely has the atom arranged the new scalp on its girdle when a quantum of aether waves runs into it. With a great explosion the electron is off again for further adventures. Elsewhere two of the atoms are meeting full tilt and rebounding, with further disaster to their scanty remains of vesture.

As we watch the scene we ask ourselves, Can this be the stately drama of stellar evolution? It is more like the jolly crockery-smashing turn of a music-hall. The knockabout comedy of atomic physics is not very considerate towards our aesthetic ideals; but it is all a question of time-scale. The motions of the electrons are as harmonious as those of the stars but in a different scale of space and time, and the music of the spheres is being played on a keyboard 50 octaves higher. To recover this elegance we must slow down the action, or alternatively accelerate our own wits; just as the slow-motion film resolves the lusty blows of the prize-fighter into movements of extreme grace—and insipidity.

And what is the result of all this bustle? Very little. Unless we have in mind an extremely long stretch of time the general state of the star remains steady. Just as many atoms are repaired as are smashed; just as many bundles of radiation are sent out as are absorbed; just as many electrons are captured as are exploded away. The atoms and the electrons for all their hurry never get anywhere; they only change places. The aether waves are the only part of the population which do actually accomplish something; although apparently darting about in all directions without purpose they do in spite of themselves make a slow general progress outwards.

(Eddington 1930, pp. 19 – 20).

The mean internal energy per particle is $^3/_2\, k_{\rm B}T$ (see also section 3.3 below). Thus the internal energy per unit volume is

$$u = \frac{3}{2} n k_{\rm B} T = \frac{3}{2} \frac{\rho k_{\rm B} T}{\mu m_{\rm u}} = \frac{3}{2} P \,, \tag{3.7}$$

in agreement with equation (3.1).

The energetics of the gas as the star evolves or the gas moves plays a very important role for stellar evolution. The basic equation describing the changes in the properties of

the gas is *the first law of thermodynamics*,

$$đQ = \mathrm{d}U + P\mathrm{d}V \ , \tag{3.8}$$

valid for a fixed amount of matter, where U is the internal energy of the matter, and V is the volume it occupies. Here $đQ$ is an amount of heat added to the matter, which, as expressed on the right hand side, goes partly into changing the internal energy and partly into work to change the volume of the gas. We let V be the volume corresponding to unit mass, so that

$$V = \frac{1}{\rho} \ . \tag{3.9}$$

Then $U = u/\rho$ is the *specific internal energy*, *i.e.*, the internal energy per unit mass; from equation (3.7) it follows that

$$U = \frac{3}{2}\frac{k_{\mathrm{B}}T}{\mu m_{\mathrm{u}}} \ . \tag{3.10}$$

We now consider a process where the volume does not change. We introduce the *specific heat at constant volume*, c_V, as the amount of heat that has to be added, per unit mass, to raise the temperature one degree. It follows from equations (3.8) and (3.10) that

$$đQ = \frac{3}{2}\frac{k_{\mathrm{B}}}{\mu m_{\mathrm{u}}}\mathrm{d}T \ ,$$

and hence

$$c_V = \frac{3}{2}\frac{k_{\mathrm{B}}}{\mu m_{\mathrm{u}}} \ . \tag{3.11}$$

It is also of interest to consider a process where the pressure is constant. To do so, we use the ideal gas law on the form (3.3), where in the present case $N = 1/(\mu m_{\mathrm{u}})$. For the changes we then obtain

$$P\mathrm{d}V + V\mathrm{d}P = \frac{k_{\mathrm{B}}}{\mu m_{\mathrm{u}}}\mathrm{d}T \ , \tag{3.12}$$

and hence from equation (3.8)

$$đQ = \mathrm{d}U - V\mathrm{d}P + \frac{k_{\mathrm{B}}}{\mu m_{\mathrm{u}}}\mathrm{d}T = \frac{5}{2}\frac{k_{\mathrm{B}}}{\mu m_{\mathrm{u}}}\mathrm{d}T - V\mathrm{d}P \ ,$$

by using equation (3.10). From this equation it follows that the *specific heat at constant pressure* is

$$c_P = \frac{5}{2}\frac{k_{\mathrm{B}}}{\mu m_{\mathrm{u}}} \ . \tag{3.13}$$

A particularly important type of process are the *adiabatic* processes, which occur without any exchange of heat, *i.e.*, with $đQ = 0$. For such a process, from equations (3.8), (3.10) and (3.11) we obtain

$$c_V\mathrm{d}T = -P\mathrm{d}V \ .$$

To obtain a relation between the changes in P and V (or ρ) for an adiabatic process, we use the ideal gas law on the form (3.12) to write this equation as

$$c_V\left(\frac{\mathrm{d}P}{P} + \frac{\mathrm{d}V}{V}\right) = -\frac{k_{\mathrm{B}}}{\mu m_{\mathrm{u}}}\frac{\mathrm{d}V}{V} = (c_V - c_P)\frac{\mathrm{d}V}{V} \ ,$$

and hence

$$\frac{\mathrm{d}P}{P} = -\frac{c_P}{c_V}\frac{\mathrm{d}V}{V} = -\gamma\frac{\mathrm{d}V}{V} = \gamma\frac{\mathrm{d}\rho}{\rho} \,, \tag{3.14}$$

where we introduced $\gamma \equiv c_P/c_V$ and used equation (3.9). For the ideal gas which we are considering it follows from equation (3.11) and (3.13) that $\gamma = 5/3$. We may also write equation (3.14) as

$$\left(\frac{\partial \ln P}{\partial \ln \rho}\right)_s = \gamma \,, \tag{3.15}$$

where the subscript "s" indicates that the partial derivative is taken at constant *specific entropy*, *i.e.*, without any heat exchange.

From equation (3.15), and using the ideal gas law, one can derive relations between the changes in other thermodynamic variables under adiabatic changes. In particular, one finds that

$$\left(\frac{\partial \ln P}{\partial \ln T}\right)_s = \frac{\gamma}{\gamma - 1} \,, \tag{3.16}$$

and

$$\left(\frac{\partial \ln T}{\partial \ln \rho}\right)_s = \gamma - 1 \,. \tag{3.17}$$

Exercise 3.2:

Verify these relations.

This derivation assumed that the motion of the particles provides the only contribution to the internal energy. This is the case for a fully ionized ideal gas, or for a gas consisting of unionized atoms.[1] Under more general circumstances the relations derived above, particularly equations (3.15) – (3.17), are not valid. Nevertheless, it is still convenient to describe adiabatic changes by means of similar equations. This motivates *defining* the adiabatic exponents Γ_1, Γ_2 and Γ_3 by

$$\Gamma_1 \equiv \left(\frac{\partial \ln P}{\partial \ln \rho}\right)_s \,, \tag{3.18}$$

$$\frac{\Gamma_2}{\Gamma_2 - 1} \equiv \left(\frac{\partial \ln P}{\partial \ln T}\right)_s \,, \tag{3.19}$$

$$\Gamma_3 - 1 \equiv \left(\frac{\partial \ln T}{\partial \ln \rho}\right)_s \,. \tag{3.20}$$

These three quantities are not independent. In fact, from the chain rule of differentiation it follows that, for example,

$$\frac{\Gamma_2}{\Gamma_2 - 1} = \left(\frac{\partial \ln P}{\partial \ln T}\right)_s = \left(\frac{\partial \ln P}{\partial \ln \rho}\right)_s \left(\frac{\partial \ln \rho}{\partial \ln T}\right)_s = \frac{\Gamma_1}{\Gamma_3 - 1} \,, \tag{3.21}$$

without *any* assumptions about the equation of state. It is obvious that for a fully ionized ideal gas (which is the case with which we shall almost exclusively be concerned), $\Gamma_1 = \Gamma_2 = \Gamma_3 = 5/3$.

[1] If the gas consists of molecules, additional contributions to the energy comes from the rotation, and possibly the internal vibrations, of the molecules.

3.2.2 Fully ionized gas consisting of a mixture of elements

In practice, stellar matter consists of a mixture of different elements, the atoms of which are largely or fully ionized. Thus the description in the previous section, which assumed only one kind of particles, is too simple. However, it is straightforward to generalize it.

If the gas consists of different types of particles each behaving like an ideal gas, with number densities n_i, the total pressure in the gas is obtained as the sum of the partial pressures $P_i = n_i k_{\rm B} T$, *i.e.*,

$$P = \sum_i P_i = \sum_i n_i k_{\rm B} T \ , \tag{3.22}$$

and similarly the internal energy of the gas is given by

$$u = \sum_i u_i = \frac{3}{2} \sum_i n_i k_{\rm B} T \ . \tag{3.23}$$

Note that it follows from the assumption of thermodynamic equilibrium that with the same number density electrons make the same contribution to the pressure as nuclei, despite their smaller mass.

To be more specific we consider a mixture of atoms of different elements, all of which are assumed to be fully ionized. We denote the atomic number and atomic mass of element j by $(\mathcal{Z}_j, \mathcal{A}_j)$, and its mass fraction by X_j. When fully ionized, each atom contributes $\mathcal{Z}_j + 1$ particles ($\mathcal{Z}_j$ electrons and one nucleus). The number of atoms of element j per unit volume is $\rho X_j/(\mathcal{A}_j m_{\rm u})$, and hence the total number of particles per unit volume from element j is $\rho X_j(\mathcal{Z}_j + 1)/(\mathcal{A}_j m_{\rm u})$. Thus, from equation (3.22) it follows that the pressure is

$$P = \sum_j \rho X_j \frac{\mathcal{Z}_j + 1}{\mathcal{A}_j m_{\rm u}} k_{\rm B} T \equiv \frac{\rho k_{\rm B} T}{\mu m_{\rm u}} \ , \tag{3.24}$$

where we introduced *the mean molecular weight* by

$$\mu^{-1} = \sum_j X_j \frac{\mathcal{Z}_j + 1}{\mathcal{A}_j} \ . \tag{3.25}$$

Therefore, with this definition of μ we recover equation (3.6) for P. Similarly, it is easy to verify that equation (3.7) for u is also valid, as is the discussion in section 3.2.1 of the energetics of the gas.

Exercise 3.3:

Verify this.

As discussed in section 2.5.3 it is conventional to denote the mass fractions of H and He by X and Y, respectively, and the mass fraction of the remaining, so-called heavy, elements by Z. This separation is useful because $Z \ll X, Y$ in most stellar compositions. Note that the normalization $X + Y + Z = 1$ must hold. To obtain an approximate expression for μ we take $\mathcal{A}_1 \simeq 1$ (for hydrogen), $\mathcal{A}_2 \simeq 4$ (for helium), and we approximate $(\mathcal{Z}_j + 1)/\mathcal{A}_j$ by $1/2$ for the heavy elements. Then

$$\mu^{-1} \simeq 2X + \frac{3}{4} Y + \frac{1}{2} Z \ , \tag{3.26}$$

or

$$\mu \simeq \frac{4}{3+5X-Z} \; . \tag{3.27}$$

The electron number density $n_{\rm e}$ plays a considerable role for the properties of the gas. It is convenient to introduce the *mean molecular weight per electron*, $\mu_{\rm e}$, such that

$$n_{\rm e} = \frac{\rho}{\mu_{\rm e} m_{\rm u}} \; . \tag{3.28}$$

Exercise 3.4:

Show that, under the same approximations as were made in deriving equation (3.26),

$$\mu_{\rm e} \simeq \frac{2}{1+X} \; . \tag{3.29}$$

3.2.3 Partial ionization

Because of the assumption of complete ionization, the number of particles is independent of T and ρ. In realistic calculations of stellar structure the dependence of the degree of ionization on T and ρ must be taken into account. It is still possible to use equation (3.6) for P, but the mean molecular weight μ must be defined by counting the actual number of free particles in the gas. Also, in the internal energy account must be taken of the energy required to ionize the atoms, and hence the simple relation (3.1) is no longer valid. The zero-point of the internal energy is essentially arbitrary. If the fully ionized state is taken as the zero-point of the internal energy of the atoms, atoms with bound electrons make a *negative* contribution to the internal energy of the gas.

In a simplified treatment of the ionization processes, the fraction of a given atom that is ionized is given by the *Saha equation*;[2] if, as a further simplification, we assume all atoms to be in the ground state, the number densities n_I and n_{II} of atoms in two successive states of ionization satisfy

$$\frac{n_{\rm e} n_{II}}{n_I} = \frac{2 g_{II}}{g_I} \frac{(2\pi m_{\rm e} k_{\rm B} T)^{3/2}}{h^3} \exp\left(-\frac{\chi_I}{k_{\rm B} T}\right) \; ; \tag{3.30}$$

here g_I and g_{II} are the statistical weights of the two ionization levels, $m_{\rm e}$ is the electron mass, h is Planck's constant and χ_I is the ionization potential of state I. Equation (3.30) clearly predicts that the degree of ionization increases with increasing temperature, as expected. It should also be noted that the ionization *decreases* with increasing electron density; with an increasing number of free electrons, it is energetically less favourable to add free electrons to the gas. This effect leads to paradoxical effects in the cores of stars, as discussed in the following exercise.

[2] known in chemistry as the *Law of Mass Action*.

Exercise 3.5:

The ionization of hydrogen in the solar core. We normally assume that matter is fully ionized in stellar interiors. To test whether this assumption is consistent with the Saha equation we make the following assumptions about conditions at the solar centre: The temperature is $T = 15 \times 10^6\,\mathrm{K}$, the density is $\rho = 150\,\mathrm{g\,cm^{-3}}$, the hydrogen and heavy element abundances are $X = 0.35$, $Z = 0.02$. The statistical weights of unionized and ionized hydrogen are $g_I = 2$, $g_{II} = 1$, and the ionization potential of hydrogen is $\chi_I = 13.6\,\mathrm{eV}$. The electron number density is assumed to be given by equations (3.28) and (3.29), valid for full ionization.

i) What is the ratio n_{II}/n_I for hydrogen?

The answer is clearly inconsistent with the assumption of full ionization. To find the reason for this, consider the following additional questions:

ii) What is the number density of unionized hydrogen atoms?

iii) Estimate the average separation between unionized hydrogen atoms.

Compare the answer to question iii) with the radius, $0.53\,\mathrm{Å}$, of a hydrogen atom.

Exercise 3.5 indicates that a naive application of the Saha equation may result in a prediction of less than complete ionization in deep stellar interiors. However, we also found that the separation between neutral hydrogen atoms was less than their size; this is obviously an unphysical result. The reason for this paradox is that the Saha equation neglects the interaction between the atoms. Such interaction must certainly take place when the density is so high that the atoms essentially touch. To describe the resulting changes in the ionization balance and the equation of state is a complex problem, which has not yet found a definite solution. As a result it is not even known with complete certainty whether matter *is* in fact fully ionized in the cores of all stars. For simplicity we shall always assume full ionization under these conditions, however.

Since the internal energy of an ionizing gas is not given by the simple expression (3.7), it also follows that the adiabatic exponents Γ_1, Γ_2 and Γ_3 are in general different, and differ from $5/3$. If a gas undergoing partial ionization is compressed adiabatically, there is a tendency for the gas to heat up; but since part of the work performed on the gas goes to increasing the degree of ionization, the temperature and pressure increases are smaller than would have been the case for a fully ionized gas. This simple argument explains why for partially ionized gasses Γ_1, Γ_2 and Γ_3 are less than $5/3$; in the ionization zone of hydrogen close to the surface of solar-like stars the Γ-s may get close to 1.

3.3 The distribution function for a classical gas

The distribution of the speed v in a gas consisting of "classical" particles[3] is given by the *Maxwell distribution*:

$$f(v) = 4\pi \left(\frac{m}{2\pi k_{\rm B} T}\right)^{3/2} \exp\left(-\frac{mv^2}{2k_{\rm B}T}\right) v^2 \,, \tag{3.31}$$

where m is the mass of the particle. This distribution function is defined such that $f(v)\mathrm{d}v$ gives the probability of finding the particle in the range of speed between v and $v + \mathrm{d}v$. Accordingly f is normalized such that

$$\int_0^\infty f(v)\mathrm{d}v = 1 \,. \tag{3.32}$$

The maximum of the distribution, *i.e.*, the most probable speed, is given by

$$v_{\rm mps} = \left(\frac{2k_{\rm B}T}{m}\right)^{1/2} \,, \tag{3.33}$$

the mean speed is

$$\langle v \rangle = \int_0^\infty v f(v)\mathrm{d}v = \left(\frac{8k_{\rm B}T}{\pi m}\right)^{1/2} \,, \tag{3.34}$$

and the *root mean square speed* $\langle v^2 \rangle^{1/2}$ is given by

$$\langle v^2 \rangle = \int_0^\infty v^2 f(v)\mathrm{d}v = \frac{3k_{\rm B}T}{m} \,. \tag{3.35}$$

Equation (3.35) may also be written

$$\langle v^2 \rangle^{1/2} \simeq 1.579 \times 10^4 \left(\frac{T}{\mathcal{A}}\right)^{1/2} \mathrm{cm\,sec^{-1}} \,, \tag{3.36}$$

where $\mathcal{A}$ is the atomic weight of the particle, and T is measured in K. Note from equation (3.35) that the mean kinetic energy of the particles is $^3\!/_2 k_{\rm B}T$, as was already used in deriving equation (3.7).

Exercise 3.6:

Verify equations (3.32) – (3.36).

3.4 The radiation pressure

Due to the high temperatures in stellar interiors, the photons make a significant contribution to the pressure and internal energy of the gas. It may be shown that the *radiation pressure*, *i.e.*, the pressure from the photons, is

$$P_r = \frac{1}{3} a T^4 \,, \tag{3.37}$$

[3] Quantum-mechanical effects on the distribution function are discussed in section 3.5.

and that the energy density is

$$u_R = aT^4 \ , \tag{3.38}$$

where a is the radiation density constant. Note that equations (3.37) and (3.38) show that the relation (3.2) is satisfied for the photon gas; this is obvious, in view of the fact that photons are definitely relativistic particles.

If the system consists of a mixture of particles behaving like an ideal gas and radiation, the total pressure and internal energy are the sum of the particle and radiation parts, so that

$$P = \frac{\rho k_{\rm B} T}{\mu m_{\rm u}} + \frac{1}{3} a T^4 \ , \tag{3.39}$$

and

$$u = \frac{3}{2} \frac{\rho k_{\rm B} T}{\mu m_{\rm u}} + a T^4 \ . \tag{3.40}$$

It is conventional to define $\beta = P_g/P$ as the fraction of the total pressure which is contributed by the particle, or gas, pressure.

As for the ideal gas, it is of interest to consider the energetics of the system, in particular its response to adiabatic changes. If the system is dominated by extremely relativistic particles, such as photons, so that equation (3.2) is satisfied, we have $U = 3PV$, and hence, for an adiabatic change

$$0 = 3{\rm d}(PV) + P{\rm d}V = 3V{\rm d}P + 4P{\rm d}V \ ,$$

so that

$$\frac{{\rm d}P}{P} = -\frac{4}{3}\frac{{\rm d}V}{V} = \frac{4}{3}\frac{{\rm d}\rho}{\rho} \ . \tag{3.41}$$

Thus in this case

$$\Gamma_1 = \frac{4}{3} \tag{3.42}$$

(*cf.* see equation (3.18)). It should be noted that this relation is valid for *any* gas that is dominated by extremely relativistic particles.

It may be shown that a gravitationally bound system (such as a star) for which the average value of Γ_1 is less than $4/3$ is dynamically unstable. Roughly speaking, the argument is as follows:[4] If the star is compressed adiabatically, the pressure increases according to equation (3.18); the pressure increase will give rise to a force which tends to expand the star again. However, the gravitational attraction between the particles also increases. If Γ_1 is too small, the pressure increase is not sufficiently strong to overcome the increase in gravitational attraction, and the star collapses. Evidently, the opposite happens if the star is expanded slightly, leading it to explode. Thus, stars that are dominated by radiation pressure are on the verge of instability. As discussed in section 4.2, this provides a natural explanation for the fact that no stars are found with masses exceeding about $100\,{\rm M}_\odot$: in such stars radiation pressure dominates, and the stars are unstable.

To determine the two other adiabatic exponents we specialize to a system dominated by radiation. To calculate Γ_3 we use that $U = aT^4V$, and equation (3.37), to get

$$0 = {\rm d}(aT^4V) + \frac{1}{3}aT^4{\rm d}V = 4aT^3V{\rm d}T + \frac{4}{3}aT^4{\rm d}V \ ,$$

[4] A more precise argument is given in section 4.4.

or

$$\frac{\mathrm{d}T}{T} = -\frac{1}{3}\frac{\mathrm{d}V}{V} = \frac{1}{3}\frac{\mathrm{d}\rho}{\rho} \,. \tag{3.43}$$

Hence

$$\Gamma_3 = \frac{4}{3} \,. \tag{3.44}$$

Finally it follows from equation (3.21) that

$$\Gamma_2 = \frac{4}{3} \,. \tag{3.45}$$

The adiabatic exponents in the general case, where equations (3.39) and (3.40) must be used, can be found through a similar although rather more cumbersome analysis. The results are

$$\Gamma_1 = \frac{32 - 24\beta - 3\beta^2}{24 - 21\beta} \,, \tag{3.46}$$

$$\Gamma_2 = \frac{32 - 24\beta - 3\beta^2}{24 - 18\beta - 3\beta^2} \,, \tag{3.47}$$

$$\Gamma_3 = \frac{32 - 27\beta}{24 - 21\beta} \,, \tag{3.48}$$

where β is the ratio between gas and total pressure introduced above. Note that these expressions have the correct values in the limits $\beta \to 1$ (pure gas pressure) and $\beta \to 0$ (pure radiation pressure).

Exercise 3.7:

Verify these limits.

3.5 Degenerate matter

At low temperature and high density, quantum-mechanical effects must be taken into account in the description of the gas. According to Pauli's exclusion principle, at most two fermions can occupy a given state. At low temperature the particles will tend to fill up the states with low energy. If the density is sufficiently high, the number of such states is inadequate, and the particles are forced into states of higher energy. This increases the internal energy, and hence the pressure, of the gas beyond the value that would be obtained if the gas satisfied the ideal gas law. In particular, the pressure and internal energy tend to finite limits for $T \to 0$.

To give a more precise description of this effect, we use that the distribution of fermions in momentum is given by the *Fermi-Dirac statistics*; thus, if p is the length of the momentum vector, the number density of particles in the interval p to $p + \mathrm{d}p$ is

$$n(p)\mathrm{d}p = \frac{2}{h^3} 4\pi p^2 \mathrm{d}p F(p) \,, \tag{3.49}$$

where

$$F(p) = \frac{1}{\exp(E/k_{\rm B}T - \psi) + 1} \tag{3.50}$$

is the occupation number for the Fermi gas. In equation (3.49) the factor 2 accounts for the two possible spin states of "normal" fermions (*i.e.*, electrons or nucleons), and the factor h^{-3} gives the density of states in the 6-dimensional space of positions and momenta. Finally in equation (3.50) E is the energy of a particle with momentum p, and ψ is a parameter, related to the chemical potential of the fermions, which determines the degree of degeneracy.

Exercise 3.8:

What is the relation between the density h^{-3} of states and the Heisenberg uncertainty principle?

If ψ is large and positive, $F(p) \simeq 1$ for all "reasonable" energies; this limit corresponds to all available quantum states being filled up, *i.e.*, to strong degeneracy. If, on the other hand, ψ is large and negative, the term $+1$ in the denominator in equation (3.50) may be ignored. Then the distribution function corresponds to the distribution of classical particles. In particular, if the particles are assumed to be non-relativistic so that $E = p^2/(2m)$ the distribution function reduces to the Maxwell distribution discussed in section 3.3.

Exercise 3.9:

Verify that the distribution in equation (3.49) is equivalent to equation (3.31) in the limit of large negative ψ.

From equation (3.49) we obtain the total number density of particles as

$$n = \int_0^\infty n(p){\rm d}p = \frac{2}{h^3} 4\pi \int_0^\infty \frac{p^2 {\rm d}p}{\exp(E/k_{\rm B}T - \psi) + 1} \; . \tag{3.51}$$

For a given number density of particles, this equation can be used to determine ψ. Then the contribution to the internal energy of the gas from the particles is obtained as

$$u = \int_0^\infty En(p){\rm d}p = \frac{2}{h^3} 4\pi \int_0^\infty \frac{Ep^2 {\rm d}p}{\exp(E/k_{\rm B}T - \psi) + 1} \; . \tag{3.52}$$

Finally the pressure can be obtained as in exercise 3.1; in particular, for the limiting cases of non-relativistic or extremely relativistic particles equations (3.1) or (3.2) may be used.

In the general case the integrals in equations (3.51) and (3.52) cannot be evaluated analytically. In the non-relativistic and the extremely relativistic limits the integrals can be expressed in terms of the *Fermi-Dirac* functions

$$\mathcal{F}_\nu(z) \equiv \int_0^\infty \frac{u^\nu}{\exp(u - z) + 1} {\rm d}u \; , \tag{3.53}$$

for which extensive tables are available. There are also analytical approximations to the integrals valid in suitable cases. Here we only consider the limit of $T \to 0$, where the integrals are drastically simplified. In this limit, known as the limit of *complete degeneracy*,

$$F(p) = \begin{cases} 1 & \text{for } E < E_{\rm F} \\ 0 & \text{for } E > E_{\rm F} \ , \end{cases} \tag{3.54}$$

where we introduced the *Fermi energy* $E_{\rm F}$ as the limit of $\psi k_{\rm B} T$ for $T \to 0$. We also introduce the Fermi momentum $p_{\rm F}$ corresponding to $E_{\rm F}$.

Exercise 3.10:

Verify equation (3.54).

In this case the integral in equation (3.51) is trivial and leads to

$$n = \frac{8\pi p_{\rm F}^3}{3h^3} \ , \tag{3.55}$$

which establishes the relation between the number density and the Fermi momentum. To determine the internal energy we must specify the relation between p and E. For nonrelativistic particles, $E = p^2/(2m)$, and hence we obtain from equation (3.52)

$$u = \frac{3}{5} n E_{\rm F} \qquad \text{nonrelativistic degeneracy} \ , \tag{3.56}$$

where in this case $E_{\rm F} = p_{\rm F}^2/(2m)$. From equation (3.1) it then follows that

$$P = \frac{2}{5} n E_{\rm F} \qquad \text{nonrelativistic degeneracy} \ . \tag{3.57}$$

In the limit of extremely relativistic particles, on the other hand, $E = p\tilde{c}$, where $\tilde{c}$ is the speed of light, and we obtain

$$u = \frac{3}{4} n E_{\rm F} \qquad \text{extremely relativistic degeneracy} \ , \tag{3.58}$$

with $E_{\rm F} = \tilde{c} p_{\rm F}$, and, from equation (3.2),

$$P = \frac{1}{4} n E_{\rm F} \qquad \text{extremely relativistic degeneracy} \ . \tag{3.59}$$

Exercise 3.11:

Verify equations (3.55), (3.56) and (3.58).

It is of interest to consider the case of nonrelativistic, completely degenerate electrons in a little more detail. We also assume that the gas is fully ionized. In this case the

electron number density is given by equations (3.28) and (3.29), and hence, from equation (3.55), the Fermi momentum is

$$p_{\rm F} = \left(\frac{3h^3 \rho}{8\pi \mu_{\rm e} m_{\rm u}} \right)^{1/3} . \tag{3.60}$$

Hence the pressure corresponding to completely degenerate electrons is

$$\begin{aligned} P_{\rm e}^{(\rm deg)} &= \frac{1}{5} \left(\frac{3}{8\pi} \right)^{2/3} \frac{h^2}{m_{\rm e} m_{\rm u}^{5/3}} \left(\frac{\rho}{\mu_{\rm e}} \right)^{5/3} \\ &= 1.0036 \times 10^{13} \left(\frac{\rho}{\mu_{\rm e}} \right)^{5/3} , \end{aligned} \tag{3.61}$$

in *cgs* units. Thus for a gas where the pressure is dominated by the pressure from degenerate electrons $P \propto \rho^{5/3}$. This is a particularly simple form of the equation of state, since it is independent of the temperature. As we shall see later, this allows a simple description of the structure of stars dominated by degenerate electrons.

We may use equation (3.61) to estimate the parameter range for which degeneracy becomes important. This may be defined by the condition $P_{\rm e}^{(\rm deg)} > P_{\rm e}^{(\rm g)}$, where $P_{\rm e}^{(\rm g)}$ is the electron pressure if the electrons are assumed to behave as classical particles; from equations (3.24), replacing μ by $\mu_{\rm e}$, and equation (3.61) this condition may be written as

$$\frac{\rho}{\mu_{\rm e}} > 2.4 \times 10^{-8} T^{3/2} . \tag{3.62}$$

Exercise 3.12:

In the centre of the Sun the temperature is $T = 15 \times 10^6\,{\rm K}$, the density is $\rho = 150\,{\rm g\,cm^{-3}}$, and the hydrogen and heavy-element abundances are $X = 0.35$, $Z = 0.02$. What is the ratio $P_{\rm e}^{(\rm deg)}/P_{\rm e}^{(\rm g)}$?

Chapter 4

Hydrostatic equilibrium

4.1 Introduction

As argued in Chapter 1, the absence of changes in most stars over time scales of hours or days indicates that the forces acting on the matter in the stars are essentially perfectly balanced. Here we analyze this constraint in more detail.

We consider a cylindrical slab in the star, of area $\mathrm{d}A$ and extending from the distance r to the distance $r + \mathrm{d}r$ from the centre of the star (*cf.* Figure 4.1). To obtain the equation of motion for the shell we must evaluate the forces acting on the slab. One force is gravity. It is well known that the gravitational force at the distance r from the centre arises solely from the mass contained within that point. Let this mass be $m = m(r)$. Then the gravitational acceleration is $-Gm/r^2$, where we count forces and accelerations positive in the direction of increasing r. The volume of the slab is $\mathrm{d}r\mathrm{d}A$. Hence, if the density of matter in the slab is ρ, the mass in the slab is $\rho\mathrm{d}r\mathrm{d}A$, and the gravitational

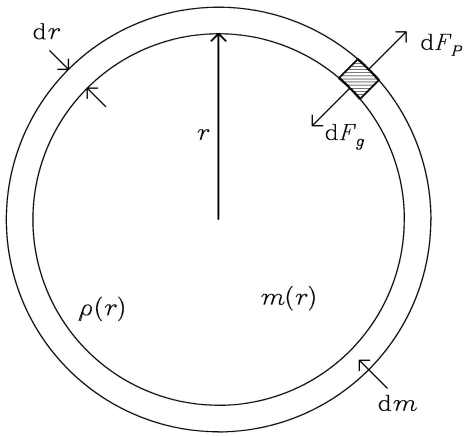

Figure 4.1: Mass shell in a spherically symmetric star, of thickness $\mathrm{d}r$ and containing the mass $\mathrm{d}m = 4\pi r^2\rho\mathrm{d}r$. In hydrostatic equilibrium, the pressure force $\mathrm{d}F_P$ on the small slab, shown hatched, balances the gravitational force $\mathrm{d}F_g$ on the slab due to the mass $m(r)$ interior to r.

force is

$$\mathrm{d}F_g = -\rho \frac{Gm}{r^2} \mathrm{d}r\mathrm{d}A \; . \tag{4.1}$$

The second force arises from the net pressure acting on the slab. Since pressure P is defined as force per unit area, this force is

$$\mathrm{d}F_P \simeq P(r)\mathrm{d}A - P(r+\mathrm{d}r)\mathrm{d}A \simeq -\frac{\mathrm{d}P}{\mathrm{d}r}\mathrm{d}r\mathrm{d}A \; , \tag{4.2}$$

by making a Taylor expansion of P; here we used that the contributions from the side of the slab vanish, by symmetry. Hence, by balancing mass times acceleration with the combined force, the equation of motion of the slab is obtained as

$$\rho \mathrm{d}r\mathrm{d}A \frac{\mathrm{d}^2 r}{\mathrm{d}t^2} = \mathrm{d}F_g + \mathrm{d}F_P \; ,$$

or

$$\rho \frac{\mathrm{d}^2 r}{\mathrm{d}t^2} = -\rho \frac{Gm}{r^2} - \frac{\mathrm{d}P}{\mathrm{d}r} \; . \tag{4.3}$$

If we demand that the star be in equilibrium so that the acceleration vanishes, the pressure gradient must be determined by

$$\frac{\mathrm{d}P}{\mathrm{d}r} = -\frac{Gm\rho}{r^2} \; . \tag{4.4}$$

This is the first of the equations of stellar structure.

This equation must be supplemented by an equation relating m to the other properties of the star. It follows immediately from the definition of m, and the fact that the mass in a shell between r and $r + \mathrm{d}r$ is $4\pi r^2 \rho \mathrm{d}r$, that

$$\mathrm{d}m = 4\pi r^2 \rho \mathrm{d}r \; ,$$

and hence

$$\frac{\mathrm{d}m}{\mathrm{d}r} = 4\pi r^2 \rho \; . \tag{4.5}$$

This is our second equation.

The equation of motion (4.3) may be used to provide further justification for the definition (1.2) of the dynamical time scale $t_{\rm dyn}$. This is a characteristic time for motion that occurs if there is *not* hydrostatic equilibrium, *e.g.* because the pressure is too small. To get an estimate of the time scale we may as a first approximation neglect the pressure term entirely, balancing the acceleration on the left-hand side of equation (4.3) by the gravitational acceleration on the right-hand side. Furthermore estimating $|\mathrm{d}^2 r/\mathrm{d}t^2|$ by $r/t_{\rm dyn}^2$, and as characteristic values of r and m taking the radius R and mass M of the star, we obtain

$$\frac{R}{t_{\rm dyn}^2} \simeq \frac{GM}{R^2} \; ,$$

or

$$t_{\rm dyn} \simeq \left(\frac{R^3}{GM} \right)^{1/2} \; , \tag{4.6}$$

which is equation (1.2).

It is important to remember the goal of estimates like this one: to get an order-of-magnitude idea about the size of the quantity being estimated, and a feeling for how it depends on, for example, the mass and radius of the star. However, it is often possible to consider cases where a more precise meaning can be given to such estimates. Several examples are considered below. The following two exercises justify that $t_{\rm dyn}$ is indeed a representative time scale for motion in a gravitational field.

Exercise 4.1:

Consider an object in a circular orbit with radius R around a mass M. Show that the orbital period is

$$\Pi_{\rm orb} = 2\pi t_{\rm dyn} \ , \tag{4.7}$$

where $t_{\rm dyn}$ is given by equation (4.6).

Exercise 4.2:

Consider the collapse of a star of mass M where the pressure is suddenly removed, by solving equation (4.3) with $P = 0$, and the initial conditions $r = R$, $\mathrm{d}r/\mathrm{d}t = 0$ for $t = 0$. Take $m = M$. What is the time required to reduce the radius by a factor 2? What is the time required for a complete collapse?
Hint: Show, by multiplying equation (4.3) by $\mathrm{d}r/\mathrm{d}t$ and integrating that

$$\frac{\mathrm{d}r}{\mathrm{d}t} = -\left[2GM(r^{-1} - R^{-1})\right]^{1/2} \ .$$

When integrating this equation it is convenient to use the substitution $r = R\cos^2 u$.

4.2 Estimates of stellar internal pressure and temperature

4.2.1 The estimates

From equation (4.4) we may obtain an estimate of the central pressure $P_{\rm c}$ of a star with mass M and radius R. We make the following approximations:

- Replace $\mathrm{d}P/\mathrm{d}r$ by $-P_{\rm c}/R$.
- Replace m by M.
- Replace r by R.
- Replace ρ by the mean density, approximated as M/R^3.

Then equation (4.4) gives

$$\frac{P_{\rm c}}{R} \simeq \frac{GM^2}{R^5} \, ,$$

or

$$P_{\rm c} \simeq \frac{GM^2}{R^4} \, . \tag{4.8}$$

If we assume the ideal gas law, equation (3.6), we may estimate the central temperature as

$$T_{\rm c} = \frac{\mu_{\rm c} m_{\rm u} P_{\rm c}}{k_{\rm B} \rho_{\rm c}} \simeq \frac{G \mu_{\rm c} m_{\rm u} M}{k_{\rm B} R} \, , \tag{4.9}$$

where $\mu_{\rm c}$ is the central mean molecular weight. In terms of solar values we obtain

$$P_{\rm c} \simeq 1.1 \times 10^{16} \left(\frac{M}{{\rm M}_\odot} \right)^2 \left(\frac{R}{{\rm R}_\odot} \right)^{-4} {\rm dyn\,cm^{-2}} \, , \tag{4.10}$$

$$T_{\rm c} \simeq 1.9 \times 10^{7} \left(\frac{M}{{\rm M}_\odot} \right) \left(\frac{R}{{\rm R}_\odot} \right)^{-1} \left(\frac{\mu_{\rm c}}{0.85} \right) {\rm K} \, , \tag{4.11}$$

where the value of $\mu_{\rm c}$ was obtained from equation (3.27), with $X = 0.35$, $Z = 0.02$.

The interpretation of these results is the usual: they are obviously not accurate estimates of the central pressure or temperature of a star, but they provide an order of magnitude. After all, without any prior knowledge it would be difficult to guess whether the central pressure of the Sun was 10^{10}, 10^{20} or $10^{30}\,{\rm dyn\,cm^{-2}}$! In fact the estimates are reasonably (in the case of the temperature, fortuitously) accurate: realistic computations of solar models show that the solar central pressure is $P_{\rm c} = 2.4 \times 10^{17}\,{\rm dyn\,cm^{-2}}$ and the solar central temperature is $1.5 \times 10^7\,{\rm K}$. It should be noted also that the estimate for the pressure is obtained solely on the basis of Newtonian mechanics; the estimate of the temperature in addition required a minimal amount of thermodynamics. Surely a good example of the power of basic physics to provide knowledge about the internal properties of stars.

The second aspect of the simple estimates is that they indicate how pressure and temperature scale with the stellar mass and radius. This dependence has a wider applicability. We shall later see several examples of how this scaling can be given a more precise meaning for particular types of simplified stellar models. And even for realistic stellar models, with detailed physics, one often find that the scalings provided by the simple estimates are surprisingly accurate when the stellar parameters are varied. Thus these estimates are very helpful for the interpretation of detailed numerical results.

4.2.2 The importance of radiation pressure

We can use the estimates in equations (4.8) and (4.9) to determine the conditions under which radiation pressure becomes important. We find, from equation (3.37)

$$\frac{P_r}{P} \simeq \frac{1}{3} \frac{a G^3 (\mu_{\rm c} m_{\rm u})^4}{k_{\rm B}^4} M^2 \simeq 0.01 \left(\frac{M}{{\rm M}_\odot} \right)^2 \left(\frac{\mu_{\rm c}}{0.62} \right)^4 \, , \tag{4.12}$$

where the reference value of $\mu_{\rm c}$ corresponds to a chemical composition with $X = 0.7$, $Z = 0.02$. This indicates that for masses of order several solar masses radiation pressure must be taken into account.

Exercise 4.3:

Verify equation (4.12)

There are several problems with equation (4.12). The estimate for the temperature assumed that the gas pressure was dominant, so that the ideal gas law could be used to determine the temperature from pressure and density. Hence equation (4.12) becomes invalid once radiation pressure becomes important. Also, as usual in these estimates, the precise numerical values cannot be trusted; in fact radiation pressure only becomes substantial at somewhat higher masses, around $50\,\mathrm{M}_\odot$. However, the principal result, namely that radiation pressure dominates in massive stars, is certainly valid.

It was argued in section 3.4 that systems where Γ_1 is close to or below 4/3 tend to be unstable. This would be the case where most of the pressure comes from radiation. Thus our results suggest that very massive stars might be unstable. In fact, it is thought that instabilities of this nature limit stellar masses to be less than about $100\,\mathrm{M}_\odot$. This is confirmed by observations.[1].

At the risk of appearing repetitive, it should be noted that this limit, or suggestion of a limit, for stellar masses was again obtained from basic physics, and could in fact have been derived without any prior knowledge about stars. A striking description of this was given by Eddington, in *The internal constitution of the stars*; it is reproduced in Box 4.1.

4.3 Strict limits on the central pressure

It is of some interest that strict limits can be obtained for the central pressure of a star, with very few assumptions. We consider two examples; a more detailed discussion, with further precise theorems concerning stellar structure, was given by Chandrasekhar (1939).

4.3.1 A simple limit

The first limit requires no assumptions beyond hydrostatic equilibrium. It is obtained by manipulating equation (4.4), using also equation (4.5):

$$\begin{aligned}\frac{\mathrm{d}P}{\mathrm{d}r} &= -\frac{Gm\rho}{r^2} = -\frac{Gm}{4\pi r^4}4\pi r^2\rho = -\frac{Gm}{4\pi r^4}\frac{\mathrm{d}m}{\mathrm{d}r} \\ &= -\frac{\mathrm{d}}{\mathrm{d}r}\left(\frac{Gm^2}{8\pi r^4}\right) - \frac{Gm^2}{2\pi r^5}\,,\end{aligned}$$

and hence

$$\frac{\mathrm{d}}{\mathrm{d}r}\left(P + \frac{Gm^2}{8\pi r^4}\right) = -\frac{Gm^2}{2\pi r^5} < 0\,. \tag{4.13}$$

[1] It was thought for a while that a much more massive star had been discovered in the nebula 30 Doradus in the Large Magellanic Cloud. This would have caused severe problems for the theory of stellar evolution. Observations with the Hubble Space Telescope have shown, however, that what appeared from the ground to be a single star was in fact a dense cluster of about 60 bright stars, each of which is well within the limits of normal stellar models. Depending on ones general attitude to science this result may be greeted with relief or disappointment.

Box 4.1

We can imagine a physicist on a cloud-bound planet who has never heard tell of the stars calculating the ratio of radiation pressure to gas pressure for a series of globes of gas of various sizes, starting, say, with a globe of mass 10 gm., then 100 gm., 1000 gm., and so on, so that his nth globe contains 10^n gm. Table 2 shows the more interesting part of his results.

Table 2.

No. of Globe	Radiation Pressure	Gas Pressure
30	·00000016	·99999984
31	·000016	·999984
32	·0016	·9984
33	·106	·894
34	·570	·430
35	·850	·150
36	·951	·049
37	·984	·016
38	·9951	·0049
39	·9984	·0016
40	·99951	·00049

The rest of the table would consist mainly of long strings of 9's and 0's. Just for the particular range of mass about the 33rd to 35th globes the table becomes interesting, and then lapses back into 9's and 0's again. Regarded as a tussle between matter and aether (gas pressure and radiation pressure) the contest is overwhelmingly one-sided except between Nos. 33–35, where we may expect something interesting to happen.

What "happens" is the stars.

We draw aside the veil of cloud beneath which our physicist has been working and let him look up at the sky. There he will find a thousand million globes of gas nearly all of mass between his 33rd and 35th globes—that is to say, between $\frac{1}{2}$ and 50 times the sun's mass. The lightest known star is about $3 \cdot 10^{32}$ gm. and the heaviest about $2 \cdot 10^{35}$ gm. The majority are between 10^{33} and 10^{34} gm. where the serious challenge of radiation pressure to compete with gas pressure is beginning.

From Eddington (1930), p. 16.

This shows that the quantity $\Psi(r) = P + Gm^2/(8\pi r^4)$ is a decreasing function of r. At the centre $P = P_c$; also, equation (4.5) shows that $m \propto r^3$ for small r, so that the second term in Ψ vanishes at $r = 0$. Hence $\Psi(0) = P_c$. At the surface P is essentially zero. Thus, from the fact that Ψ is a decreasing function of r it follows that

$$P_c = \Psi(0) > \Psi(R) = \frac{GM^2}{8\pi R^4} , \tag{4.14}$$

and this is the desired limit.

It is remarkable that this limit is a strict mathematical result, valid for any stellar model in hydrostatic equilibrium, regardless of its other properties, such as equation of state or energy transport and production. Also, it confirms that GM^2/R^4 is indeed a characteristic value for the internal pressure of stars. On the other hand, the limit is fairly

weak, compared with the actual solar central pressure quoted above.

4.3.2 A stronger limit

A stronger limit on the central pressure can be obtained if in addition to hydrostatic equilibrium we assume that the mean density $\rho(r)$ inside r, defined by

$$\overline{\rho}(r) = \frac{m}{\frac{4}{3}\pi r^3} \ , \tag{4.15}$$

decreases with increasing r. As discussed in Chapter 6 a condition of this nature is in fact required for the star to be stable towards convection. The argument is similar to that given in the preceding section, but uses an additional trick; it is reproduced here from Chandrasekhar (1939).

We consider the function $\Psi_\alpha(r) = P + \alpha G m^2/(8\pi r^4)$, where, initially, we leave unspecified the value of the constant α. Then, using again equations (4.4) and (4.5),

$$\begin{aligned} \frac{\mathrm{d}\Psi_\alpha}{\mathrm{d}r} &= -\frac{Gm\rho}{r^2} + \alpha\frac{Gm}{4\pi r^4}4\pi r^2\rho - \alpha\frac{Gm^2}{2\pi r^5} \\ &= (\alpha-1)\frac{Gm\rho}{r^2} - \alpha\frac{Gm^2}{2\pi r^5} = \frac{Gm}{r^2}\left[(\alpha-1)\rho - \frac{2\alpha}{3}\overline{\rho}(r)\right] \ . \end{aligned}$$

If $\overline{\rho}(r)$ decreases outwards, it follows that $\overline{\rho}(r) \geq \rho$. Hence, if we choose $\alpha = 3$, we have that

$$\frac{\mathrm{d}\Psi_3}{\mathrm{d}r} = -2\frac{Gm}{r^2}[\overline{\rho}(r) - \rho] \leq 0 \ , \tag{4.16}$$

i.e., that Ψ_3 is a decreasing function of r. As before it then follows that

$$P_\mathrm{c} = \Psi_3(0) \geq \Psi_3(R) = \frac{3}{8\pi}\frac{GM^2}{R^4} \ . \tag{4.17}$$

Hence by adding the constraint that the mean density is a decreasing function of r the lower bound on the central pressure has been increased by a factor 3.

4.4 The virial theorem

4.4.1 Introduction

From the equation of hydrostatic equilibrium we can derive an equation for the energetics of a star, which is of the greatest importance for understanding stellar evolution. We begin by deriving an expression for the gravitational potential energy of the star. At the distance r from the centre the gravitational potential is $-Gm/r$, if we choose the arbitrary constant in the potential such that it is zero infinitely far from the star. Hence the total potential energy is

$$\Omega = -\int_0^R \frac{Gm}{r}4\pi r^2\rho\mathrm{d}r = -4\pi\int_0^R Gmr\rho\mathrm{d}r \ . \tag{4.18}$$

This may be rewritten, by using equation (4.4) and integrating by parts:

$$\begin{aligned} \Omega &= -4\pi\int_0^R \frac{Gm\rho}{r^2}r^3\mathrm{d}r = 4\pi\int_0^R \frac{\mathrm{d}P}{\mathrm{d}r}r^3\mathrm{d}r \\ &= 4\pi P r^3\,|_0^R - 3\int_0^R P4\pi r^2\mathrm{d}r \ . \end{aligned} \tag{4.19}$$

Here the integrated term vanishes, since $P = 0$ at the surface, $r = R$.[2] Hence

$$\Omega = -3 \int_0^R P 4\pi r^2 \mathrm{d}r \; . \tag{4.20}$$

This integral may be related to the total thermal energy of the gas in the star.

4.4.2 The nonrelativistic case

We first consider the case where the gas is ideal and the particles in it are non-relativistic. Then pressure and internal energy per unit volume are related by equation (3.1); since in equation (4.20) $4\pi r^2 \mathrm{d}r$ is a volume element, we finally obtain

$$\Omega = -2 \int_0^R u 4\pi r^2 \mathrm{d}r = -2U_{\rm tot} \; , \qquad \text{nonrelativistic} \; , \tag{4.21}$$

where $U_{\rm tot}$ is the total thermal energy of the star. This relation is called the *virial theorem*. From equation (4.21) it follows that the total energy of the star is

$$E = \Omega + U_{\rm tot} = -U_{\rm tot} = \frac{1}{2}\Omega \; ; \tag{4.22}$$

that the total energy is negative indicates that the star is stable: the thermal energy in the star is insufficient to cause it to explode.

Equation (4.22) allows us to understand the evolution of stars where there are no sources of nuclear energy. Since the surface of the star is hot it looses energy which has to be supplied, and the only source of energy available to the star is the release of gravitational potential energy that results from the star contracting and hence becoming more strongly gravitationally bound. From equation (4.22) it follows that contraction also causes the total energy of the star to become more negative. However, since globally there has to be energy conservation, the energy lost by the star has to go somewhere else, and this is what is radiated from the star. Specifically, the luminosity of a contracting star is given by

$$L_G = -\frac{1}{2}\frac{\mathrm{d}\Omega}{\mathrm{d}t} \simeq -\frac{1}{2}\frac{GM^2}{R^2}\frac{\mathrm{d}R}{\mathrm{d}t} \; , \tag{4.23}$$

where in the last approximate identity we used the estimate in equation (1.4) for the total gravitational potential energy. From equation (4.22) it follows also that the thermal energy $U_{\rm tot}$ increases; so therefore does the average temperature in the gas.[3] Of the gravitational potential energy that is released in the contraction half is radiated away and the other half goes to heat up the gas. This demonstrates the paradoxical property of selfgravitating systems that they have a *negative specific heat*: as they lose energy they become warmer.

It follows from equation (4.23) that

$$\frac{\mathrm{d}R}{\mathrm{d}t} \simeq -2\frac{R}{t_{\rm KH}} \; , \tag{4.24}$$

[2] However, it is sometimes useful to consider an expression like equation (4.19) for some part of the star, so that the integrated terms must be taken into account.

[3] Note that it follows already from the estimate in equation (4.9) that the temperature increases as the radius decreases, when the ideal gas law is assumed.

where $t_{\rm KH}$ is the Kelvin-Helmholtz time defined in equation (1.5). This confirms that $t_{\rm KH}$ is a characteristic time for the gravitational contraction of a star. It might be noted that the equality in equation (4.21) shows that $t_{\rm KH}$ is also a characteristic time for the radiation of the thermal energy of the star. Hence changes that involve substantial losses or gains of energy cannot take place on time scales shorter than $t_{\rm KH}$, at least as long as hydrostatic equilibrium is nearly maintained. Correspondingly, for changes that *do* occur on much shorter time scales the changes in energy must be very small; in other words, such changes are nearly adiabatic.

Exercise 4.4:

Estimate the annual change in the solar radius, if one were to assume that the entire solar luminosity came from gravitational contraction. The best current measurements of the solar radius have a precision of $\pm 0.1\,\text{"}$; for how long should one observe the Sun to detect such a radius change?

Similar effects occur in later stages of stellar evolution, as nuclear fuels are exhausted in the core of the star: again, the result is a gravitational contraction which releases energy and heats up the core, until the point is reached where further nuclear reactions set in. In this case, however, the situation may be complicated by the presence elsewhere in the star of nuclear burning shells; also, one often finds that the outer parts of the star expand (which require energy to work against gravity) as the core contracts. Thus the understanding of these evolutionary phases is less straightforward; but the virial theorem still plays a central role.

When the gas cannot be regarded as ideal, or effects of ionization have to be taken into account, the simple equation (4.22) must be modified; but the general principles remain the same.

4.4.3 The relativistic case

If the particles in the gas are extremely relativistic, equation (3.2) must be used to relate pressure and internal energy. In this case we obtain from equation (4.20) that

$$\Omega = -U_{\rm tot}, \qquad \text{extremely relativistic}\ , \tag{4.25}$$

and hence for the total energy

$$E = 0\ . \tag{4.26}$$

This result shows that an extremely relativistic system is marginally stable: it may expand or contract indefinitely without any change in the total energy. Hence a small change to the system may be sufficient to push it into instability. An important example of extremely relativistic systems is a star dominated by radiation pressure; thus this argument supports the postulate that such stars are unstable.

4.5 Simple solutions to the equation of hydrostatic equilibrium

In the general case equations (4.4) and (4.5) cannot be solved as they stand; this requires further equations, to be discussed in subsequent chapters, to determine ρ. There are two exceptions, however:

a) When ρ is a known function of r.

b) When ρ is a known function of P.

If $\rho(r)$ is known, equation (4.5) may be integrated, starting from $m(0) = 0$, to yield $m(r)$; given $m(r)$ equation (4.4) may be integrated starting from $r = R$, with the boundary condition $P(R) = 0$. Although this case has little practical utility for the construction of realistic stellar models, it is interesting that knowledge of $\rho(r)$ completely determines the hydrostatic structure of a star. A simple example, where ρ is prescribed as a linear function of r, is discussed in section 4.5.1 below.

The second case, where ρ is a known function of P, evidently assumes a rather special form of the equation of state. A general class of models where this is the case is discussed in some detail in section 4.6. A very simple example is the case where the temperature is assumed to be given; this provides a simplified model of a stellar atmosphere. It is discussed in section 4.5.2.

4.5.1 The linear model

We assume that ρ is a linear function of r, between $\rho = \rho_{\rm c}$ at $r = 0$ and $\rho = 0$ at $r = R$, *i.e.*,

$$\rho = \rho_{\rm c}\left(1 - \frac{r}{R}\right) \ . \tag{4.27}$$

By integrating equation (4.5) with this expression for ρ we obtain

$$m = \frac{4\pi}{3}\rho_{\rm c} r^3 \left(1 - \frac{3}{4}\frac{r}{R}\right) = M(4x^3 - 3x^4) \ , \tag{4.28}$$

where we required that the star have total mass M, and we introduced $x = r/R$. It follows also that the central density is related to the mass and radius by

$$\rho_{\rm c} = \frac{3M}{\pi R^3} \ . \tag{4.29}$$

Using this expression and equation (4.27) in equation (4.4) yields, after some manipulations,

$$P = \frac{5}{4\pi}\frac{GM^2}{R^4}\left(1 - \frac{24}{5}x^2 + \frac{28}{5}x^3 - \frac{9}{5}x^4\right) \ , \tag{4.30}$$

where we assumed that $P = 0$ at the surface, $r = R$. It should be noted that the dependence of pressure on mass and radius is again characterized by M^2R^{-4}.

Exercise 4.5:

Fill in the missing details in the derivation of equations (4.28) – (4.30). Compare the central pressure in equation (4.30) with the exact bounds obtained in section 4.3.

If we assume the ideal gas law with no radiation pressure, equation (3.6), we find from equations (4.27), (4.29) and (4.30) that the temperature is

$$T = \frac{5}{12}\frac{G\mu m_{\rm u} M}{k_{\rm B} R}\left(1 + x - \frac{19}{5}x^2 + \frac{9}{5}x^3\right) . \tag{4.31}$$

Note that this leads to an expression for the central temperature on the same form as equation (4.9), although with a somewhat different numerical constant.

Exercise 4.6:

Verify equation (4.31).

4.5.2 The isothermal atmosphere

We assume that the temperature T is constant in the atmosphere. Furthermore we assume that the extent of the atmosphere is so small that it can be neglected compared with the radius of the star. Then the gravitational acceleration $g = GM/R^2$ can be assumed to be constant. Finally we assume that the ideal gas law, equation (3.6), is valid. In this case we obtain from equation (4.4) that

$$\frac{{\rm d}P}{{\rm d}r} = -g\rho = -\frac{P}{H} , \tag{4.32}$$

where the *pressure scale height* H is given by

$$H = \frac{k_{\rm B} T}{g\mu m_{\rm u}} . \tag{4.33}$$

Since H is a constant, equation (4.32) may be integrated immediately. We introduce the altitude $h = r - r_0$, where r_0 defines some arbitrary reference level in the atmosphere, and obtain

$$P = P_0 \exp\left(-\frac{h}{H}\right) , \tag{4.34}$$

where P_0 is the value of P at $h = 0$. From the ideal gas law it then follows

$$\rho = \rho_0 \exp\left(-\frac{h}{H}\right) , \tag{4.35}$$

where ρ_0 is the value of ρ at $h = 0$. Thus in an isothermal atmosphere pressure and density decrease exponentially.

Exercise 4.7:

Estimate the scale height in the solar atmosphere ($T \simeq 6000\,\mathrm{K}$) and in the Earth's atmosphere ($T \simeq 300\,\mathrm{K}$). Both the solar and the Earth's atmosphere can be assumed to be totally unionized; remember also that the chemical composition is rather different in the Earth's atmosphere from the composition of typical stellar atmospheres. What is the density of air at the top of Mt Everest, compared with the density at sea level?

4.6 Polytropic models

As mentioned above, the equation of hydrostatic equilibrium can be solved in the case where ρ is a known function of P. A particular example of this is a relation on the form

$$P = K\rho^{\gamma} \,, \tag{4.36}$$

where K and γ are constants; this is called a *polytropic relation*, and the resulting models are called *polytropic models*. Models of this nature have played a very important role in the development of the subject; they are still useful as simple examples which are nevertheless not too dissimilar from realistic models. More importantly, there are cases where a polytropic equation of state is a good approximation to reality. An example is a gas where the pressure is dominated by degenerate electrons (*cf.* equation (3.61)); another example, to which we return in Chapter 6, is the case where pressure and density are related adiabatically, as in equation (3.15).

To obtain the equation satisfied by polytropic models we note that from equations (4.4) and (4.5)

$$\frac{\mathrm{d}}{\mathrm{d}r}\left(\frac{r^2}{\rho}\frac{\mathrm{d}P}{\mathrm{d}r}\right) = -G\frac{\mathrm{d}m}{\mathrm{d}r} = -4\pi G\rho r^2 \,.$$

Hence, using equation (4.36), we obtain

$$\frac{\mathrm{d}}{\mathrm{d}r}\left(r^2 K\gamma\rho^{\gamma-2}\frac{\mathrm{d}\rho}{\mathrm{d}r}\right) = -4\pi G\rho r^2 \,. \tag{4.37}$$

It is convenient to replace γ by *the polytropic index* n, defined by

$$n = \frac{1}{\gamma - 1} \qquad \text{or} \qquad \gamma = 1 + \frac{1}{n} \,. \tag{4.38}$$

Furthermore, we introduce a dimensionless measure θ of ρ by

$$\rho = \rho_{\mathrm{c}}\theta^n \,, \tag{4.39}$$

where ρ_{c} is the central density. Then equation (4.37) becomes

$$\frac{(n+1)K\rho_{\mathrm{c}}^{1/n\,-1}}{4\pi G}\frac{1}{r^2}\frac{\mathrm{d}}{\mathrm{d}r}\left(r^2\frac{\mathrm{d}\theta}{\mathrm{d}r}\right) = -\theta^n \,. \tag{4.40}$$

To simplify the equation further, we introduce a new measure, ξ, of the distance to the centre by

$$r = \alpha\xi, \qquad \text{where} \qquad \alpha^2 = \frac{(n+1)K\rho_{\rm c}^{1/n\,-1}}{4\pi G}\ . \tag{4.41}$$

Then the equation finally becomes

$$\frac{1}{\xi^2}\frac{\rm d}{{\rm d}\xi}\left(\xi^2\frac{{\rm d}\theta}{{\rm d}\xi}\right) = -\theta^n\ . \tag{4.42}$$

This equation is called the *Lane-Emden equation*, and the solution $\theta = \theta_n(\xi)$ is called the Lane-Emden function. From equation (4.39) it follows that θ_n must satisfy the boundary condition

$$\theta_n = 1 \quad \text{for} \quad \xi = 0\ . \tag{4.43}$$

The surface of the model is defined by the point, $\xi = \xi_1$, where $\theta = 0$.

Given the solution θ_n, we can obtain relations between the various quantities characterizing the model. It follows immediately from equation (4.41) that the surface radius of the model is

$$R = \left[\frac{(n+1)K\rho_{\rm c}^{1/n\,-1}}{4\pi G}\right]^{1/2}\xi_1\ . \tag{4.44}$$

The mass $m(\xi)$ interior to ξ may be obtained by integrating equation (4.5), using equations (4.39), (4.41) and (4.42), as

$$\begin{aligned} m(\xi) &= \int_0^{\alpha\xi} 4\pi r^2\rho{\rm d}r = 4\pi\alpha^3\rho_{\rm c}\int_0^{\xi}\xi^2\theta_n^n{\rm d}\xi \\ &= -4\pi\alpha^3\rho_{\rm c}\int_0^{\xi}\frac{\rm d}{{\rm d}\xi}\left(\xi^2\frac{{\rm d}\theta_n}{{\rm d}\xi}\right){\rm d}\xi = -4\pi\alpha^3\rho_{\rm c}\xi^2\frac{{\rm d}\theta_n}{{\rm d}\xi}\ . \end{aligned} \tag{4.45}$$

Using the second of equations (4.41) we finally obtain

$$m(\xi) = -4\pi\left[\frac{(n+1)K}{4\pi G}\right]^{3/2}\rho_{\rm c}^{(3-n)/2n}\xi^2\frac{{\rm d}\theta_n}{{\rm d}\xi}\ . \tag{4.46}$$

In particular, the total mass is given by

$$M = -4\pi\left[\frac{(n+1)K}{4\pi G}\right]^{3/2}\rho_{\rm c}^{(3-n)/2n}\left(\xi^2\frac{{\rm d}\theta_n}{{\rm d}\xi}\right)_{\xi=\xi_1}\ . \tag{4.47}$$

From equations (4.44) and (4.47) we may find a relation between M, R and K, by eliminating $\rho_{\rm c}$. The result is

$$K = N_n G M^{(n-1)/n}R^{(3-n)/n}\ , \tag{4.48}$$

where

$$N_n = \frac{(4\pi)^{1/n}}{n+1}\left[-\xi_1^{(n+1)/(n-1)}\left(\frac{{\rm d}\theta_n}{{\rm d}\xi}\right)_{\xi=\xi_1}\right]^{(1-n)/n}\ . \tag{4.49}$$

There are two different interpretations of these relations, depending on the physical basis for assuming a polytropic equation of state. If the constant K in equation (4.36) is given

in terms of basic constants and hence is known, equation (4.48) defines a relation between the mass and the radius of the star; this is the case, for example, for a star dominated by the pressure of degenerate electrons, since here K is determined in equation (3.61). If, on the other hand, equation (4.36) just expresses proportionality, the constant K being essentially arbitrary, then equation (4.48) may be used to determine K for a star with a given mass and radius; as shown below one may then determine other quantities for the star. In the former case, therefore, there is a unique polytropic model for a given mass, whereas in the latter case a model can be constructed for any value of M and R.

Exercise 4.8:

Verify equations (4.48) and (4.49).
Find the relation between M and R for a star dominated by degenerate electrons. What is the radius of such a star if the mass is $0.6\,\mathrm{M}_\odot$, and it is assumed to consist of fully ionized carbon? (Use the appropriate value of N_n from Table 4.1 below).

From the last of equations (4.45) we find that the mean density of the star is

$$\overline{\rho} = \frac{M}{\frac{4}{3}\pi R^3} = -\frac{3}{\xi_1}\left(\frac{\mathrm{d}\theta_n}{\mathrm{d}\xi}\right)_{\xi=\xi_1}\rho_\mathrm{c}\ , \tag{4.50}$$

and hence the central density is determined by the mass and radius as

$$\rho_\mathrm{c} = -\left[\frac{\xi}{3}\frac{1}{\dfrac{\mathrm{d}\theta_n}{\mathrm{d}\xi}}\right]_{\xi=\xi_1}\frac{M}{\frac{4}{3}\pi R^3}\ . \tag{4.51}$$

Finally, using that from equation (4.36)

$$P_\mathrm{c} = K\rho_\mathrm{c}^{(n+1)/n}\ ,$$

and using equations (4.48) and (4.51), we find that

$$P_\mathrm{c} = W_n\frac{GM^2}{R^4}\ , \tag{4.52}$$

where

$$W_n = \left\{4\pi(n+1)\left[\left(\frac{\mathrm{d}\theta_n}{\mathrm{d}\xi}\right)_{\xi=\xi_1}\right]^2\right\}^{-1}\ . \tag{4.53}$$

The pressure throughout the model is then determined by

$$P = P_\mathrm{c}\theta_n^{n+1}\ . \tag{4.54}$$

Exercise 4.9:

Fill in the missing details in the derivation of equations (4.50) – (4.53).

Exercise 4.10:

Show that the gravitational potential energy of a polytrope of index n is

$$\Omega = -\frac{3}{5-n}\frac{GM^2}{R} \ . \tag{4.55}$$

(This is quite difficult. It may help to look in Chandrasekhar 1939).

In the case where the temperature is related to pressure and density through the ideal gas law (3.6), assuming μ to be constant, equations (4.39) and (4.54) yield

$$T = T_{\rm c}\theta_n \ , \tag{4.56}$$

where

$$T_{\rm c} = \Theta_n \frac{GM\mu m_{\rm u}}{k_{\rm B}R} \ , \tag{4.57}$$

and

$$\Theta_n = \left[-(n+1)\xi_1 \left(\frac{{\rm d}\theta_n}{{\rm d}\xi}\right)_{\xi=\xi_1}\right]^{-1} \ . \tag{4.58}$$

In this case, therefore, θ is a measure of the temperature.

To determine the structure of a polytropic star completely, we only need to find the solution to the Lane-Emden equation (4.42). Unfortunately, in general no analytical solution is possible. The only exceptions are $n = 0$, 1 and 5 where the solutions are

$$n = 0: \qquad \theta_0 = 1 - \frac{1}{6}\xi^2 \qquad \xi_1 = \sqrt{6} \ , \tag{4.59}$$

$$n = 1: \qquad \theta_1 = \frac{\sin\xi}{\xi} \qquad \xi_1 = \pi \ , \tag{4.60}$$

$$n = 5: \qquad \theta_5 = (1 + \frac{1}{3}\xi^2)^{-1/2} \qquad \xi_1 = \infty \ . \tag{4.61}$$

Exercise 4.11:

Verify that these solutions satisfy the Lane-Emden equation (4.42) and the boundary condition (4.43).

The solution for $n = 5$ is evidently peculiar, in that it has infinite radius; also it follows from equation (4.55) that the gravitational potential energy of the model is infinite. On the other hand, since

$$\lim_{\xi\to\infty}\left(-\xi^2\frac{{\rm d}\theta_5}{{\rm d}\xi}\right) = \sqrt{3} \tag{4.62}$$

is finite, so is the mass of the model (*cf.* equation (4.47)). It may be shown that only for $n < 5$ does the Lane-Emden equation have solutions corresponding to finite radius.

Table 4.1

n	ξ_1	$-\xi_1^2\left(\frac{\mathrm{d}\theta_n}{\mathrm{d}\xi}\right)_{\xi=\xi_1}$	$\frac{\rho_\mathrm{c}}{\overline{\rho}}$	N_n	W_n	Θ_n
0.	2.44949	4.89898	1.00000	$\cdots$	0.119366	0.50000
0.50	2.75270	3.78865	1.83514	2.52360	0.212209	0.48438
1.00	3.14159	3.14159	3.28987	0.63662	0.392699	0.50000
1.50	3.65375	2.71406	5.99070	0.42422	0.770140	0.53849
2.00	4.35287	2.41105	11.40254	0.36475	1.638183	0.60180
2.50	5.35528	2.18720	23.40646	0.35150	3.909062	0.69956
3.00	6.89685	2.01824	54.1825	0.36394	11.050679	0.85432
3.25	8.01894	1.94980	88.1532	0.37898	20.36510	0.96769
3.50	9.53581	1.89056	152.8837	0.40104	40.90982	1.12087
4.00	14.97155	1.79723	622.408	0.47720	247.559	1.66607
4.50	31.83646	1.73780	6189.47	0.65798	4921.84	3.33091
4.90	171.4335	1.72462	973806	1.35323	3.916826×10^6	16.84808
5.0	∞	1.73205	∞	∞	∞	∞

Properties of polytropic models.

For values of n other than 0, 1 and 5 the Lane-Emden equation must be solved numerically. Extensive tables of the solution exist; in any case, with modern computational facilities the solution of the equation is a simple numerical problem. Table 4.1 lists a number of useful quantities, which enter into the expressions given above, for a selection of polytropic models. Furthermore, Table 4.2 presents the solution for the particular case of $n = 3$, at selected values of ξ. To illustrate the distribution of mass in the model, according to equation (4.47), the last column gives the quantity

$$q = \frac{m}{M} = \left(\xi^2 \frac{\mathrm{d}\theta_n}{\mathrm{d}\xi}\right)\left(\xi^2 \frac{\mathrm{d}\theta_n}{\mathrm{d}\xi}\right)^{-1}_{\xi=\xi_1} . \tag{4.63}$$

From Table 4.1 it follows that the properties of polytropic models vary widely with n. This is true in particular of the degree of central condensation, as measured by the ratio $\rho_\mathrm{c}/\overline{\rho}$ between central and mean density. For $n = 0$ is is obvious from equation (4.39) that ρ is constant, and hence $\rho_\mathrm{c}/\overline{\rho} = 1$, whereas the ratio clearly tends to infinity as $n \to 5$. For stars on the main sequence the central condensation is typically around 10^2, corresponding to a polytrope of index around 3.3. It should be noticed also that equation (4.52) for the central pressure and, in the ideal-gas case, equation (4.57) for the central temperature, confirm the simple scalings derived in section 4.2. However, the polytropic relations contain the additional numerical constants W_n and Θ_n. It is obvious from Table 4.1 that W_n varies strongly with n; hence the estimate in equation (4.8) is at most a rough approximation. On the other hand, the range of variation of Θ_n is much more modest, except when n is very close to the critical case $n = 5$. Thus equation (4.9) gives a reasonable estimate for the central temperature for a wide range of models.

Table 4.2

ξ	θ_3	θ_3^3	θ_3^4	$-\frac{\mathrm{d}\theta_3}{\mathrm{d}\xi}$	q
0.	1.	1.	1.	0.	0.
0.25	0.98968	0.96936	0.95935	0.08179	0.00253
0.50	0.95984	0.88429	0.84878	0.15484	0.01918
0.75	0.91354	0.76240	0.69649	0.21263	0.05926
1.00	0.85506	0.62515	0.53454	0.25213	0.12493
1.25	0.78898	0.49113	0.38749	0.27367	0.21187
1.50	0.71950	0.37247	0.26800	0.27991	0.31206
1.75	0.64999	0.27461	0.17849	0.27460	0.41668
2.00	0.58285	0.19800	0.11541	0.26149	0.51826
2.25	0.51962	0.14030	0.07290	0.24380	0.61154
2.50	0.46113	0.09805	0.04521	0.22397	0.69358
2.75	0.40767	0.06775	0.02762	0.20369	0.76325
3.00	0.35923	0.04636	0.01665	0.18405	0.82074
3.25	0.31554	0.03142	0.009914	0.16567	0.86702
3.50	0.27626	0.02109	0.005825	0.14885	0.90344
3.75	0.24098	0.01399	0.003372	0.13369	0.93151
4.00	0.20928	0.009166	0.001918	0.12017	0.95266
4.25	0.18077	0.005907	0.001068	0.10819	0.96826
4.50	0.15507	0.003729	0.000578	0.09762	0.97946
4.75	0.13185	0.002292	0.000302	0.08831	0.98727
5.00	0.11082	0.001361	0.000151	0.08013	0.99252
5.25	0.09171	0.000771	0.000071	0.07292	0.99590
5.50	0.07429	0.000410	0.000030	0.06658	0.99795
5.75	0.05835	0.000199	0.000012	0.06099	0.99910
6.00	0.04374	0.000084	0.000004	0.05604	0.99967
6.25	0.03029	0.000028	0.000001	0.05166	0.99991
6.50	0.01787	0.000006	0.000000	0.04777	0.99999
6.75	0.00637	0.000000	0.000000	0.04430	1.00000
6.89685	0.00000	0.000000	0.000000	0.04243	1.00000

Properties of a polytrope of index $n = 3$. From equations (4.39) and (4.54) it follows that θ_3^3 and θ_3^4 correspond to ρ/ρ_c and P/P_c, respectively. The last column gives the mass fraction $q = m/M$.

Exercise 4.12:

Find ρ_c, P_c and T_c in a polytrope of index 3 with solar mass and radius and chemical composition $X = 0.7$, $Z = 0.02$, where the ideal gas law is assumed to be valid. Find also ρ, P and T at the point where $r = R/2$. (Use the data in Tables 4.1 and 4.2).

Chapter 5

Radiative energy transport

5.1 Radiative transport in stellar interiors

The complete treatment of the transport of energy by radiation, and the interaction between radiation and matter, is a research topic in its own right, which has been extensively treated in the literature (*e.g.* Mihalas 1978; see also Clayton 1968, Chapter 3). Such a complete treatment is required to analyze the properties of, for example, stellar atmospheres or the interstellar medium. In stellar interiors, however, it is possible to get by with a simplified description whose results agree with those of the more complete theory in the limit where the mean free path of the photons is very short.

As discussed in Section 3.4, one can show that the energy density of radiation is $u_{\rm R} = aT^4$, where a is the radiation density constant. T, and hence $u_{\rm R}$, decreases with increasing distance r from the centre of the star. As a result, photons moving away from the centre carry a slightly higher energy on average than photons that move towards the centre, and this gives rise to a net transport of energy towards the surface of the star. In the following this argument is made more quantitative.

We consider the energy transport in the time interval $\mathrm{d}t$ through an area $\mathrm{d}A$ orthogonal to the direction to the centre of the star, at $r = r_0$. We describe the direction of motion of the photons by the angle θ between the outward directed normal to $\mathrm{d}A$ and the direction of motion (see Figure 5.1). The motion of the photons is assumed to be almost isotropically distributed in direction; then out of the total number of photons the fraction of photons with directions between θ and $\theta + \mathrm{d}\theta$ is $2\pi \sin\theta \mathrm{d}\theta / 4\pi = \frac{1}{2} \sin\theta \mathrm{d}\theta$.

The motion of the photons through the gas is described in terms of the *mean free path* λ between interactions (absorption, scattering, *etc.*) between a photon and a particle in the gas; λ is defined such that the probability that the photon is scattered or absorbed over a small distance $\Delta\ell$ is $\Delta\ell/\lambda$. In the interior of a star $\lambda \ll r$.

Exercise 5.1:

Show that the probability that a photon moves over the finite distance ℓ is $\exp(-\ell/\lambda)$. Show from this that λ is in fact the mean value of the distance that a photon moves.

We first consider photons that go through $\mathrm{d}A$ with directions between θ and $\theta + \mathrm{d}\theta$. On average they come from the distance $r' = r_0 - \lambda\cos\theta$ from the centre (*cf.* Figure 5.2).

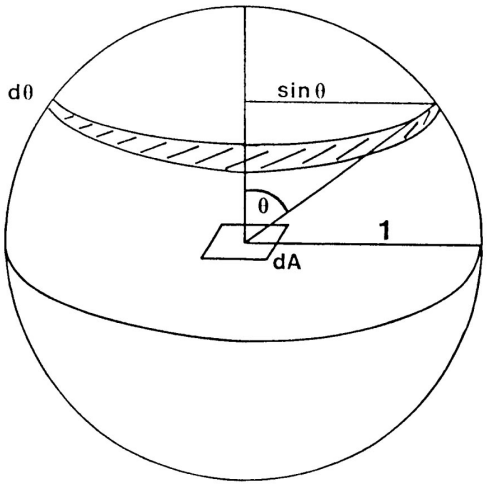

Figure 5.1: The geometry of the angular distribution of photons. Photons with directions θ to $\theta + \mathrm{d}\theta$ relative to the outward directed normal to the area $\mathrm{d}A$ fall within the shaded band, of area $2\pi \sin\theta \mathrm{d}\theta$, on the unit sphere.

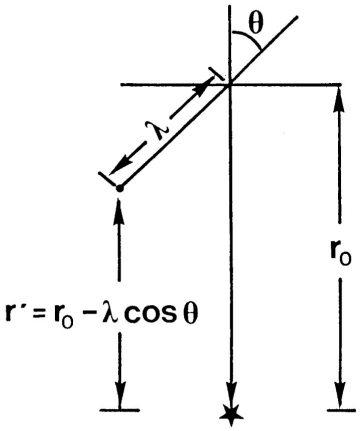

Figure 5.2: Photons passing through the plane at $r = r_0$ at the angle θ with the normal on average originate at $r = r' = r_0 - \lambda\cos\theta$ where λ is the mean free path.

Hence they correspond to the energy density $u_{\mathrm{R}}(r')$, and their contribution to the energy transport through $\mathrm{d}A$ is

$$\begin{array}{ccccc} \frac{1}{2}\sin\theta\,\mathrm{d}\theta\,u_{\mathrm{R}}(r_0-\lambda\cos\theta) & \times & \cos\theta\,\mathrm{d}A & \times & \tilde{c}\mathrm{d}t \\ \text{Contribution to energy density} & & \text{Projected area} & & \text{path length} \end{array} \tag{5.1}$$

The total energy transport through $\mathrm{d}A$ in the time $\mathrm{d}t$ is obtained by integrating over

all directions:

$$\begin{aligned} \mathrm{d}E &= \frac{1}{2}\tilde{c}\int_0^\pi u_\mathrm{R}(r_0-\lambda\cos\theta)\cos\theta\sin\theta\,\mathrm{d}\theta\,\mathrm{d}A\,\mathrm{d}t \\ &\simeq \frac{1}{2}\tilde{c}\int_0^\pi u_\mathrm{R}(r_0)\cos\theta\sin\theta\,\mathrm{d}\theta\,\mathrm{d}A\,\mathrm{d}t - \frac{1}{2}\lambda\tilde{c}\int_0^\pi \frac{\mathrm{d}u_\mathrm{R}}{\mathrm{d}r}\cos^2\theta\sin\theta\,\mathrm{d}\theta\,\mathrm{d}A\,\mathrm{d}t \\ &= -\frac{\lambda\tilde{c}}{3}\frac{\mathrm{d}u_\mathrm{R}}{\mathrm{d}r}\,\mathrm{d}A\,\mathrm{d}t\ , \end{aligned} \tag{5.2}$$

where we used a Taylor expansion of u_R in r. Note that this derivation is consistent with the discussion in the introduction to this section: the uniform part of the radiation energy density, *viz.* $u_\mathrm{R}(r_0)$, makes no contribution to the energy transport, which is determined by the change with position in the energy density.

The radiative flux F_R is defined by

$$\mathrm{d}E = F_\mathrm{R}\,\mathrm{d}A\,\mathrm{d}t\ . \tag{5.3}$$

Hence

$$F_\mathrm{R} = -\frac{\lambda\tilde{c}}{3}\frac{\mathrm{d}u_\mathrm{R}}{\mathrm{d}r}\ . \tag{5.4}$$

Instead of using λ to describe the interaction between matter and radiation it is conventional, and convenient, to use the opacity κ. It is defined such that

$$\lambda = (\kappa\rho)^{-1}\ . \tag{5.5}$$

By using the expression for u_R in terms of T we then obtain

$$F_\mathrm{R} = -\frac{4a\tilde{c}T^3}{3\kappa\rho}\frac{\mathrm{d}T}{\mathrm{d}r}\ . \tag{5.6}$$

If the energy transport occurs only through radiation, the total amount of energy transported through a sphere of radius r is

$$L(r) = 4\pi r^2 F_\mathrm{R}\ . \tag{5.7}$$

We therefore finally have the equation

$$\frac{\mathrm{d}T}{\mathrm{d}r} = -\frac{3\kappa\rho L(r)}{16\pi a\tilde{c}r^2T^3}\ , \tag{5.8}$$

which is one of the fundamental equations of stellar structure.

5.2 Radiation from the stellar surface

Near the surface of the star the density is very low, and hence the mean free path is large. Thus we cannot use the description given above. However, it is possible to estimate the amount of energy radiated from the stellar surface. The only contribution comes from photons directed outwards, *i.e.*, with $\theta < \pi/2$. There is no near balance between photons directed outwards and inwards, and hence we need not take the r-dependence of u_R into account. Therefore, instead of equation (5.2) we obtain

$$\mathrm{d}E \simeq \frac{1}{2}\tilde{c}\int_0^{\pi/2} u_\mathrm{R}\cos\theta\sin\theta\,\mathrm{d}\theta\,\mathrm{d}A\,\mathrm{d}t = \frac{1}{4}\tilde{c}\,u_\mathrm{R}\,\mathrm{d}A\,\mathrm{d}t\ , \tag{5.9}$$

or

$$F_{\rm R} \simeq \frac{a\tilde{c}}{4} T^4 \ . \tag{5.10}$$

As discussed in section 2.3 (*cf.* equation (2.20)) we define the *effective temperature* $T_{\rm eff}$ for the star by

$$F_{\rm R} = \frac{a\tilde{c}}{4} T_{\rm eff}^4 = \sigma T_{\rm eff}^4 \ ; \tag{5.11}$$

then the surface luminosity $L_{\rm s} = L(r)$ is given by

$$L_{\rm s} = 4\pi R^2 \sigma T_{\rm eff}^4 \ , \tag{5.12}$$

where R is the surface radius and $\sigma \equiv a\tilde{c}/4$ is the so-called Stefan-Boltzmann constant.

5.3 The opacity

The mean free path of a photon, and hence the opacity, depends on the microscopic interaction between radiation and matter. Traditionally this interaction is described in terms of a *cross section* $\sigma_{\rm R}$, such that, roughly speaking, a photon interacts with an atom if it passes within the area $\sigma_{\rm R}$ around the atom. If the number of atoms per unit volume is n, the mean free path is thus

$$\lambda = \frac{1}{n\sigma_{\rm R}} \qquad i.e., \qquad \kappa = \sigma_{\rm R} \frac{n}{\rho} \ . \tag{5.13}$$

Exercise 5.2:

Prove these relations.

Note that n/ρ is the number of atoms per unit mass; hence κ is the total cross section per unit mass. If $\sigma_{\rm R}$ and n/ρ are independent of the state of the gas (as described by ρ og T) it follows that κ is also independent of ρ and T.

The computation of the cross section is in general a very complicated numerical problem, where account must be taken of the detailed interaction between the radiation and the different atoms in the gas. Hence it is common in computations of stellar models to use tables over the dependence of opacity on ρ, T and the chemical composition. However, there are simple approximations which give a feel for the dependence of the opacity on the thermodynamical state.

The opacity arising from the interaction between radiation and atoms can approximately be expressed as

$$\kappa = \kappa_0 \rho T^{-3.5} \tag{5.14}$$

(the so-called *Kramers approximation*), where κ_0 is a constant, which depends on the chemical composition.[1] This contribution dominates in the interior of relatively light stars, where the temperature is relatively low. Another contribution to the opacity is

[1] This dependence can be expressed by $\kappa_0 = Z(1+X)\kappa_1$, where κ_1 is a new constant, which is independent of chemical composition.

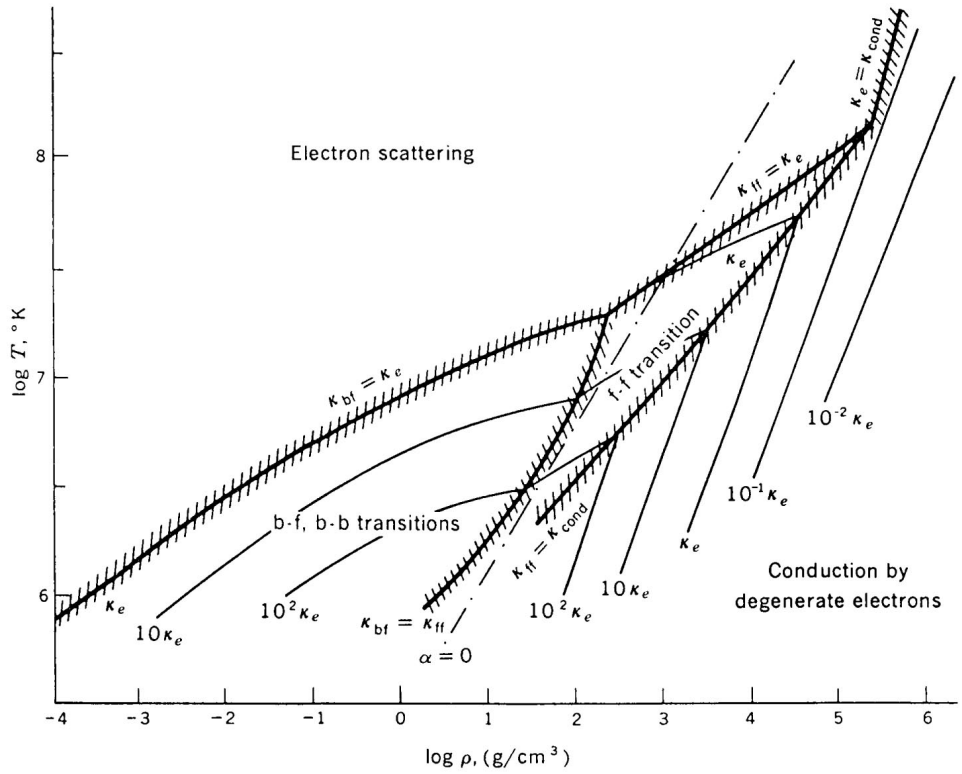

Figure 5.3: Summary of the dominant contributions to the opacity, as a function of $\log \rho$ and $\log T$, for a chemical composition typical for a Population I star. In the lower right-hand corner energy transport is dominated by conduction by degenerate electrons, and in the upper left-hand corner electron scattering (*cf.* equation (5.15)) dominates. In the remainder of the diagram the opacity predominantly comes from atomic interactions; "b-b" and "b-f" refer to bound-bound and bound-free transitions (between two bound states, and a bound state and the continuum, respectively), and "f-f" refers to so-called free-free transitions, involving interactions between radiation, an unbound electron and an atom. The atomic contributions depend on ρ and T roughly as indicated by the Kramers approximation, equation (5.14). The dot-dashed line marked '$\alpha = 0$' marks the transition to beginning degeneracy. (From Hayashi, Hoshi & Sugimoto 1962.)

scattering off free electrons. The cross section for this process is independent of ρ and T; the same is true of the number n_e/ρ of electrons per unit mass, if we assume that the gas is completely ionized. Hence the opacity is also independent of ρ and T; one finds that

$$\kappa = \kappa_e = 0.2(1 + X)\,\mathrm{cm}^2\,\mathrm{g}^{-1}\ . \tag{5.15}$$

Thus this contribution dominates over the atomic contribution in equation (5.14) at relatively high temperature, *i.e.*, in more massive stars.

Figure 5.3 gives an overview of the different contributions to opacity. In addition to the contributions mentioned above, transitions between bound levels in those atoms that are not yet fully ionized give a substantial contribution to the opacity, indicated by "b-b"

in the diagram. This contribution was originally thought to be relatively minor, but was revised in two major efforts to recompute the opacities; one set of calculations, at the Livermore Laboratories, resulted in the so-called OPAL tables (*e.g.* Iglesias, Rogers & Wilson 1992), while a second set of calculations, involving a large international team in the Opacity Project, has produced the OP tables (Seaton *et al.* 1994). Although the details of the computations are rather different, the resulting tables agree to within a few per cent. Strikingly, the inclusion of literally millions of bound-bound transitions resulted in increases in the computed opacity by factors of 3 – 5 over the older tables. These opacity improvements have led to the resolution of a number of long-standing problems in stellar astrophysics (for an overview, see Christensen-Dalsgaard 1995).

At temperatures below 6 – 10 000 K the opacity is dominated by absorption in H^- (*i.e.*, a hydrogen atom with an extra electron); this is typically the case in the atmospheres of stars of solar mass or less. The additional electron comes from the ionization of metals. The opacity increases with the number density of H^- and hence of electrons, *i.e.*, with the degree of ionization; therefore the opacity *increases* with increasing temperature, as opposed to the behaviour in equation (5.14), which is valid in the interior of the stars.

5.4 Stellar atmospheres

The computation of models of stellar atmospheres is a complicated problem, which we cannot treat here (see, for example, Mihalas 1978). In the atmosphere it is necessary to make a detailed description of the radiative transfer, taking into account the absorption of radiation from all states of the individual atoms. In particular, one has to consider transitions between bound states. These transitions remove energy from the radiation in narrow wavelength intervals and hence cause the dark lines in the spectrum of the light which the star radiates. On the other hand the distribution of the atoms among different states of ionization and excitation is determined by the radiation. Hence there is an intimate, and complex, coupling between matter and the radiation field.

These complications have no serious effect on the structure of stellar interiors. However, to compute stellar models one must know the relation between pressure and temperature in the stellar atmosphere. As discussed in Chapter 9 this relation provides one of the *boundary conditions* for the calculation. Here we derive a simple, but for our purpose adequate, form of this relation.

The temperature gradient in the interior of the star is required to ensure the transport of energy. In the stellar atmosphere the photons are radiated directly to space, without being substantially absorbed, and hence the transport of energy does not require a temperature gradient. Thus we may expect that the temperature is approximately constant in (simple) models of stellar atmospheres, where the energy transport occurs only through radiation. This is confirmed by detailed calculations.[2] The temperature in the approximately isothermal part of the atmosphere is a little below $T_{\rm eff}$.

The bottom of the atmosphere, defined as the region from which photons are no longer radiated directly to space, is normally called the *photosphere* and corresponds roughly to the visible surface of the star. We can find a relation for the pressure $P_{\rm ph}$ at this point.

[2]However, other effects may lead to temperature variations in stellar atmospheres. An important example is the solar atmosphere where heating due to dissipation of waves, and to magnetic effects, leads to substantial variations in temperature with altitude in the so-called chromosphere, and to the very hot outer atmosphere, or *corona*. Evidence for similar effects has been found in other stars.

Let h be the height in the atmosphere above the photosphere. It is easy to generalize the argument in exercise 5.1 to show that the probability that a photon escapes from the height h is $\exp(-\int_h^\infty \mathrm{d}h/\lambda)$. A reasonable measure for the location of the bottom of the atmosphere, *i.e.*, $h = 0$, is that this probability is e^{-1}; hence

$$1 \simeq \int_0^\infty \frac{\mathrm{d}h}{\lambda} = \int_0^\infty \kappa\rho \mathrm{d}h \ . \tag{5.16}$$

If we furthermore assume that the atmosphere is isothermal, the variation of density with height is given by

$$\rho = \rho_{\rm ph} \exp(-h/H) \tag{5.17}$$

(*cf.* equation (4.35)), where the density scale height H is given by

$$H = \frac{k_{\rm B}T}{\mu m_{\rm u} g} \ , \tag{5.18}$$

$g = GM/R^2$ is the gravitational acceleration in the atmosphere, and the subscript "ph" indicates the value at $h = 0$. We approximate the opacity by a power law,[3]

$$\kappa = \kappa_0^{(\rm ph)} \rho^a T^b \ ; \tag{5.19}$$

as discussed above the opacity increases with increasing temperature when the temperature is low (where H^- dominates), so we expect that $b > 0$. Hence from equation (5.16) the relation determining conditions at the base of the atmosphere is

$$1 \simeq \int_0^\infty \kappa_{\rm ph}\rho_{\rm ph} \exp\left[-(a+1)\frac{h}{H}\right] \mathrm{d}h = \frac{H}{a+1}\kappa_{\rm ph}\rho_{\rm ph} \ , \tag{5.20}$$

where $\kappa_{\rm ph} = \kappa_0^{(\rm ph)} \rho_{\rm ph}^a T_{\rm eff}^b$ is the opacity at the photosphere.

To obtain an expression for $P_{\rm ph}$ we use the ideal gas law, equation (3.6), to get

$$P_{\rm ph} = \frac{GM(a+1)}{\kappa_{\rm ph} R^2} \ . \tag{5.21}$$

Using again the ideal gas law, and equation (5.19) for κ, we finally get an equation which can be solved for $P_{\rm ph}$, assuming that $T \simeq T_{\rm eff}$.

Exercise 5.3:

Show that

$$P_{\rm ph} = \left[\frac{GM(a+1)}{R^2\kappa_0^{(\rm ph)}}\right]^{1/(a+1)} \left(\frac{k_{\rm B}}{\mu m_{\rm u}}\right)^{a/(a+1)} T_{\rm eff}^{(a-b)/(a+1)} \ . \tag{5.22}$$

Furthermore show that

$$\rho_{\rm ph} = \left[\frac{GM(a+1)}{R^2\kappa_0^{(\rm ph)}}\right]^{1/(a+1)} \left(\frac{k_{\rm B}}{\mu m_{\rm u}}\right)^{-1/(a+1)} T_{\rm eff}^{-(b+1)/(a+1)} \ . \tag{5.23}$$

[3]The use of a in this equation should not be confused with the radiation density constant introduced above.

In the case of the Sun we can take

$$\kappa_0^{(\mathrm{ph})} = 1.6 \times 10^{-33} \,, \qquad a = 0.4 \,, b = 9.3 \,,$$

in cgs units. Estimate the pressure and density in the solar photosphere.

Note that, as might have been anticipated, the atmospheric pressure and density are high in stars with high surface gravity. This fact was already used in the discussion in section 2.5.2 of the luminosity class in the spectral classification: at a given effective temperature, a small radius corresponds to low luminosity, according to equation (5.12); also, a small radius leads to high surface gravity and hence to high density which, in turn, causes broad spectral lines because of the increased perturbation of the atoms in the gas. This allows such stars to be classified as belonging to a high luminosity class.

5.5 The energy equation

Equation (5.8) must be supplemented by an equation for the luminosity L as a function of r. During most of the evolution of the star the energy derives predominantly from nuclear reactions (see Chapter 8). If the rate of energy production per unit mass is ϵ, in the spherical shell between radius r and $r + \mathrm{d}r$ the energy $4\pi r^2 \rho \epsilon \mathrm{d}r$ is produced per unit time, giving rise to the increase $\mathrm{d}L$ in L over the shell. We therefore have the differential equation

$$\frac{\mathrm{d}L}{\mathrm{d}r} = 4\pi r^2 \rho \epsilon \tag{5.24}$$

for L.

Equation (5.24) does not describe the liberation of energy during gravitational contraction (*cf.* section 4.4) and hence cannot be used, for example, in the early phases of stellar evolution. To get a more complete expression we use the first law of thermodynamics (equation (3.8)):

$$đQ = \mathrm{d}U + P\mathrm{d}V \,. \tag{5.25}$$

Here V is the volume of the thermodynamic system under consideration, U is the internal energy of the system and $đQ$ is the heat added or subtracted from the system. We consider the system containing unit mass, so that $V = 1/\rho$ and $U = u/\rho$, where u is the internal energy per unit volume. The heat input during the time $\mathrm{d}t$ has two contributions. One is the heat ϵ liberated by nuclear reactions. The second is the heat deposited from or extracted by the energy flowing through the layer; since the mass of the shell between r and $r + \mathrm{d}r$ is $4\pi r^2 \rho \mathrm{d}r$, this contribution in the time $\mathrm{d}t$, per unit mass, is $[L(r) - L(r + \mathrm{d}r)]\mathrm{d}t/(4\pi r^2 \rho \mathrm{d}r)$. Thus we obtain from equation (5.25)

$$\epsilon \,\mathrm{d}t + \frac{[L(r) - L(r + \mathrm{d}r)]\mathrm{d}t}{4\pi r^2 \rho \mathrm{d}r} = \mathrm{d}\left(\frac{u}{\rho}\right) + P\mathrm{d}\left(\frac{1}{\rho}\right) \,, \tag{5.26}$$

or

$$\frac{\mathrm{d}L}{\mathrm{d}r} = 4\pi r^2 \left[\rho\epsilon - \rho \frac{\mathrm{d}}{\mathrm{d}t}\left(\frac{u}{\rho}\right) + \frac{P}{\rho}\frac{\mathrm{d}\rho}{\mathrm{d}t}\right] \,. \tag{5.27}$$

This is the desired equation.

The interpretation of equation (5.27) is reasonably clear. The energy radiated comes from the energy produced by the nuclear reactions; but the contribution required to increase the internal energy of the gas or to do work on the gas must be subtracted. During gravitational contraction, before nuclear reactions start, only the last two terms on the right hand side of equation (5.27) contribute. As the temperature in the star is increasing, u/ρ increases, so that the term in $\mathrm{d}(u/\rho)/\mathrm{d}t$ gives a negative contribution to $\mathrm{d}L/\mathrm{d}r$; but this is more than compensated for by the positive term in $\mathrm{d}\rho/\mathrm{d}t$, which corresponds to the work of gravity on matter in the star.

Exercise 5.4:

Assume, during gravitational contraction, that ρ changes as R^{-3}, and T changes as R^{-1}. Estimate the relative size of the last two terms in equation (5.27). How can the result be interpreted in terms of the virial theorem?

In equation (5.27) the two terms in $\mathrm{d}/\mathrm{d}t$ are essentially negligible during the normal nuclear burning phases of the evolution of the star. To see this we consider the Kelvin-Helmholz time $t_{\rm KH}$, *i.e.*, the time during which the star can maintain its energy output by radiating the internal thermal energy,

$$t_{\rm KH} = \frac{U_{\rm tot}}{L_{\rm s}} \, , \tag{5.28}$$

where $U_{\rm tot} \simeq R^3 u$ is the total internal energy of the star (see sections 1.1.2 and 4.4.2). For the Sun $t_{\rm KH}$ is of order 10^7 years. During nuclear burning evolution takes place over the nuclear time scale $t_{\rm nuc}$ which, as discussed in section 1.1.3, is of order 10^{10} years for the Sun. In equation (5.27) we replace, as usual, $\mathrm{d}L/\mathrm{d}r$ by $L_{\rm s}/R$. Similarly we replace $\mathrm{d}u/\mathrm{d}t$ by $u/t_{\rm nuc}$. Then we obtain the following estimate of the relative magnitude of the term in $\mathrm{d}u/\mathrm{d}t$:

$$\frac{\left| 4\pi r^2 \rho \dfrac{\mathrm{d}}{\mathrm{d}t}\left(\dfrac{u}{\rho}\right)\right|}{\dfrac{\mathrm{d}L}{\mathrm{d}r}} \simeq \frac{\dfrac{U_{\rm tot}}{t_{\rm nuc}}}{L_{\rm s}} \simeq \frac{t_{\rm KH}}{t_{\rm nuc}} \ll 1 \, , \tag{5.29}$$

given the typical values of $t_{\rm KH}$ and $t_{\rm nuc}$ quoted above.

Chapter 6

Energy transport by convection

6.1 Introduction

It is possible to calculate stellar models assuming that energy transport takes place through radiation alone. Such models do not provide a realistic description of real stars, however, because in general they are *unstable*.

Any theoretical model should be tested for possible instabilities, before it can be accepted as realistic. An instability manifests itself through the growth of any small disturbance with time, often exponentially. If the characteristic growth time is less than the evolutionary time scale for the star, the disturbance may in the end dominate the properties of the star. Such stability investigations have been carried out for stellar models, generally showing that these are stable. However, a particular type of instability is often found, namely the instability corresponding to having a layer of higher density on top of a layer with lower density.[1] An extreme analogy to this instability would be a glass where a layer of mercury had been placed on top of a layer of water. This is evidently an unstable situation.

In a star this type of instability can occur if the temperature decreases too rapidly with distance from the centre. The decrease of pressure with r is determined by hydrostatic equilibrium, and is therefore largely given, and the only possibility for compensating for a rapid decrease in temperature is therefore, according to the ideal gas law, that the density decreases slowly or even increases; this leads to the instability. From the equation for radiative transfer (equation (5.8)) it follows that the temperature decreases rapidly with increasing r when the opacity is high or the luminosity is high. These are therefore, roughly speaking, the circumstances which may lead to instability.

As a result of the instability hotter, relatively light elements of fluid rise and cooler, relatively heavy elements sink. When the motion gets sufficiently strong, the elements are dissolved and the gas is mixed. As a result, the rising elements deposit their excess heat to the surroundings, and this leads to a net transport of energy out through the star (obviously the sinking elements similarly contribute to the energy transport). This process is called *convection*, and the instability is therefore called *convective instability*. Convection is well known from everyday life, for example when air rises over a heater. Besides contributing to the energy transport convection also leads to mixing of the parts of the star where it occurs. As we shall see later this has a substantial effect on the

[1] The precise description of the instability will be given below.

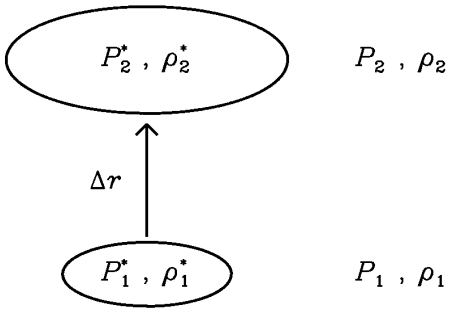

Figure 6.1: The motion of a convective element, from the initial position indicated by "1", to a later position, indicated by "2".

evolution of some stars.

6.2 The instability condition

To determine the condition for instability we consider an element of gas (*cf.* Figure 6.1) which is moved the distance Δr outwards. As indicated we denote the pressure and density outside (inside) the element before and after the motion by P_1, ρ_1, (P_1^*, ρ_1^*), and P_2, ρ_2, (P_2^*, ρ_2^*). The element is initially identical to its surroundings, so that $P_1^* = P_1$ and $\rho_1^* = \rho_1$. Its motion is determined by *buoyancy*, which in turn is given by the difference in density between the element and its surroundings (think of a cork pushed down into water). The force per unit volume at the point 2 is

$$f_{\rm buoy} = -g(\rho_2^* - \rho_2) \equiv -g\Delta\rho \; , \tag{6.1}$$

where $g = Gm/r^2$ is the gravitational acceleration. If $f_{\rm buoy} > 0$ the force on the element is directed outwards, and the motion is accelerated; hence this corresponds to instability. In the opposite case the force is directed downwards, the element has a tendency to return to its original position, and the situation is stable.

To determine $\Delta\rho$, and hence decide between stability and instability, we make the following assumptions:

1) The motion is so slow that there is pressure balance between the element and the surroundings.

2) The motion is so fast that there is no heat loss to the surroundings.

Note that pressure balance is established on the dynamical time scale $t_{\rm dyn}$, which we estimated as

$$t_{\rm dyn} \simeq \left(\frac{GM}{R^3}\right)^{-1/2} \tag{6.2}$$

(*cf.* equation (4.6)). A characteristic time scale for the heat loss is the Kelvin-Helmholtz time

$$t_{\rm KH} \simeq \frac{U_{\rm tot}}{L_{\rm s}} \ , \tag{6.3}$$

where $U_{\rm tot}$ is the total internal energy, integrated over the star, and $L_{\rm s}$ is the surface luminosity (see section 4.4.2). For the Sun $t_{\rm dyn} \simeq 1$ hour, while $t_{\rm KH} \simeq 10^7$ years. This makes it plausible that the assumptions may be satisfied. We shall show below (*cf.* section 6.4.3) that the time scale for the convective motion is indeed intermediate between $t_{\rm dyn}$ and $t_{\rm KH}$.

From assumption 1) we have that $P_2^* = P_2$. Assumption 2) expresses that the motion takes place *adiabatically*; from equation (3.18) it therefore follows that

$$\frac{{\rm d}\rho^*}{\rho^*} = \frac{1}{\Gamma_1}\frac{{\rm d}P^*}{P^*} = \frac{1}{\Gamma_1}\frac{{\rm d}P}{P} \ , \tag{6.4}$$

where ${\rm d}\rho^*$ and ${\rm d}P^*$ are the changes in ρ and P inside the element. From Taylor expansion we therefore obtain

$$\begin{aligned} \Delta\rho &= \rho_2^* - \rho_2 = \rho_2^* - \rho_1 - (\rho_2 - \rho_1) \\ &\simeq \rho_1 \frac{1}{\Gamma_1}\frac{1}{P_1}\frac{{\rm d}P}{{\rm d}r}\Delta r - \frac{{\rm d}\rho}{{\rm d}r}\Delta r \\ &= \left(\frac{\rho_1}{P_1}\frac{1}{\Gamma_1}\frac{{\rm d}P}{{\rm d}r} - \frac{{\rm d}\rho}{{\rm d}r}\right)\Delta r = \left[\left(\frac{{\rm d}\rho}{{\rm d}r}\right)_{\rm ad} - \frac{{\rm d}\rho}{{\rm d}r}\right]\Delta r \ , \end{aligned} \tag{6.5}$$

where we introduced[2]

$$\left(\frac{{\rm d}\rho}{{\rm d}r}\right)_{\rm ad} \equiv \frac{1}{\Gamma_1}\frac{\rho}{P}\frac{{\rm d}P}{{\rm d}r} \ . \tag{6.6}$$

The condition for *instability* is that $\Delta\rho < 0$ (see equation (6.1)), *i.e.*,

$$\left(\frac{{\rm d}\rho}{{\rm d}r}\right)_{\rm ad} < \frac{{\rm d}\rho}{{\rm d}r} \ . \tag{6.7}$$

After division by $\rho {\rm d}\ln P/{\rm d}r$ this condition can also be expressed as

$$\frac{{\rm d}\ln\rho}{{\rm d}\ln P} < \frac{1}{\Gamma_1} \tag{6.8}$$

(recall that as a result of the equation of hydrostatic equilibrium ${\rm d}P/{\rm d}r$ is always negative). This instability condition is known as the *Ledoux criterion*. Note that for a completely ionized ideal gas $1/\Gamma_1 = 3/5$.

Exercise 6.1:

Use equations (6.1) and (6.5) to determine an equation of motion for the element, expressed as a differential equation for Δr as a function of time. Discuss the solution in the simple case where ρ, Γ_1 and ${\rm d}P/{\rm d}r$ can be assumed to be almost constant, and describe the behaviour of the element in the case of instability. Show that in the case of stability the element executes an oscillation around the equilibrium position.

---

[2] hence $({\rm d}\rho/{\rm d}r)_{\rm ad}$ is the density gradient resulting from adiabatic motion in the given pressure gradient.

The interpretation of equation (6.8) is entirely in accordance with the introduction: instability occurs when the density does not decrease sufficiently rapidly, or even increases, towards the surface of the star. That instability does not require (as indicated by our simple argument) that density increases towards the surface is due to the fact that we consider a gas whose density decreases with decreasing pressure.

The instability condition is normally expressed in terms of the gradient in temperature, rather than the gradient in density. We use the ideal gas law, written in the form

$$\rho = \frac{\mu m_{\rm u} P}{k_{\rm B} T} \ . \tag{6.9}$$

It is normally assumed that the chemical composition is independent of position; if we furthermore assume that the gas is fully ionized, μ is constant, and we obtain by differentiation

$$\frac{1}{\rho}\frac{{\rm d}\rho}{{\rm d}r} = \frac{1}{P}\frac{{\rm d}P}{{\rm d}r} - \frac{1}{T}\frac{{\rm d}T}{{\rm d}r} \ . \tag{6.10}$$

This leads to

$$\begin{aligned} \left(\frac{{\rm d}\rho}{{\rm d}r}\right)_{\rm ad} - \frac{{\rm d}\rho}{{\rm d}r} &= \frac{1}{\Gamma_1}\frac{\rho}{P}\frac{{\rm d}P}{{\rm d}r} - \frac{\rho}{P}\frac{{\rm d}P}{{\rm d}r} + \frac{\rho}{T}\frac{{\rm d}T}{{\rm d}r} \\ &= -\frac{\Gamma_1 - 1}{\Gamma_1}\frac{\rho}{P}\frac{{\rm d}P}{{\rm d}r} + \frac{\rho}{T}\frac{{\rm d}T}{{\rm d}r} \ . \end{aligned} \tag{6.11}$$

A correct thermodynamical treatment, taking into account partial ionization and departures from the ideal gas law, shows that Γ_1 in equation (6.11) must be replaced by Γ_2, *i.e.*, the adiabatic exponent for the relation between P and T. Hence the instability condition becomes

$$\left(\frac{{\rm d}T}{{\rm d}r}\right)_{\rm ad} > \frac{{\rm d}T}{{\rm d}r} \ , \tag{6.12}$$

where

$$\left(\frac{{\rm d}T}{{\rm d}r}\right)_{\rm ad} \equiv \frac{\Gamma_2 - 1}{\Gamma_2}\frac{T}{P}\frac{{\rm d}P}{{\rm d}r} \tag{6.13}$$

is the adiabatic temperature gradient. In analogy with equation (6.8), equation (6.12) can also be written as

$$\frac{{\rm d}\ln T}{{\rm d}\ln P} > \frac{\Gamma_2 - 1}{\Gamma_2} \ . \tag{6.14}$$

This equation shows that there is instability if the temperature decreases too rapidly out through the star, in perfect agreement with our simple discussion.

It is the convention to introduce the notation

$$\nabla = \frac{{\rm d}\ln T}{{\rm d}\ln P} \ , \qquad \nabla_{\rm ad} \equiv \frac{\Gamma_2 - 1}{\Gamma_2} = \left(\frac{\partial \ln T}{\partial \ln P}\right)_{\rm ad} \ . \tag{6.15}$$

Then the instability condition in equation (6.14) can be written

$$\nabla > \nabla_{\rm ad} \ , \tag{6.16}$$

known as the *Schwarzschild criterion*. This condition is normally expressed by saying that the temperature gradient is super-adiabatic. For a fully ionized ideal gas $\nabla_{\rm ad} = 2/5$.

Note that our assumption that the chemical composition is constant, in the derivation of equations (6.12) and (6.13), is incorrect in regions where nuclear burning is taking place.

In a region of hydrogen burning, for example, the hydrogen abundance increases outwards (because of the steep increase in the rate of burning with increasing temperature), and hence μ decreases outwards. It is evident from the derivation of the instability condition that the condition (6.8) in terms of P and ρ is correct, regardless of this complication. Hence, strictly speaking the condition in equation (6.14) should be corrected, by including a term in the gradient in μ. In actual computations the instability criterion in equation (6.14) is almost always used, largely due to tradition and computational convenience. This error probably has little qualitative effect on the results of the computations, however.

6.3 Where does convection occur?

To determine the circumstances under which one may expect convection, we consider a model where energy transport takes place through radiation and investigate its stability. Here (*cf.* equation (5.8))

$$\frac{\mathrm{d}T}{\mathrm{d}r} = -\frac{3\kappa\rho L(r)}{16\pi a\tilde{c}r^2T^3} \ . \tag{6.17}$$

By using the equation for hydrostatic equilibrium (4.4) and the ideal gas law (6.9), the temperature gradient, in the form introduced in equation (6.15), can be written

$$\nabla = \nabla_{\mathrm{R}} \equiv \frac{3k_{\mathrm{B}}}{16\pi a\tilde{c}\,Gm_{\mathrm{u}}}\frac{\kappa}{\mu}\frac{L(r)}{m(r)}\frac{\rho}{T^3} \ , \tag{6.18}$$

where we introduced the *radiative temperature gradient* ∇_{R}, *i.e.*, the gradient required to transport the entire luminosity by radiation. The condition for instability can now be written as

$$\nabla_{\mathrm{R}} > \nabla_{\mathrm{ad}} \ . \tag{6.19}$$

When this condition is satisfied, energy transport by radiation requires too steep a temperature gradient, and convection must take place.

From equations (6.18) and (6.19) it is evident that, roughly speaking, one may expect convection if

a) $L(r)/m(r)$ is large. This condition expresses that the average rate of energy generation per unit mass within the radius r is large. This is typically the case in the interiors of massive stars. As we shall see later the energy generation in such stars is a rapidly increasing function of temperature and hence is strongly concentrated towards the centre of the star. Therefore L/m is large, and the star has a convective core.

b) κ is large. This is satisfied in the outer parts of relatively light stars on the main sequence, or more generally in stars with low surface temperatures, where the temperature in the outer parts of the star is low, and the opacity consequently high (*cf.* equation (5.14)). A further contribution to the high opacities in these regions comes from the ionization of hydrogen (see also Figure 6.3 below).

c) ρ/T^3 is large. This is also typically satisfied in the outer parts of relatively cool stars. Indeed, it follows from equation (5.23) that in the photosphere ρ/T^3 increases rapidly with decreasing effective temperature.

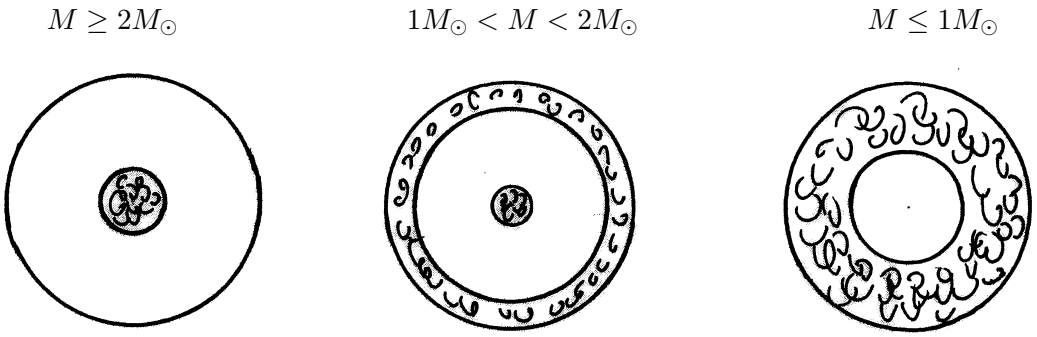

Figure 6.2: The typical occurrence of convection zones in main-sequence stars. In relatively massive stars there is a convective core, whereas in relatively light stars on the main sequence, and in general in stars with low effective temperature, there is an outer convection zone. In red giants this convection zone occupies by far the largest fraction of the stellar radius, and a substantial fraction of the stellar mass.

d) $\nabla_{\rm ad}$ is small. This is satisfied in the ionization zone of hydrogen, *i.e.*, again in the outer parts of cool stars.

Thus condition a) predicts convection in the core of massive stars, whereas the remaining conditions indicate a tendency for convection in the outer parts of cool stars, *i.e.*, in relatively light stars on the main sequence, and in the so-called red giants. These locations of convection zones are summarized in Figure 6.2.

The situation in a model of the present Sun is shown in Figure 6.3. As indicated, $\nabla_{\rm R}$ gets very large in the outer parts of the model, mainly as a result of the increase in the opacity (mechanism b) above). Furthermore, $\nabla_{\rm ad}$ is decreased substantially below $2/5$ in the outer ionization zones of hydrogen and helium,[3] to a minimum value of around 0.12 (mechanism d)). The figure also illustrates the behaviour of the actual temperature gradient ∇, which is discussed in more detail in the following section: in the convectively stable region obviously $\nabla = \nabla_{\rm R}$, and the energy is carried exclusively by radiation; in almost all of the convection zone ∇ is only slightly above $\nabla_{\rm ad}$, the only exception being a very thin region near the top of the convection zone.

6.4 Properties of convection

6.4.1 Introduction

The dynamics of the stellar fluid after the onset of instability, in the simple picture given by the behaviour of a convective element, is extremely difficult to describe. As a result, there is no definitive method for calculating the motion or the convective energy transport. One might imagine that the velocity of the element increases up to the point where new hydrodynamical instabilities set in, making the motion turbulent and dissolving the element. In this way the excess heat in the element is deposited in the surroundings, hence leading to energy transport. The description of such turbulent processes is, and has

[3] When gas in an ionization zone is compressed, part of the work goes towards increasing the degree of ionization, rather than to increasing the temperature.

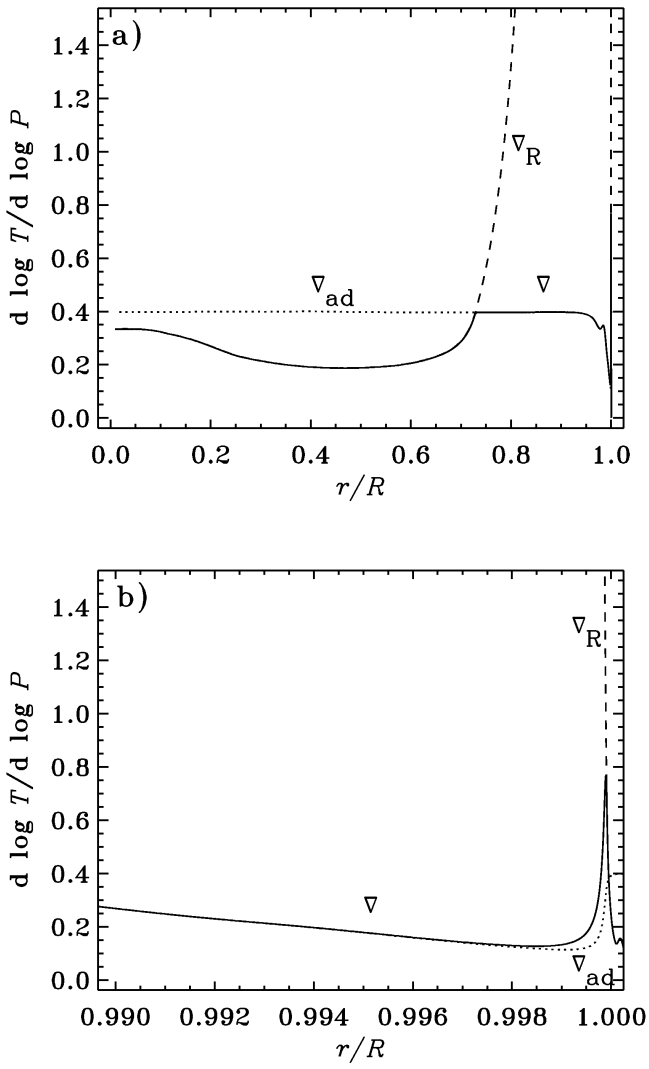

Figure 6.3: Temperature gradients in a model of the present Sun. The solid line shows the actual temperature gradient ∇, and the dotted line shows the adiabatic gradient $\nabla_{\rm ad}$ (*cf.* equation (6.15)); the dashed line shows the radiative gradient $\nabla_{\rm R}$ (equation (6.18)). Panel a) shows the entire model, panel b) a very small region near its surface. In the radiative region, for $r \lesssim 0.72R$, $\nabla = \nabla_{\rm R}$, and the solid and dashed lines coincide. In the convection zone ∇ is so close to $\nabla_{\rm ad}$ that the solid and dotted lines are indistinguishable, except very near the surface.

for a long time been, the subject of intensive investigations;[4] so far a fully satisfactory understanding, or sufficiently efficient methods for numerical computation, have not been achieved. As described in Section 6.4.4 below, it is possible to carry out quite realistic numerical simulations of convection near a stellar surface, but this is far too computationally costly to be implemented in calculations of stellar evolution.

Fortunately a less complete description is adequate for such computations, at least as far as the overall properties of the stars are concerned. This only requires a relation for the temperature gradient required to transport the luminosity by convection, to replace equation (6.17) for radiative transport. It is possible to make a rough estimate of the relationship between the temperature gradient and the luminosity. This is carried out in Section 6.4.2 below. The result is that in most of the star the temperature gradient is only slightly steeper than the adiabatic gradient determined by equation (6.13). Hence for the purpose of computing stellar models the effect of convection is to replace equation (6.17) by

$$\frac{\mathrm{d}T}{\mathrm{d}r} = \left(\frac{\mathrm{d}T}{\mathrm{d}r}\right)_{\mathrm{ad}} = \frac{\Gamma_2 - 1}{\Gamma_2}\frac{T}{P}\frac{\mathrm{d}P}{\mathrm{d}r} = -\frac{\Gamma_2 - 1}{\Gamma_2}\frac{T}{P}\frac{Gm\rho}{r^2} \ , \tag{6.20}$$

in regions where there is convective instability. This can conveniently be expressed by writing the actual temperature gradient ∇ as

$$\nabla = \min(\nabla_{\mathrm{R}}, \nabla_{\mathrm{ad}})$$

(see also Fig. 6.3).

A second conclusion is that the typical time scale for convective motion is much shorter than the evolutionary time scale (see Section 6.4.3). Consequently convection zones are very efficiently mixed, and we may assume that their chemical composition is uniform at all times. This has important effects on the evolution of stars with convective cores.

6.4.2 Estimate of the superadiabatic temperature gradient

As usual in these estimates, we neglect factors of order unity, and make rough approximations of the physics involved. We assume that a given convective element moves a distance Δr, before being destroyed. In the destruction the surroundings receive the energy $\Delta u \simeq \rho c_P \Delta T$ per unit volume, where

$$\Delta T = \left[\left(\frac{\mathrm{d}T}{\mathrm{d}r}\right)_{\mathrm{ad}} - \frac{\mathrm{d}T}{\mathrm{d}r}\right]\Delta r \tag{6.21}$$

is the temperature difference between the element and the surroundings. If the mean speed of the element is $\bar{v}$, the convective energy flux can thus be estimated as

$$F_{\mathrm{con}} \simeq \bar{v} c_P \rho \Delta T \ . \tag{6.22}$$

To obtain an estimate of $\bar{v}$ we equate the kinetic energy $\frac{1}{2}\rho\bar{v}^2$ of the element per unit volume to the work of buoyancy over the distance Δr. From equations (6.1), (6.5) and (6.11) we obtain (neglecting the factor $\frac{1}{2}$)

$$\begin{aligned} \rho\bar{v}^2 &\simeq f_{\mathrm{buoy}}\Delta r \simeq -\left[\left(\frac{\mathrm{d}\rho}{\mathrm{d}r}\right)_{\mathrm{ad}} - \frac{\mathrm{d}\rho}{\mathrm{d}r}\right] g\Delta r^2 \\ &= \frac{\rho}{T}\left[\left(\frac{\mathrm{d}T}{\mathrm{d}r}\right)_{\mathrm{ad}} - \frac{\mathrm{d}T}{\mathrm{d}r}\right] g\Delta r^2 \ . \end{aligned} \tag{6.23}$$

[4] Turbulent motion is of immense practical importance under a wide range of circumstances, from the motion of air around an airplane to the flow of liquids through a pipe.

To simplify the notation we introduce the dimensionless measure

$$\delta \equiv \frac{R}{T}\left[\left(\frac{\mathrm{d}T}{\mathrm{d}r}\right)_{\mathrm{ad}} - \frac{\mathrm{d}T}{\mathrm{d}r}\right] \tag{6.24}$$

of the departure of the temperature gradient from its adiabatic value. Then we finally obtain

$$F_{\mathrm{con}} \simeq \rho c_P T \delta^{3/2} \left(\frac{\Delta r}{R}\right)^2 (gR)^{1/2} , \tag{6.25}$$

and hence the convective luminosity

$$L_{\mathrm{con}} \simeq R^2 F_{\mathrm{con}} \simeq R^3 \rho c_P T \delta^{3/2} \left(\frac{\Delta r}{R}\right)^2 \left(\frac{g}{R}\right)^{1/2} . \tag{6.26}$$

In the interior of the star we can estimate L_{con} as

$$L_{\mathrm{con}} \simeq U_{\mathrm{tot}} \delta^{3/2} \left(\frac{\Delta r}{R}\right)^2 t_{\mathrm{dyn}}^{-1} ,$$

where we used that $t_{\mathrm{dyn}} \simeq (R/g)^{1/2}$ (*cf.* equation (6.2)), and $U_{\mathrm{tot}} \simeq \rho c_P T R^3$ is the total internal energy of the star. This equation has a simple physical interpretation. If we neglect the factor $(\Delta r/R)^2$ we have that $L_{\mathrm{con}} \simeq (U_{\mathrm{tot}}\delta)(\delta^{1/2}/t_{\mathrm{dyn}})$. Here $U_{\mathrm{tot}}\delta$ is a measure of the internal energy that is transported; the factor δ reduces the energy transport, since it is only the *excess* internal energy which contributes to the energy transport. Correspondingly $t_{\mathrm{dyn}}/\delta^{1/2}$ is the *convective time scale* t_{con}, which can be defined as

$$t_{\mathrm{con}} = \frac{\Delta r}{\bar{v}} \simeq \delta^{-1/2} \left(\frac{R}{g}\right)^{1/2} \simeq \delta^{-1/2} t_{\mathrm{dyn}} , \tag{6.27}$$

which determines the time taken to transport the energy; t_{con} is a dynamical time scale, but the effective gravitational acceleration is reduced, since it is only the *difference* in density which provides the force. Therefore the time scale is increased by the factor $\delta^{-1/2}$.

In the case of radiative transport the temperature gradient was determined as being sufficiently large to transport the energy by radiation. Correspondingly, in the case of convection, δ must be sufficiently large that the energy can be transported by convection. If we assume that $L_{\mathrm{con}} = L_{\mathrm{s}}$ we obtain

$$\delta \simeq \left[\frac{L_{\mathrm{s}}}{U_{\mathrm{tot}}} \left(\frac{\Delta r}{R}\right)^{-2} t_{\mathrm{dyn}}\right]^{2/3} \simeq \left(\frac{t_{\mathrm{dyn}}}{t_{\mathrm{KH}}}\right)^{2/3} \left(\frac{\Delta r}{R}\right)^{-4/3} , \tag{6.28}$$

by using equation (6.3). In the interior of a star we may assume, very roughly, that $\Delta r \simeq R/10$. Using the values of t_{dyn} and t_{KH} for the Sun, we obtain

$$\delta \simeq 10^{-6} . \tag{6.29}$$

Although these estimates are very uncertain, it is obvious that even an extremely small superadiabatic gradient is sufficient to transport the entire energy by convection (see also Figure 6.3). This simplifies the treatment of convection tremendously: at a given point

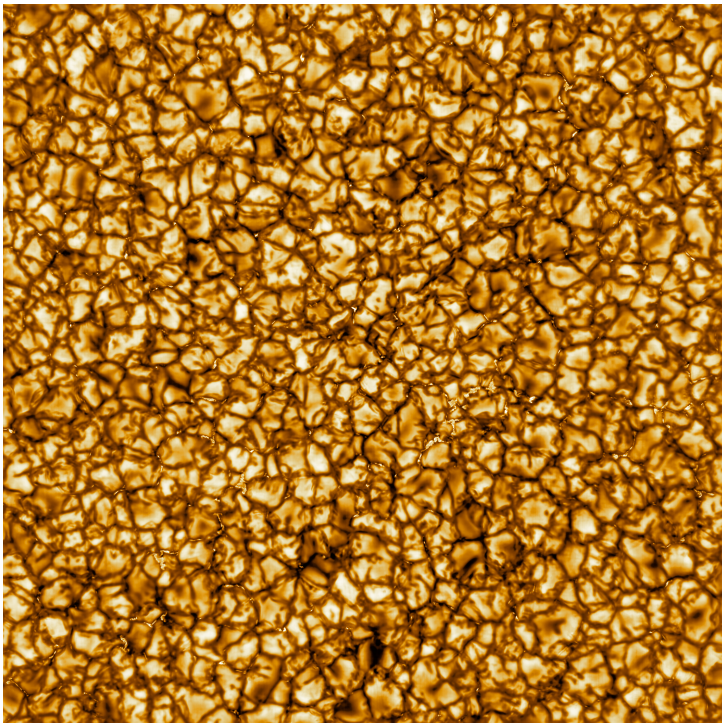

Figure 6.4: Image of small part of the solar surface, showing the effect of convection in the form of granulation. The bright areas, up to 1000 km across, are warmer rising gas and the dark lanes are cooler sinking gas. (Courtesy DKIST, National Solar Observatory, USA.)

in the star one determines, by means of equation (6.14), whether the layer is unstable; if this is the case, energy transport occurs through convection, and $\delta \simeq 0$, and hence

$$\frac{\mathrm{d}T}{\mathrm{d}r} = \left(\frac{\mathrm{d}T}{\mathrm{d}r}\right)_{\mathrm{ad}} = \frac{\Gamma_2 - 1}{\Gamma_2}\frac{T}{P}\frac{\mathrm{d}P}{\mathrm{d}r} = -\frac{\Gamma_2 - 1}{\Gamma_2}\frac{T}{P}\frac{Gm\rho}{r^2} \ . \tag{6.30}$$

At such a point equation (6.30) replaces the usual equation (6.17) for the temperature gradient.

In convection zones there is also a contribution from radiation to the energy transport, given by (*cf.* equation (6.17))

$$L_{\mathrm{rad}} = -\frac{16\pi a\tilde{c}r^2T^3}{3\kappa\rho}\frac{\mathrm{d}T}{\mathrm{d}r} \ , \tag{6.31}$$

where $\mathrm{d}T/\mathrm{d}r$ is given by equation (6.30). Hence, δ is actually *smaller* than the value given in equation (6.28), where the entire energy transport was assumed to be carried by convection. In stars with convective envelopes, near the stellar surface convection typically dominates and $L_{\mathrm{rad}} \ll L$. However, in the bulk of the convection zones the radiative and convective contributions to L are of a similar magnitude, and there is a gradual transition from convective to radiative transport at the boundaries of the convective regions.

Detailed computations of stellar models use a formalism that is somewhat more complex, in the so-called *mixing-length theory* (see Kippenhahn *et al.*, 2012), but the underlying

ideas, and the results, are by and large similar to the those of the simple analysis presented here. An important exception, however, is the fact that near the surface of a star convection does not transport energy very efficiently. It may be seen from equation (6.26) that $L_{\rm con}$ is proportional to the density ρ, which is very low near the surface. Furthermore one might expect that the distance Δr is small near the stellar surface. This is confirmed indirectly by observations of the Sun, where the convective elements can be seen in the solar atmosphere as the so-called *granulation* (see Fig. 6.4); the size of these convective elements, which is probably typical of Δr in the outer layers of the Sun, is only about $10^{-3}R$. As a result a substantial δ is required to transport the energy by convection; this was also evident from Figure 6.3b. Thus when computing stellar models one has to take into account the departure of $\mathrm{d}T/\mathrm{d}r$ from $(\mathrm{d}T/\mathrm{d}r)_{\rm ad}$ as determined by δ; hence a more detailed description of convection is required. The effects of this for computations of stellar models were discussed by Gough & Weiss (1976).

With our present limited understanding of convection this description contains a free parameter (related to the distance Δr moved by the convective elements), which cannot be obtained from fundamental physical quantities. This determines the efficiency of convection, and hence the superadiabatic gradient $\nabla - \nabla_{\rm ad}$ required to transport the energy. In the case of the Sun this parameter can be found by requiring that the radius of the computed model agrees with the observed solar radius. In the bulk of the solar convection zone, where the temperature gradient is almost adiabatic, the entropy is constant; the structure of this region, which in turn determines the radius of the model, is essentially fixed by the value of the entropy. Adjusting the parameter in the description of convection, changes the entropy in the adiabatic part of the convection zone and hence the radius of the model. The uncertain details of the description of convection then only affects the region very near the surface where $\nabla - \nabla_{\rm ad}$ is substantial. When computing models of other stars it is then normally *assumed* that the parameter is the same for all stars, despite the wide range of their properties (such as effective temperature and surface gravity), and the solar calibration is used in computations of stellar models. Remarkably enough the resulting models are not too dissimilar from the observed properties of, for example, stellar clusters (*e.g.* Pedersen, VandenBerg & Irwin 1990).

6.4.3 The convective time scale

From equations (6.27) and (6.28) we can estimate $t_{\rm con}$ as

$$t_{\rm con} \simeq \delta^{-1/2} t_{\rm dyn} \simeq \left(\frac{t_{\rm KH}}{t_{\rm dyn}}\right)^{1/3} \left(\frac{\Delta r}{R}\right)^{2/3} t_{\rm dyn} = t_{\rm KH}^{1/3} t_{\rm dyn}^{2/3} \left(\frac{\Delta r}{R}\right)^{2/3} . \qquad (6.32)$$

Assuming again that $\Delta r \simeq R/10$, we find in the case of the Sun that $t_{\rm con} \simeq 0.2$ year. This is much shorter than the characteristic evolutionary time scale. Over a time scale not much longer than $t_{\rm con}$ matter in a convection zone must be completely mixed. Hence, we can assume that convection zones are *chemically homogeneous* with the same chemical composition everywhere. We shall later discuss the consequences of this for stellar evolution.

6.4.4 Hydrodynamical simulations of convection

Advanced computations of convection near the solar surface have been developed over the last several decades (pioneered by Åke Nordlund, Copenhagen and R. W. Stein, (*e.g.*, Stein & Nordlund 1989, 1998).[5] These three-dimensional radiative-hydrodynamical simulations revealed that near-surface convection operates in a way that is fundamentally different from that described by the mixing-length theory of convection: At the photosphere, fluid is cooled through strong radiative cooling; this results in negative buoyancy, leading to streams of gas descending through the optical surface. Conservation of mass forces the relatively hot and light material to rise back up through the thin optical surface, forming so-called granules (see Fig. 6.4). Rather than distinct and coherent fluid parcels assumed in the MLT, convective regions show finger-like downflows that merge together as they descend from the photosphere to the deep convective layers.

Originally, when carried out on the then fastest possible computers, these simulations took much longer than the actual motion, even when restricted to a very small part of the Sun. Several hundred hours of computing time were used to simulate a few hours of solar time. With the development of computing power, such simulations can now run 'in real time', such that simulating one hour of solar time takes one hour of computing time. (Obviously, this is still far too slow to be included in stellar-evolution calculations.) These 3D simulations of stellar convection are able to predict highly realistic granulation patterns, center-to-limb brightness variations, line profiles and asymmetries, *etc.* that are in excellent agreement with observations. They have been extended to other stars in grids of models covering a large range of parameters (*e.g.*, Magic *et al.*, 2013; Trampedach *et al.*, 2013). Also, hydrodynamic modelling has been carried out of the full convection zone of the Sun and stars, although with less physical realism (*e.g.*, Miesch *et al.*, 2008; Hotta *et al.*, 2022). A recent development by Nordlund and his collaborators (Popovas *et al.*, 2022) aims at modelling the structure of the entire Sun, with the required resolution of the convective dynamics.

It should be noted that the detailed hydrodyamical simulations of near-surface solar and stellar convection provide a measure of the average conditions in the outermost layers of the Sun and stars. The simulations can be used to estimate appropriate parameters for simple convection treatments, such as the mixing-length theory (Trampedach *et al.* 2014). Alternatively, averages of the simulated structure can be patched to the stellar models during the stellar-evolution calculations (Mosumgaard *et al.* 2020). The results are again fairly similar to those of traditional model computations, as far as their effect on the overall structure of the stars is concerned. Thus there may be some hope that our inadequate treatment of convection has not introduced gross errors in the computed models. Nevertheless, improving the treatment of convective energy transport remains one of the key goals in the further development of computations of stellar models.

[5] Much of this section was kindly provided by Yixiao Zhou.

Chapter 7

Mass-luminosity relations

7.1 Stars dominated by radiative transport

We can estimate the luminosity of stars, from the equation of radiative transport combined with our previous estimates of the temperature and density in the stars. As usual the purpose is to get a feeling, within a few orders of magnitude, for the characteristic value of the luminosity, and an idea about how it varies with the parameters characterizing the star. Hence in general we neglect factors of order unity.

We assume the ideal gas law and neglect radiation pressure. Then we have the estimate for the temperature

$$T \simeq \frac{GMm_{\rm u}\mu}{k_{\rm B}R} \tag{7.1}$$

(*cf.* equation (4.9)), and we estimate the density by the mean density

$$\rho \simeq \frac{M}{R^3} \, . \tag{7.2}$$

The luminosity is determined by the equation of radiative transport (equation (5.8)), which we write as

$$L = -\frac{4\pi r^2 a\tilde{c}}{3\kappa\rho}\frac{{\rm d}T^4}{{\rm d}r} \, . \tag{7.3}$$

We approximate the opacity by a power law

$$\kappa \simeq \kappa_0 \rho^\lambda T^{-\nu} \tag{7.4}$$

(*cf.* equations (5.14) and (5.15)). Finally we replace r by R, and approximate $-{\rm d}T^4/{\rm d}r$ by T^4/R. Since the luminosity is essentially constant throughout most of the star, we may use the resulting average value of L as representative of the surface luminosity $L_{\rm s}$. Thus we obtain

$$L_{\rm s} \simeq \frac{a\tilde{c}RT^{4+\nu}}{\kappa_0\rho^{\lambda+1}} \simeq \frac{a\tilde{c}}{\kappa_0}\left(\frac{Gm_{\rm u}\mu}{k_{\rm B}}\right)^{4+\nu} R^{3\lambda-\nu}M^{3+\nu-\lambda} \, . \tag{7.5}$$

We distinguish between two cases:

1) Lower main sequence, relatively low masses.

Here the temperature is relatively low, and the opacity is dominated by atomic processes, in particular bound-free transitions. Hence the opacity can be approximated by the Kramers law, *i.e.*, $\lambda = 1$, $\nu = 3.5$. Furthermore the constant in the law is

$$\kappa_0 \equiv \kappa_0^{(\mathrm{bf})} \simeq 4 \times 10^{25} Z(1+X) \quad \text{in cgs units} . \tag{7.6}$$

Then equation (7.5) gives

$$\begin{aligned} L_\mathrm{s} \simeq L_\mathrm{bf} &= \frac{a\tilde{c}}{\kappa_0^{(\mathrm{bf})}} \left(\frac{G m_\mathrm{u} \mu}{k_\mathrm{B}}\right)^{7.5} R^{-0.5} M^{5.5} \\ &\simeq 1.4 \times 10^{35} \left(\frac{M}{\mathrm{M}_\odot}\right)^{5.5} \frac{1.7}{1+X} \frac{0.02}{Z} \left(\frac{\mu}{0.62}\right)^{7.5} \left(\frac{R}{\mathrm{R}_\odot}\right)^{-0.5} \mathrm{erg\,sec}^{-1} , \end{aligned} \tag{7.7}$$

where, as indicated, we assumed $X = 0.7$, $Z = 0.02$ as reference. This estimate is rather too high, compared with the solar luminosity of 3.846×10^{33} erg/sec. In view of the approximations made, this is hardly surprising. In fact, it is striking that the result is so relatively close to the correct value. This is yet another example of the ability from laboratory physics to predict properties of stars. All the quantities used in the estimate, including $\kappa_0^{(\mathrm{bf})}$ can either be measured or calculated from the laws of physics.

In equation (7.7) L_s depends on both M and R. However, the exponent in the dependence on R is much smaller than the exponent in the M-dependence. Numerical calculations show that on the main sequence R is approximately proportional to M; hence the variation of L_s is dominated by the M-dependence.

2) Upper main sequence, relatively massive stars

Here the temperature is relatively high, and the opacity is dominated by electron scattering. Then we obtain (*cf.* equation (5.15)) $\lambda = \nu = 0$, $\kappa_0 = \kappa_0^{(\mathrm{e})} = 0.2(1+X)$ in cgs units, and hence

$$L_\mathrm{s} \simeq L_\mathrm{e} = \frac{a\tilde{c}}{\kappa_0^{(e)}} \left(\frac{G m_\mathrm{u} \mu}{k_\mathrm{B}}\right)^4 M^3 \simeq 3 \times 10^{35} \left(\frac{M}{\mathrm{M}_\odot}\right)^3 \left(\frac{\mu}{0.62}\right)^4 \frac{1.7}{1+X} \mathrm{erg\,sec}^{-1} . \tag{7.8}$$

Note that L_s is independent of R in this approximation, while the M-dependence is less steep than on the lower main sequence.

The choice between these two expressions depends on the relative magnitude of κ_e and κ_bf; when $\kappa_\mathrm{e} > \kappa_\mathrm{bf}$ the opacity is dominated by electron scattering and equation (7.8) must be used. It is easy to show that this condition is equivalent to $L_\mathrm{e} < L_\mathrm{bf}$, *i.e.*,

$$\frac{M}{\mathrm{M}_\odot} > 1.4 \left(\frac{R}{\mathrm{R}_\odot}\right)^{1/5} , \tag{7.9}$$

for $X = 0.7$, $Z = 0.02$.

Exercise 7.1:

Show this.

This confirms that equation (7.7) is valid on the lower, and equation (7.8) on the upper, part of the main sequence; the transition takes place at a mass somewhat higher than the solar mass.

It may seem peculiar that we can calculate the stellar luminosities, particularly on the upper main sequence, without taking into account the processes that are responsible for the energy generation. The explanation is that the star is in equilibrium, so that all parts of the star have to "fit together". The energy production has to adjust itself to produce the amount of energy necessary to satisfy equation (7.7) or equation (7.8). This is possible because the rate of energy production is a very sensitive function of temperature, as shown in Chapter 8. Hence a small modification of the central temperature is sufficient to obtain the correct luminosity.

It should also be noted that the present description, at least for the lower main sequence, assumes that the radius is known. In reality, the radius should also be determined by similar arguments, and this requires that the complete set of constraints on the model be taken into account. There exist well-defined procedures for doing that in the case where the ideal-gas law is assumed and energy generation and opacity are approximated by power laws in density and temperature; this results in the so-called homology-scaling relations for stellar structure (*e.g.* Kippenhahn *et al.*, 2012). The results are quite similar to those obtained here, however; in particular, the luminosity is approximately inversely proportional to opacity and depends very little on the details of energy production.

The relations found here do not depend on the star being on the main sequence, and hence should also describe the evolution of the star before it arrives on, and after it leaves, the main sequence, at least as long as the physical properties assumed here are valid.[1] Since this is often depicted in a $(\log T_{\rm eff}, \log L_{\rm s})$ diagram, it is convenient in equation (7.7) to express R in terms of $T_{\rm eff}$, by means of

$$L_{\rm s} = 4\pi\sigma R^2 T_{\rm eff}^4 \tag{7.10}$$

(*cf.* equation (5.12)). The result is

$$L_{\rm s} \propto T_{\rm eff}^{0.8} M^{4.4} \ . \tag{7.11}$$

Exercise 7.2:

Verify this.

Of course equation (7.8) is unchanged.

7.2 Predominantly convective stars

7.2.1 Introduction

In section 7.1 we assumed that the energy transport takes place by radiation in substantial parts of the star. Hence the relations derived there are invalid for stars that are

[1] On the other hand the relations are not valid for, *e.g.*, white dwarfs where the physical conditions are quite different.

predominantly convective. In particular, there are problems for stars with low effective temperature, and hence having extensive convection zones in the outer parts where the temperature is low and the opacity consequently high (*cf.* Chapter 6). Here we consider such stars.

The analysis leading to the appropriate mass-luminosity relation for this case is rather intricate; it is presented below. The result is a relation between mass, effective temperature and luminosity, which may be written as

$$\frac{L_{\rm s}}{\rm L_\odot} \simeq 0.03 \left(\frac{M}{\rm M_\odot}\right)^{-7} \left(\frac{T_{\rm eff}}{2400{\rm K}}\right)^{40} \ . \tag{7.12}$$

A notable feature of this relation is the very large exponent on $T_{\rm eff}$. Hence stars of this type all have nearly the same effective temperature, which according to equation (7.12) is close to 2400 K. An important example of the use of this relation is to describe the contraction of a star that is being formed; it may be shown that such a star is almost completely convective and hence, during its evolution, the luminosity decreases with decreasing radius while $T_{\rm eff}$ is almost constant. Hence the evolution takes place along an almost vertical track in the $(\log T_{\rm eff}, \log L_{\rm s})$ diagram; the location of the track depends little on M. This is known as the *Hayashi track*, after the Japanese astrophysicist who was the first to describe it. Equation (7.12) is illustrated schematically by the solid lines in Figure 7.1.

This overall behaviour is largely confirmed by numerical calculations (see Chapter 10), although the details are somewhat different. Thus computationally $T_{\rm eff}$ on the Hayashi track is around $4000 - 5000$ K. Also, the sign of the exponent on $T_{\rm eff}$, and hence the slope of the Hayashi track is wrong: the detailed calculations show that the exponent is negative, although still with a very large absolute value, so that the luminosity decreases steeply with increasing effective temperature (see Figure 7.1). However, the qualitative agreement between equation (7.12) and the numerical results is reasonable.

It may also be shown (*cf.* section 7.3) that stars on the left hand side of the Hayashi track (*i.e.*, at higher effective temperature) have a small core with radiative transport. There are no stable stars on the right hand side of the Hayashi track. If one attempts to construct a star with lower effective temperature than on the Hayashi track, the result is a star with a void at the centre, and hence an obviously unstable situation.

7.2.2 Convective envelopes

In the convection zone

$$\frac{{\rm d}\ln P}{{\rm d}\ln \rho} = \Gamma_1 \ . \tag{7.13}$$

We assume that Γ_1 is constant, $\Gamma_1 = \gamma$, where we use the value $\gamma = 5/3$ for a completely ionized ideal gas. Then equation (7.13) can be integrated, to yield

$$P = K\rho^\gamma \ , \tag{7.14}$$

where K is a constant. Therefore the relation between P and ρ corresponds to a polytropic equation of state.

As a further simplification we assume that the convection zone extends all the way up to the photosphere and is adiabatically stratified everywhere, with a continuous transition

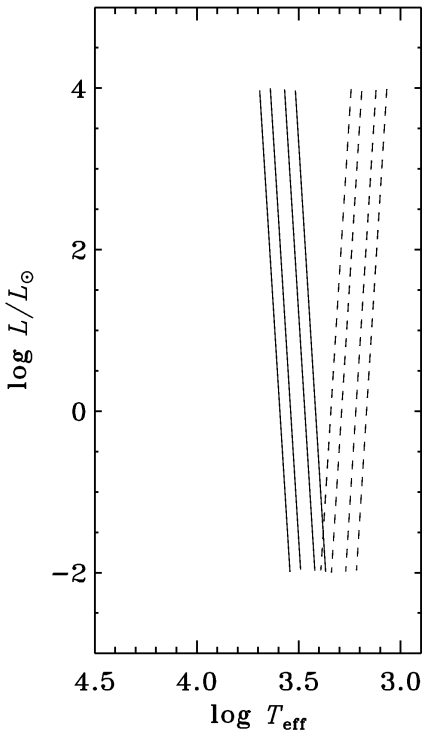

Figure 7.1: Schematic illustration of the Hayashi track. The solid lines were obtained from equation (7.12), for the masses $1, 2, 5$ and $10\,\mathrm{M}_\odot$. The dashed lines used the same relation, except that the exponent 40 to $T_{\rm eff}$ was replaced by -40. This corresponds more closely to the behaviour obtained from numerical computations (*cf.* Figure 10.4).

in P and ρ to the values in the photosphere. Then the constant K is determined by conditions in the photosphere as

$$K = \frac{P_{\rm ph}}{\rho_{\rm ph}^{\gamma}} \,, \tag{7.15}$$

where the index "ph" indicates the values in the photosphere. They can be found from the results of section 5.4, in particular equations (5.22) and (5.23) for $P_{\rm ph}$ and $\rho_{\rm ph}$. By substituting into equation (7.15) we obtain

$$K = \left[\frac{GM(a+1)}{R^2\kappa_0^{\rm (ph)}}\right]^{-\eta} \left(\frac{k_{\rm B}}{\mu m_{\rm u}}\right)^{1+\eta} T_{\rm eff}^{1+\eta(b+1)} \,, \tag{7.16}$$

where $\eta = (\gamma - 1)/(a + 1)$

According to equation (7.16) the properties of the atmosphere, described by $T_{\rm eff}$, apparently determine K, and hence the structure of the interior of the star. This may seem as a rather extreme case of the tail wagging the dog. In fact, the situation is the opposite: the structure of the star is determined by the polytropic relation (7.14); when the density is sufficiently low that radiation can escape (as expressed by equation (5.20)), the photosphere of the star is reached, and the temperature at that point is the effective

temperature. Hence equation (7.16) determines $T_{\rm eff}$ as a function of the structure of the star, as given by the value of K, the mass and the radius. Given $T_{\rm eff}$ the luminosity is determined by

$$L_{\rm s} = 4\pi\sigma R^2 T_{\rm eff}^4 \ . \tag{7.17}$$

Hence, if K is known, we obtain a mass-luminosity relation, corresponding to the relations derived in section 7.1 for the case of radiative transfer.

It should be noted, however, that the assumption that equation (7.14) is valid up to the photosphere is questionable. This assumes that convection is so efficient that the density gradient is adiabatic everywhere. In fact, convection is rather inefficient near the surface of the star, where the density is low. This is a problem in particular for stars of large radius (*cf.* equation (5.23)). To relate the value of K in the interior of the star, which determines its structure, to the properties in the photosphere we need a more detailed description of convection. Another problem is that Γ_1 is not constant in the ionization zones for H and He, and hence that equation (7.14) does not always follow from equation (7.13). Thus we cannot expect from the relations derived here to obtain an accurate description of the star; on the other hand the analysis largely explains the results of more complete models.

7.2.3 Completely convective stars

For such stars equation (7.14) is valid everywhere, and hence the star is a complete polytrope of index $n = 1/(\gamma - 1) = 3/2$. Then we may use the relations in section 4.6; in particular, we have that

$$K = K_{\rm pol} \equiv N_{3/2} G R M^{1/3} \tag{7.18}$$

(*cf.* equation (4.48)), where we have defined $K_{\rm pol}$ as the value of K corresponding to complete polytrope, and the coefficient N_n is given in Table 4.1. From equations (7.16) and (7.18) we then obtain

$$N_{3/2} G R M^{1/3} = \left[\frac{GM(a+1)}{R^2 \kappa_0^{\rm (ph)}}\right]^{-\eta} \left(\frac{k_{\rm B}}{\mu m_{\rm u}}\right)^{1+\eta} T_{\rm eff}^{1+\eta(b+1)} \ , \tag{7.19}$$

and hence

$$T_{\rm eff} = N_{3/2}^{\xi} \left(\frac{G\mu m_{\rm u}}{k_{\rm B}}\right)^{\xi(\eta+1)} \left(\frac{\kappa_0^{\rm (ph)}}{a+1}\right)^{-\xi\eta} R^{\xi(1-2\eta)} M^{\xi(\eta+\frac{1}{3})} \ , \tag{7.20}$$

where $\xi = 1/[1 + \eta(b+1)]$. Finally equation (7.17) gives

$$L_{\rm s} = 4\pi\sigma N_{3/2}^{4\xi} \left(\frac{G\mu m_{\rm u}}{k_{\rm B}}\right)^{4\xi(\eta+1)} \left(\frac{\kappa_0^{\rm (ph)}}{a+1}\right)^{-4\xi\eta} R^{4\xi(1-2\eta)+2} M^{4\xi(\eta+\frac{1}{3})} \ . \tag{7.21}$$

This is the desired mass-radius-luminosity relation.

As in the radiative case (*cf.* equation (7.11)) it is instructive to eliminate R; this gives a relation between $T_{\rm eff}$ and $L_{\rm s}$, which can be used to interpret evolutionary tracks in a $(\log T_{\rm eff}, \log L_{\rm s})$ diagram. The result is

$$R = N_{3/2}^{-\zeta} \left(\frac{k_{\rm B}}{G\mu m_{\rm u}}\right)^{\zeta(1+\eta)} \left(\frac{\kappa_0^{\rm (ph)}}{a+1}\right)^{\zeta\eta} M^{-\zeta(\eta+\frac{1}{3})} T_{\rm eff}^{\zeta/\xi} \ , \tag{7.22}$$

and hence

$$L_{\rm s} = 4\pi\sigma N_{3/2}^{-2\zeta} \left(\frac{k_{\rm B}}{G\mu m_{\rm u}}\right)^{2\zeta(1+\eta)} \left(\frac{\kappa_0^{(\rm ph)}}{a+1}\right)^{2\zeta\eta} M^{-2\zeta(\eta+\frac{1}{3})} T_{\rm eff}^{4+2\zeta/\xi} \,, \tag{7.23}$$

where $\zeta = 1/(1-2\eta)$.

To get an impression of the numerical values we may use $\kappa_0^{(\rm ph)} = 2\times10^{-20}$ in cgs units, $a = 0.7$, $b = 6$, which is typical for a Population I chemical composition, $X = 0.7$, $Z = 0.02$. After suitably truncating the coefficients and exponents we then obtain

$$T_{\rm eff} \simeq 2400\,{\rm K} \left(\frac{M}{{\rm M}_\odot}\right)^{0.2} \left(\frac{R}{{\rm R}_\odot}\right)^{0.06} \,, \tag{7.24}$$

$$\frac{L_{\rm s}}{{\rm L}_\odot} \simeq 0.03 \left(\frac{M}{{\rm M}_\odot}\right)^{0.8} \left(\frac{R}{{\rm R}_\odot}\right)^{2.2} \,, \tag{7.25}$$

and

$$\frac{L_{\rm s}}{{\rm L}_\odot} \simeq 0.03 \left(\frac{M}{{\rm M}_\odot}\right)^{-7} \left(\frac{T_{\rm eff}}{2400{\rm K}}\right)^{40} \,. \tag{7.26}$$

There are several noteworthy features of these relations. The exponent on R is very small in equation (7.24), and hence $T_{\rm eff}$ is almost independent of R; the dependence on M is also weak. Thus stars of this type all have nearly the same effective temperature. This is reflected in the very large exponent on $T_{\rm eff}$ in equation (7.26). As discussed in section 7.2.1 this causes the evolution of almost convective stars to follow the Hayashi track.

Numerical computations of stars of this type largely confirm the results, although the details are different. In particular, a qualitative difference is that unlike the numerical results equation (7.26) predicts that the luminosity *decreases* with increasing mass at fixed $T_{\rm eff}$ and increases with increasing $T_{\rm eff}$ for fixed mass. Hence, roughly speaking the evolution tracks in the $(\log T_{\rm eff}, \log L_{\rm s})$ diagram obtained from the approximation have been rotated, so that they have a positive slope rather than the correct negative slope. This problem can be traced back to the sign of the exponent on R in equation (7.20) for $T_{\rm eff}$, and hence to the magnitude of η; had η been slightly larger than 0.5 rather than, as here, slightly below 0.5 the slope would have been at least qualitatively correct. It is obvious that one cannot expect correct results for such relatively subtle details, with approximations as coarse as those that we have made. Particularly troublesome is probably the assumption that adiabatic convection extends all the way to the photosphere.

7.3 The "forbidden" region

In section 7.2 we assumed that the star was convective everywhere, so that the structure corresponded to a complete polytrope. However, it is also possible to get a qualitative understanding of the properties of a star where the convection zone extends over most, but not all of, the star. In particular, it may be shown that the region in the $(\log T_{\rm eff}, \log L_{\rm s})$ diagram corresponding to lower $T_{\rm eff}$ than on the Hayashi track (for given $L_{\rm s}$) is "forbidden", in the sense that it is impossible to construct stellar models in hydrostatic equilibrium in that region. Here we present the ideas of this argument.

When the model is not a complete polytrope, $K \neq K_{\rm pol}$. However, it is still the case that *the outer parts* of the model, where the temperature is lowest and the opacity consequently highest, are convective. Hence we can find the structure of the outer parts by integrating the polytropic equation from $r = R$ in the direction of decreasing r. The relevant differential equation is still equation (4.37):

$$\frac{1}{r^2}\frac{\mathrm{d}}{\mathrm{d}r}\left(\frac{r^2 K}{\rho}\gamma\rho^{\gamma-1}\frac{\mathrm{d}\rho}{\mathrm{d}r}\right) = -4\pi G\rho \; , \tag{7.27}$$

and we again introduce $n = 1/(\gamma - 1)$. However, since the conditions at the centre are not immediately relevant for the solution, it is not convenient to scale the density in terms of the central density, as was done in equation (4.39). Instead we introduce the dimensionless variable ϕ, by

$$\rho = \overline{\rho}\phi^n = \frac{3M}{4\pi R^3}\phi^n \; . \tag{7.28}$$

Then we obtain

$$\frac{1}{r^2}\frac{\mathrm{d}}{\mathrm{d}r}\left(r^2\frac{\mathrm{d}\phi}{\mathrm{d}r}\right) = -\frac{4\pi G}{(n+1)K}\left(\frac{3M}{4\pi R^3}\right)^{1-\,1/n}\phi^n \; ; \tag{7.29}$$

of course this equation is, apart from the scaling of the dependent and independent variables, entirely equivalent to the Lane-Emden equation (*cf.* equation (4.40)). Assuming, as an approximation, that the equation is valid to the surface of the star we obtain the boundary conditions

$$\left.\begin{array}{l} \phi = 0 \\ \dfrac{\mathrm{d}\phi}{\mathrm{d}r} = -\left(\dfrac{4\pi}{3}\right)^{1/n}\dfrac{GM^{1-\,1/n}}{(n+1)KR^{2-\,3/n}} \end{array}\right\} \quad \text{for} \quad r = R \; , \tag{7.30}$$

where the last condition follows from the equation of hydrostatic equilibrium.

We now consider three models, with the same M and R:

Model 1, with $K = K_{\rm pol}$.

Model 2, with $K = K_2 > K_{\rm pol}$.

Model 3, with $K = K_3 < K_{\rm pol}$.

Thus Model 1 is on the Hayashi track. The effective temperature and the luminosity for the other two models can be obtained from equations (7.16) and (7.17). We obtain

$$\frac{T_{\rm eff,2}}{T_{\rm eff,1}} = \left(\frac{K_2}{K_{\rm pol}}\right)^{\xi} \; , \tag{7.31}$$

and

$$\frac{L_2}{L_1} = \left(\frac{K_2}{K_{\rm pol}}\right)^{4\xi} \; , \tag{7.32}$$

where indices "1" and "2" indicate Model 1 and Model 2. Corresponding relations are of course obtained for Model 3. By using equation (7.23) we then find that Model 2 is on the side of Hayashi track corresponding to higher $T_{\rm eff}$, while Model 3 is on the opposite side.

Exercise 7.3:

Verify equations (7.31) and (7.32), as well as the location of Model 2 and 3 relative to the Hayashi track.

We can now compare the structure of Models 1 and 2. From equation (7.30) it follows that $\mathrm{d}\phi/\mathrm{d}r$ is smaller in absolute value at the surface of Model 2 than for Model 1, and equation (7.29) then shows that $|\mathrm{d}\phi/\mathrm{d}r|$ increases more slowly with increasing r. Hence ϕ also increases more slowly with decreasing r in Model 2, so that

$$\phi_2(r) < \phi_1(r) \ , \tag{7.33}$$

or

$$\rho_2(r) < \rho_1(r) \ . \tag{7.34}$$

Thus at given r the density is lower in Model 2. Furthermore, from the equation for m we obtain

$$m_2(r) = M - \int_r^R 4\pi r^2 \rho_2(r)\mathrm{d}r > M - \int_r^R 4\pi r^2 \rho_1(r)\mathrm{d}r = m_1(r) \ . \tag{7.35}$$

These relations are valid in the convective part of Model 2. Had Model 2 been convective to the centre, we would obtain from equation (7.35) that $m_2(0) > m_1(0) = 0$. Thus Model 2 would have had a point-mass at the centre. This is rather unrealistic. In fact, there has to be a transition to radiative transport somewhere in the interior; here the density gradient is steeper than in Model 1, and hence the density increases more rapidly with decreasing r, thus compensating for the lower mass in the outer parts of Model 2. If the model is close to the Hayashi track, the region with radiative transfer is small; thus the star has a small compact core surrounded by an extended convective envelope. As discussed in Chapter 12 this corresponds to the structure of *red giants*, which are late phases of stellar evolution.

For Model 3 the opposite argument may be made. Here we find that

$$\rho_3(r) > \rho_1(r) \ , \tag{7.36}$$

and hence

$$m_3(r) < m_1(r) \ . \tag{7.37}$$

But this gives rise to serious problems. Had Model 3 been everywhere convective, so that equations (7.36) and (7.37) were valid at all r, there would be a point, $r = r_0 > 0$, so that $m_3(r_0) = 0$. Thus the star would have a hole in the middle! The only way to avoid this is for the density to increase *more slowly* than corresponding to the adiabatic gradient. But then the star would be convectively unstable, and hence this solution is impossible. Thus we see that one cannot construct a stable model with $K < K_{\rm pol}$, *i.e.*, with lower $T_{\rm eff}$ than on the Hayashi track.

Chapter 8

Nuclear energy generation

8.1 Introduction

During most of their lifetimes stars derive the energy which they radiate from nuclear reactions. The gradual change in chemical composition as the reactions proceed determines the evolution of the stars. Hence, to follow the life history of a star it is important to understand the properties of the nuclear reactions. For this reason we describe the physics of the nuclear energy generation in rather more detail than, for example, the opacity. Nevertheless, a complete description is beyond the scope of these notes. Clayton (1968) describes many aspects of the problem, and relates them to the detailed structure of the nuclei involved.

The goal is to compute the rate ϵ of energy generation per unit mass, which was introduced in equation (5.24). The computation can be separated into three parts, discussed in separate sections below: the cross section for a reaction between a pair of nuclei, which is determined predominantly by the properties of the nuclei; the amount of energy generated per reaction, which again is a property of the nuclei; and the total reaction rate which, beside the cross section, also depends on the statistics of the motion of the nuclei.

An additional consequence of the nuclear processes is a gradual change of the chemical composition, which controls the evolution of the star. Hence we must determine the rate of change of the abundances; for example, the rate of change of the hydrogen abundance X may be written as

$$\frac{\mathrm{d}X}{\mathrm{d}t} = r_X \ , \tag{8.1}$$

where r_X is determined as a sum over the reactions which consume hydrogen.

For the purposes of the following discussion, it is convenient to introduce a compact notation for nuclear reactions. The reaction

$$A + a \rightarrow Y + y \qquad \text{is written} \qquad A(a,y)Y \ , \tag{8.2}$$

where in the bracket the particle(s) in front of the comma is the one (are those) entering into the reaction, and that (those) after the comma is (are) the particle(s) resulting from the reaction. Clearly the reaction could equivalently be written as $a(A,y)Y$, $a(A,Y)y$ or $A(a,Y)y$, although there is a tendency to place the primary reactant and the primary

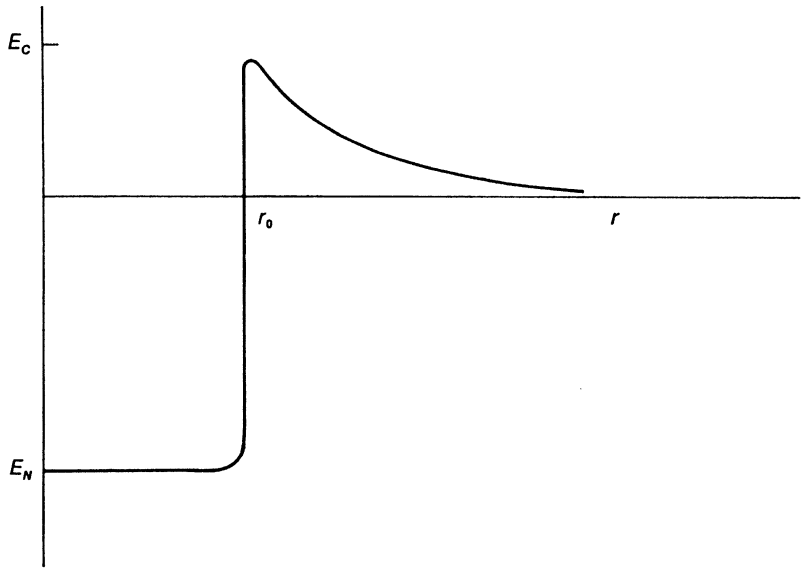

Figure 8.1: Schematic potential energy between two nuclei. For $r < r_0$ the attractive nuclear forces dominate; for $r > r_0$ Coulomb repulsion dominates.

product outside the brackets.[1] As a specific example, the reaction

$$^{12}\mathrm{C} + {}^{1}\mathrm{H} \rightarrow \gamma + {}^{13}\mathrm{N} \tag{8.3}$$

is written as $^{12}\mathrm{C}(^{1}\mathrm{H},\gamma)\,^{13}\mathrm{N}$, or $^{12}\mathrm{C}(p,\gamma)\,^{13}\mathrm{N}$, using p for the proton.

8.2 The cross sections

The reaction between nuclei is caused by the *strong force* acting between nucleons (protons and neutrons). The range of the strong force is essentially limited to the extent of the nucleus; hence, for a reaction to occur the nuclei must be brought so close together that they almost touch, and this requires that the Coulomb repulsion between them must be overcome.[2] Hence the potential for a reaction is as indicated in Figure 8.1.

The magnitude of the difficulty in achieving a reaction may be appreciated by noting that the height of the Coulomb barrier at the surface of the nucleus, corresponding to a typical radius of $r_0 \simeq 10^{-13}$ cm, is

$$E_{\mathrm{Coul}} \simeq \frac{\mathcal{Z}_1 \mathcal{Z}_2 e^2}{r_0} \simeq \mathcal{Z}_1 \mathcal{Z}_2 \ \mathrm{MeV}\ , \tag{8.4}$$

where $\mathcal{Z}_1$ and $\mathcal{Z}_2$ are the atomic numbers of the nuclei taking part in the reaction. This is consistent with the fact that typical nuclear energies are in the MeV range. In contrast,

[1] For laboratory reactions the target would probably in general be placed in front of the bracket.

[2] The only exception are reactions involving capture of neutrons, where there is no Coulomb repulsion. These play no role during normal stellar evolution; but, as discussed in Chapter 14, they become important in very advanced stages of evolution. They are also decisive for nucleo-synthesis of the light elements shortly after the Big Bang.

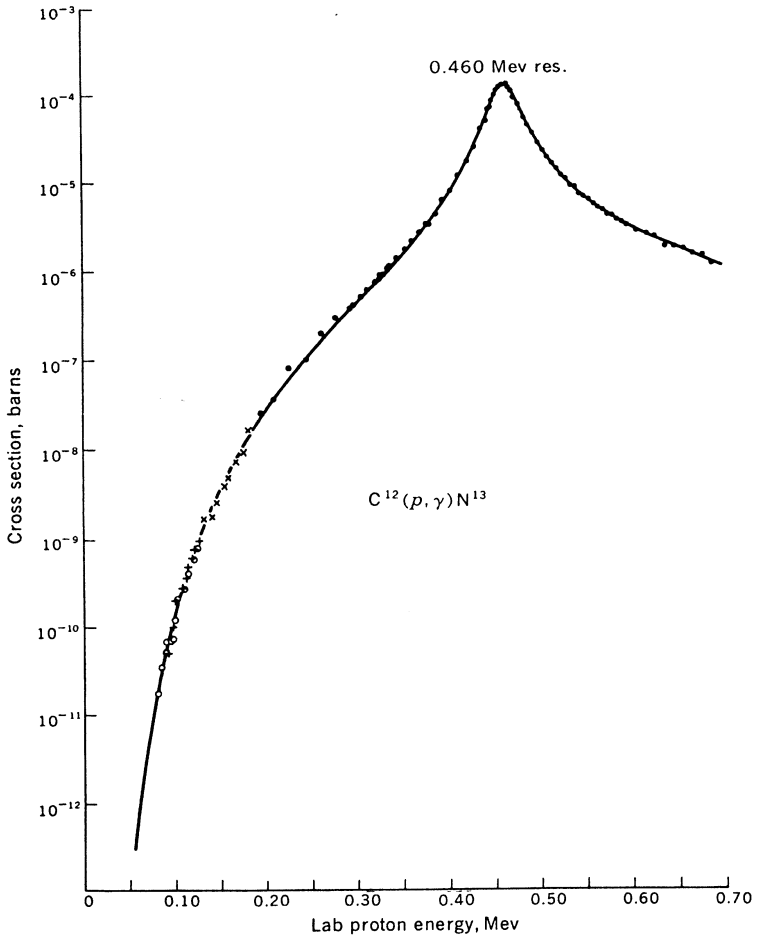

Figure 8.2: Measured cross section for the reaction $^{12}\mathrm{C}(^{1}\mathrm{H},\gamma)\,^{13}\mathrm{N}$, as a function of the laboratory proton energy. A four-parameter theoretical curve has been fitted to the experimental points. It is clearly impossible to extrapolate to the energy, of order 25 keV, which is relevant in astrophysics. (From Clayton 1968.)

the average kinetic energy of the nuclei is

$$\langle E_{\mathrm{kin}} \rangle = \frac{3}{2} k_{\mathrm{B}} T \simeq 130\,\mathrm{eV}\,T_6 \tag{8.5}$$

(*cf.* section 3.3), where $T_6 \equiv T/10^6\,\mathrm{K}$. Since typical temperatures in the cores of hydrogen-burning stars are $1 - 2 \times 10^7\,\mathrm{K}$, the average kinetic energy is roughly three orders of magnitude smaller than the energy required to overcome the potential barrier. Even taking into account the distribution of energies, it is clear that within the framework of classical mechanics essentially no reactions would be possible.[3]

What makes reactions, and hence ultimately our existence, possible is that according to quantum mechanics there is a finite probability that the nuclei may tunnel through the barrier and react. Even so, the extent of the barrier means that this probability is small. Thus, in fact the nuclear burning in stellar interiors is generally a very slow process.

[3]Even quantum-mechanically, it is found that the reactions mainly occur at several times the average thermal energy; *cf.* equation (8.37).

Exercise 8.1:

What is the average energy generation rate in the Sun, per unit mass? Compare it with the average rate of energy production per unit mass in a typical car engine; and the rate of energy consumption per unit mass in a human being.

The very low energies also make it extremely difficult to measure the cross sections under stellar conditions for the relevant reactions. As an example, Figure 8.2 shows measured cross sections for proton capture by ^{12}C. It is obviously meaningless, on the basis of data on this form, to extrapolate the measurements to the energy range where the reactions take place in stellar interiors. However, a reasonable extrapolation can be obtained by using that most of the variation with energy of the cross section is caused by the energy dependence of the probability that the nuclei penetrate the potential barrier. The same probability enters into the problem of α decay since, to decay, the α particle must tunnel out through the potential barrier (see for example Krane 1988, Chapter 8). It was shown by Gamow that this probability is proportional to

$$\exp\left(-\frac{2\pi\mathcal{Z}_1\mathcal{Z}_2e^2}{\hbar v}\right) , \tag{8.6}$$

where v is the relative speed between the two nuclei and, as usual, $\hbar = h/2\pi$, where h is Planck's constant. An additional energy dependence enters into the cross sections from the fact that, roughly speaking, the nuclei have a geometrical extent given by their de Broglie wavelengths $\lambda \propto 1/p$, where p is the momentum of the nucleus; this results in a geometrical cross section

$$\pi\lambda^2 \propto p^{-2} \propto E^{-1} , \tag{8.7}$$

where E is the energy of the nucleus.

These considerations justify characterizing the cross section by the *cross-section factor* $S(E)$, defined such that the cross section is

$$\sigma(E) \equiv \frac{S(E)}{E}\exp\left(-\frac{2\pi\mathcal{Z}_1\mathcal{Z}_2e^2}{\hbar v}\right) . \tag{8.8}$$

Hence $S(E)$ essentially describes the energy dependence of the reaction once the nuclei have penetrated the potential barrier. It varies far less with E than does the full cross section. As an example, Figure 8.3 shows $S(E)$ for the same reaction that was illustrated in Figure 8.2. Clearly in this case one may extrapolate to low energies with some confidence.

In equation (8.8) E is the energy of the particles in the centre-of-mass system. This is related to the relative speed of the particles by

$$E = \frac{1}{2}\frac{m_1m_2}{m_1+m_2}v^2 = \frac{1}{2}\mathcal{A}m_{\rm u}v^2 , \tag{8.9}$$

where m_1 and m_2 are the masses of the nuclei, and $\mathcal{A}$ is the reduced atomic weight,

$$\mathcal{A} = \frac{\mathcal{A}_1\mathcal{A}_2}{\mathcal{A}_1+\mathcal{A}_2} , \tag{8.10}$$

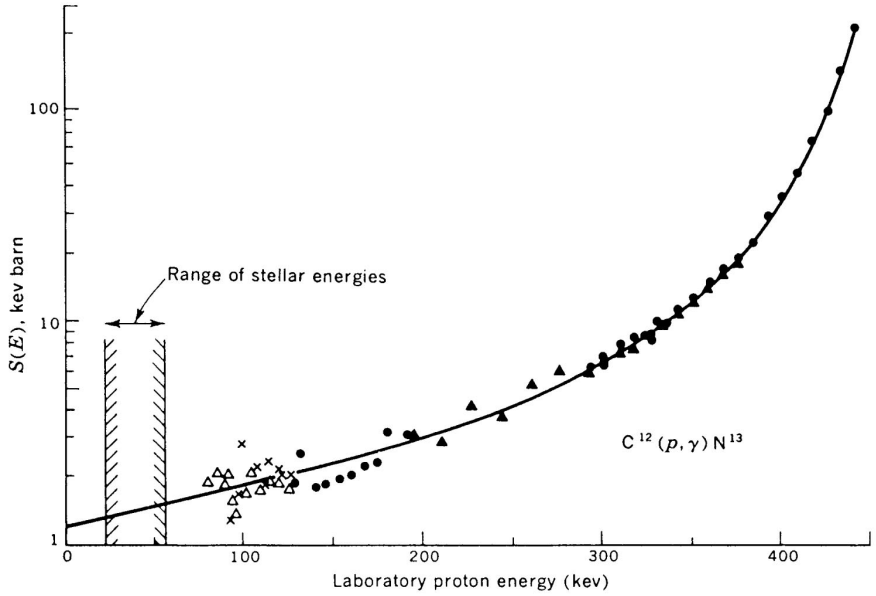

Figure 8.3: The cross-section factor $S(E)$ corresponding to measured cross sections for the reaction $^{12}\mathrm{C}(^{1}\mathrm{H},\gamma)\,^{13}\mathrm{N}$, as a function of the laboratory proton energy. This curve is more readily extrapolated than the one in Figure 8.2 (From Clayton 1968.)

where $\mathcal{A}_1$ and $\mathcal{A}_2$ are the atomic weights of the nuclei. From equation (8.8) it therefore follows that the cross section can be written as

$$\sigma(E) \equiv \frac{S(E)}{E} \exp\left(-bE^{-1/2}\right) \ , \tag{8.11}$$

where

$$b = 31.291 \mathcal{Z}_1 \mathcal{Z}_2 \mathcal{A}^{1/2} \ \ \mathrm{keV}^{1/2} \ . \tag{8.12}$$

Exercise 8.2:

Verify this equation.

From equations (8.11) and (8.12) it follows that the cross section is very sensitive to the charges of the nuclei involved, as a result of the effect of the charges on the extent of the Coulomb barrier. Hence in general reactions amongst nuclei of low charges are faster, and are possible at lower temperature, than reactions involving nuclei of higher charges. However, this general tendency may be reversed by differences in the cross-section factor $S(E)$, due to differences in the nuclear structure.

The measurement of nuclear cross sections is an extensive and ongoing research effort at several laboratories. (Recently it has even become possible to make some measurements at energies corresponding to stellar conditions; an example is shown in Figure 8.4.) The results of these efforts are available in the form of compilations of parameters characterizing

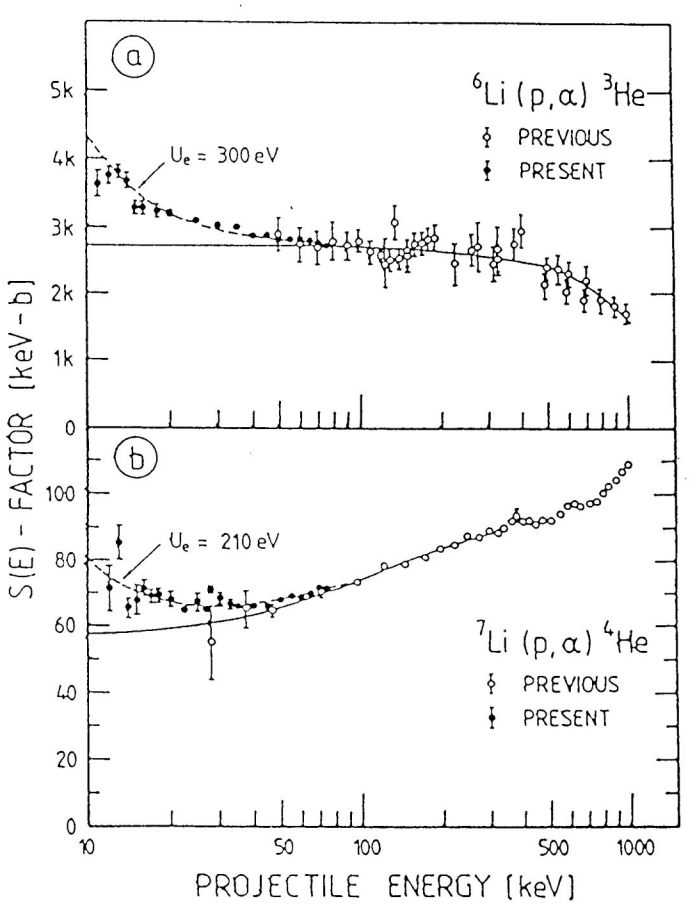

Figure 8.4: Cross-section factors for the reactions ^{6}Li(^{1}H, ^{4}He) ^{3}He and ^{7}Li(^{1}H, ^{4}He) ^{4}He, extending to energies comparable with those found under stellar conditions. The departure from a constant value at very low energies results from the screening from the electrons in the target ^{6}Li or ^{7}Li atoms, which reduces the Coulomb potential around the nucleus, and hence increases the cross section. A similar effect occurs in stellar interiors due to the clustering of otherwise free electrons around the nuclei; this must be taken into account in accurate calculations of nuclear reaction rates. (From Parker & Rolfs 1991.)

the cross-section factors, often given in terms of Taylor expansions of $S(E)$ around $E = 0$ or, equivalently, parameters giving the temperature dependence of the energy-averaged cross sections (see below). A comprehensive compilation was given by Caughlan & Fowler (1988). More recent compilations include Angulo *et al.* (1999) and, for the specific case of the reactions relevant to the Sun, Adelberger *et al.* (1998).

Table 8.1 provides data for the reactions that are relevant to the hydrogen burning in stellar interiors.

Table 8.1

Reaction[a]	Q value, MeV	Average ν loss, MeV	S_0, keV barns	$\frac{dS}{dE}$, barns	B^c	τ_{12}, years[b]
The pp *chain*						
$H^1(p, \beta^+\nu)D$	1.442	0.263	3.78×10^{-22}	4.2×10^{-24}	33.81	7.9×10^9
$D(p, \gamma)He^3$	5.493		2.5×10^{-4}	7.9×10^{-6}	37.21	4.4×10^{-8}
$He^3(He^3, 2p)He^4$	12.859		5.0×10^3		122.77	2.4×10^5
$He^3(\alpha, \gamma)Be^7$	1.586		4.7×10^{-1}	-2.8×10^{-4}	128.26	9.7×10^5
$Be^7(e^-, \nu)Li^7$	0.861	0.80				3.9×10^{-1}
$Li^7(p, \alpha)He^4$	17.347		1.2×10^2		84.73	1.8×10^{-5}
$Be^7(p, \gamma)B^8$	0.135		4.0×10^{-2}		102.65	6.6×10^1
$B^8(\beta^+ \nu)Be^{8*}(\alpha)He^4$	18.074	7.2				3×10^{-8}
The CNO *cycle*						
$C^{12}(p, \gamma)N^{13}$	1.944		1.40	4.26×10^{-3}	136.93	
$N^{13}(\beta^+\nu)C^{13}$	2.221	0.710				
$C^{13}(p, \gamma)N^{14}$	7.550		5.50	1.34×10^{-2}	137.20	
$N^{14}(p, \gamma)O^{15}$	7.293		2.75		152.31	
$O^{15}(\beta^+ \nu)N^{15}$	2.761	1.00				
$N^{15}(p, \alpha)C^{12}$	4.965		5.34×10^4	8.22×10^2	152.54	
$N^{15}(p, \gamma)O^{16}$	12.126		2.74×10^1	1.86×10^{-1}	152.54	
$O^{16}(p, \gamma)F^{17}$	0.601		1.03×10^1	-2.81×10^{-2}	166.96	
$F^{17}(\beta^+\nu)O^{17}$	2.762	0.94				
$O^{17}(p, \alpha)N^{14}$	1.193		Resonant reaction		167.15	

Thermonuclear parameters for the principal reactions contributing to hydrogen burning, through the PP chains and the CNO cycle. Note that in this table only the positron is indicated by β^+ (rather than e^+), and the electron neutrino is shown as ν; as usual α indicates an α particle, *i.e.*, a ^{4}He nucleus. The third column gives the energy carried off by the neutrino emitted per reaction. The fourth and and fifth columns give the cross-section factor extrapolated to $E = 0$ and its derivative; the unit of cross section is *barn*, with $1\,\text{barn} = 10^{-24}\,\text{cm}^2$. The quantity B in the penultimate column is defined in equation (8.34). The last column gives the characteristic time for the reaction (*cf.* equation (8.44)), evaluated for the conditions $T = 15 \times 10^6\,\text{K}$, $\rho = 100\,\text{g cm}^{-3}$ and $X = Y = 0.5$, corresponding roughly to the solar core. (Adapted from Clayton 1968).

8.3 The release of energy

To compute the total energy release we need to know the energy released by each reaction. Because of the equivalence between mass and energy, this follows from the difference in mass between the particles entering on the two sides of the reaction, and hence can be determined with the help of tables of nuclear masses.

To be specific, consider the reaction

$$A + a \rightarrow Y + y\ . \tag{8.13}$$

The energy released in this reaction is

$$Q = \tilde{c}^2[m(A) + m(a) - m(Y) - m(y)]\ , \tag{8.14}$$

where, for example, $m(A)$ is the mass of particle A and $\tilde{c}$ is the speed of light. Since the loss of mass is generally very small compared with the individual masses, it is more convenient to work with the *mass excess* Δm. For a nucleus with $\mathcal{Z}$ protons and $\mathcal{N}$ neutrons we define the mass excess as

$$\Delta m = m - m_{\rm u}(\mathcal{Z} + \mathcal{N})\ , \tag{8.15}$$

where $m_{\rm u}$ is the atomic mass unit. Then, since the combined number of protons and neutrons must be conserved in the reaction (8.13), it follows that equation (8.14) can be written as

$$Q = \tilde{c}^2[\Delta m(A) + \Delta m(a) - \Delta m(Y) - \Delta m(y)] \; . \tag{8.16}$$

A particular problem is caused by reactions where electrons or positrons are emitted, or electrons are absorbed. As discussed in section 1.2 this must occur in the fusion of hydrogen into helium, to preserve charge neutrality, where positron emission results from the conversion of a proton into a neutron. To see how the energetics of such a reaction is calculated, consider the reaction

$$A' + a' \rightarrow Y' + y' + {\rm e}^+ + \nu_{\rm e} \; , \tag{8.17}$$

where a positron and an electron neutrino are emitted.[4] Since the positron is immediately annihilated by an electron in the gas, this reaction may equivalently be written as

$${\rm e}^- + A' + a' \rightarrow Y' + y' + \nu_{\rm e} \; . \tag{8.18}$$

However, in the reaction a proton has been converted into a neutron, so that the atomic numbers on the two sides of the reaction satisfy $\mathcal{Z}(A') + \mathcal{Z}(a') - 1 = \mathcal{Z}(Y') + \mathcal{Z}(y')$. Hence, by adding $\mathcal{Z}(Y') + \mathcal{Z}(y')$ electrons on each side of equation (8.17), this equation may be written as

$$\mathcal{Z}(A'){\rm e}^- + A' + \mathcal{Z}(a'){\rm e}^- + a' \rightarrow \mathcal{Z}(Y'){\rm e}^- + Y' + \mathcal{Z}(y'){\rm e}^- + y' + \nu_{\rm e} \; . \tag{8.19}$$

This obviously corresponds to a reaction between the complete atoms A' and a'; hence the energy release may be calculated as in equation (8.16), provided the mass excesses refer to the *atomic* (rather than nuclear) masses. From the condition of charge conservation it evidently follows that this is true for any reactions involving emission or absorption of positrons or electrons.

A table of atomic mass excesses is given in Appendix B, in the form of $\tilde{c}^2\Delta m$, expressed in MeV. Hence this table immediately allows the calculation of the energy release in any reaction.

The energy produced in the reactions is released as kinetic energy of the particles which result, as well as in some cases in the form of γ photons. This energy is redistributed among the other constituents of the gas through collisions, and through absorption of the photons. As a result of the assumption of thermodynamic equilibrium in the gas, the details of this redistribution process is irrelevant; all that matters is the total amount of heat that is added to the gas. An exception to this general statement results in the cases where *neutrinos* are emitted in the reaction. Because of their extremely small interaction cross section, in almost all cases[5] these do not react with the other particles in the gas but escape directly from the star. Hence, to compute the energy release in the region where the nuclear reactions take place, the energy carried away by the neutrinos must be subtracted. Examples of this are discussed in section 8.5.

[4] Emission of the neutrino is a result of the requirement of lepton-number conservation. Since the neutrino mass is extremely small compared with the mass of the positron, it does not contribute to the mass budget discussed here.

[5] The only exception is in *supernova explosions*, where the density may be so high that the neutrinos are partially absorbed.

8.4 The average reaction rate

We now need to relate the total rate of reactions, between particles A and a in equation (8.13), say, to the cross section discussed in section 8.2. For simplicity we first assume that the particles move with a relative speed v. Also, we take all particles A to be stationary, with a number density n_A. Consider a box such that the area of the side is $\mathrm{d}A$, and the length is $\mathrm{d}l$. We may think about the cross section σ as being defined such that a reaction occurs if a particle a passes within the area σ around a particle A. Then the probability of reaction for a particle of type a, which is shot towards the box in a direction orthogonal to $\mathrm{d}A$, is the ratio of the total area in the box "covered" by cross section to the area $\mathrm{d}A$, *i.e.*,

$$\frac{\sigma n_A \mathrm{d}A \mathrm{d}l}{\mathrm{d}A} = \sigma n_A \mathrm{d}l \ . \tag{8.20}$$

(note that this argument, together with the definition of the mean free path, also establishes the validity of equation (5.13) for the relation between the cross section and the mean free path of a photon). If the number density of particles a is n_a, their flux is vn_a, and hence the number of reactions per unit time in the box is

$$\sigma n_A \mathrm{d}l \ vn_a \mathrm{d}A = \sigma v n_a n_A \mathrm{d}V \ , \tag{8.21}$$

where $\mathrm{d}V$ is the volume of the box. Thus we finally obtain the *reaction rate* r_{aA} *per unit volume* as

$$r_{aA} = \sigma v n_a n_A \ . \tag{8.22}$$

In reality of course there is a distribution of relative velocities; if $f(v)\mathrm{d}v$ denotes the fraction of pairs of particles with relative speed between v and $v + \mathrm{d}v$, equation (8.22) must be replaced by

$$r_{aA} = \langle \sigma v \rangle n_a n_A \ , \tag{8.23}$$

where

$$\langle \sigma v \rangle = \int_0^\infty v \sigma(E) f(v) \mathrm{d}v \ , \tag{8.24}$$

and we explicitly indicated that σ depends on the energy in the reaction, and hence on v (*cf.* equation (8.9)).

A small complication arises in reactions involving just one type of particle (*i.e.*, with $a = A$ in equation (8.16)). In this case we have counted each particle twice in the argument leading to equation (8.23): once as "target" and once as "projectile". As a result in this case equation (8.23) must be replaced by

$$r_{AA} = \frac{1}{2} \langle \sigma v \rangle n_A^2 \ . \tag{8.25}$$

To evaluate $\langle \sigma v \rangle$ we must know the distribution function $f(v)$. We assume that both nuclei have a Maxwellian distribution (*cf.* section 3.3). Then, as shown by Clayton (1968), the distribution of v is also Maxwellian, with a mass given by the reduced mass, *i.e.*,

$$f(v)\mathrm{d}v = 4\pi \left(\frac{m}{2\pi k_\mathrm{B} T} \right)^{3/2} \exp\left(-\frac{mv^2}{2k_\mathrm{B}T} \right) v^2 \mathrm{d}v \ , \tag{8.26}$$

where $m = \mathcal{A}m_{\rm u}$, and $\mathcal{A}$ is given by equation (8.10). This may also be written in terms of the distribution of centre-of-mass energy, as

$$f(v)\mathrm{d}v = \phi(E)\mathrm{d}E = \frac{2}{\sqrt{\pi}}\frac{E^{1/2}}{(k_{\rm B}T)^{3/2}}\exp\left(-\frac{E}{k_{\rm B}T}\right)\mathrm{d}E\ . \tag{8.27}$$

Using equation (8.9) to express v, and equation (8.11) for σ, we finally obtain from equation (8.24) that

$$\langle\sigma v\rangle = \left(\frac{8}{m\pi}\right)^{1/2}\frac{1}{(k_{\rm B}T)^{3/2}}\int_0^\infty S(E)\exp\left(-\frac{E}{k_{\rm B}T}-\frac{b}{E^{1/2}}\right)\mathrm{d}E\ . \tag{8.28}$$

Equation (8.28) demonstrates the two opposing effects that determine the total reaction rate: the cross section increases steeply with increasing energy, as shown by the factor $\exp(-bE^{-1/2})$, whereas the number of particles decreases with increasing energy, as shown by the factor $\exp(-E/k_{\rm B}T)$. As a result, the reactions are dominated by the nuclei in a fairly narrow range of energies, near the maximum of $\exp(-E/k_{\rm B}T - bE^{-1/2})$. This function is illustrated in Figure 8.5; it is commonly called the *Gamow peak*, in recognition of Gamow's work on barrier penetration in nuclear reactions. The maximum of the Gamow peak is at the energy

$$E_0 = \left(\frac{bk_{\rm B}T}{2}\right)^{2/3}\ , \tag{8.29}$$

which therefore corresponds to the energy of the nuclei dominating the reactions.

Exercise 8.3:

Verify equation (8.29). Show also that E_0 may be written as

$$E_0 = 1.22042(\mathcal{Z}_1^2\mathcal{Z}_2^2\mathcal{A}T_6^2)^{1/3}\ \text{keV}\ . \tag{8.30}$$

Given $S(E)$, the integral in equation (8.28) may be evaluated numerically as a function of T. However, an approximate (and for many purposes adequate) expression for $\langle\sigma v\rangle$ may be obtained by neglecting the variation of $S(E)$ over the Gamow peak,[6] and approximating the function $\exp(-E/k_{\rm B}T - bE^{-1/2})$ by a Gaussian,

$$\exp\left(-\frac{3E_0}{k_{\rm B}T}\right)\exp\left[-\left(\frac{E-E_0}{\Delta/2}\right)^2\right]\ , \tag{8.31}$$

where the width is determined as $\Delta = 4(E_0k_{\rm B}T/3)^{1/2}$, by requiring that the approximation have the same curvature at the maximum as the Gamow peak. The result (after some algebra, which is described in more detail by Clayton 1968), is that

$$\langle\sigma v\rangle = 4\left(\frac{2}{3m}\right)^{1/2}\frac{S(E_0)}{(k_{\rm B}T)^{3/2}}(E_0k_{\rm B}T)^{1/2}\exp\left(-\frac{3E_0}{k_{\rm B}T}\right)\ . \tag{8.32}$$

[6] More accurate expressions can be obtained by including additional terms in a Taylor expansion of $S(E)$ around E_0.

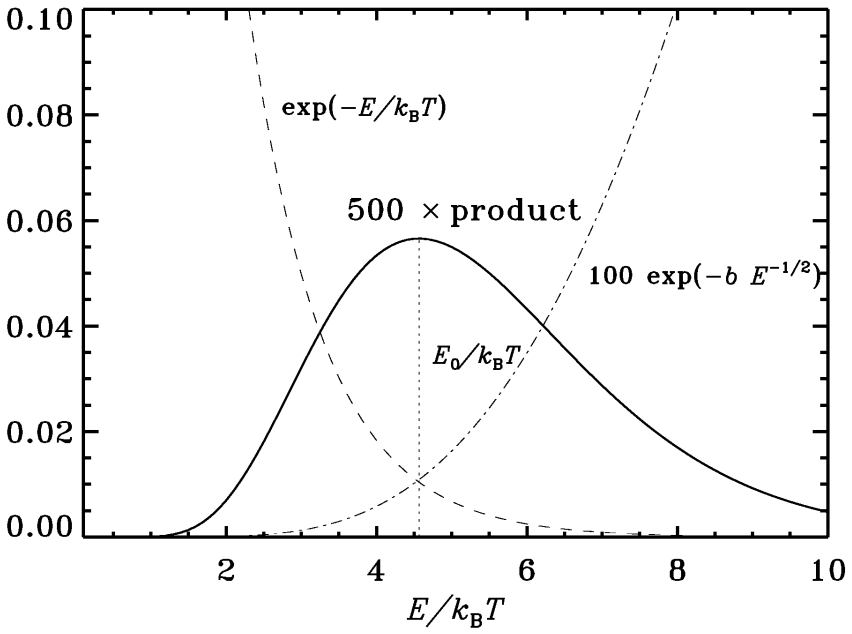

Figure 8.5: The dominant energy-dependent factors in a thermonuclear reaction, evaluated for the reaction $^1\mathrm{H} + {}^1\mathrm{H}$ at 15×10^6 K. Most of the reactions occur in the high-energy tail of the Maxwellian energy distribution, which introduces the rapidly falling factor $\exp(-E/k_\mathrm{B}T)$. Penetration through the Coulomb barrier introduces the factor $\exp(-bE^{-1/2})$, which vanishes strongly at low energy. Their product is a fairly sharp peak near an energy designated by E_0, which is generally substantially higher than $k_\mathrm{B}T$. This peak is commonly known as the *Gamow peak*.

The factor $(E_0 k_\mathrm{B}T)^{1/2}$ essentially comes from the width of the Gaussian, whereas the factor $\exp(-3E_0/k_\mathrm{B}T)$ clearly gives the maximum value of the Gamow peak. We introduce

$$\eta = \frac{3E_0}{k_\mathrm{B}T} = BT_6^{-1/3} \ , \tag{8.33}$$

where the last equality follows from equation (8.29); by using equation (8.12), the constant B may be written as

$$B = 42.487(\mathcal{Z}_1^2 \mathcal{Z}_2^2 \mathcal{A})^{1/3} \ . \tag{8.34}$$

(Values of B for the reactions involved in hydrogen burning are given in Table 8.1.) Then equation (8.32) finally yields

$$\langle \sigma v \rangle = \frac{8\sqrt{2}}{9\sqrt{3}} \frac{S(E_0)}{\sqrt{mb}} \eta^2 \exp(-\eta) \ . \tag{8.35}$$

This determines the temperature dependence of the average reaction rate.

From equations (8.33) and (8.34) it follows that the reactions typically occur at fairly large values of η, where $\langle \sigma v \rangle$ is a decreasing function of η; hence the reaction rate decreases with increasing $\mathcal{Z}_1 \mathcal{Z}_2$, as was also discussed in connection with equation (8.12). Furthermore, for fixed $\mathcal{Z}_1 \mathcal{Z}_2$ the reaction rate decreases with increasing $\mathcal{A}$, due to the decrease

in the speed of the nuclei at fixed energy. Equation (8.33) also provides a measure of the energy E_0 which dominates the reactions. Specifically, E_0 in units of the average thermal energy is obtained as

$$\frac{E_0}{{}^3\!/_2\, k_{\rm B}T} = \frac{2}{9}\eta = \frac{2}{9}BT_6^{-1/3} \ . \tag{8.36}$$

At the temperature of the solar core, $T = 15 \times 10^6\,{\rm K}$, we find

$$\frac{E_0}{{}^3\!/_2\, k_{\rm B}T} = 3.8(\mathcal{Z}_1^2\mathcal{Z}_2^2\mathcal{A})^{1/3} \ . \tag{8.37}$$

This confirms that the reactions occur quite far out in the tail of the Maxwellian distribution.

Although greatly simplified compared with the original expression (8.28), equation (8.35) is nevertheless sufficiently complicated that it is difficult to visualize the variation of $\langle\sigma v\rangle$ with T. A further simplification may be obtained by approximating $\langle\sigma v\rangle$ over a limited range in T around $T = T_0$, by

$$\langle\sigma v\rangle \simeq \langle\sigma v\rangle_0 \left(\frac{T}{T_0}\right)^n \ , \tag{8.38}$$

where $\langle\sigma v\rangle_0$ is the value of $\langle\sigma v\rangle$ at $T = T_0$ and

$$n = \frac{{\rm d}\ln\langle\sigma v\rangle}{{\rm d}\ln T} = \frac{{\rm d}\ln\langle\sigma v\rangle}{{\rm d}\ln\eta}\frac{{\rm d}\ln\eta}{{\rm d}\ln T} = \frac{\eta - 2}{3} \ , \tag{8.39}$$

evaluated at $T = T_0$. From equation (8.33) it follows that $\eta \propto T^{-1/3}$, so that n depends quite weakly on T_0; hence we expect that equation (8.38) is reasonably accurate over a substantial range in T. Also, equation (8.34) shows that $\eta \propto (\mathcal{Z}_1\mathcal{Z}_2)^{2/3}$; thus the temperature sensitivity of the reactions increases quite strongly with increasing nuclear charge.

We may now write the reaction rate r_{aA} in equation (8.23), using the approximation (8.38), as

$$r_{aA} = \langle\sigma v\rangle_0 n_a n_A \left(\frac{T}{T_0}\right)^n \ . \tag{8.40}$$

It is convenient to express the number densities in terms of the abundances X_A and X_a by mass, by using, for example,

$$n_A = \frac{X_A\rho}{\mathcal{A}_A m_{\rm u}} \ ; \tag{8.41}$$

then we finally obtain

$$r_{aA} = \langle\sigma v\rangle_0 \frac{X_a X_A}{\mathcal{A}_A\mathcal{A}_a m_{\rm u}^2}\rho^2 \left(\frac{T}{T_0}\right)^n \ . \tag{8.42}$$

This corresponds to the contribution

$$\epsilon_{aA} = Q_{aA}\langle\sigma v\rangle_0 \frac{X_a X_A}{\mathcal{A}_A\mathcal{A}_a m_{\rm u}^2}\rho \left(\frac{T}{T_0}\right)^n \tag{8.43}$$

to the energy generation rate ϵ per unit mass, where Q_{aA} is the energy released per reaction, as determined in section 8.3. Also, the rate of change in X_A *due to reactions with nuclei of type* a, is given by

$$\frac{{\rm d}X_A}{{\rm d}t} = -\langle\sigma v\rangle_0 \frac{X_a X_A}{\mathcal{A}_a m_{\rm u}}\rho \left(\frac{T}{T_0}\right)^n \equiv -\frac{X_A}{\tau_{aA}} \ , \tag{8.44}$$

where we introduced the characteristic time τ_{aA}. Note that in reactions between identical nuclei we must introduce the correction factor $1/2$ in equations (8.42) and (8.43), corresponding to equation (8.25), but not in equation (8.44).

The total energy generation rate is obviously the sum over all possible reactions of equation (8.43). Similarly, to evaluate the total rate of change of the abundance of a given element, we must take into account both the reactions that destroy and the reactions that create the element. Thus the computation of ϵ and the evolution of the chemical composition requires careful consideration of the possible reaction network. Examples of this are considered in the following sections.

8.5 Hydrogen burning

During most of their life stars derive their energy from the fusion of hydrogen into helium. This reaction may be written schematically as

$$4\,{}^1\mathrm{H} \rightarrow {}^4\mathrm{He} + 2\mathrm{e}^+ + 2\nu_\mathrm{e}\ . \tag{8.45}$$

As discussed in section 1.2 (see also section 8.3) the release of the two positrons is required to maintain charge balance, and results from the conversion of two protons into neutrons. Due to the requirement of lepton number conservation, the emission of two anti-leptons (the positrons) must be balanced by the emission of two leptons, the two electron neutrinos.

It is obvious that the reaction does not take place as indicated in equation (8.45): the probability that four protons come together and react at one point is entirely negligible. Instead the reaction may proceed through a number of different paths, discussed in more detail below. Regardless of these details we can determine the total amount of energy liberated in the reaction (8.45) from equation (8.16), using the data in Appendix B. The result is

$$Q_\mathrm{tot} = 26.73\,\mathrm{MeV} \qquad \text{for hydrogen burning}\ . \tag{8.46}$$

However, as discussed in section 8.3 the neutrinos escape directly from the star, without interacting with the matter in it, and hence do not contribute to the energy release within the star. Hence to compute the effective energy Q_eff released per ^{4}He that is formed, and hence the energy generation rate ϵ, we must subtract the neutrino energy. This depends on the detailed reactions in which the neutrinos are produced. Also, it is evident that to compute the reaction rate, and hence the energy generation rate, we need to consider the actual reactions which take place.

Given Q_eff, the rate of change in the hydrogen abundance is related to ϵ by

$$\frac{\mathrm{d}X}{\mathrm{d}t} = r_X = -4\mathcal{A}_\mathrm{H} m_\mathrm{u} \frac{\epsilon}{Q_\mathrm{eff}}\ , \tag{8.47}$$

where $\mathcal{A}_\mathrm{H}$ is the atomic weight of hydrogen. If we introduce the mass-averaged hydrogen abundance $\overline{X}$ by

$$\overline{X} = \frac{1}{M}\int_0^M X\,\mathrm{d}m\ , \tag{8.48}$$

we also find that

$$\frac{\mathrm{d}\overline{X}}{\mathrm{d}t} = -\frac{1}{M}\int_0^M 4\mathcal{A}_\mathrm{H} m_\mathrm{u} \frac{\epsilon}{Q_\mathrm{eff}}\mathrm{d}m = -\frac{4\mathcal{A}_\mathrm{H} m_\mathrm{u}}{\overline{Q}_\mathrm{eff}}\frac{L_\mathrm{s}}{M}\ , \tag{8.49}$$

where $\overline{Q}_{\rm eff}$ is a suitable average over the star of $Q_{\rm eff}$.

In principle, all possible reactions between the constituents of the gas must be considered, to determine which reactions dominate. The outcome is that there are two basically different ways (each with some variations) in which the overall reaction (8.45) may be accomplished: one (the PP-chains) which directly involves fusion of protons, the second (the CNO-cycle) in which the fusion occurs through a sequence of reactions involving C, N and O, which effectively act as catalysts.

Exercise 8.4:

Estimate the total number of neutrinos generated in the Sun per second, and the flux of solar neutrinos on the Earth (*i.e.*, the number of neutrinos per unit area and per unit time).
Assume that the cross section for reaction between a neutrino and a nucleus is $10^{-46}\,{\rm cm}^2$. Estimate the total number of neutrino reactions per year in the body of a typical student.

8.5.1 The PP-chains

The basic sequence of reactions may be written as[7]

$$^1{\rm H}(^1{\rm H},{\rm e}^+\nu_{\rm e})\,^2{\rm D}(^1{\rm H},\gamma)\,^3{\rm He}(^3{\rm He},2\,^1{\rm H})\,^4{\rm He}\;. \tag{8.50}$$

This sequence of reactions is known as the *PP-I chain*. Note that the production of one ^{4}He nucleus uses two ^{3}He nuclei, and hence requires that the first two reactions in the chain take place twice. It follows that the net reaction is in fact (8.45).

Exercise 8.5:

Verify this.

The average neutrino loss in each of the $^1{\rm H}(^1{\rm H},{\rm e}^+\nu_{\rm e})\,^2{\rm D}$ reactions is $0.263\,{\rm MeV}$. Hence the effective Q-value for the PP-I chain is

$$Q_{\rm eff}({\rm PP\text{-}I}) = 26.21\,{\rm MeV}\;. \tag{8.51}$$

Despite having the lowest possible Coulomb barrier the first reaction in the chain is by far the slowest. The reason is that this reaction involves the conversion of a proton into a neutron through the effect of the weak interaction; this leads to an extremely small cross-section factor (*cf.* Table 8.1). The remaining reactions are *in equilibrium*, in the sense that the abundances of ^{2}D and ^{3}He adjust themselves so that equal amounts of ^{2}D and ^{3}He

[7]Here the notation of equation (8.2) is used; note that this illustrates an important advantage of that notation: it is possible to string together several reactions.

are produced and destroyed. Hence the combined rate of energy generation is controlled by the $^1\mathrm{H}(^1\mathrm{H}, \mathrm{e}^+\nu_\mathrm{e})\,^2\mathrm{D}$ reaction. According to equation (8.43) we may approximate it as

$$\epsilon(\text{PP-I}) = \epsilon_0^{(\text{PP}-\text{I})} X^2 \rho T^n \ , \tag{8.52}$$

where $\epsilon_0^{(\text{PP}-\text{I})}$ is a constant.

Exercise 8.6:

Verify equation (8.52). Show that at a temperature $T = 15 \times 10^6\,\mathrm{K}$ the temperature exponent is $n \simeq 4$.

In addition to the reactions in (8.50) there are two additional chains which may produce ^{4}He, following the production of ^{3}He:

$$\begin{array}{ll} {}^3\mathrm{He}({}^4\mathrm{He}, \gamma)\,{}^7\mathrm{Be}(\mathrm{e}^-, \nu_\mathrm{e})\,{}^7\mathrm{Li}({}^1\mathrm{H}, {}^4\mathrm{He})\,{}^4\mathrm{He} & \text{(PP-II)} \\ \Downarrow & \\ {}^7\mathrm{Be}({}^1\mathrm{H}, \gamma)\,{}^8\mathrm{B}(, \mathrm{e}^+\nu_\mathrm{e})\,{}^8\mathrm{Be}(, {}^4\mathrm{He})\,{}^4\mathrm{He} & \text{(PP-III)} \end{array} \tag{8.53}$$

In the PP-II chain the neutrino is emitted in the electron capture in ^{7}Be; the average neutrino energy is 0.80 MeV, and hence the effective Q-value is

$$Q_\text{eff}(\text{PP-II}) = 25.67\,\mathrm{MeV} \ . \tag{8.54}$$

In the PP-III chain the neutrinos result from the positron decay of ^{8}B,[8] with average neutrino energy of 7.2 MeV, resulting in an effective Q-value of

$$Q_\text{eff}(\text{PP-III}) = 19.27\,\mathrm{MeV} \ . \tag{8.55}$$

Exercise 8.7:

Show that the reactions in the PP-II and PP-III chains are consistent with the net reaction in equation (8.45). Verify also the effective Q-values in equations (8.54) and (8.55).

The branching ratios between the different parts of the PP chains depend on the balance between the competing reactions, and hence on the temperature. Under the conditions in the solar core the PP-I chain dominates, and the PP-III chain makes a very small contribution to the energy generation. On the other hand, the PP-III chain is very important for attempts to detect solar neutrinos: due to their high energies the neutrinos from this chain dominate the measurements in the ^{37}Cl detector, and only the PP-III neutrinos can be seen by the detector based on neutrino scattering in water

[8] written as $^8\mathrm{B}(, \mathrm{e}^+\nu_\mathrm{e})\,^8\mathrm{Be}$, and hence stretching the notation in equation (8.2) a little; this reaction could also be written as $^8\mathrm{B}(\mathrm{e}^+\nu_\mathrm{e})\,^8\mathrm{Be}$, since it is obvious from charge conservation that the positron is emitted, rather than absorbed.

(*cf.* section 2.10.1). Since the electron capture in ^{7}Be depends weakly on temperature, the branching ratio between the PP-II and the PP-III chains, and hence the flux of PP-III neutrinos, in principle provides a very sensitive measurement of the temperature in the solar core. As discussed in Chapter 11, these measurements involve further complications related to the properties of the neutrino.

Exercise 8.8:

We consider the temperature sensitivity of the branching ratios amongst the PP-chains, expressed as exponents in power-law approximations similar to equation (8.42). The temperature is assumed to be 15×10^6 K, corresponding to conditions at the centre of the present Sun.

i) Find the temperature sensitivity of the equilibrium abundance of ^{3}He, assuming that most of the reactions go through the PP-I chain.

ii) Find the temperature sensitivity of the branching between the PP-I and the PP-II chains,

iii) Find the temperature sensitivity of the branching between the PP-II and PP-III chains, assuming that electron capture in ^{7}Be is temperature-independent.

iv) Assume that the total energy generation rate is dominated by the PP-I chain, as given in equation (8.52), and that the total amount of energy generated is held fixed. Estimate the sensitivity of the flux of PP-III neutrinos to the central temperature of the Sun, for temperatures near 15×10^6 K.

As for the PP-I chain, the subsequent reactions of the PP-II and PP-III chains may be assumed to be in equilibrium; hence the reaction rates in these chains are determined by the rate of production of ^{3}He, and therefore again by the $^1\mathrm{H}(^1\mathrm{H}, \mathrm{e}^+\nu_\mathrm{e})\,^2\mathrm{D}$ reaction. The combined energy generation rate $\epsilon(\mathrm{PP})$ from the PP chains depends on the branching between the different chains: for the PP-I chain it takes two $^1\mathrm{H}(^1\mathrm{H}, \mathrm{e}^+\nu_\mathrm{e})\,^2\mathrm{D}$ reactions to produce a ^{4}He, whereas for the PP-II and PP-III chains only one such reaction per ^{4}He is needed; on the other hand the neutrino loss is larger in the PP-II, and particularly in the PP-III, chain than in the PP-I chain. Similar considerations evidently arise in the computation of the rate of change r_X in the hydrogen abundance (*cf.* equation (8.1)). Nevertheless, as a first approximation these complications may be neglected; it then follows that $\epsilon(\mathrm{PP})$ may be determined as in equation (8.52), with the same exponent n, but with a different constant $\epsilon_0^{(\mathrm{PP})}$.

8.5.2 The CNO cycles

A second sequence of reactions is possible in stars that contain C, N, and O. This may be written as

$$^{12}\mathrm{C}(^1\mathrm{H}, \gamma)\,^{13}\mathrm{N}(\mathrm{e}^+\nu_\mathrm{e})\,^{13}\mathrm{C}(^1\mathrm{H}, \gamma)\,^{14}\mathrm{N}(^1\mathrm{H}, \gamma)\,^{15}\mathrm{O}(\mathrm{e}^+\nu_\mathrm{e})\,^{15}\mathrm{N}(^1\mathrm{H}, ^4\mathrm{He})\,^{12}\mathrm{C}\,. \tag{8.56}$$

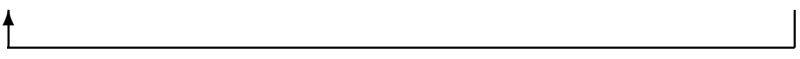

Thus the reactions proceed through a sequence of proton captures, interrupted by positron decay (with emission of neutrinos) to convert protons into neutrons; as indicated ^{12}C is produced at the end of the sequence of reactions, and hence acts as a catalyst. The total average neutrino loss in the cycle is 1.71 MeV, and hence the effective Q-value is

$$Q_{\rm eff}({\rm CNO}) = 25.02\,{\rm MeV}\ . \tag{8.57}$$

The $^{14}{\rm N}(^1{\rm H},\gamma)\,^{15}{\rm O}$ reaction has the smallest probability amongst the reactions in the cycle; hence, once the cycle operates in equilibrium this reaction determines the overall reaction rate. A second consequence is that in equilibrium almost all the original C and N is converted into ^{14}N.[9] As a result, the energy-generation rate for the CNO-cycle may be written as

$$\epsilon({\rm CNO}) = \epsilon_0^{({\rm CNO})} ZX\rho T^n\ , \tag{8.58}$$

where $\epsilon_0^{({\rm CNO})}$ is a constant, and we assumed that the total abundance of CNO elements is a fixed fraction of the total heavy-element abundance Z.

Exercise 8.9:

Verify equation (8.58). Show that at a temperature $T = 15 \times 10^6\,{\rm K}$ the temperature exponent is $n \simeq 20$.

From the results of exercise 8.6 and 8.9 it follows that the energy-generation rate from the CNO cycle is much more temperature-dependent than the energy-generation rate for the PP-chains. Hence the PP-chains dominate at relatively low temperature, whereas the CNO cycle dominates at relatively high temperature. From the estimate of stellar internal temperature in section 4.1.1 (*cf.* equation (4.11)) we therefore expect the CNO cycle to be important in massive stars. This is confirmed by more detailed calculations; as mentioned in section 6.3, and discussed in more detail in Chapter 11, this leads to the presence of a convective core in such stars, with significant effects for their evolution.

It turns out that the first reactions of the CNO cycle, *i.e.*, the reactions

$$^{12}{\rm C}(^1{\rm H},\gamma)\,^{13}{\rm N}({\rm e}^+\nu_{\rm e})\,^{13}{\rm C}(^1{\rm H},\gamma)\,^{14}{\rm N}\ , \tag{8.59}$$

have a comparatively high reaction rate, despite the substantial Coulomb barrier resulting from the charge of the carbon nuclei. Thus they set in at lower temperatures than even the proton-proton reaction. During the final stages of gravitational contraction, leading to the formation of a star, this causes a brief episode of nuclear reaction where the original ^{12}C

[9] Additional reactions involving C, N and O are

$$^{16}{\rm O}(^1{\rm H},\gamma)\,^{17}{\rm F}({\rm e}^+\nu_{\rm e})\,^{17}{\rm O}(^1{\rm H},{}^4{\rm He})\,^{14}{\rm N}\ ,$$

and

$$^{15}{\rm N}(^1{\rm H},\gamma)\,^{16}{\rm O}\ .$$

These give rise to a subsidiary cycle, whose main effect is to convert almost all the original ^{16}O into ^{14}N. Unlike the primary cycle in equation (8.56), however, this cycle reaches equilibrium only over a substantial fraction of a stellar lifetime; in the case of the Sun, for example, very little ^{16}O has been consumed up to the present time. In more massive stars the conversion of ^{16}O into ^{14}N causes a gradual increase in the efficiency of the CNO cycle.

is converted into ^{14}N, with some release of energy which slows the contraction. Once the ^{12}C has been consumed, the nuclear burning virtually stops, until the temperature gets so high that the reactions controlling primary hydrogen-burning, *viz.* $^{1}\mathrm{H}(^{1}\mathrm{H}, \mathrm{e}^{+}\nu_{\mathrm{e}})\,^{2}\mathrm{D}$ and $^{14}\mathrm{N}(^{1}\mathrm{H}, \gamma)\,^{15}\mathrm{O}$, set in.

8.6 Later reactions

After the exhaustion of hydrogen, the next reactions that may take place involve ^{4}He. Indeed, given that the $^{3}\mathrm{He} + {}^{4}\mathrm{He}$ reaction plays a role in the PP-chains (*cf.* equation (8.53)) one might have expected that the $^{4}\mathrm{He} + {}^{4}\mathrm{He}$ reaction could also have set in during hydrogen burning. That this is not the case is due to the fact that there are no stable nuclei with atomic weight eight.[10] Thus ^{4}He-burning has to take place through the so-called triple-alpha process:

$$3\,{}^{4}\mathrm{He} \rightarrow {}^{12}\mathrm{C} + \gamma\ . \tag{8.60}$$

In practice the probability that three ^{4}He should come together at precisely the same time is negligible, and hence the reaction actually occurs through the generation of ^{8}Be:

$$^{4}\mathrm{He}(^{4}\mathrm{He},)\,^{8}\mathrm{Be}(^{4}\mathrm{He}, \gamma)\,^{12}\mathrm{C}\ ; \tag{8.61}$$

but since ^{8}Be is unstable, the complete reaction requires that the third ^{4}He arrives within a very short time after the initial reaction. Thus the reaction is effectively a three-body process. At the typical temperatures where it takes place ($T = 1 - 2 \times 10^{8}\,\mathrm{K}$), the energy generation rate may be written as

$$\epsilon(3\alpha) = \epsilon_{0}^{(3\alpha)} Y^{3} \rho^{2} T^{30}\ . \tag{8.62}$$

Exercise 8.10:

Why is $\epsilon(3\alpha)$ proportional to ρ^{2} and Y^{3}, rather than to ρ as is, for example, ϵ(PP-I) as given in equation (8.52)?

The triple-alpha reaction is followed by successive α-captures:

$$\begin{array}{l} {}^{12}\mathrm{C} + {}^{4}\mathrm{He} \rightarrow {}^{16}\mathrm{O} \\ {}^{16}\mathrm{O} + {}^{4}\mathrm{He} \rightarrow {}^{20}\mathrm{Ne} \\ {}^{20}\mathrm{Ne} + {}^{4}\mathrm{He} \rightarrow {}^{24}\mathrm{Mg} \\ \quad \vdots \qquad\qquad ; \end{array} \tag{8.63}$$

in principle, this could continue to even more massive nuclei, although the total production of these nuclei during the helium-burning phase is probably relatively small. In addition, ^{14}N reacts to produce ^{22}Ne:

$$^{14}\mathrm{N}(^{4}\mathrm{He}, \mathrm{e}^{+}\nu_{\mathrm{e}})\,^{18}\mathrm{O}(^{4}\mathrm{He}, \gamma)\,^{22}\mathrm{Ne}\ . \tag{8.64}$$

[10] Formally ^{8}Be is formed in the PP-III chain but, as indicated in equation (8.54), it immediately decays into two ^{4}He nuclei.

When helium is exhausted, the next element to react is ^{12}C; indeed the $^{12}\mathrm{C} + {}^{12}\mathrm{C}$ reaction has the lowest Coulomb barrier amongst the possible reactions in the gas at this point. This takes place at temperatures around $5 - 10 \times 10^8$ K. There is a whole range of possible end products of this reaction:

$$ {}^{12}\mathrm{C} + {}^{12}\mathrm{C} \rightarrow \begin{cases} {}^{24}\mathrm{Mg} + \gamma \ , \\ {}^{23}\mathrm{Mg} + n \ , \\ {}^{23}\mathrm{Na} + p \ , \\ {}^{20}\mathrm{Ne} + {}^{4}\mathrm{He} \ , \\ {}^{16}\mathrm{O} + 2\,{}^{4}\mathrm{He} \ . \end{cases} \tag{8.65} $$

Following the ^{12}C exhaustion, the next lowest Coulomb barrier is in the reaction between two ^{16}O, which occurs at temperatures exceeding 10^9 K:

$$ {}^{16}\mathrm{O} + {}^{16}\mathrm{O} \rightarrow \begin{cases} {}^{32}\mathrm{S} + \gamma \ , \\ {}^{31}\mathrm{P} + p \ , \\ {}^{31}\mathrm{S} + n \ , \\ {}^{28}\mathrm{Si} + {}^{4}\mathrm{He} \ , \\ {}^{24}\mathrm{Mg} + 2\,{}^{4}\mathrm{He} \ . \end{cases} \tag{8.66} $$

A detailed discussion of these reactions, as well as of the reactions involved in the helium burning, was given by Clayton (1968).

In fact, even before this point complications set in, leading to departures from the orderly sequence of fusion of ever heavier elements; this involves a totally different type of reaction, namely *photodisintegration and subsequent α capture*. The reason is that the temperature gets so high that a substantial fraction of the photons in the gas have energies in the MeV range; these may be absorbed in nuclei, causing them to break up, typically in an α decay. Thus, after the end of ^{12}C burning, at a temperature of $T \simeq 10^9$ K, photodisintegration of ^{20}Ne sets in:

$$ {}^{20}\mathrm{Ne} + \gamma \rightarrow {}^{16}\mathrm{O} + {}^{4}\mathrm{He} \ ; \tag{8.67} $$

the resulting ^{4}He is probably captured in the remaining ^{20}Ne, to form ^{24}Mg:

$$ {}^{20}\mathrm{Ne} + {}^{4}\mathrm{He} \rightarrow {}^{24}\mathrm{Mg} \ . \tag{8.68} $$

This process may be termed *Ne burning*; as indicated in Figure 1.3 it takes place before the oxygen burning reactions in equation (8.66).

Following oxygen burning, photodisintegration and α capture dominate entirely, as a result of the very high Coulomb barrier for nuclei heavier than oxygen. The ^{4}He so released are absorbed in other nuclei, leading to the gradual build-up of heavier nuclei; this may continue until the iron group of elements, where the binding energy per nucleon is largest. This process, which is somewhat loosely called Si burning, is discussed in more detail in Chapter 14.

Chapter 9

Numerical calculation of stellar structure and evolution

9.1 Introduction

The equations of stellar structure and evolution are far too complicated to permit analytical solution. There are a few, highly simplified exceptions (in Chapter 4 we considered the linear model, and polytropes of indices 0 and 1). In the general case, when solving the full set of equations with realistic physics, a numerical solution is unavoidable.

9.2 Equations and boundary conditions

One almost always considers the evolution of a star of a given mass. Hence it is convenient to rewrite the equations of stellar structure with the mass $m = m(r)$ as the dependent variable. This may be done by noting that for any quantity ϕ

$$\frac{\mathrm{d}\phi}{\mathrm{d}m} = \frac{\mathrm{d}\phi}{\mathrm{d}r}\frac{\mathrm{d}r}{\mathrm{d}m} = \frac{1}{4\pi\rho r^2}\frac{\mathrm{d}\phi}{\mathrm{d}r} \,, \tag{9.1}$$

by using equation (4.5).

By transforming equations (4.4), (5.27), (5.8) and (6.20) in this manner, and including equation (8.1) for the rate of change of X, we obtain the following set of equations:

$$\frac{\mathrm{d}r}{\mathrm{d}m} = \frac{1}{4\pi r^2\rho} \tag{9.2}$$

$$\frac{\mathrm{d}P}{\mathrm{d}m} = -\frac{Gm}{4\pi r^4} \tag{9.3}$$

$$\frac{\mathrm{d}L}{\mathrm{d}m} = \epsilon - \left[\frac{\mathrm{d}}{\mathrm{d}t}\left(\frac{u}{\rho}\right) - \frac{P}{\rho^2}\frac{\mathrm{d}\rho}{\mathrm{d}t}\right] \tag{9.4}$$

$$\frac{\mathrm{d}T}{\mathrm{d}m} = \begin{cases} -\dfrac{3\kappa}{4a\tilde{c}T^3}\dfrac{L}{16\pi^2 r^4} & \text{radiative energy transport} \\ \dfrac{\Gamma_2 - 1}{\Gamma_2}\dfrac{T}{P}\dfrac{\mathrm{d}P}{\mathrm{d}m} & \text{convective energy transport} \end{cases} \tag{9.5}$$

$$\frac{\mathrm{d}X}{\mathrm{d}t} = r_X \,. \tag{9.6}$$

Here r_X is the change per unit time in X as a result of the nuclear reactions, and the remaining quantities have their usual meaning. For simplicity we have included only an equation for the change in the hydrogen abundance; in reality there are equations corresponding to equation (9.6) for each of the elements which take part in the nuclear reactions.

The differential equations (9.2) – (9.6) are formulated in terms of the dependent variables $\{r, P, L, T, X\}$. Hence we must be able to express the right-hand sides of the equations in terms of these variables. To do so requires expressions for ρ, u, Γ_2, κ, ϵ and r_X, as functions of P, T and the chemical composition. As we have seen, these expressions are obtained from thermodynamics, atomic physics and nuclear physics.

The differential equations (9.2) – (9.6) must be supplemented by suitable boundary conditions. Obviously

$$\left.\begin{array}{c} r = 0 \\ L = 0 \end{array}\right\} \quad \text{for} \quad m = 0 \; . \tag{9.7}$$

We can choose the surface of the model as the point where $T = T_{\rm eff}$. Furthermore we can, for example, use the simple relation for the pressure given in equation (5.21). Then the surface boundary conditions are

$$\left.\begin{array}{c} L = 4\pi\sigma R^2 T^4 \\ P = \dfrac{(a+1)GM}{\kappa R^2} \end{array}\right\} \quad \text{for} \quad m = M \; . \tag{9.8}$$

Here as usual $R = r(M)$ is the surface radius of the star. Finally, we need an initial model. This can be obtained from more or less detailed studies of the early phases of stellar evolution, starting from the contraction of the original interstellar cloud. A simple alternative is to neglect the early history of the star, and assume that it is initially chemically homogeneous (*i.e.*, with the same chemical composition everywhere), and in thermal equilibrium, so that the terms in $\mathrm{d}/\mathrm{d}t$ in equation (9.4) can be neglected. Fortunately it turns out that the later evolution of the star is quite insensitive to the assumed initial conditions.

Advanced numerical techniques have been developed to solve these equations. Here we give a very simplified description of the numerical solution of differential equations. It illustrates the principal features of the solution methods, but is totally inadequate for a proper computation of stellar models. More detailed descriptions can be found in books on stellar evolution theory[1] or in works on numerical analysis.

9.3 Numerical solution of differential equations

We consider the very simple ordinary differential equation

$$\frac{\mathrm{d}y}{\mathrm{d}x} = f(x, y) \; . \tag{9.9}$$

As indicated we assume that the derivative is a function of both x and y. We also assume that the solution $y_0 = y(x_0)$ is known at an initial point $x = x_0$. Now consider a small

[1] See for example Clayton (1968) or Kippenhahn *et al.* (2012).

increment Δx in x, to the point $x_1 = x_0 + \Delta x$; we have approximately that

$$\frac{y(x_1) - y(x_0)}{\Delta x} \simeq f(x_0, y_0) \ , \tag{9.10}$$

and hence

$$y_1 \equiv y(x_1) \simeq y_0 + \Delta x f(x_0, y_0) \ . \tag{9.11}$$

Notice that the approximation gets increasingly accurate if Δx is reduced. More generally, if $x_i = x_{i-1} + \Delta x$ and $y_i = y(x_i)$, we have that

$$y_i \simeq y_{i-1} + \Delta x f(x_{i-1}, y_{i-1}) \ . \tag{9.12}$$

In this way we can calculate an approximate solution at all x. This method is the most primitive method for solving a differential equation, and it is rather inaccurate. However, the main principle of many solution methods is the same as the one discussed here: the derivative is approximated by a difference, yielding a set of difference equations which is solved to obtain the approximate solution to the original differential equation. A more accurate, but still fairly simple, method is an example of the so-called *predictor-corrector* techniques: given $y_{i-1} = y(x_{i-1})$ we first compute a "predicted" value $y_i^{(\mathrm{p})}$ for $y(x_i)$ as

$$y_i^{(\mathrm{p})} = y_{i-1} + \Delta x f(x_{i-1}, y_{i-1}) \ , \tag{9.13}$$

and then the corrected value as

$$y_i = y_{i-1} + \frac{1}{2}\Delta x [f(x_{i-1}, y_{i-1}) + f(x_i, y_i^{(\mathrm{p})})] \ . \tag{9.14}$$

For simplicity we have here considered the case with a single differential equation; but the methods can be immediately generalized to a system of equations.

Exercise 9.1:

Solution of the Lane-Emden equation. (Requires access to a computer, or a programmable pocket calculator).

Consider the Lane-Emden equation (equation (4.42))

$$\frac{\mathrm{d}}{\mathrm{d}\xi}\left(\xi^2 \frac{\mathrm{d}\theta}{\mathrm{d}\xi}\right) = -\xi^2 \theta^n \ .$$

It can be written as a system of two first-order differential equations by introducing

$$y = \theta \ ,$$
$$z = \xi^2 \frac{\mathrm{d}\theta}{\mathrm{d}\xi} \ .$$

Then we have the equations

$$\frac{\mathrm{d}y}{\mathrm{d}\xi} = \frac{z}{\xi^2} \ ,$$

$$\frac{\mathrm{d}z}{\mathrm{d}\xi} = -\xi^2 y^n \ .$$

The equation is a little unpleasant (singular) at $\xi = 0$, so vi start the integration at the point $\xi = \Delta\xi$. One can show that for small $\Delta\xi$

$$y(\Delta\xi) \simeq 1 - \frac{(\Delta\xi)^2}{6} \ ,$$

$$z(\Delta\xi) \simeq -\frac{(\Delta\xi)^3}{3} \ .$$

Find the numerical solution to these equations by means of equation (9.12), *e.g.* for a polytrope of index $n = 3$, and using different values for the step $\Delta\xi$. Compare the results with Tables 4.1 and 4.2. Possibly also try to use the method described by equations (9.13) and (9.14). Compare the convergence of the solution, with decreasing $\Delta\xi$, for the two methods.

9.4 Computation of stellar models

For a chemically homogeneous star in thermal equilibrium we can in principle integrate equations (9.2) – (9.5) by means of the techniques discussed above. Specifically, we wish to compute a model of given mass, and assuming that the chemical composition is known and is the same throughout the star. Then the differential equations are completely defined. A remaining problem, however, is that we do not know all the initial conditions. It is true that equations (9.7) provide the initial values for r and L, but to start the integration we also need the central values P_c and T_c of P and T. Similarly equations (9.8) only provide two relations amongst r, P, T and L at $m = M$, and this is insufficient to determine these quantities at the surface. The problem considered in section 9.3 was an *initial value problem*. In contrast, the equations and boundary conditions for stellar structure constitute a *boundary value problem*, where the solution has to satisfy conditions at both ends of the interval of integration. There are efficient techniques for solving such problems. Here we consider a very simple approach which cannot be used in practice, but which nevertheless illustrates the basic principles in some of the methods used for actual calculations.

If we had known P_c and T_c we could have integrated equations (9.2) – (9.5) from $m = 0$. Therefore we begin by "guessing" values for P_c and T_c, and integrate from $m = 0$ towards $m = M$. If the solution satisfies equation (9.8), we have obviously solved the problem; but in general that will not be the case. Therefore we have to guess new values for P_c and T_c to try to get a solution that is closer to satisfying the surface boundary conditions. In this way we can gradually work towards the correct solution.

The guesswork can be made more systematic by considering

$$\begin{aligned} F_1(P_\mathrm{c}, T_\mathrm{c}) &= L(M) - 4\pi\sigma R^2 T(M)^4 \ , \\ F_2(P_\mathrm{c}, T_\mathrm{c}) &= P(M) - \frac{(a+1)GM}{\kappa(M)R^2} \ . \end{aligned} \tag{9.15}$$

For each choice of (P_c, T_c) we obtain a value of F_1 and F_2, and they can therefore, as indicated, be regarded as functions of P_c and T_c. Hence the problem is reduced to finding a common zero for $F_1(P_c, T_c)$ and $F_2(P_c, T_c)$.

The determination of zeros is another very common numerical problem. It is most simply illustrated in one dimension. We consider the equation

$$f(x) = 0 \,, \tag{9.16}$$

where f is a known function of x. A simple, but not very efficient, method to find a zero x_0 is the *binary chop*: one starts by locating two values of x, x_1 and x_2, where f has different sign, *e.g.*

$$f(x_1) < 0 \,, \quad f(x_2) > 0 \,. \tag{9.17}$$

Letting $x_3 = \frac{1}{2}(x_1 + x_2)$ the next approximation to x_0 is obtained as

$$x_4 = \begin{cases} \frac{1}{2}(x_1 + x_3) & \text{if} \quad f(x_3) > 0 \,, \\ \frac{1}{2}(x_3 + x_2) & \text{if} \quad f(x_3) < 0 \,, \end{cases} \tag{9.18}$$

and so on. In this way one determines a sequence x_n which converges towards the solution.

Exercise 9.2:

Use this method to solve

$$\cos x = 0 \,.$$

Start for example with $x_1 = 0$, $x_2 = 3$.

In realistic computations the solution of equations (9.15) is carried out by means of more advanced methods; a description of them is beyond the scope of these notes, however.

9.5 The evolution with time

In section 9.4 we discussed the computation of a static model of a chemically homogeneous star. However, we must also follow the *changes in time* of the star. We assume that we have calculated a model at time t, so that $r(m,t)$, $P(m,t)$, $T(m,t)$, $L(m,t)$ and the chemical composition, specified by $X(m,t)$, are known. The goal is to calculate a model at a later time $t + \Delta t$. In particular this requires a determination of the chemical composition at the later time. This is found by approximating equation (9.6) in the same way as we approximated equation (9.9) by equation (9.10). Hence we obtain the approximation

$$X(m, t + \Delta t) \simeq X(m,t) + \Delta t \, r_X(m,t) \,. \tag{9.19}$$

Having determined $X(m, t + \Delta t)$ in this way, we can compute the new model by solving equations (9.2) – (9.5) as before. However, we still need to approximate the time derivatives in equation (9.4). This can be done, again as in equation (9.10), by *e.g.* setting

$$\frac{\mathrm{d}\rho}{\mathrm{d}t} \simeq \frac{\rho(m,t) - \rho(m, t - \Delta t)}{\Delta t} \,, \tag{9.20}$$

where we assume that we already know the solution at the time $t - \Delta t$.

We have here assumed a fixed step Δt in time, and similarly a fixed step Δm in mass between the meshpoints where the solution is calculated. In practice Δt must be chosen such that the changes in the model are reasonably small between one point in time and the next; this requires very short timesteps during the contraction towards the main sequence, or in late evolutionary stages, where the structure changes rapidly, whereas the timestep can be longer during main sequence evolution. Similarly one has to use a small Δm near the centre and surface of the model, where conditions within the star change rapidly with m, whereas a larger step can be used in the intermediate parts of the model. The determination of Δm and Δt must take into account the need for reasonable precision in the solution, without leading to an excessive computing time. Such complications make the development of a stellar evolution programme a major project; they also explain why existing standard packages for the solution of differential equations are rarely used: such packages do not adequately take into account the special features of this problem.

9.6 Concluding remarks

The description of numerical techniques in this chapter was intended to make plausible that the evolution of a star of a given mass can be followed numerically. The result of the calculation is that one obtains the variation in the stellar surface luminosity and effective temperature with time; this may be used to illustrate the evolution in a Hertzsprung-Russell diagram. Furthermore, the calculations yield tables of the variation of r, P, T, L and X as functions of m, at each of the time steps. The remainder of these notes describes results of such calculations and tries to explain their main features.

Chapter 10

Evolution before the main sequence

10.1 Introduction

Stars are formed out of interstellar gas clouds, which become unstable to gravitational collapse. During the collapse the cloud is heated up by the release of gravitational potential energy. When the temperature gets sufficiently high in the core of the star, nuclear burning starts, and the star settles down on the main sequence.

This brief sketch hides a mass of complex detail, which is far from understood (for discussions, see Boss 1985; Stahler 1991, 1994; Ray 2000). The initial collapse of the gas cloud is a hydrodynamical process, which depends critically on the initial motion in the cloud, particularly its rotation, on the possible presence of interstellar magnetic fields, and on the chemical evolution of the cloud and the energy loss through radiation. After the proto-star reaches hydrostatic equilibrium, the evolution still depends on possible mass loss or accretion of matter, on the rotation, which again would be strongly affected by mass loss or accretion, and on the energy transport in the star. Hence current models of the early stellar evolution are at best indicative of the processes that might be going on, and of the overall trends in the evolution.

Observationally, major recent developments have resulted from observations in the infrared from ground-based observatories and from satellites, including the infrared and submillimetre Herschel mission launched by the European Space Agency in 2009, at the time the largest space observatory. This was followed by the James Webb Space Telescope, a joint optical/infrared mission by NASA and ESA, launched Christmas Day 2021 and operational since the summer of 2022, which already (Summer 2023) has provided major breakthroughs throughout astrophysics, including the study of star formation. Also, given their cool nature, much of the radiation from star-forming clouds and early stars is emitted at radio wavelengths. Spectacular results have been obtained with the Atacama Large Millimeter/submillimetre Array (ALMA), an interferometer with a maximum separation of 16 km, operating in Chile. These observations, and the ongoing theoretical efforts, have greatly improved our understanding of this important phase of stellar evolution. This includes the fascinating issue of the formation of planetary systems, and the properties of such systems, and on the initial distribution of stars according to mass,[1] which is of great

[1] described by the so-called *initial mass function* (IMF)

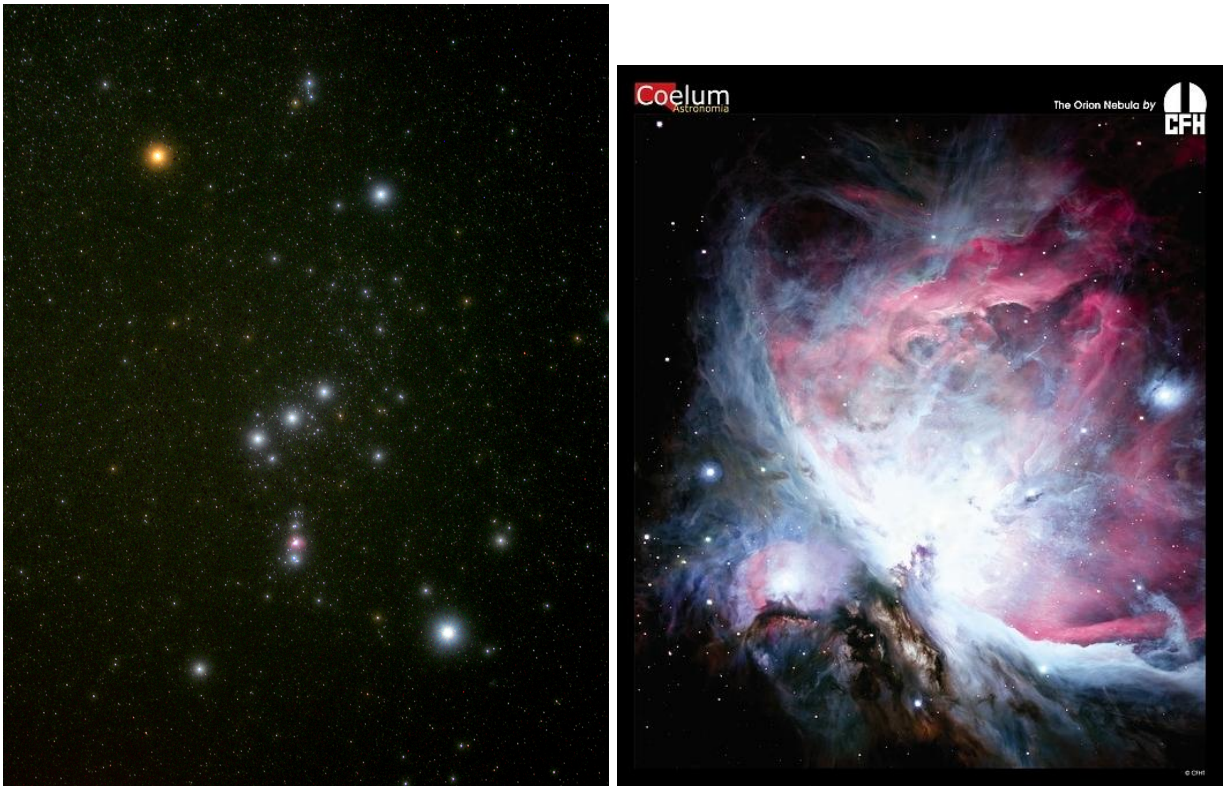

Figure 10.1: Left image: the constellation Orion, dominating the winter sky in the northern hemisphere. (Credit: John Gavreau.) The Orion nebula (right image) is in Orion's sword, below the three bright stars marking his belt. (Credit: Canada-France-Hawaii Telescope/Coelum.)

importance for studies of the evolution of the Galaxy.

Star formation is still taking place in the Milky Way Galaxy. Perhaps the most spectacular example of a star-forming region is the Orion Nebula (see Fig. 10.1) clearly visible (at least with binoculars) in Orion's sword.

Here we consider some simple aspects of the problem of star formation and early evolution, partly on the basis of numerical results. Here and in the subsequent chapters we largely base the discussion of numerical results on extensive calculations carried out by Icko Iben in the sixties. These were among the first comprehensive stellar evolution calculations, covering a variety of stellar masses and extending to quite late evolutionary stages. Although later calculations have improved on Iben's results, they have often not changed the conclusions in a qualitative way. Furthermore, Iben presented substantially more detail about the results than has been common since then; this is very useful for attempts to understand the behaviour of stars as they evolve. Reviews of the calculations were given by Iben (1967a, 1985, 1991). It might also be noted that Novotny (1973) gave detailed tables for several of the models computed by Iben.

10.2 The Jeans instability and the onset of star formation

An essential question is the condition for the gravitational instability which causes the initial collapse of the gas cloud. This can be treated in varying degrees of hydrodynamical detail. However, the main result can be obtained from a very simple argument.

We consider a gas cloud of mass M and typical size R. The density in the cloud is ρ, so that mass and size are related by

$$M \simeq \rho R^3 \ , \tag{10.1}$$

The gravitational potential in the cloud is GM/R. Hence the total energy of a hydrogen atom in the cloud is

$$E_{\rm tot} \simeq k_{\rm B}T - \frac{GMm_{\rm u}}{R} \ , \tag{10.2}$$

where the first term is the kinetic energy, and the second term is the gravitational potential energy. The condition that the cloud is gravitationally bound, and hence potentially unstable towards collapse, is that $E_{\rm tot} < 0$, or

$$GMm_{\rm u} > Rk_{\rm B}T \ . \tag{10.3}$$

Using equation (10.1), this may also be written

$$R > R_{\rm J} \equiv \left(\frac{\pi k_{\rm B}T}{G\rho m_{\rm u}}\right)^{1/2} \ , \tag{10.4}$$

where we introduced the *Jeans length* $R_{\rm J}$; in writing down equation (10.4) we included a factor π in the definition of $R_{\rm J}$ which comes out in more precise stability analysis. This condition may also be written as

$$M > M_{\rm J} = \frac{4}{3}\pi\rho R_{\rm J}^3 \simeq 5 \times 10^{-10} \left(\frac{T^3}{\rho}\right)^{1/2} {\rm M}_\odot \ , \tag{10.5}$$

where $M_{\rm J}$ is the *Jeans mass*. Typical values for the temperature and density in the relevant gas clouds are $T = 100\,{\rm K}$, $\rho = 10^{-22}\,{\rm g\,cm^{-3}}$; hence we obtain $M_{\rm J} \simeq 5 \times 10^4\,{\rm M}_\odot$.

It is obvious that this value is inconsistent with the upper bound on stellar masses which was discussed in Chapter 4, and it does not immediately explain the presence of a range of stellar masses. On the other hand, the estimate is reasonably consistent with the masses of open clusters of stars. Hence it is tempting to speculate that the initial gravitational instability leads to the collapse of a cloud of gas which eventually breaks up into the stars in a cluster. Indeed this breakup may be caused by several mechanisms. In the initial phases of the collapse the gas is so thin that radiation escapes immediately from the cloud. Consequently, the temperature of the cloud is roughly constant. It follows that the critical mass $M_{\rm J}$ decreases as the cloud contracts and the density increases. Thus as long as the cloud is roughly isothermal, it becomes unstable to gravitational collapse on smaller and smaller scales as it contracts. This may lead to the break-up into masses that are closer to stellar mass. An additional contribution to the break-up may come from rotational instability. If the cloud is isolated from its surroundings, its original angular momentum (which comes from the participation of the cloud in the rotation of the Galaxy) is conserved. Thus

$$\mathcal{L} \simeq MR^2\omega_{\rm rot} \ , \tag{10.6}$$

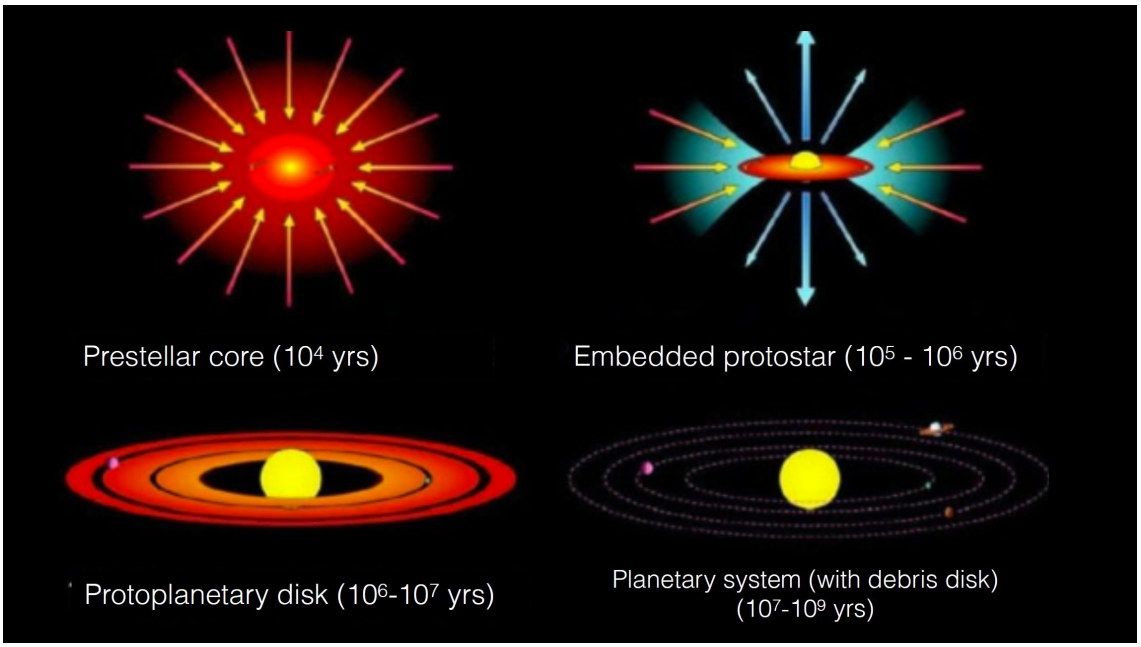

Figure 10.2: Schematic illustration of star formation and early evolution. Courtesy Nienke van der Marel.

where $\omega_{\rm rot}$ is the angular velocity of the cloud, is constant. It follows that $\omega_{\rm rot}$ increases rapidly as the cloud contracts. As a result, the ratio between the centrifugal acceleration $g_{\rm rot}$ and the gravitational acceleration, $g_{\rm grav}$,

$$\frac{g_{\rm rot}}{g_{\rm grav}} \simeq \frac{R\omega_{\rm rot}^2}{GM/R^2} \propto R^{-1} \, , \tag{10.7}$$

increases during the contraction, possibly to the point where the cloud becomes unstable to rotational breakup. This process may then repeat itself, again perhaps leading to the point where clouds of stellar mass are formed.[2]

10.3 Formation of a star and its planetary system

The early evolution of a star and its planetary system is schematically illustrated in Fig. 10.2.[3] The initial collapse of an interstellar cloud results in the formation of a core which subsequently accretes matter from the surrounding cloud; detailed simulations of these early phases of stellar evolution have been carried out by, for example, Baraffe *et al.* (2009). The angular momentum of the infalling material probably leads to the formation of a disk around the star while processes likely involving magnetic fields often result in outflow from the proto-star in highly collimated jets along the rotation axis, giving rise to the so-called *Herbig–Haro objects* (e.g., Reipurth & Bally, 2001).

It is likely that the early contraction, and the accretion of matter in the disk, leads to an initial rapid rotation of the star. In fact, it is observed that young stars generally

[2]one might speculate that the last step in such a sequence of rotational break-ups could result in the formation of a close binary star.

[3]This section is adapted from Christensen-Dalsgaard (2021), Section 3.7.

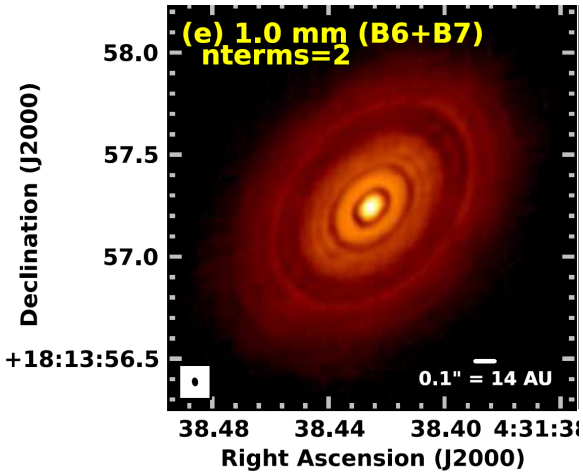

Figure 10.3: ALMA observations, at a wavelength of 1 mm, of the planet-forming disk around the young star HL Tau. The lower-left inset shows the resolution. Adapted from ALMA Partnership (2015).

rotate much more rapidly than the present Sun. However, in young open clusters where the stars may be assumed to share the same age, substantial scatter in the rotation rates is found. This is a strong indication of the complex processes controlling the evolution of angular momentum in the initial phases of proto-stellar evolution, involving interactions between the star, the accreting disk and the outflows, likely of magnetic origin, including magnetic locking between the outer layers of the star and the inner parts of a truncated accretion disk.

Disks are commonly observed around protostars, confirming also this part of the description (e.g., Williams & Cieza, 2011). The ubiquitous presence of planetary systems around other stars (Winn & Fabrycky, 2015) strongly suggests that the formation of planets in such *protoplanetary disks* is a common phenomenon. This likely takes place through the formation and subsequent coalescence of dust grains into objects of increasing size, and finally the formation of a planetary system. Dramatic illustrations of these planet-forming processes have been obtained with the Atacama Large Millimeter/submillimeter Array (ALMA) high-resolution observations. An example is illustrated in Fig. 10.3; modelling has shown that the observed gaps are indeed consistent with the presence of newly formed planets. The planet-forming processes probably happen on a time scale comparable with, or shorter than, the gravitational contraction of the star. Thus the ages of meteorites as determined from radioactive dating likely provide good measures of the age of the Sun since it arrived on the main sequence.

10.4 Early stellar evolution

10.4.1 Reaching hydrostatic equilibrium

In the initial collapse, while the temperature is held roughly constant, the pressure does not increase sufficiently rapidly to balance the increasing gravitational force. Indeed, when

T is constant it follows from the ideal gas law that the force from the pressure gradient is

$$\left|\frac{\mathrm{d}P}{\mathrm{d}r}\right| \simeq \frac{P}{R} \propto \frac{\rho}{R} \simeq \frac{M}{R^4} \,, \tag{10.8}$$

while the gravitational force is

$$\frac{GM\rho}{R^2} \simeq \frac{GM^2}{R^5} \,, \tag{10.9}$$

which clearly increases more rapidly with decreasing R than does the force from pressure.[4] However, when the density becomes so high that the gas becomes opaque to radiation, the contraction changes to being effectively adiabatic. Then (once the gas is heated up sufficiently that it is dissociated into individual atoms) $P \propto \rho^{5/3}$, and instead of equation (10.8) we obtain

$$\left|\frac{\mathrm{d}P}{\mathrm{d}r}\right| \propto \frac{M^{5/3}}{R^6} \,, \tag{10.10}$$

which increases with decreasing R more rapidly than does the gravitational force. Although hardly compelling, this argument suggests that when the gas becomes approximately adiabatic, pressure may increase sufficiently to balance gravity, so that hydrostatic equilibrium can be achieved.

When the star is approximately in hydrostatic equilibrium, the virial theorem (*cf.* section 4.4) is satisfied. Assuming that the gas is non-relativistic, so that pressure and internal energy are related by equation (3.1), the total gravitational potential energy Ω, the total thermal energy $U_{\rm tot}$ and the total energy E of the star are then related by

$$E = \Omega + U_{\rm tot} = -U_{\rm tot} = \frac{1}{2}\Omega \tag{10.11}$$

(*cf.* equation [4.22]). Thus, as the star contracts half of the gravitational potential energy which is released is converted into thermal energy, hence in general increasing the temperature of the star. Also, the luminosity of the star is approximately related to the change in its radius by

$$L_G = -\frac{1}{2}\frac{\mathrm{d}\Omega}{\mathrm{d}t} \simeq -\frac{1}{2}\frac{GM^2}{R^2}\frac{\mathrm{d}R}{\mathrm{d}t} \tag{10.12}$$

(*cf.* equation [4.23]).

To obtain a more precise idea about the properties of the star, the estimate (4.8) of the internal pressure may be used; if the gas satisfies the ideal gas law, the temperature can then be estimated from equation (4.9):

$$T_{\rm c} = \frac{\mu_{\rm c} m_{\rm u} P_{\rm c}}{k_{\rm B}\rho_{\rm c}} \simeq \frac{G\mu_{\rm c} m_{\rm u} M}{k_{\rm B} R} \,. \tag{10.13}$$

Since the radius of the contracting star is still quite large, the temperature is low; it follows from section 5.3 (particularly the Kramers law [5.14]) that the opacity is high, and hence, according to equation (6.19), that there is a tendency for convective instability. Thus we would expect the star to evolve initially down the Hayashi track (*cf.* section 7.2.1), at almost constant effective temperature. This is confirmed by numerical calculations. Figure 10.4 shows Iben's results for pre-main-sequence evolution plotted in a $(\log T_{\rm eff}, \log L_{\rm s})$

[4] This argument should be compared with the estimate of stellar internal pressure in section 4.2.1.

diagram; the computed duration of the different evolutionary phases is given in Table 10.1. During the initial phases of the hydrostatic contraction the star is almost entirely convective, and lies close to the Hayashi track. An important consequence of the convective instability during the contraction is that the stars are mixed very efficiently; thus one normally assumes that stars are chemically homogeneous when the nuclear burning starts.

The gravitational energy released in the contraction of the protostar partly goes to heating it up and is partly released as radiation from the star; the radiation finally stops the accretion and blows away the surrounding material, such that the star becomes directly observable: the star has reached the so-called '*birthline*'.

More recent calculations have modified this simple description somewhat, particularly for stars above $2\,\mathrm{M}_\odot$. These have shown a fairly complex interaction between the contracting central part of the star and the surrounding cloud which continues to accrete onto the forming star. As a result, the stars emerge as well-defined and observable objects on the birthline only somewhat later in the formation process (*cf.* Fig. 10.5). This appears to be consistent with observations of star-forming regions. For lower-mass stars, including the early stages of solar evolution, the models still still show a considerable phase of evolution along the Hayashi track, however.

Recent detailed calculations of the material infall have led to doubts about this relatively simple description of the early evolution, in which the protostar is fully convective and hence follows the Hayashi line (Steindl *et al.*, 2022). However, the subsequent evolution of the star is largely insensitive to these details of the early evolution.

10.4.2 The minimum mass of a star

The subsequent evolution of the star depends crucially on whether or not the temperature in its core rises sufficiently for nuclear reactions to set in. It is evident that as long as equation (4.9) is valid, the temperature increases as the star contracts; the same conclusion follows from the virial theorem, since for an ideal gas the internal energy is proportional to temperature. However, it is not obvious that the gas remains ideal. It follows from equation (3.62) that the gas becomes degenerate if the ratio $\rho/T^{3/2}$ is too large. Assuming equation (10.1) for ρ and equation (4.9) for T, this ratio changes with R as $R^{-3/2}$; hence the star moves towards being degenerate as it contracts. Once the gas is degenerate, the increase in pressure caused by contraction no longer leads to an increase in temperature (since the pressure of a strongly degenerate gas only depends on density), and the temperature may never get high enough that nuclear burning is initiated.[5]

The condition for nuclear burning to start is that the temperature becomes sufficiently high *before* degeneracy sets in. To get a rough estimate of the limits on stellar parameters imposed by this condition, we assume that the central temperature is given by equation (4.9), that the central density is given by equation (10.1), and require that at the centre the pressure from degenerate electrons, given by equation (3.61), is less than the total ideal gas pressure:

$$\frac{1}{5}\left(\frac{3}{8\pi}\right)^{2/3}\frac{h^2}{m_\mathrm{e}m_\mathrm{u}^{5/3}}\left(\frac{\rho_\mathrm{c}}{\mu_\mathrm{e}}\right)^{5/3} < \frac{k_\mathrm{B}T_\mathrm{c}\rho_\mathrm{c}}{\mu m_\mathrm{u}}\ . \tag{10.14}$$

[5] Again the same conclusion is reached from the virial theorem: in a strongly degenerate (non-relativistic) gas the internal energy per unit volume is given by equation (3.57), and is independent of temperature; hence the increase in the thermal energy which accompanies the gravitational contraction does not lead to an increase in the temperature.

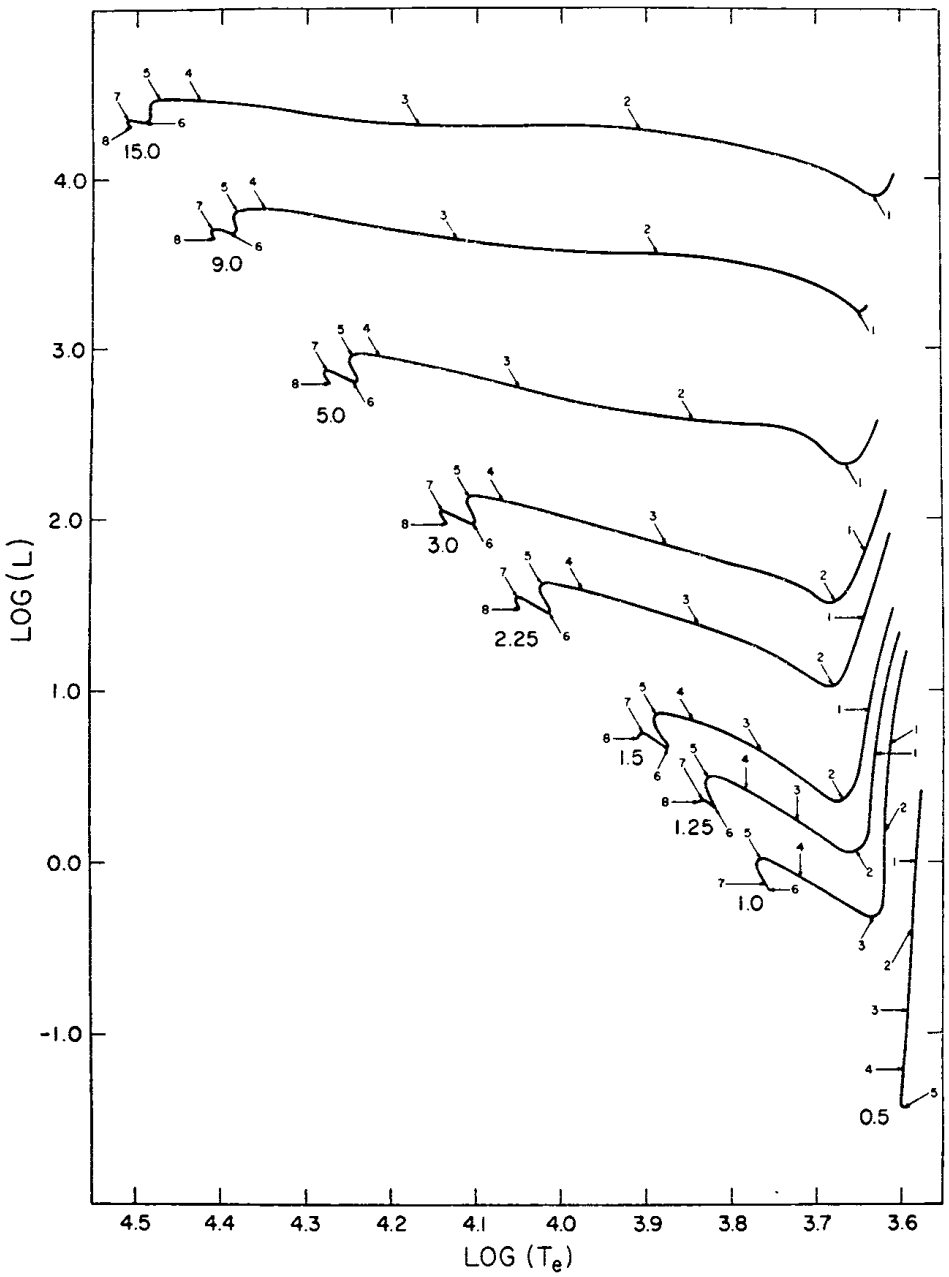

Figure 10.4: Evolutionary tracks in the Hertzsprung-Russell diagram for pre-main-sequence evolution of models of mass $M/\,\mathrm{M}_\odot = 0.5$, 1.0, 1.25, 1.5, 2.25, 3, 5, 9 and 15. The luminosity L_s is in units of $3.86 \times 10^{33}\,\mathrm{erg\,sec}^{-1}$, and T_e is the effective temperature in K. The composition of the models is $X = 0.708$, $Z = 0.02$. (From Iben 1965.)

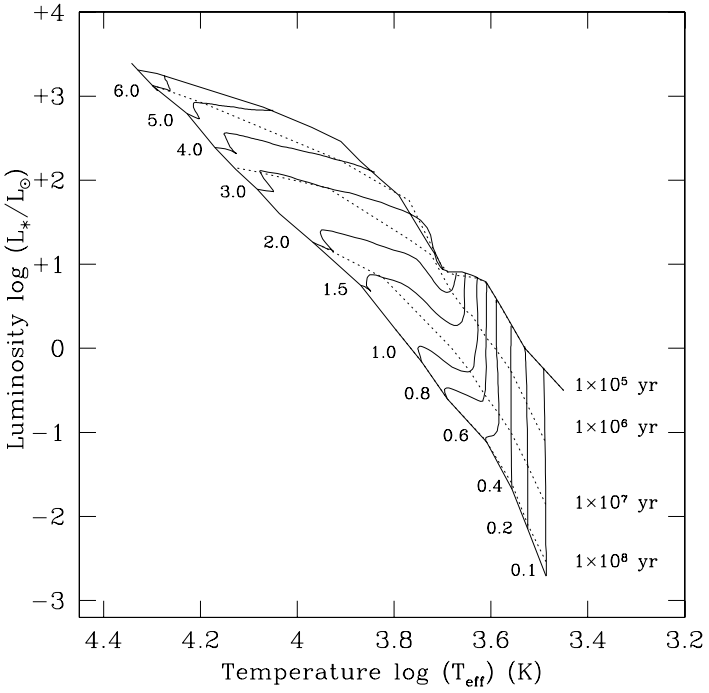

Figure 10.5: Theoretical pre-main-sequence evolution tracks, labelled by stellar mass in $M_\odot$. Selected isochrones are shown by the dotted lines, labelled by age. For each track, evolution starts at the birthline (upper solid line) and ends on the zero-age main sequence, which is also indicated. (From Palla & Stahler 1999.)

Table 10.1

Point	$(M/M_\odot)$								
	15.0	9.0	5.0	3.0	2.25	1.5	1.25	1.0	0.5
1.....	6.740×10^{2}	1.443×10^{3}	2.936×10^{4}	3.420×10^{4}	7.862×10^{4}	2.347×10^{5}	4.508×10^{5}	1.189×10^{8}	3.195×10^{8}
2.....	3.766×10^{3}	1.473×10^{4}	1.069×10^{5}	2.078×10^{5}	5.940×10^{5}	2.363×10^{6}	3.957×10^{6}	1.058×10^{6}	1.786×10^{6}
3.....	9.350×10^{3}	3.645×10^{4}	2.001×10^{5}	7.633×10^{5}	1.883×10^{6}	5.801×10^{6}	8.800×10^{6}	8.910×10^{6}	8.711×10^{6}
4.....	2.203×10^{4}	6.987×10^{4}	2.860×10^{5}	1.135×10^{6}	2.505×10^{6}	7.584×10^{6}	1.155×10^{7}	1.821×10^{7}	3.092×10^{7}
5.....	2.657×10^{4}	7.922×10^{4}	3.137×10^{4}	1.250×10^{6}	2.818×10^{6}	8.620×10^{6}	1.404×10^{7}	2.529×10^{7}	1.550×10^{8}
6.....	3.984×10^{4}	1.019×10^{5}	3.880×10^{5}	1.465×10^{6}	3.319×10^{6}	1.043×10^{7}	1.755×10^{7}	3.418×10^{7}	.....
7.....	4.585×10^{4}	1.195×10^{5}	4.559×10^{5}	1.741×10^{6}	3.993×10^{6}	1.339×10^{7}	2.796×10^{7}	5.016×10^{7}	.....
8.....	6.170×10^{4}	1.505×10^{5}	5.759×10^{5}	2.514×10^{6}	5.855×10^{6}	1.821×10^{7}	2.954×10^{7}	.....	.....

Evolutionary lifetimes (in years) for the models shown in Figure 10.4. The table lists the time required for the model to reach the various points indicated in the figure, from the start of the calculation (which roughly corresponds to the time where the model gets into hydrostatic equilibrium). (From Iben 1965.)

As argued above, the left-hand side of this inequality increases more rapidly during the contraction than does the right-hand side. The condition for start of nuclear burning is that the condition is still satisfied when the temperature reaches the value $T_{\rm ig}$ required for ignition of the hydrogen burning. Hence it is convenient to describe the contraction in terms of the central temperature. In fact, R may be written in terms of $T_{\rm c}$ by means of equation (4.9). When substituted into equation (10.1) this leads to a relation for $\rho_{\rm c}$ in terms of $T_{\rm c}$:

$$\rho_{\rm c} \simeq \left(\frac{k_{\rm B}T_{\rm c}}{G\mu m_{\rm u}}\right)^3 M^{-2} \; . \tag{10.15}$$

Hence equation (10.14) may be written

$$\frac{1}{5}\left(\frac{3}{8\pi}\right)^{2/3} \frac{h^2}{m_{\rm e}(\mu_{\rm e}m_{\rm u})^{5/3}} M^{-4/3} \left(\frac{k_{\rm B}T_{\rm c}}{G\mu m_{\rm u}}\right)^2 < \frac{k_{\rm B}T_{\rm c}}{\mu m_{\rm u}} \; . \tag{10.16}$$

This condition may be rearranged, to yield

$$\mu_{\rm e}^{5/4}\mu^{3/4}\frac{M}{\rm M_\odot} > \left[\frac{3}{8\pi}\frac{h^3(k_{\rm B}T_{\rm c})^{3/2}}{m_{\rm u}^4(5m_{\rm e})^{3/2}G^3\,{\rm M_\odot^2}}\right]^{1/2} \simeq 5\times10^{-3}T_{\rm c,6}^{3/4} \; , \tag{10.17}$$

where, as usual, $T_{\rm c,6} = T_{\rm c}/(10^6\,{\rm K})$.

This relation was derived under the assumption that the temperature was given by the ideal gas law. If during contraction T *exceeds* the limit given in equation (10.17), degeneracy sets in, and the temperature no longer increases. The equation therefore provides an estimate of the *maximum* temperature that can be reached before matter becomes degenerate. Conversely it defines the *minimum* mass of a star that can reach a given temperature before becoming degenerate. If the ignition temperature $T_{\rm ig}$ for a given nuclear reaction is used, we obtain the minimum mass of a star where this process can occur. To ignite hydrogen burning, a temperature of a few million degrees is required; hence it follows from equation (10.17) that hydrogen burning will never set in if the mass of the proto-star is less than of order $0.01\,{\rm M_\odot}$.

The derivation leading to equation (10.17) is obviously extremely rough. In particular, equation (10.1) provides a substantial underestimate of the central density, leading to an underestimate of the critical mass in equation (10.17). Also, one must take into account that as the star contracts there is a gradual transition from the ideal gas law to degenerate electrons being dominant. As discussed in exercise 10.1, these effects may be treated approximately, to obtain a more realistic estimate of the minimum mass.

Exercise 10.1:

As a (fairly rough) approximation to the equation of state of a partially degenerate gas we assume that the pressure may be obtained as the sum of the ideal gas contribution and the contribution from degenerate electrons:

$$P = \frac{k_{\rm B}T\rho}{\mu m_{\rm u}} + \frac{1}{5}\left(\frac{3}{8\pi}\right)^{2/3}\frac{h^2}{m_{\rm e}m_{\rm u}^{5/3}}\left(\frac{\rho}{\mu_{\rm e}}\right)^{5/3} \; . \tag{10.18}$$

Furthermore, we assume that the star is on the Hayashi track, so that its structure is that of a polytrope of index $n = 3/2$.

Determine the central temperature T_c as a function of M and R. Show that T_c has a maximum as a function of R, and determine the maximal value of T_c.
Use the results to show that equation (10.17) for the minimal mass corresponding to a given ignition temperature should be replaced by

$$\mu_\mathrm{e}^{5/4}\mu^{3/4}\frac{M}{\mathrm{M}_\odot} > \left[\frac{3}{\pi}\frac{h^3(k_\mathrm{B}T_\mathrm{c})^{3/2}Q_{3/2}^4}{m_\mathrm{u}^4(5W_{3/2}^2 m_\mathrm{e})^{3/2}\,G^3\,\mathrm{M}_\odot^2}\right]^{1/2} \simeq 0.039T_{\mathrm{c},6}^{3/4}\ . \tag{10.19}$$

Here W_n (with $n = 3/2$ in the present case) was defined in equations (4.52) and (4.53), and we have introduced Q_n such that

$$\rho_\mathrm{c} = Q_n\frac{M}{R^3} \qquad i.e., \qquad Q_n = \frac{3}{4\pi}\frac{\rho_\mathrm{c}}{\overline{\rho}}\ ; \tag{10.20}$$

W_n and $\rho_\mathrm{c}/\overline{\rho}$ are tabulated in Table 4.1. For a chemical composition $X = 0.7$, $Z = 0.02$, and assuming that ignition of hydrogen burning requires a temperature in excess of 2×10^6 K, equation (10.19) shows that the minimum mass for hydrogen burning is about $0.09\,\mathrm{M}_\odot$.

Detailed calculations of low-mass stellar evolution (see, for example, D'Antona & Mazzitelli 1985) generally confirm the results of this exercise. In particular, *the physical principle* determining the minimum mass, *viz.* the onset of degeneracy with increasing contraction, is broadly speaking the same as was used to obtain the estimate. One finds that for a given mass the central temperature has a maximum as a function of R. The condition for ignition is then that this maximum temperature is sufficiently high. This leads to a condition with the same functional form, and a similar numerical value, as equation (10.19). The results show that the minimum mass where a star can burn hydrogen in thermal equilibrium (*i.e.*, without a substantial part of the energy being supplied by contraction) is about 0.08 $\mathrm{M}_\odot$, in excellent agreement with the estimate obtained here.

Objects with even lower masses may radiate for a substantial length of time due to the release of gravitational energy caused by contraction.[6] Thus calculations show that a "star" with a mass of 0.04 $\mathrm{M}_\odot$ can maintain an effective temperature higher than 1000 K for about 2×10^9 years in this way. Such objects are known as *brown dwarfs*. They are extremely faint and therefore difficult to detect. Even so, since 1995 a substantial number have been observed; there is evidence (Mužić *et al.*, 2017) that their number density is comparable to that of 'normal' stars in the Galaxy. A brief overview of the properties of brown dwarfs was given by Basri (2000a); a detailed review of the then current observational situation was provided by Basri (2000b), Burrows *et al.* (2001) discussed models of brown dwarfs, while Jayawardhana (2004) gave a brief discussion of their formation.

Ongoing systematic surveys of the sky are likely over the next few years to provide further insight into the number and properties of the brown dwarfs.

[6] Some additional energy is provided by fusion of the original deuterium ($^2\mathrm{D}(^1\mathrm{H},\gamma)\,^3\mathrm{He}$), which can take place at lower temperature than the full PP-I chain.

10.5 The approach to the main sequence

From Figure 10.4 it is evident that the $0.5\,\mathrm{M}_\odot$ star continues on the Hayashi track down to the point where it is established on the main sequence. In fact, stars of such low masses have very extensive outer convection zones, even during the hydrogen burning phase. At somewhat higher mass, the star eventually departs from the Hayashi track and evolves towards higher effective temperature. The reason for this is fairly obvious: as the temperature increases in the core of the star, the opacity decreases, and a point is finally reached where the core becomes stable towards convection. When the radiative core grows sufficiently, the luminosity is predominantly determined by the condition that it can be carried by radiation in the interior of the star; hence it is approximately given by the mass–effective-temperature–luminosity relations for radiative stars, *i.e.*,

$$L_\mathrm{s} \propto T_\mathrm{eff}^{0.8} M^{4.4} \qquad \text{for low mass ,} \tag{10.21}$$

and

$$L_\mathrm{s} \propto M^3 \qquad \text{for high mass} \tag{10.22}$$

(*cf.* section 7.1). It follows that as the star contracts, its effective temperature increases, leading either to an increase, or an approximately constant value, of the luminosity, depending on whether equation (10.21) or equation (10.22) is the better approximation. This takes place along the so-called *Henyey line* (Henyey *et al.* 1955).

Exercise 10.2:

Verify the preceding statements.

The transition to predominantly radiative transport is illustrated in more detail in Figure 10.6, which shows the time dependence of a number of quantities during the contraction of a $1\,\mathrm{M}_\odot$ star. To fit these rather different variables onto a single figure, they have been scaled so as to have unit range. The actual ranges of the variables are given in the figure caption.[7] During the Hayashi-track part of the contraction, the effective temperature is essentially constant; so is $\rho_\mathrm{c}/\overline{\rho}$, corresponding to the value for an $n = 3/2$ polytrope. However, once the mass fraction $Q_{RC} = m_{RC}/M$, where m_{RC} is the mass contained in the radiative core, exceeds about 0.8, the star starts to depart from the Hayashi track, the effective temperature and $\rho_\mathrm{c}/\overline{\rho}$ increase rapidly, and the luminosity increases somewhat.

The contraction is stopped when hydrogen burning begins. This is marked in the evolution tracks in Figure 10.4 by a *drop* in luminosity, apparently a somewhat paradoxical result! In fact, in most stars the initial nuclear reactions are those involved in the burning of ^{12}C to ^{14}N (*cf.* equation [8.59]). Because of the high temperature sensitivity of these reactions, the energy transport in the core has to take place by convection. The addition of nuclear energy in the core causes the core to cool and expand, essentially corresponding to the effects of the virial theorem. This is visible in the ratio $\rho_\mathrm{c}/\overline{\rho}$ in Figure 10.6. The energy required to overcome the gravitational potential energy during the core expansion

[7] Several other diagrams of this nature are shown in Chapter 12. They are collectively known as *Iben diagrams*, and take a little effort to get used to.

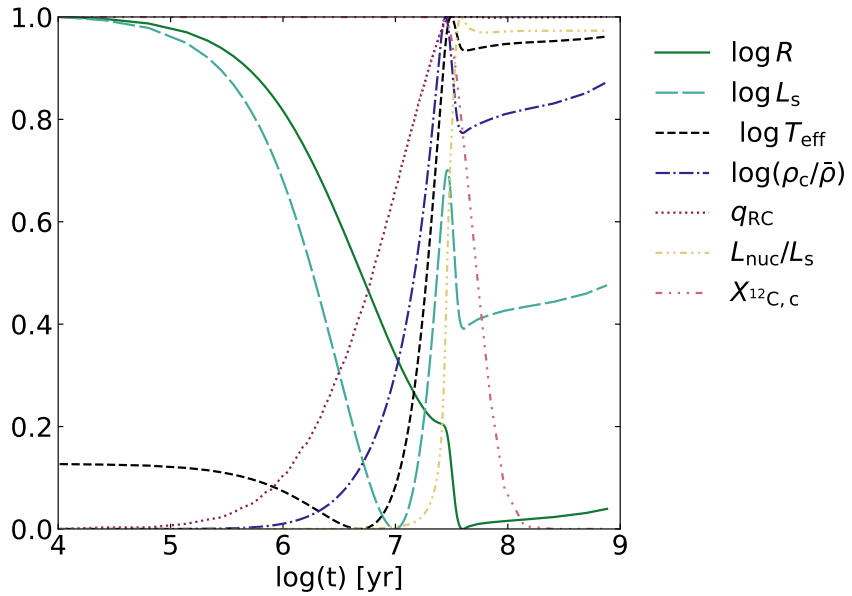

Figure 10.6: The variation with time t (in years) of important quantities during the contraction of a $1\,\mathrm{M}_\odot$ star towards the main sequence. The figure illustrates the effective temperature $T_{\rm eff}$ (in units of K), luminosity $L_{\rm s}$ (in units of $3.86 \times 10^{33}\,\mathrm{erg\,sec}^{-1}$), stellar radius R (in units of $6.96 \times 10^{10}\,\mathrm{cm}$), central over mean density $\rho_{\rm c}/\overline{\rho}$, mass fraction $q_{\rm RC}$ in the radiative interior, total energy generation $L_{\rm nuc}$ in units of $L_{\rm s}$ and the central ^{12}C abundance $X_{^{12}\mathrm{C,c}}$. The variables have been scaled to fit within the range $[0, 1]$. This corresponds to the following ranges: $-0.06 \leq \log R \leq 0.29$ [$\mathrm{R}_\odot$], $-0.35 \leq \log L_{\rm s} \leq 0.14$ [$\mathrm{L}_\odot$], $3.63 \leq \log T_{\rm eff} \leq 3.76$ [K], $0.79 \leq \log(\rho_{\rm c}/\bar{\rho}) \leq 1.79$, $0.00 \leq q_{\rm RC} \leq 0.97$, $0.00 \leq L_{\rm nuc}/L_{\rm s} \leq 1.03$ and $1.4 \times 10^{-5} \leq X_{^{12}\mathrm{C,c}} \leq 3.2 \times 10^{-3}$. Results from a MESA calculation (*e.g.*, Paxton *et al.*, 2019) by Johannes Holm Jørgensen. (Inspired by Iben 1965.)

causes the drop in luminosity, despite the continuing contraction of the outer parts of the star and the energy released by the nuclear reactions.

In the $1\,\mathrm{M}_\odot$ star, equilibrium nuclear burning is established during the burning of ^{12}C, and the star settles down on the main sequence at the end of the drop in luminosity. For masses greater than $1.5\,\mathrm{M}_\odot$, however, nuclear burning essentially stops once the ^{12}C has been consumed. The star then resumes gravitational contraction, increasing its effective temperature, luminosity and core temperature, until it reaches the point where the principal reactions in the hydrogen burning become effective. At that point there is another expansion of the core, and hence of the rest of the star, with a consequent drop in luminosity; and the star finally reaches equilibrium on the main sequence.

Generally speaking the contraction must occur on the Kelvin-Helmholz time scale defined in equation (1.5),

$$t_{\rm KH} = \frac{GM^2}{RL_{\rm s}}\,, \tag{10.23}$$

since the star derives its luminosity from the release of gravitational energy. As the luminosity increases strongly with increasing mass (*cf.* Figure 10.4), the contraction is much

faster for high-mass stars than for low-mass stars. This is in agreement with the computed duration of the various phases of the pre-main-sequence contraction as shown in Table 10.1; it is obvious that the speed of evolution does indeed depend strongly on the stellar mass. Furthermore, the time scale for a $1\,M_\odot$ star is obviously roughly consistent with equation (1.6). In particular, the pre-main-sequence phase is quite brief compared with the main-sequence phase, which for a $1\,M_\odot$ star lasts of order 10^{10} years (see Chapter 11).

Exercise 10.3:

Attempt to make a more quantitative comparison between equation (10.23) and the values given in Table 10.1, using also the information available in Figure 10.4.

Chapter 11

The main sequence

11.1 Introduction

Apart from very late stages of evolution stars spend most of their life burning hydrogen on the main sequence.[1] Hence it is of considerable interest to understand the properties of main-sequence stars, and to describe the changes that occur as a result of hydrogen burning. A main-sequence star of somewhat special interest is the Sun: this is partly motivated by our desire to understand an object of such importance to our daily life; a more interesting consideration is that changes in the properties of the Sun over its life may have had an effect on conditions on Earth (changes in the Sun as it evolves towards the red giant stage, in approximately 7×10^9 years, will certainly have dramatic effects). From the point of view of astrophysics, the proximity of the Sun, and hence our ability to observe it in very great detail, makes it extremely important as a test of stellar evolution theory. For these reasons we return to the Sun towards the end of this chapter, after considering more general properties of main-sequence stars.

11.2 The zero-age main sequence

The zero-age main sequence (or *ZAMS*) may be defined, somewhat loosely, as the location of stars that have just settled down to hydrogen burning.[2]. Figures 11.1 – 11.3 illustrate the relation between mass, luminosity, radius and effective temperature for such stars, comparing the numerical results with observed properties of binary stars (*cf.* section 2.7). The most striking feature is the rapid increase in luminosity with stellar mass, as was also predicted by the mass-luminosity relations in section 7.1. Indeed, as indicated in the figure, these relations show some similarity with the computed behaviour; in particular there is a tendency towards a steepening of the slope for masses below solar.[3] In contrast, the radius increases only roughly proportionally with M. Hence the effective temperature also increases substantially with increasing mass, as shown in Figure 11.1.

[1] Properly speaking *the hydrogen main sequence*. One sometimes talks about other "main sequences", particularly for helium burning; *cf.* Chapter 12.

[2] Computationally, such models may approximately be obtained by solving numerically the equations of stellar structure (9.2) – (9.6), without the time-derivative terms in equation (9.4), for a homogeneous composition.

[3] At even lower masses, this trend is reversed; here, however, the stars have very extensive outer convection zones, and the applicability of the radiative mass-luminosity relation is certainly questionable.

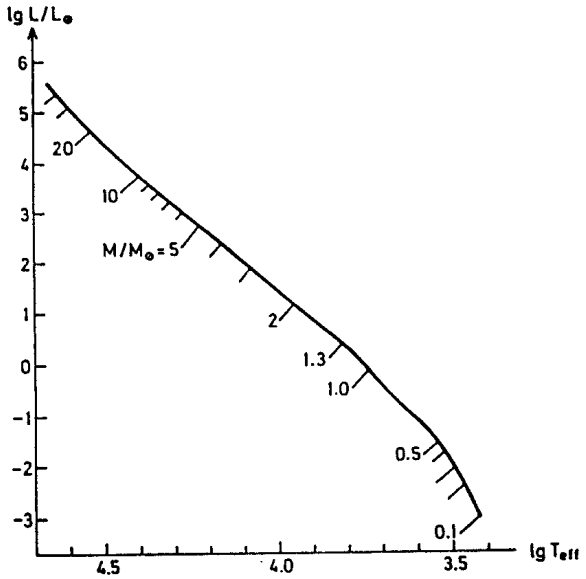

Figure 11.1: Hertzsprung-Russell diagram of the zero-age main sequence computed for the composition $X = 0.685$, $Y = 0.294$. The location of several models with masses between 0.1 and 22 $M_\odot$ are indicated below the sequence (From Kippenhahn & Weigert, 1990.)

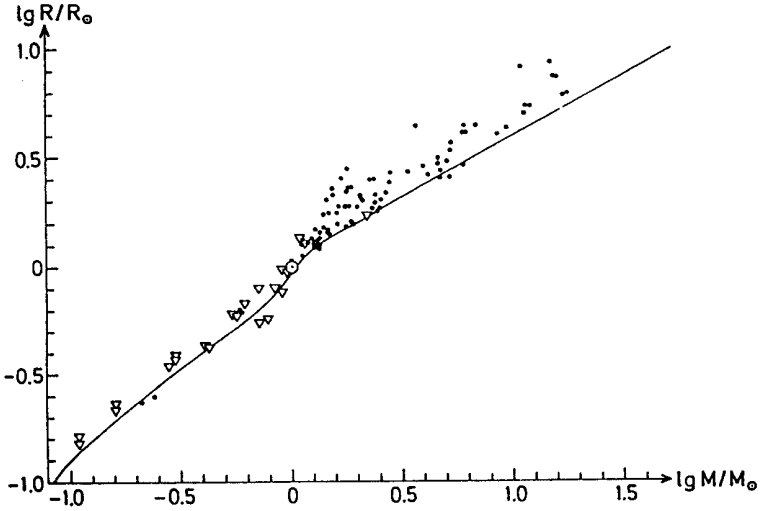

Figure 11.2: The line shows the mass-radius relation for the zero-age main sequence plotted in Figure 11.1. For comparison measured properties of binary stars are indicated by the symbols (triangles for visual, and dots for detached eclipsing, systems), and '$\odot$' shows the properties of the Sun. (From Kippenhahn & Weigert, 1990.)

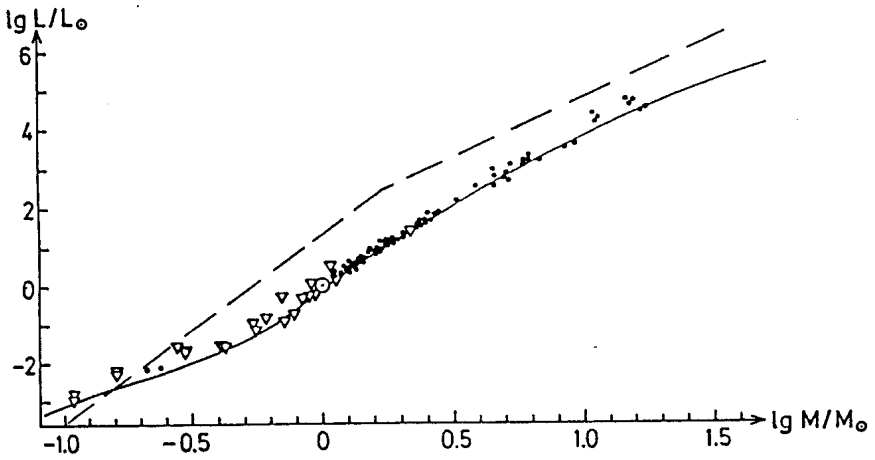

Figure 11.3: The continuous line gives the mass-luminosity relation for the zero-age main-sequence models shown in Figure 11.1. The symbols show measured properties of binary stars (see caption to Fig. 11.2). For comparison, the dashed lines indicate the simple mass-luminosity relations (7.7) (assuming that $R \propto M$) and (7.8) derived in Chapter 7. (Adapted from Kippenhahn & Weigert, 1990.)

Figure 11.4 gives an indication of the interior structure of main-sequence stars. Each value of the abscissa corresponds to a given total mass of the star; a vertical slice through the diagram at that point describes the interior structure for that star. The "cloudy" areas show the location of convection zones in the models; in addition, the masses corresponding to $0.25R$ and $0.5R$, and to $0.5L_{\rm s}$ and $0.9L_{\rm s}$, are shown by means of continuous and dashed curves, respectively. (For example, in the star with $\log M/\,{\rm M}_\odot = -0.4$, there is a convective envelope extending over approximately the outer 30 per cent of the mass; half of the total luminosity is generated within the inner 10 per cent of the mass, corresponding to a quarter of the radius). As discussed in Chapter 6, in low-mass stars there are extensive outer convective envelopes, which in this calculation grow to encompass the entire star at a mass of about $0.25\,{\rm M}_\odot$. Stars of masses larger than the solar mass have convective cores, the extent of which grow rapidly with increasing mass. The reason is the increasing importance of the CNO cycle in the energy generation: because of the resulting high temperature sensitivity of the energy generation rate the energy production gets highly concentrated towards the centre (as is also evident from the $0.5L_{\rm s}$ and $0.9L_{\rm s}$ curves), and this leads to convective instability [*cf.* equation (6.19)].

11.3 Evolution during core hydrogen burning

11.3.1 The evolution in the HR diagram

Evolution tracks, from Iben's calculations, for the evolution after the ZAMS are shown in Figure 11.5. The duration of the different phases of evolution, as indicated by the numbered points on the tracks, is given in Table 11.1. Here we concentrate on the initial parts of the tracks, roughly between points 1 and 2, which correspond to the phase of hydrogen burning in the core.

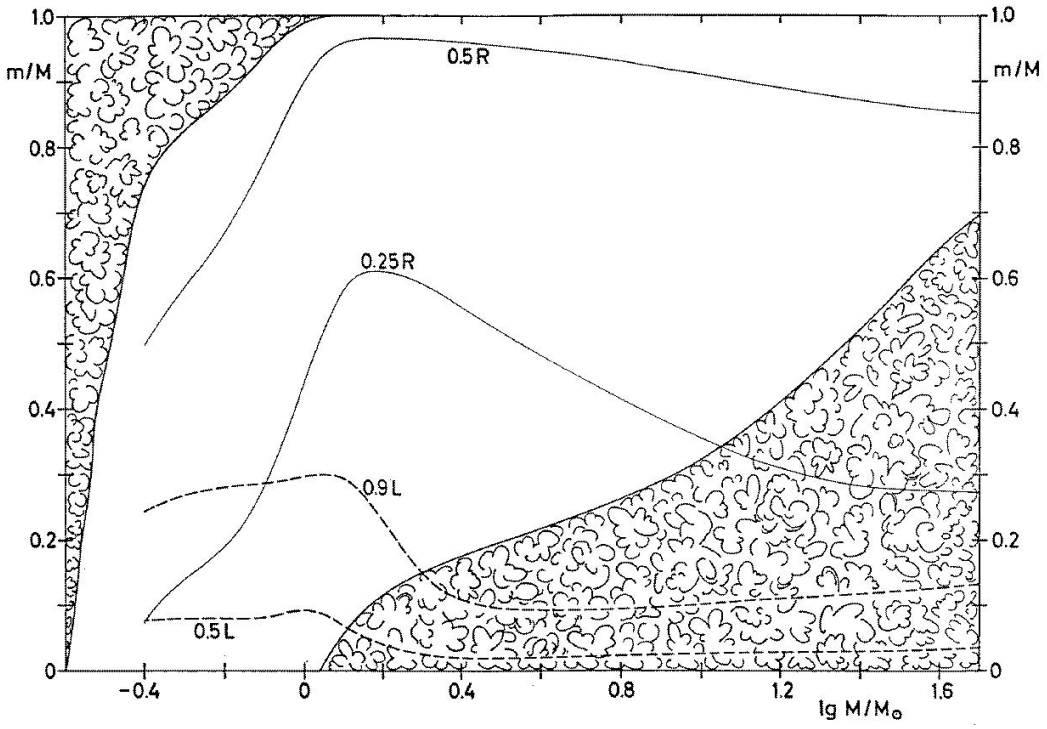

Figure 11.4: The mass values m from centre to surface are plotted against the stellar mass M for the zero-age main-sequence models which were shown in Figures 11.1 – 11.3. "Cloudy" areas indicate the extent of the convection zones inside the models. Two solid lines give the mass values at which r is $1/4$ and $1/2$ of the total radius R. The dashed lines show the mass values inside which 50 per cent and 90 per cent of the total luminosity L_s are produced. (From Kippenhahn *et al.*, 2012.)

A general tendency at all masses is that the luminosity increases during the central hydrogen burning. This may be understood in terms of the changes that take place in the core of the star. As hydrogen is converted into helium, the hydrogen abundance X decreases; hence, according to equation (3.27)[4] the mean molecular weight μ increases. Since the pressure has to be sufficient to balance the weight of the overlying material and hence cannot decrease, it follows from the ideal gas law, equation (3.24), that ρT must increase to compensate for the increase in μ. In fact, the core contracts, thus increasing ρ. The contraction releases gravitational potential energy which, according to the virial theorem, goes partly towards increasing the internal energy of the gas; as a result the temperature increases. This tends to increase the nuclear energy generation rate, as does the increase in density; furthermore, the increase in temperature increases the radiative flux of energy, partly through the resulting reduction in opacity [*cf.* equations (5.6) and (5.14)]. The result is that the luminosity of the star increases.

The steep increase in luminosity with increasing mean molecular weight was in fact already predicted in equations (7.7) and (7.8). There it followed exclusively from the changes in the radiative energy transport. In fact, there must be a balance between the

[4]or common sense: helium is heavier than hydrogen.

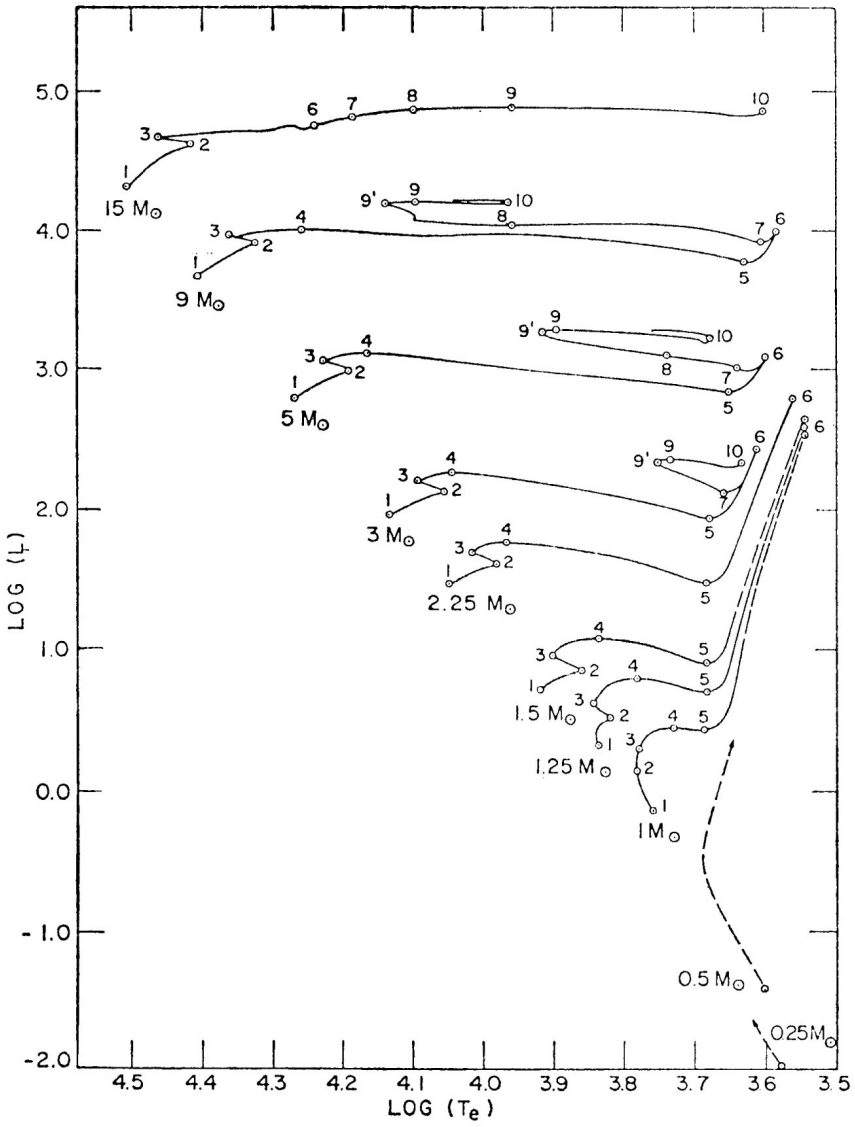

Figure 11.5: Evolutionary tracks in the Hertzsprung-Russell diagram for the evolution following the main sequence. The unit of luminosity $L_{\rm s}$ is $3.86 \times 10^{33}\,{\rm erg\,sec^{-1}}$, and the effective temperature $T_{\rm e}$ is in K. The models were computed with the composition $X = 0.708$, $Z = 0.02$. Tracks are shown for models of mass $M/\,{\rm M}_\odot = 0.5$, 1.0, 1.25, 1.5, 2.25, 3, 5, 9 and 15. Dashed portions of the evolutionary tracks are estimates. (From Iben 1967a.)

Table 11.1

Mass ($M_\odot$) \ Interval (i–j)	(1–2)	(2–3)	(3–4)	(4–5)	(5–6)
15	1.010 (7)	2.270 (5)		7.55 (4)	
9	2.144 (7)	6.053 (5)	9.113 (4)	1.477 (5)	6.552 (4)
5	6.547 (7)	2.173 (6)	1.372 (6)	7.532 (5)	4.857 (5)
3	2.212 (8)	1.042 (7)	1.033 (7)	4.505 (6)	4.238 (6)
2.25	4.802 (8)	1.647 (7)	3.696 (7)	1.310 (7)	3.829 (7)
1.5	1.553 (9)	8.10 (7)	3.490 (8)	1.049 (8)	≥2 (8)
1.25	2.803 (9)	1.824 (8)	1.045 (9)	1.463 (8)	≥4 (8)
1.0	7 (9)	2 (9)	1.20 (9)	1.57 (8)	≥1 (9)

Mass ($M_\odot$) \ Interval (i–j)	(6–7)	(7–8)	(8–9)	(9–10)
15	7.17 (5)	6.20 (5)	1.9 (5)	3.5 (4)
9	4.90 (5)	9.50 (4)	3.28 (6)	1.55 (5)
5	6.05 (6)	1.02 (6)	9.00 (6)	9.30 (5)
3	2.51 (7)	4.08 (7)		6.00 (6)

The duration (in years) of different phases in the evolutionary tracks illustrated in Figure 11.5. The numbers refer to the points indicated in that figure, and the entries give the duration of the corresponding interval. Numbers in parenthesis beside each entry give the power of ten with which that entry is to be multiplied. For example, the duration of the evolution from point 1 to point 2 for a $1\,M_\odot$ star is 7×10^9 years. (From Iben 1967a.)

energy production and the energy transport, which determines the equilibrium structure of the star; also, equations (7.7) and (7.8) essentially assumed a uniform chemical composition, whereas in fact the nuclear burning, and hence the change in μ, predominantly take place near the centre. Thus the dependence of luminosity on μ derived in section 7.1 cannot be used directly for an evolving star; however, the principles underlying the derivation in that section are rather similar to the discussion given above of the changes in the star as it evolves.

Exercise 11.1:

Review the derivation in section 7.1, and compare it with the discussion given here.

While the change in luminosity may be understood in fairly simple terms, as discussed above, the reasons for the variation in the other global properties of the star, *i.e.*, radius and effective temperature, are less obvious. In all cases the surface radius of the star expands as the star evolves, but at very different rates. For low masses the expansion is relatively modest; as a result the increase in luminosity leads to an increase in effective temperature [see equation (5.12)]. For higher mass, however, the expansion is more rapid,

and the effective temperature decreases. The trend that core contraction is associated with surface expansion may be an example of a more general principle, as discussed in Chapter 12. There is no doubt about the correctness of the numerical results; however, the behaviour is so regular that one might expect an underlying mechanism that is sufficiently simple to be understandable, at least qualitatively.

Currently, no generally accepted explanation exists. However, to my mind, the most reasonable suggestion has been given by Douglas Gough, in an unpublished set of lecture notes. It was argued above that the virial theorem predicts the core contraction to lead to heating of the core. This, however, is strictly speaking an incorrect application of the virial theorem to just the core. In fact we need to consider the changes in the entire star, and the result provides a measure of the change of the total thermal energy, and hence some average of the temperature, rather than the change in the core temperature. It seems likely that if the entire star were to contract as a result of the core contraction, the decrease in the gravitational potential energy, and hence the increase in the thermal energy, would be so large that the core temperature would increase too much; the result would be an increase in the energy generation rate beyond what could be transported out through the star. Hence the outer parts of the star have to expand, to compensate for the contraction of the core, and hence keep the increase in core temperature at an acceptable level. Some support for this idea comes from the difference between low- and high-mass stars: for high-mass stars the energy generation is dominated by the highly temperature-sensitive CNO cycle; hence the acceptable increase in core temperature is smaller than at low stellar mass, and the required expansion is consequently larger.

This is clearly not a very compelling argument,[5] but it does provide a possible explanation for the computed behaviour. Furthermore, the explanation might in principle be tested by analyzing the computed models in detail. In fact, surprisingly little work has been done towards trying to understand the results of stellar evolution calculations in this manner. This would appear to be an interesting line of research.

11.3.2 The changes in the hydrogen abundance

The details of the way in which hydrogen is used up during core hydrogen burning have substantial effect on the subsequent evolution of the star. Because of the temperature sensitivity of the nuclear reactions, hydrogen is consumed most rapidly at the centre. In a star with radiative energy transport in the core, it is normally assumed that there is no core mixing.[6] It follows that helium produced by hydrogen burning remains where it is created, and hence the hydrogen abundance decreases most rapidly at the centre. The result is a variation of the hydrogen abundance with time and with location in the star such as is illustrated in Figure 11.6. In evolved stars X increases gradually from the centre, and complete exhaustion of hydrogen first occurs precisely at the centre.

Massive stars have convective cores, which are mixed on a time scale very short compared with the evolutionary time scale (*cf.* section 6.4.3). Hence within the convective cores the chemical composition can be assumed to be uniform at all times. As a result, the

[5] I once attended a mathematics lecture in which an argument was described as being "not strong enough to hang a man". The present argument is barely sufficient for handing out a parking ticket.

[6] While not unreasonable, this assumption is not entirely obvious. It is possible that there are other sources of, possibly very slow, mixing, which could affect the composition of the cores of low-mass stars. On the other hand, there is no evidence for such mixing in the case of the Sun.

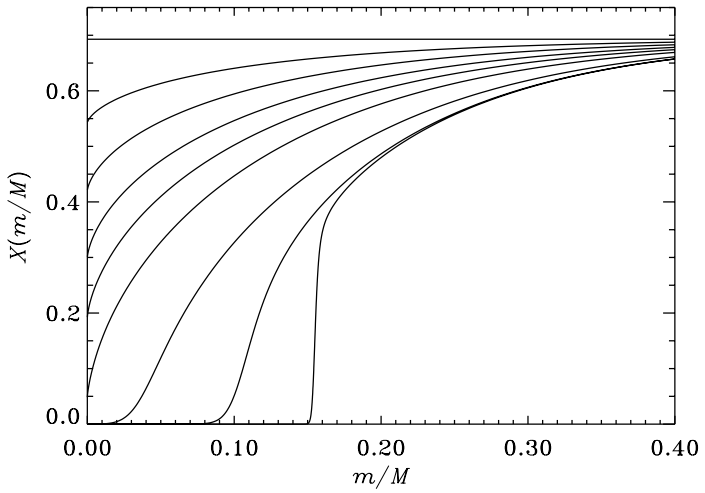

Figure 11.6: Hydrogen profiles showing the gradual exhaustion of hydrogen in a star of $1\,\mathrm{M}_\odot$. The homogeneous initial model consists of a mixture with a hydrogen abundance by mass of 0.699. X as a function of the mass fraction m/M is plotted for nine models which correspond to ages of 0, 2.0, 3.6, 5.0, 6.2, 7.5, 9.6, 11.0 and 11.6 times 10^9 years, after the onset of hydrogen burning. The model at 5.0×10^9 years corresponds roughly to the present Sun, whereas the last two models are in the *shell hydrogen burning phase*, which is discussed in Chapter 12.

fusion of hydrogen to helium, which still predominantly takes place near the centre where the temperature is highest, leads to a uniform reduction in the hydrogen abundance in the convective core. The computations also show that the extent of the core generally shrinks as the star evolves; the most important reason for this is the reduction in the opacity, which may be assumed to be dominated by electron scattering, with the reduction in the hydrogen abundance [*cf.* equation (5.15)]. The result is the evolution in the hydrogen profile which is illustrated in Figure 11.7.

Figure 11.4 shows that for masses exceeding about $3\,\mathrm{M}_\odot$ the convective core extends substantially beyond the region where the energy generation takes place. Hence, hydrogen is exhausted simultaneously throughout the nuclear-burning core. The consequences of this for the subsequent evolution of the star are discussed in Chapter 12.

11.3.3 The evolution time scale

The duration of the core hydrogen-burning phase is determined by the amount of hydrogen available for burning, and by the luminosity of the star. If q_c is the fraction of the stellar mass which takes part in the nuclear burning, and $\overline{Q}_\mathrm{eff}$ is the average amount of energy produced per generated helium atom, it follows from a relation similar to equation (8.49) that the duration of main-sequence phase may be estimated as

$$t_\mathrm{MS} \simeq \frac{q_\mathrm{c} X_0 \overline{Q}_\mathrm{eff}}{4 \mathcal{A}_\mathrm{H} m_\mathrm{u}} \frac{M}{L_\mathrm{s}} \,, \tag{11.1}$$

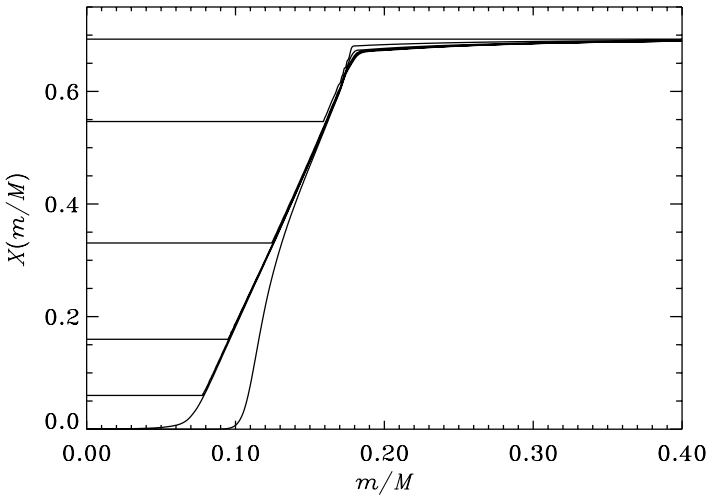

Figure 11.7: Hydrogen depletion in a $2.5\,M_\odot$ star with a shrinking convective core. The homogeneous initial model has $X = 0.699$. The lines show the hydrogen profiles for models of age 0, 1.5, 3.1, 4.0, 4.4, 4.6, and 4.8 times 10^8 years. Note that since hydrogen burning is negligible at the edge of the convective core during the main-sequence phase, the hydrogen profile established during this phase reflects the decrease in the extent of the core. In contrast, the last model is in the hydrogen shell-burning phase, the helium core having grown substantially beyond the smallest extent of the convective core.

where X_0 is the initial hydrogen abundance. Assuming that q_c and $\overline{Q}_{\rm eff}$ are roughly independent of stellar mass, and that the mass-luminosity relation can be represented as $L_s \propto M^\nu$, we obtain[7]

$$t_{\rm MS} \propto M^{-(\nu-1)} \; . \tag{11.2}$$

From the estimates given in section 7.1 the exponent ν is 3 – 5 (see also Figure 11.4); hence the main-sequence lifetime decreases steeply with increasing mass. This is confirmed by the computed values given in Table 11.1.

11.4 The evolution of the Sun

As the closest star, the Sun provides a unique possibility for testing our stellar modelling, in one specific case. Furthermore, solar evolution is of course critically important for the past and future evolution of the Earth. Here we consider some aspects of solar evolution,

[7]In fact, the assumption of constant core mass fraction is rather dubious. In particular, it follows from Figure 11.4 that the extent of the convective core, and hence the fraction of the mass which may contribute fuel to the hydrogen burning, increases substantially with increasing stellar mass. A further uncertainty in estimates of the main-sequence lifetime is the extent of *overshoot* from the convective core: it is virtually certain that convective motion does not stop at the boundary of the convectively unstable region, but penetrates somewhat into the surrounding stable region; this increases the amount of hydrogen available for burning, but the extent of the penetration is very uncertain.

while Section 11.5 discusses detailed tests of models of the present Sun. A comprehensive presentation of these aspects was provided by Christensen-Dalsgaard (2021).

11.4.1 Introduction

The computation of solar models follows the procedures discussed for other stars. However, a particular feature of the solar calculations is that the models should match the observed radius and luminosity of the present Sun, which are known with considerable precision. In fact, agreement with the observed values could have been regarded as a test of the computed models, were it not for the fact that the computations effectively contain two parameters, which are not known *ab initio* with sufficient precision: the abundance of helium in the initial Sun,[8] and a parameter determining the efficiency of convection near the solar surface, where convection cannot be assumed to be essentially adiabatic. Given assumptions about the other physical parameters characterizing the solar model (in particular the opacity tables) these two parameters are adjusted until the model fits the observed radius and luminosity, at the age of the present Sun; the age has been estimated on the basis of radioactive age determinations for meteorites.

A typical example of a model of the present Sun is shown in Table 11.2. It differs from the models discussed so far by including also the effect of element diffusion and settling; in particular, there is a tendency for heavier elements including helium to sink towards the centre while hydrogen rises towards the surface. This effect is fairly weak in the Sun; even so, it causes a significant increase in the hydrogen abundance X in the convection zone, seen in Table 11.2, relative to the original abundance, $X_0 = 0.709$. As discussed in Section 11.5.2, this effect has been confirmed by observations of solar oscillations.

11.4.2 Changes during the evolution of the Sun

It is evident from Figure 11.5 that the $1\,M_\odot$ star shares the general trend of an increase in luminosity as the star evolves. To illustrate this in more detail, and to investigate the simplified analysis of the reasons for the increase which was given in section 11.3.1, Figure 11.8 shows the changes in a number of quantities during the evolution of a solar model from the ZAMS to the present age. The driver of the evolution is the decrease in the central hydrogen abundance X_c, from the initial value of 0.709 to the value of 0.335 in the present Sun. As argued in section 11.3.1 the resulting increase in the central mean molecular weight forces a core contraction, hence increasing the central density. This leads to an increase in the central temperature T_c. It is interesting, however, that the effect on the central energy generation rate ϵ_c is fairly modest; the increase in T_c should cause a substantially larger increase in ϵ_c due to the comparatively high temperature sensitivity of nuclear reactions; but this is largely compensated for by the decrease in the hydrogen abundance [since the energy generation is dominated by the PP chains, $\epsilon \propto X^2$; *cf.* equation (8.52)]. Also, there is a substantial reduction in the central opacity κ_c, caused by the increase in the temperature and the decrease in the hydrogen abundance. The combined effect of the increase in ϵ and the decrease in κ finally leads to the increase in

[8] The helium abundance cannot be measured spectroscopically in the case of the Sun, because the solar photospheric spectrum does not contain helium lines. It is true that helium was first discovered in the Sun, but only in lines formed in the upper parts of the solar atmosphere; here conditions are so uncertain that the measured line strengths cannot be used for a reliable abundance determination. In contrast, fairly accurate observations have been made of the abundances of most other important elements in the Sun.

Table 11.2

$\frac{r}{R}$	$\frac{m}{M}$	$\frac{L_r}{L_s}$	X	$\log P$	$\log T$	$\log \rho$	κ	ϵ	$\frac{N_e}{N_{e,0}}$
0.000	0.000	0.000	0.335	17.371	7.195	2.188	1.24	16.99	1.000
0.020	0.001	0.007	0.350	17.359	7.191	2.174	1.26	16.54	1.000
0.040	0.007	0.053	0.385	17.326	7.180	2.135	1.30	15.07	1.000
0.060	0.020	0.153	0.434	17.274	7.163	2.080	1.36	12.96	1.000
0.080	0.044	0.293	0.488	17.208	7.142	2.013	1.44	10.58	1.000
0.100	0.076	0.452	0.540	17.131	7.117	1.941	1.54	8.20	1.000
0.120	0.118	0.602	0.585	17.045	7.090	1.866	1.65	6.04	1.000
0.140	0.166	0.729	0.622	16.952	7.061	1.789	1.77	4.23	1.000
0.160	0.220	0.826	0.650	16.852	7.032	1.710	1.90	2.82	1.000
0.180	0.277	0.894	0.670	16.747	7.002	1.628	2.05	1.82	1.000
0.200	0.336	0.938	0.684	16.637	6.972	1.543	2.21	1.13	1.000
0.250	0.482	0.988	0.702	16.346	6.900	1.319	2.69	0.33	1.000
0.300	0.610	0.999	0.708	16.041	6.832	1.081	3.31	0.05	1.000
0.350	0.712	1.000	0.712	15.734	6.769	0.837	4.10	0.01	1.000
0.400	0.790	1.000	0.713	15.433	6.709	0.595	5.10	0.00	0.999
0.450	0.848	1.000	0.715	15.141	6.653	0.359	6.29	0.00	0.996
0.500	0.890	1.000	0.716	14.861	6.600	0.131	7.71	0.00	0.993
0.550	0.921	1.000	0.717	14.591	6.548	-0.087	9.42	0.00	0.991
0.600	0.944	1.000	0.718	14.331	6.495	-0.295	11.54	0.00	0.991
0.650	0.960	1.000	0.719	14.076	6.439	-0.494	14.49	0.00	0.991
0.700	0.973	1.000	0.732	13.820	6.367	-0.681	19.26	0.00	0.991
0.750	0.983	1.000	0.737	13.547	6.260	-0.848	31.59	0.00	0.990
0.800	0.990	1.000	0.737	13.232	6.135	-1.038	50.94	0.00	0.989
0.820	0.992	1.000	0.737	13.089	6.079	-1.124	61.32	0.00	0.988
0.840	0.994	1.000	0.737	12.932	6.017	-1.218	74.83	0.00	0.988
0.860	0.996	1.000	0.737	12.757	5.947	-1.323	94.31	0.00	0.987
0.880	0.997	1.000	0.737	12.559	5.869	-1.442	1.2×10^2	0.00	0.986
0.900	0.998	1.000	0.737	12.328	5.777	-1.581	1.7×10^2	0.00	0.985
0.910	0.999	1.000	0.737	12.195	5.725	-1.660	2.1×10^2	0.00	0.984
0.920	0.999	1.000	0.737	12.048	5.667	-1.749	2.7×10^2	0.00	0.984
0.930	0.999	1.000	0.737	11.881	5.602	-1.849	3.8×10^2	0.00	0.982
0.940	1.000	1.000	0.737	11.688	5.526	-1.964	5.9×10^2	0.00	0.980
0.950	1.000	1.000	0.737	11.459	5.437	-2.102	1.1×10^3	0.00	0.977
0.960	1.000	1.000	0.737	11.176	5.328	-2.273	2.4×10^3	0.00	0.970
0.970	1.000	1.000	0.737	10.802	5.189	-2.500	8.0×10^3	0.00	0.954
0.980	1.000	1.000	0.737	10.256	4.998	-2.842	2.5×10^4	0.00	0.911
0.990	1.000	1.000	0.737	9.237	4.660	-3.489	1.3×10^5	0.00	0.800
0.992	1.000	1.000	0.737	8.875	4.565	-3.737	1.3×10^5	0.00	0.726
0.994	1.000	1.000	0.737	8.398	4.460	-4.084	7.4×10^4	0.00	0.617
0.996	1.000	1.000	0.737	7.741	4.343	-4.588	2.4×10^4	0.00	0.468
0.998	1.000	1.000	0.737	6.768	4.206	-5.368	4.1×10^3	0.00	0.280
0.999	1.000	1.000	0.737	6.063	4.115	-5.937	9.7×10^2	0.00	0.157
1.000	1.000	1.000	0.737	4.881	3.762	-6.699	0.34	0.00	0.000

Model of the present Sun (Model S of Christensen-Dalsgaard *et al.* 1996). The columns show: (1) distance from the centre in units of the surface radius; (2) mass in units of the total mass; (3) luminosity in units of the surface luminosity; (4) hydrogen abundance; (5) pressure P ($\mathrm{dyn\,cm^{-2}}$); (6) temperature T (K); (7) density ρ ($\mathrm{g\,cm^{-3}}$); (8) opacity κ ($\mathrm{cm^2\,g^{-1}}$); (9) the rate of energy generation ϵ ($\mathrm{erg\,g^{-1}\,sec^{-1}}$); (10) the ratio between the number N_e of free electrons, and the total number of electrons $N_{e,0}$, per gram; this illustrates the transition from almost no ionization near the surface, where the ratio is zero, to complete ionization in the interior, where the ratio is 1.

The model was adjusted to have the observed surface radius of $6.96 \times 10^{10}\,\mathrm{cm}$ and the surface luminosity $3.846 \times 10^{33}\,\mathrm{erg\,sec^{-1}}$ at the age of the present Sun, which was taken to be 4.6×10^9 years. The model has an outer convection zone extending from just below the surface to $r/R = 0.711$.

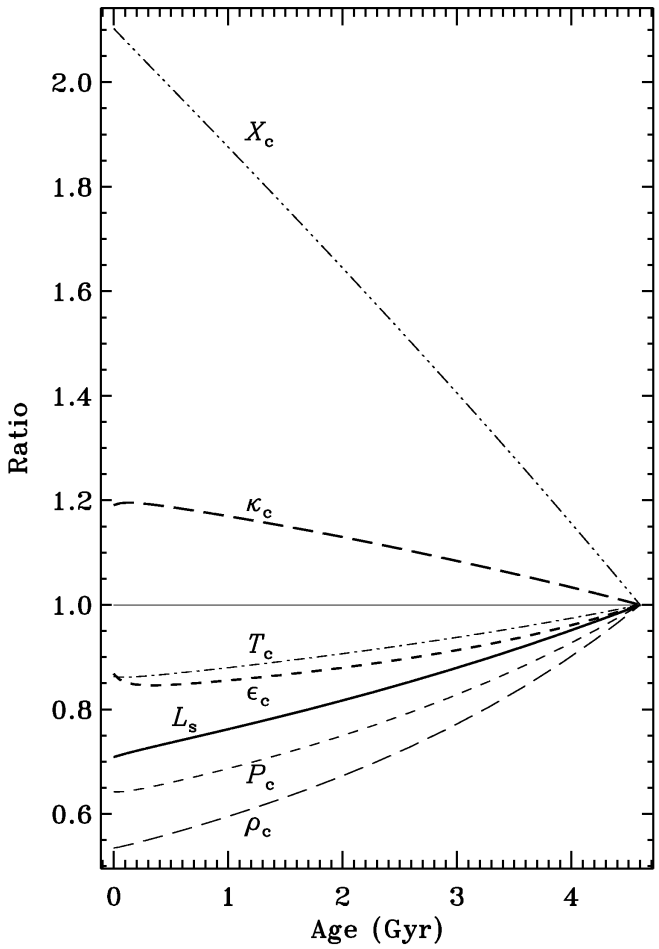

Figure 11.8: Variation in the surface luminosity and in properties at the centre during the evolution of a solar model. All variables have been normalized with their value in the present Sun. The heavy lines show the surface luminosity L_s (——————), the central energy generation rate ϵ_c (- - - - - - - - - - - -), and the central opacity κ_c (– – – – – – – –). The thin lines show the central density ρ_c (– – – – – – – –), the central pressure P_c (- - - - - - - - - - - -), the central temperature T_c (— - — - — - —), and the central hydrogen abundance X_c (— ··· — ··· — ···).

the surface luminosity L_s; the results show that L_s was approximately 30 per cent lower on the ZAMS than at present.

11.4.3 Climatic effects of solar evolution?

An obvious question is whether the climate of the Earth may have been affected by this increase in the luminosity of the Sun since it arrived on the main sequence. A simple estimate suggests that this may be possible. To maintain equilibrium, there must be a balance between the amount of heat received by the Earth from the Sun, and the amount of heat radiated by the Earth (if we neglect the heat generated by radioactive processes in

the Earth's interior). If we assume that the Earth absorbs all the energy it receives, that the energy is redistributed evenly over the surface of the Earth (due to the rotation of the Earth, and the effects of winds and ocean currents), and that the Earth radiates as a black body with temperature $T_{\rm E}$, the equilibrium terrestrial temperature may be estimated as

$$T_{\rm E} = \left(\frac{\rm L_\odot}{16\pi d^2 \sigma}\right)^{1/4} = \left(\frac{\rm R_\odot}{2d}\right)^{1/2} T_{\rm eff,\odot} \ , \tag{11.3}$$

where d is the distance between the Sun and the Earth.

Exercise 11.2:

Prove this relation. What is the predicted average temperature of the Earth?

According to equation (11.3), the initial average temperature of the Earth should have been about 7 per cent, or 20 K, lower than the present temperature, which is about 290 K. This suggests that the Earth may initially have been frozen over, in conflict with geological evidence which indicates development of life, almost certainly requiring liquid water, at least 3.5×10^9 years ago. Furthermore, with a substantial ice cover, the Earth would have reflected a large fraction of the incoming solar heat, further reducing the average temperature. Simple estimates of this effect suggest that if the Earth had at any time in its history been covered with ice, even an increase in the solar luminosity to a value substantially higher than the present would have been unable to melt the ice.[9]

This so-called "faint early Sun" problem caused some discussion around the middle of the seventies, and attempts were made to produce solar models that did not display an increase in luminosity during main-sequence evolution. However, this increase is one of the most robust predictions of stellar evolution theory. As was discussed in sections 11.3.1 and 11.4.2, it results from the changes in structure caused by the depletion of hydrogen in the solar core. Even if the Sun were assumed to be completely mixed, thus increasing the supply of nuclear fuel and hence presumably decreasing the effects of evolution, a luminosity increase of about 20 per cent is still predicted. Under this assumption the dependence given in equation (7.7) of luminosity on mean molecular weight may be used to estimate the change in luminosity over the solar lifetime.

Exercise 11.3:

Assuming that the Sun has been fully mixed during its evolution, estimate the change in the hydrogen abundance from the ZAMS to the present. Then use equation (7.7) to estimate the change in the solar luminosity, assuming that the change in R can be ignored. The initial hydrogen abundance may be taken to be $X_0 = 0.7$, and the heavy element abundance is $Z = 0.02$.

---

[9] This argument is based on somewhat simplified models of the Earth's climate. There have been suggestions that the Earth has in fact passed through episodes of nearly complete ice cover, which were reversed by a run-away greenhouse effect caused by volcanic release of CO_2; see, for example, Hoffman & Schrag (2000).

Models with a constant solar luminosity can be constructed, but only by involving fairly drastic modifications in the basic physics. One proposal which has been studied in some detail is to invoke a change with time in the gravitational constant G, and possibly the solar mass (*e.g.*, Maeder 1977). Such changes have received no independent support, however, and are probably inconsistent with very accurate measurements of the motion in the solar system. On the other hand Sackmann & Boothroyd (2003) showed that a modest mass loss in early stages of solar evolution would involve a slightly more massive, and hence brighter, young Sun; such models can apparently not be ruled out by current observations, including the detailed helioseismic inferences discussed in section 11.5.2.

It should be noted, however, that the estimate given above of the change in the Earth's temperature was extremely naive, in that it ignored all the complications of terrestrial climatology. In particular, it did not take into account the so-called *greenhouse effect*: the atmosphere of the Earth is largely transparent to radiation at wavelengths where most of the Sun's energy is radiated; but because the temperature of the Earth is much lower, it radiates predominantly at much longer wavelengths [*cf.* equation (2.18)], and at these wavelengths there is strong absorption in the atmosphere, particularly due to certain molecules, such as water vapour and carbon dioxide (CO_2). Hence the energy is partially trapped in the Earth's atmosphere, the degree of trapping depending on the abundance of CO_2.[10]

It is now clear that *if* there has been a suitable reduction in the abundance of CO_2 in the Earth's atmosphere during solar evolution, the decreasing efficiency of the greenhouse effect might have compensated for the increase in solar luminosity, keeping the temperature at the Earth's surface approximately constant. That this should be so could seem as an incredible coincidence. However, there are mechanisms which may link the absorption or release of CO_2 to the surface temperature of the Earth, in such a way that CO_2 is bound up, *e.g.* in rocks, if the temperature gets too high, thereby decreasing the efficiency of the greenhouse effect; and CO_2 is released if the temperature gets too low. There have even been speculations that these mechanisms could be of a biological nature, involving the photosynthesis in the plants and the metabolism in animals.[11] On the other hand, there appears to be also inorganic mechanisms which may provide the required feedback. A very interesting discussion of these questions was given by Kasting, Toon & Pollack (1988); they also analyzed the reasons for the striking differences between the climates of Venus, the Earth and Mars.

Computations of solar evolution show, as also indicated in Figure 11.5, that the solar luminosity will continue to increase. Hence, to maintain the same surface temperature the efficiency of the greenhouse effect should be reduced even further, by reducing the CO_2 abundance in the Earth's atmosphere. There is an obvious limit to how far this reduction may go. In fact Lovelock & Whitfield (1982) estimated that in approximately 150 million years the acceptable CO_2 abundance may become too low for photosynthesis to be possible. While this is no immediate cause for worry, the time estimate is nevertheless very short compared with the age of the Earth. There is a much more serious concern, however: currently the atmospheric CO_2 abundance is rising fairly rapidly, as a result of

[10] A similar mechanism is responsible for the heating up of a greenhouse: glass is transparent to solar radiation, but absorbs and hence traps the radiation from the interior of the greenhouse.

[11] This idea underlies the *Gaia hypothesis*, which has been proposed by J. E. Lovelock and L. Margulis; according to it, the entire biosphere should be regarded as a "living being", which adjusts conditions so that they are optimal.

the burning of fossil fuel (coal and oil) and the reduction in the tree cover. As discussed by Schneider (1989) this may already have had effects on the Earth's climate, and it is virtually certain to lead to a significant increase in the temperature of the Earth over our lifetime, with very serious economical and sociological consequences. How to deal with this problem is one of the major challenges, to all of us, of the present time.

There is mounting evidence that the Sun affects the climate of the Earth (beyond the obvious effects) on shorter time scales also. This appears to be related to the magnetic activity of the Sun, leading to the appearance of sunspots the number of which varies roughly cyclically with a period around 11 years. During the period 1640 – 1710, however, where there were already fairly systematic observations of the Sun, the sunspots apparently almost disappeared; interestingly, this so-called *Maunder minimum* in solar activity coincides with the 'little ice age', an unusually cold period.[12] More quantitative evidence for a climatic effect has been obtained through careful analyses by Labitzke & van Loon (1993) and by Friis-Christensen & Lassen (1991); the latter authors found an apparently strong correlation between the *period* of the solar cycle and the temperature on the northern hemisphere, over the past few centuries. The physical mechanisms behind these correlations are not yet completely understood. An interesting possible cause was found by Svensmark & Friis-Christensen (1997) (see also Svensmark 1998), who showed that the cloud cover was strongly positively correlated with the intensity of the galactic cosmic rays; the propagation of cosmic rays through the solar system is affected by the solar wind and hence by solar activity, in such a way that the intensity of cosmic rays is decreased at periods of high solar activity.

These results raised the question whether the consequences of the increasing greenhouse effect resulting from burning fossil fuel have already been seen in the Earth's climate, or whether any possible climatic changes in the past century can be blamed solely on the Sun (for a rather one-eyed, but enjoyable, presentation of the latter view, see Calder 1997). It seems likely that both the Sun and human activities on Earth have the potential to affect the climate, but it is becoming increasingly clear that substantial antropogenic effects on climate are already evident.[13] Thus restraint in the burning of fossil fuels and other production of greenhouse gasses is certainly required.

11.5 Tests of solar models

11.5.1 Introduction

In general it is difficult to obtain sufficiently detailed observations of an individual star to permit a careful test of computed models of the star. Hence much of the testing of stellar evolution calculations has been based on "statistical" properties of large groups of stars, particularly stars in open clusters. We return to this in Chapter 13. However, in the case of the Sun much more information is available. Here we present a brief discussion of two types of observations which, at least in principle, give information about the solar interior: the solar five-minute oscillations and the solar neutrinos. The results of using these data to test

[12] An unfortunate consequence of the cold winters was the ability of the Swedish army to cross the Danish belts over the ice during the war from 1657 – 1660, contributing significantly to the Danish defeat and hence to the loss of Scania (Skåne).

[13] See the 2023 IPCC material (`https://www.un.org/en/climatechange/reports`), in particular the Synthesis Report.

the computed models long appeared contradictory: the observed oscillation frequencies indicated that there are no major problems with our models of the Sun, while there were substantial differences between the computed and observed flux of neutrinos from the Sun. As is now known, this discrepancy was an indication that modifications were required in our description of the neutrino.

11.5.2 Solar oscillations

It is not possible here to present more than a very brief overview of the properties of solar oscillations, and what they have taught us about the solar interior. For more detailed descriptions the reviews by, for example, Leibacher *et al.* (1985), Libbrecht (1988), Gough & Toomre (1991), Harvey (1995) and Christensen-Dalsgaard (2002) may be consulted.

An oscillating string has many different *eigenmodes*, characterized by the number n of nodes, or places where the string does not move. Similarly there is a large number of different modes of oscillation of a star. However, while the oscillations of a one-dimensional object like a string can be characterized by a single number n, the characterization of the oscillations of a three-dimensional star requires three numbers. It may be shown that the variation of a mode of oscillation with co-latitude θ and longitude ϕ can be described in terms of a spherical harmonic $Y_l^m(\theta, \phi)$; hence two of the three wave-numbers characterizing the mode are the *degree* l and the *azimuthal order* m of the spherical harmonic. The third wavenumber, the *radial order* n, describes the variation of the mode with the distance r from the centre of the star. To each mode of oscillation corresponds an *eigenfrequency* ν_{nlm}, such that for the mode the velocity, say, at a given point in the star varies with time as

$$\sin(2\pi\nu_{nlm}t) \; . \tag{11.4}$$

In general the frequency depends on all three wave-numbers. However, it turns out that if rotation of the star is neglected, the frequencies are independent of m;[14] we make this approximation and regard the frequencies ν_{nl} as being determined by just n and l.

It is straightforward to compute precise oscillation frequencies for a given stellar model. An example, for a model of the present Sun, is shown in Figure 11.9. The modes fall into three different categories:

- The *p modes* which are standing sound waves.
- The *f modes* which are essentially surface gravity waves.
- The *g modes* which are essentially internal gravity waves.

The frequencies depend on the structure of the model. For example, since the p modes are sound waves, their frequencies are largely determined by the speed of sound c in the stellar interior, which is given by

$$c^2 = \frac{\Gamma_1 P}{\rho} \simeq \frac{\gamma k_{\rm B} T}{\mu m_{\rm u}} \; ; \tag{11.5}$$

[14] Rotation introduces a splitting after m of the frequencies, rather similar to the Zeeman splitting of the energy levels of an atom in a magnetic field. This *rotational splitting* may be used to get information about the rotation in stellar interiors.

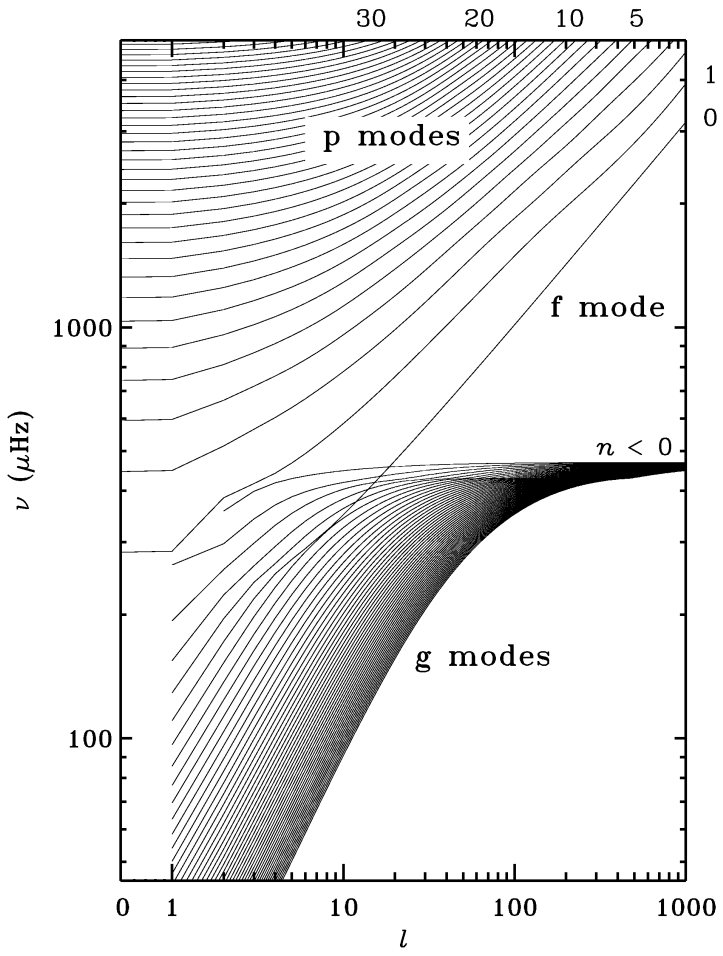

Figure 11.9: Computed frequencies of a solar model, as functions of the degree l. For clarity, points corresponding to a given value of the radial order n have been connected. Selected values of n are indicated.

the last approximation assumes the ideal gas law. Thus, frequencies of p modes may in principle give information about the temperature in stellar interiors; in practice, this requires some additional constraints on the chemical composition, and hence the mean molecular weight.

Of course, Figure 11.9 just shows the modes of oscillation that are *possible* in a given star (in the same way as for a string an infinite number of eigenmodes are possible). Whether any of these oscillations are actually seen in a given star depends on the mechanisms that excite and damp the oscillations. As discussed in section 2.8, in the case of the Sun a large number of modes are in fact excited, namely apparently modes in the frequency range between approximately 1500 and 5000 μHz, corresponding to periods between about 10 and 3 minutes, at all degrees from 0 to greater than 1000. The distribution of mode amplitude with frequency is largely independent of the degree l, and hence corresponds to the spectrum shown in Figure 2.10.

The observed frequencies ν_{nl} provide a very rich material against which to test the

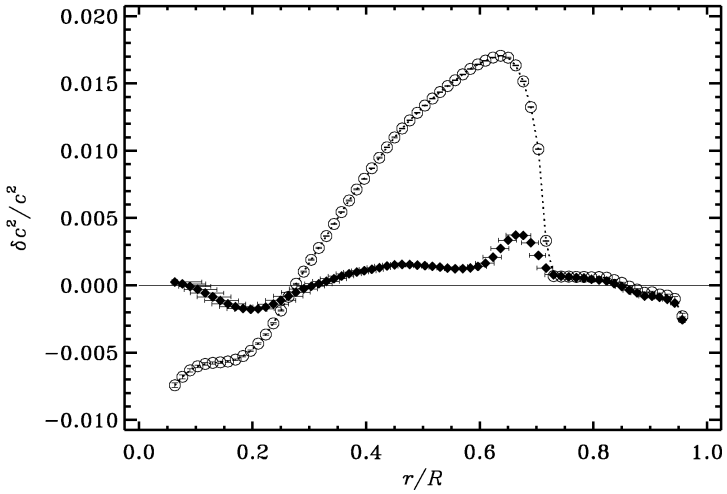

Figure 11.10: Relative difference in squared sound speed between the Sun and two solar models, obtained from analysis of observed frequencies of five-minute oscillations; the differences are shown in the sense (Sun) – (model). The open circles show results using a model without diffusion and settling, whereas the solid symbols were obtained with Model S (*cf.* Table 11.2) where diffusion and settling of helium and heavy elements were taken into account. The vertical error bars (barely visible) indicate the formal errors in the differences, based on the errors in the observed frequencies, whereas the horizontal bars provide a measure of the resolution in the determination.

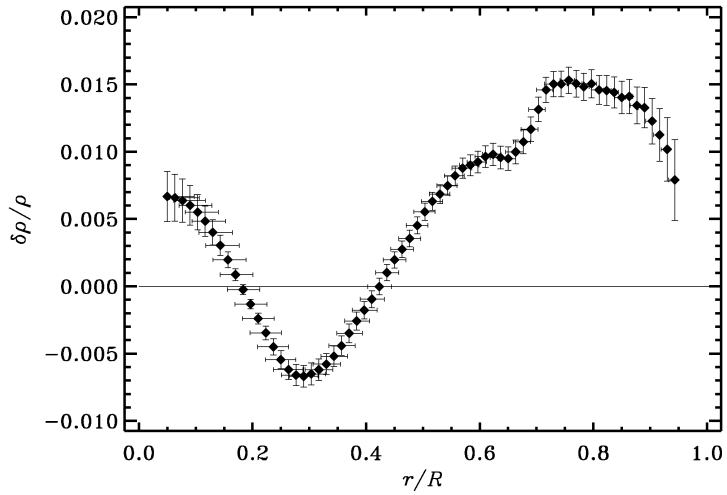

Figure 11.11: Relative difference in density between the Sun and Model S, obtained from analysis of observed frequencies of five-minute oscillations.

computed solar models. The analysis of these data, which in many ways are similar to seismic data for the Earth, is referred to as *helioseismology*. The results are somewhat surprising: for recent models the differences between computed and observed frequencies are generally less than 10 μHz. This is still considerably more than the estimated errors in the observations, which in some cases are less than 0.01 μHz; but the agreement between computations and observations indicates that there are probably at least no gross errors in our computation of solar models. Hence we may also have some confidence in models of other main-sequence stars. Furthermore, the results of the comparison are quite sensitive to the details of the physics in the models. For example, the inclusion of Coulomb interaction in the equation of state led to a very significant improvement in the agreement between computations and observations, Also, a ten per cent change in the assumed opacity in part of the Sun has a noticeable effect on the computed frequencies; analysis of the oscillation frequencies has indicated that the tabulated opacity near the base of the solar convection zone was too low, a result which has later been confirmed by new opacity computations. Thus observations of this nature may lead to improvements in the physics used in computing stellar models.

However, it is possible to go further than merely comparing observed and computed frequencies. By applying *inverse analysis* one may determine differences between the properties of the Sun and the model, from the differences between observed and computed frequencies. As examples, Figures 11.10 and 11.11 show the relative differences in sound speed and density between the Sun and the model given in Table 11.2; in addition, sound-speed results for a model neglecting diffusion and settling are also shown. Without going into the detailed interpretation of the results, it is obvious that the sound speed in the model agrees quite precisely with the Sun; also, it is striking that the inclusion of settling, which in the past has often been neglected in solar modelling, leads to such a dramatic improvement in the agreement between the model and the Sun. The differences in density are somewhat larger than those in sound speed, especially in the convection zone. Nonetheless, given the simplifications made in computing the model it is perhaps surprising that it is so close to reality.

Indeed, the close agreement between the Sun and the model in Figure 11.10 has been somewhat challenged by further determinations of the solar surface composition. Model S assumes a ratio $Z_{\rm s}/X_{\rm s} = 0.0245$ between the present solar surface heavy-element and hydrogen abundances. Analyses of the solar radiation spectrum using more realistic models and taking into account departure from local thermodynamic equilibrium in the atmosphere have yielded somewhat lower values, such as $Z_{\rm s}/X_{\rm s} = 0.0181$ obtained by Asplund *et al.* (2009), predominantly from a reduction in the abundances of C, N and O. The lower content of heavier elements reduces the opacity in the solar interior, resulting in a substantially higher difference between the solar and model sound speed. It is plausible that this discrepancy can at least in part be eliminated by changes to the opacity computations, but no definite solution has yet been found. For detailed reviews of these issues, see Basu & Antia (2008) and Christensen-Dalsgaard (2021).

11.5.3 Solar neutrinos

As discussed in section 8.5, the production of one ^{4}He nucleus necessarily leads to the generation of two neutrinos. Since the neutrinos are virtually certain to escape from the Sun they may, at least in principle, be detected on the Earth. The measurement of the

flux of neutrinos would then provide a direct measure of the rate of nuclear reactions in the core of the Sun.

To carry out this simple principle in practice involves numerous difficulties, however. The main problem is again the very small cross section of the neutrino, which makes it extremely hard to detect. Furthermore, the results that were obtained over almost three decades were consistently lower than the theoretically predicted values. This *solar neutrino problem* led to a very large effort towards trying to modify the solar models with a view towards bringing the predicted neutrino flux into agreement with observations. A comprehensive discussion of the observations and model computations, and of the possible solutions to the problem, was given by Bahcall (1989). For additional reviews, see, for example, Bahcall *et al.* (1995), Bahcall (1996), Castellani *et al.* (1997), Kirsten (1999), and Haxton *et al.* (2013). Solar neutrino studies have been awarded two Nobel prizes; the prize lectures (Davis, 2003; Koshiba, 2003; McDonald, 2016) give brief introductions to the history of the field.

It is now known that the origin of the discrepancy is not primarily with the solar models but rather relates to properties of the neutrinos that were neglected in the earlier analyses. Even so it is instructive to consider how such a substantial challenge to our understanding of stellar evolution was handled.

It follows from the analysis in section 8.5 that the neutrinos may be emitted in a number of different reactions, with very different energies. The distribution of the neutrinos depends on the branching ratios between the PP-I, PP-II and PP-III chains, and on the relative importance of the CNO cycle. Since the sensitivity of the neutrino detectors depends strongly on the neutrino energy, the observed number of neutrinos depends on the details of the neutrino spectrum. An example of a computed neutrino spectrum is shown in Figure 11.12.

The initial experiment to detect solar neutrinos was established by R. Davis in the Homestake Gold Mine, South Dakota, in 1970 and operated until 1994 (for a overview of the results, see Cleveland *et al.* 1998); it used the reaction

$$\nu_{\rm e} + {}^{37}{\rm Cl} \rightarrow {\rm e}^- + {}^{37}{\rm Ar} \tag{11.6}$$

(*cf.* section 2.10). This reaction is in principle sensitive to neutrinos with energies exceeding about 0.8 MeV. In practice the predicted capture rate was dominated by the ^{8}B neutrinos, with the ^{7}Be neutrinos also making a significant contribution. On the other hand, the experiment was insensitive to the neutrinos emitted in the PP-I chain, which dominates the energy generation in the Sun. The predicted capture rates for this experiment from the different sources of neutrinos are listed in Table 11.3. The unit is *Solar Neutrino Unit*, or *SNU* which is defined as 10^{-36} captures per target atom in the detector per second. The total predicted capture rate was quoted by Bahcall (1989) as

$$\text{Predicted capture rate} = 7.9(1 \pm 0.33)\,\text{SNU}\ , \tag{11.7}$$

where the indicated uncertainty takes into account the uncertainties in the model computations. More recent model calculations, including effects of settling and diffusion, give similar results: Bahcall & Pinsonneault (1995) found a rate of 9.3 SNU, whereas the prediction for Model S (*cf.* Table 11.2) is 8.2 SNU.

The measured capture rate is shown in Figure 11.13.[15] An average over these data gives an observed capture rate of (2.05 ± 0.3) SNU; including more recent data the average

[15]It should be noted that the left-hand axis gives the argon production rate per day, as typically 0.5

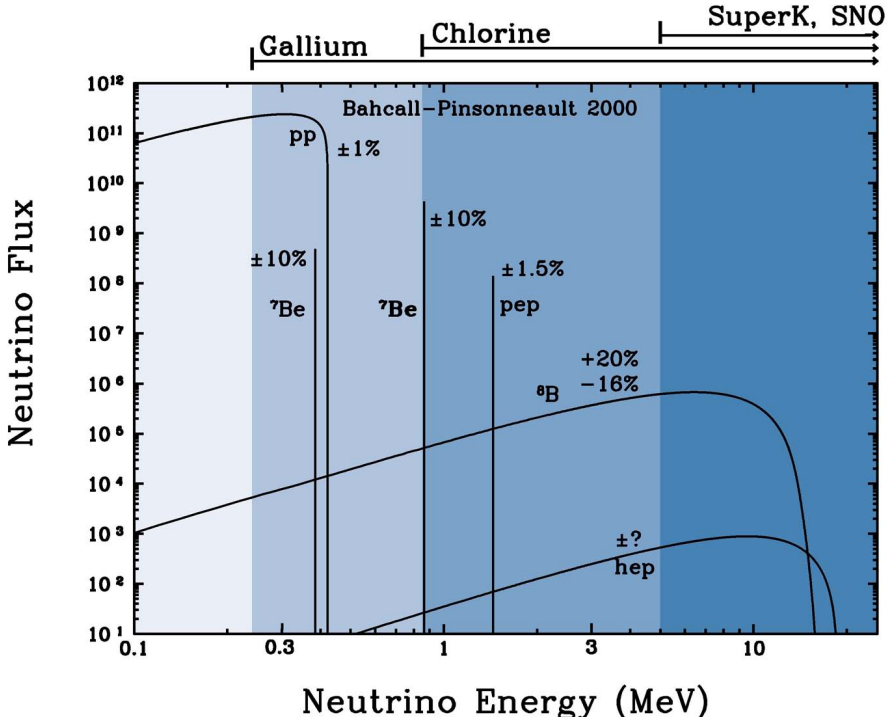

Figure 11.12: The energy spectrum of neutrinos predicted by a normal model of the present Sun. The neutrino fluxes from continuous sources are given in units of $\mathrm{cm}^{-2}\,\mathrm{sec}^{-1}\,\mathrm{MeV}^{-1}$ at one astronomical unit; the line fluxes are in units of $\mathrm{cm}^{-2}\,\mathrm{sec}^{-1}$. The spectra from the PP chains are shown with continuous lines: pp refers to the reaction $^1\mathrm{H}(^1\mathrm{H}, \mathrm{e}^+\nu_\mathrm{e})\,^2\mathrm{D}$, ^{7}Be to the reaction $^7\mathrm{Be}(\mathrm{e}^-, \nu_\mathrm{e})\,^7\mathrm{Li}$, ^{8}B to the reaction $^8\mathrm{B}(\mathrm{e}^+\nu_\mathrm{e})\,^8\mathrm{Be}$, pep to the reaction $^1\mathrm{H}(^1\mathrm{H}\ \mathrm{e}^-, \nu_\mathrm{e})\,^2\mathrm{D}$, and hep to the reaction $^3\mathrm{He}(^1\mathrm{H}, \nu_\mathrm{e})\,^4\mathrm{He}$ (note that the last two reactions were not discussed in section 8.5). In addition, modest contributions are made by the reactions in the CNO cycle. The shadings and the bars at the top of the figure indicate the ranges of sensitivity of the different techniques for detecting the neutrinos. (Adapted from Bahcall 1989.)

Table 11.3

Neutrino source	Capture rate (SNU)
pp	0.0
pep	0.2
hep	0.03
^{7}Be	1.1
^{8}B	6.1
^{13}N	0.1
^{15}O	0.3
^{17}F	0.003
Total	7.9 SNU

The predicted capture rates for neutrinos from a normal solar model in the ^{37}Cl detector. (From Bahcall 1989.)

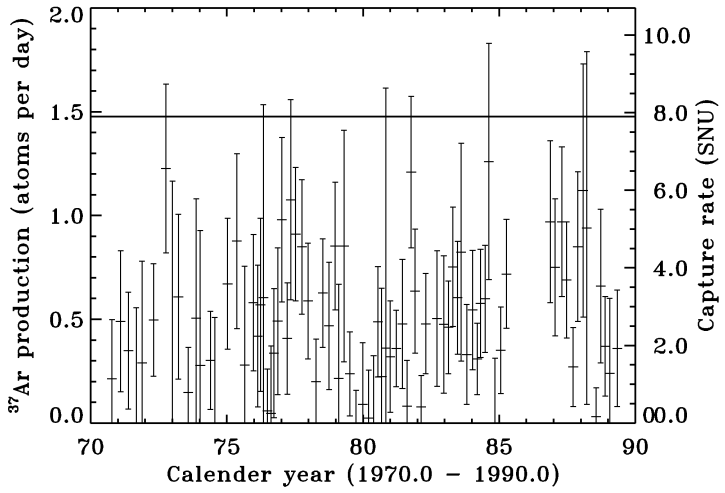

Figure 11.13: Observational results from the chlorine solar neutrino experiment. The line at 7.9 SNU across the top of the figure represents the prediction of a normal solar model. (Adapted from Bahcall 1989.)

is 2.56 SNU (Cleveland *et al.* 1998). Thus the predicted rates were clearly inconsistent with these measurements. This inconsistency constituted the solar neutrino problem.

A second type of experiment to detect solar neutrinos uses scattering of the neutrinos on electrons in water. Since the electrons are predominantly scattered in the direction in which the neutrino arrives, this type experiment provides information about the direction to the source of neutrinos. Figure 11.14 shows the observed distribution as a function of the direction $\theta_{\rm sun}$ to the Sun, compared with the predictions of a normal solar model; the measurements were made with the *Super-Kamiokande detector* in Japan, utilizing a tank of 50 000 tons of water buried deep in a mine. This provided the first evidence that neutrinos are actually coming from the Sun. The experiment is only sensitive to neutrinos of energy exceeding 6.5 MeV, *i.e.*, largely to the ^{8}B neutrinos. The results again showed that the observed neutrino rate was smaller than the predicted rate (Fukuda *et al.* 1998a); a recent value for the ratio between measurements and predictions is 0.47.[16]

These measurements of solar neutrinos led to the award of the 2002 Nobel prize in physics to Raymond Davis and Masatoshi Koshiba, for establishing, respectively, the ^{37}Cl and the Kamiokande experiments (Davis 2003; Koshiba 2003); they shared the prize with Riccardo Giacconi, who got his share for work in X-ray astronomy.

It should be noted that the neutrinos observed in these two experiments all come from the PP-II and PP-III chains. The electron-scattering experiment is only sensitive to the ^{8}B neutrinos from the PP-III chain, which also dominate the detections in the ^{37}Cl detector (*cf.* Table 11.3). Hence the predicted flux is very sensitive to the branching ratios

atoms per day. In practice, the experiment is run for two months at a time, and the resulting roughly 30 argon atoms are collected and counted. Careful tests have shown that the methods used for extraction and counting were in fact able to detect such a small number of argon atoms accurately.

[16]Unfortunately, neutrino experiments suffered a serious setback in November 2001 when the Japanese Super-Kamiokande neutrino detector, measuring electron scattering in 50,000 tons of water, was seriously damaged (see *Nature*, **414**, 381; 2001). However, the detector is now up and running again.

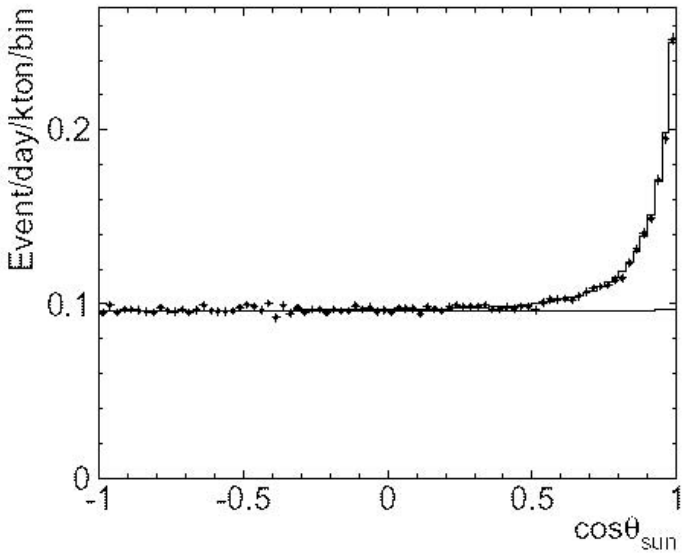

Figure 11.14: The distribution in $\cos\theta_{\rm sun}$ (where $\theta_{\rm sun}$ is the angle to the direction to the Sun) of neutrinos detected in an electron-scattering experiment. The histogram is the calculated distribution based on the predicted neutrino flux from a normal solar model. (See Fukuda *et al.* 2001.)

between the PP-I, the PP-II and the PP-III chain, which in turn are highly sensitive to the central temperature of the Sun (see also exercise 8.8). Thus, to reduce the predicted capture rate to the observed value from these experiments would only required a reduction in the core temperature of the Sun by about 5 per cent, while of course maintaining the correct total integrated energy generation rate and hence surface luminosity. It is possible to construct such models, although only by making fairly drastic modifications to the normal assumptions or parameters of stellar evolution calculations. However, in all cases considered the resulting models had oscillation frequencies which are inconsistent with the observed values (*cf.* section 11.4.3). As an example may be mentioned the suggestion that part of the energy transport in the solar core was carried out through the motion of hypothetical elementary particles, the so-called "Weakly Interacting Massive Particles" (or WIMPs).[17] This would reduce the temperature gradient required to maintain radiative energy transport, and hence reduce the central temperature of the Sun. By a suitable choice of parameters it was possible to construct models which did indeed have the observed neutrino capture rate; furthermore, the effect on the structure of the model was fairly subtle, and hence, at the time where the suggestion was made, it was not obviously inconsistent with the observed oscillation frequencies. However, more careful observations (*e.g.* Elsworth *et al.* 1990) convincingly demonstrated that while normal solar models were consistent with the observed frequencies, models with WIMPs were not. More generally, the excellent agreement between the sound speed in standard solar models and the Sun, found from helioseismology and extending well into the core where nuclear reactions take

[17]WIMPs had also been suggested as the dark matter inferred from the observed dynamics of the Universe.

place (*cf.* Fig. 11.10) strongly suggested that the neutrino predictions of standard solar models were reasonably reliable (*e.g.* Bahcall *et al.* 1997).

Measurements that are sensitive to the basic pp neutrinos are obviously of great interest. Such measurements can be based on the reaction

$$\nu_{\rm e} + {}^{71}{\rm Ga} \rightarrow {\rm e}^- + {}^{71}{\rm Ge}\ , \tag{11.8}$$

which is sensitive to neutrinos of energy exceeding 0.23 MeV. Two such experiments have been carried out, using 30 and 60 tons of gallium (corresponding to a large fraction of the total World reserve at the time the experiments were established). One of the experiments was the GALLEX experiment at the Gran Sasso in Italy (*e.g.* Anselmann *et al.* 1995); a compilation of the results of this experiment showed a capture rate of 78 ± 8 SNU (Kirsten 1999). The second experiment, the SAGE experiment at the Baksan Neutrino Observatory, found a capture rate of 67 ± 10 SNU (Abdurashitov *et al.* 1999), consistent with the GALLEX result. This is substantially below the total predicted value of around 135 SNU (*e.g.* Bahcall & Pinsonneault 1995), but consistent with the rate coming from the low-energy neutrinos produced in the PP-I chain.

Given the increasing precision of the solar oscillation measurements, by the late 1990es it was difficult to imagine that a solar model could be found which was both consistent with the oscillation frequencies and with the observationally inferred neutrino flux. In view of the amount of oscillation data, and the ability to use these data to infer detailed properties of the Sun which were largely in agreement with the models, it appeared most reasonable to assume that the structure of solar models was basically correct, and that the solution to the neutrino problem had to be found in terms of the properties of the neutrino.

Already Gribov & Pontecorvo (1969) speculated that some of the neutrinos produced by nuclear reactions in the Sun changed character between the source and the detector, such that they would not be detected. The basis for this effect is the existence of two additional types of neutrinos, in addition to the electron neutrino $\nu_{\rm e}$: the *muon neutrino* ν_μ and the *tau neutrino* ν_τ. The detectors considered so far are exclusively or predominantly sensitive to the electron neutrinos. Neutrinos are normally considered to be massless; however, if the neutrinos have masses, and if the mass of the $\nu_{\rm e}$ differs from that of the other types, there is a finite probability that the $\nu_{\rm e}$ neutrino may be transformed into a ν_μ or ν_τ. This can happen either in vacuum or through interaction with matter in the Sun as proposed in the Mikheyev-Smirnov-Wolfenstein (or MSW) effect (Wolfenstein 1978; Mikheyev & Smirnov 1985). Of the experiments discussed so far, the electron-scattering experiment is predominantly sensitive to the $\nu_{\rm e}$, although with some sensitivity to the other types, whereas the ^{37}Cl and ^{71}Ga experiments are exclusively sensitive to $\nu_{\rm e}$. Thus, conversion of a substantial fraction of the $\nu_{\rm e}$ to the other types may explain the observed deficit. The magnitude of the effect depends on the mass differences, and on parameters describing the interaction; however, it was possible to choose parameters such that the predictions were consistent with the observations (for an overview, see Bahcall, Krastev & Smirnov 1998). Some evidence for neutrino oscillations, involving the muon neutrinos, had been obtained from measurements of neutrinos produced in the Earth's atmosphere by reactions involving cosmic rays (*e.g.* Fukuda *et al.* 1998b; Kearns, Kajita & Totsuka 1999); this lent credence to the MSW effect as an explanation of the solar neutrino deficit.

Decisive tests of the mechanism came from the Sudbury Neutrino Observatory (SNO) in Canada (see Boger *et al.* 2000). SNO measured solar high-energy (^{8}B) neutrinos through reactions with deuterium (^{2}H) in heavy water as well as through electron scattering. Of the two relevant reactions with ^{2}H, one (the so-called charged-current reaction) is sensitive exclusively to $\nu_{\rm e}$, whereas the second (the neutral-current reaction) has comparable sensitivity to all three types. The rate measured with the charged-current reaction may therefore be compared with the rate from previous electron-scattering measurements to deduce the number of ν_μ and ν_τ, to which the electron-scattering experiments also have some modest sensitivity. This provides a measure of the extent to which neutrino conversion has taken place and therefore allows an estimate of the original neutrino production rate in the solar core. The striking result was that the answer agreed, to within errors, with the predictions of standard solar models (Ahmad *et al.*, 2001). The decisive demonstration of neutrino conversion was obtained by Ahmad *et al.* (2002), who used SNO to measure the neutrino flux with the neutral-current reaction. The results yielded a flux at the Earth of $\nu_{\rm e}$ of $(1.76 \pm 0.1) \times 10^6\,{\rm cm}^{-2}\,{\rm sec}^{-1}$ and a flux of other neutrino types (ν_μ and ν_τ) of $(3.41 \pm 0.66) \times 10^6\,{\rm cm}^{-2}\,{\rm sec}^{-1}$. This was again consistent with solar models, and furthermore provided strong constraints on the parameters controlling the neutrino conversions.

In parallel with these efforts to study neutrino conversion from solar observations, terrestrial experiments have been carried out. Eguchi *et al.* (2003) measured the flux of electron antineutrinos $\overline{\nu}_{\rm e}$ from commercial nuclear reactors, and found strong evidence for neutrino oscillations. Other experiments use beams of neutrinos from accelerators, where the neutrinos travel over distances of several hundred kilometers towards neutrino detectors. However, the size of the Earth sets a natural limit to the scale of such experiments. Thus, observations of solar neutrinos remain a very important possibility for studying the properties of the neutrino experimentally, provided that conditions in the solar core can be determined with sufficient accuracy, from observations of solar oscillations, that the Sun can be regarded as a well-calibrated neutrino source.

A recent important result is the first definite detection by the Borexino experiment[18] of solar neutrinos from the CNO cycle (Agostini *et al.*, 2020; Appel *et al.*, 2022). Such observations may eventually provide information concerning the potential issues with the heavy-element abundances in the deep solar interior (see Section 11.5.2). In fact, the latest results provide a slight preference for a higher ratio $Z_{\rm s}/X_{\rm s}$ than found in more recent spectroscopic analyses such as Asplund *et al.* (2009).

[18] A liquid scintillator experiment conveniently placed next to a motorway tunnel through the Appenine Mountains in central Italy, which operated between 2007 and 2021.

Chapter 12

Evolution after the main sequence

12.1 Introduction

When hydrogen is exhausted near the centre, the star is left with a core consisting of helium and a small amount of heavy elements. Initially the temperature of the core is far below the 10^8 K required for helium ignition, and hence there is no nuclear energy generation in the core. Although there may still be some release of energy due to gravitational contraction (see below) the luminosity in the core is generally very low. It then follows from equation (5.8) that the temperature gradient is small, *i.e.*, the core is almost *isothermal*.

Surrounding the core is a region containing hydrogen where the temperature is still high enough for hydrogen burning to proceed. This region, which is known as a *hydrogen shell source*, provides the energy from which the luminosity of the star is derived. As the hydrogen is converted into helium in the shell source, the mass of the inert helium core increases. This leads to contraction of the core. As usual the contraction releases gravitational potential energy, part of which goes towards increasing the thermal energy of the core. As long as the core is not degenerate the increase in thermal energy leads to an increase in temperature,[1] up to the point where the temperature of the core is sufficiently high for helium burning to begin. Very roughly the process is then repeated: the star burns helium in the core (while still maintaining a hydrogen shell source) until helium is exhausted; the star then has a contracting core consisting of ^{12}C and ^{16}O (*cf.* section 8.6), surrounded by a helium shell source and a hydrogen shell source; the contraction of the core may proceed up to the point where the temperature is high enough for carbon ignition; and so on.

This rough sketch ignores a large amount of fascinating detail. Particularly important is the response of the observable properties of the star to the changes in the core. This response can to a large extent be understood in terms of a very simple principle, which may be called

> **The shell-burning law:** When the region within a burning shell contracts, the region outside the shell expands; and when the region inside the shell expands, the region outside the shell contracts.

As discussed in section 12.2, this rule appears to apply also in some cases where there are two shell-burning regions present.

[1] Compare with the discussion of the evolution of a proto-star towards hydrogen ignition in section 10.3.2.

The shell-burning law is undoubtedly confirmed by numerical computations; in particular, during the hydrogen shell-burning phase the star expands to such an extent that it becomes a red giant. Despite many attempts,[2] there has been no convincing arguments, in simple terms, for why this should be the case. A problem for such an explanation is obviously that all parts of the star interact with each other, and hence it is not easy from the numerical results to see which part of the change in structure is the dominant cause of the evolution, and which parts are secondary effects. An example of the complications that one may get into when investigating this question is given in Figure 12.1; one might hope, perhaps a little naively, that a simpler picture may eventually emerge.

A recent paper by Miller Bertolami (2022) does in fact provide some insight at least in the evolution during the hydrogen-shell-burning phase. This is based on combining simple scaling relations, such as those used in Chapter 7, to investigate the interaction between the properties of the shell source, the core and the envelope. A result, also seen in the numerical model, is a drastic decrease in density across the shell source and consequently a low density in the envelope (see also Fig. 12.14 below). Given the mass remaining in the envelope, this requires a larger volume to hold the mass and hence an increase in the radius.

In the following, we take the simpler attitude of accepting the shell-burning law and on that basis trying to interpret the results of numerical calculations. To illustrate this, let us consider the evolutionary tracks shown in Figure 11.5. The change in effective temperature and luminosity may be understood by noting that, as long as the star has a substantial region dominated by radiative energy transport, mass, radius and luminosity must be related by equations (7.7) or (7.8), depending on the dominant source of opacity. This corresponds to the situation for the contracting star before it reached the main sequence; hence, as the star expands, it reverts the evolution before the main sequence: the effective temperature decreases and the luminosity either decreases somewhat or stays constant, depending on the appropriate mass-luminosity relation. As argued in section 7.1, the high temperature sensitivity of the nuclear reactions (which in the shell are probably dominated by the CNO cycle) makes it possible for the luminosity to adjust itself to match the requirements for equilibrium. Once the effective temperature gets so low that the star approaches the Hayashi track, the star develops a very deep outer convection zone. Furthermore, as mentioned in section 7.2.1, the region to the right of the Hayashi track is "forbidden". Hence, as the star continues to expand, it is forced to move up the Hayashi track, with a resulting strong increase in the luminosity; again, it is possible to achieve this luminosity increase with a fairly modest increase in the temperature in the shell-burning source.[3]

An important feature of the evolution of stars with masses more than a few solar masses is the occurrence of loops in the $(\log T_{\rm eff}, \log L_{\rm s})$ diagram. As discussed in the following, these are associated with the onset or burn-out of different sources of nuclear energy and can to some extent be understood in terms of the shell-burning law and the relation between effective temperature and luminosity. When the surface radius of the

[2] See, for example, Höppner & Weigert (1973); Eggleton & Faulkner (1981); Iben & Renzini (1984); Weiss (1989). A short summary was given by Tayler (1988).

[3] This argument is sometimes reversed: it is stated that the increase in luminosity moves the star up the Hayashi track, and hence forces the expansion. However, it seems more satisfactory, particularly in view of the ease with which the star may increase its nuclear energy generation, to assume that the same principle is operating both before and after the star reaches the Hayashi track, and hence to take the expansion as the primary effect.

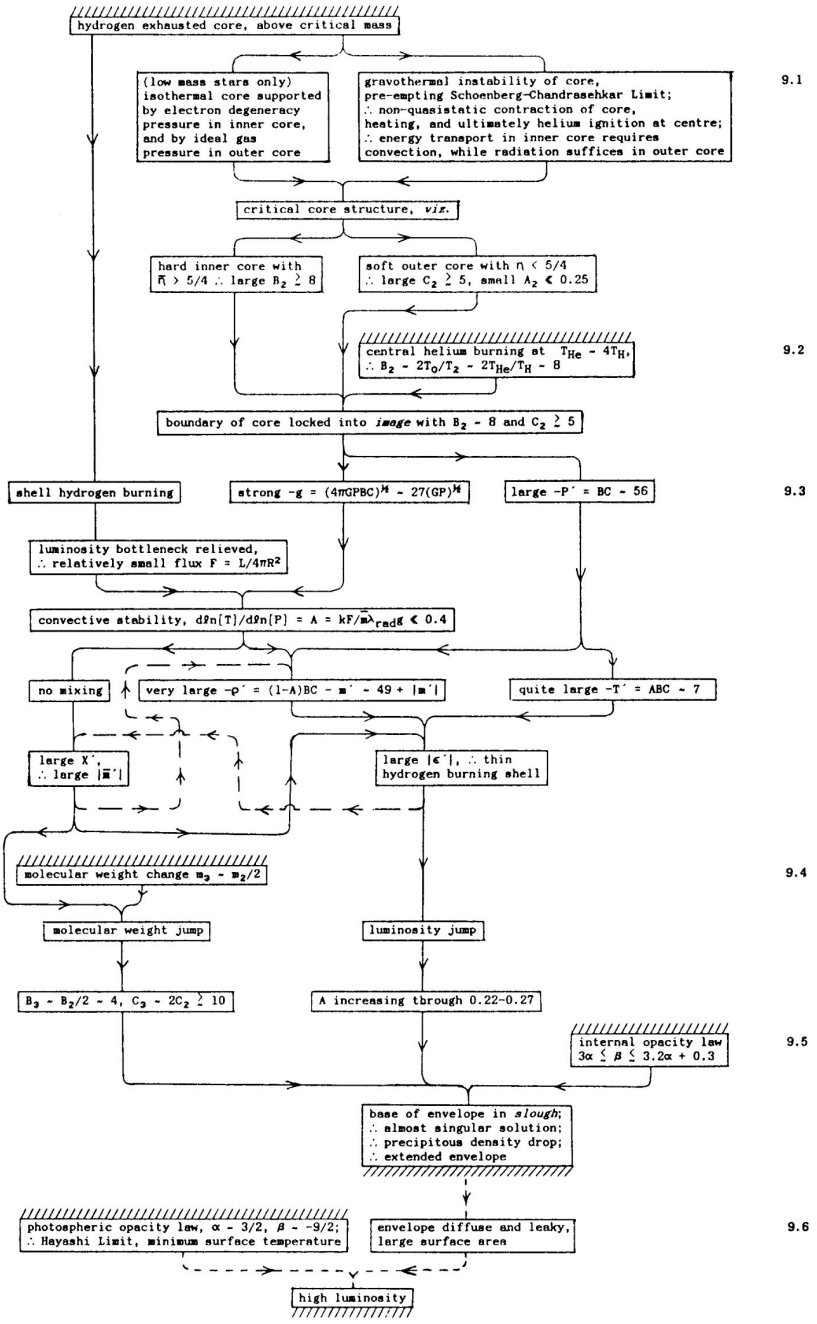

Figure 12.1: An attempt, made by Whitworth (1989), to illustrate the hierarchy of cause and effect which leads to stars becoming red giants. For further detail, and explanation of the notation, reference should be made to the original paper.

star decreases, the effective temperature increases, and the star moves to the left in the $(\log T_{\rm eff}, \log L_{\rm s})$ diagram. The opposite is true when the surface radius increases. The behaviour of the surface radius is ultimately controlled by the evolution of the stellar core, the connection being established through the shell-burning law. The presence of loops is important for comparisons with observed properties of stars (see also section 13.3). Furthermore, the loops are essential for understanding the *Cepheid pulsating stars*. These stars, which are observed to execute radial oscillations, are found in a narrow strip in the HR diagram which crosses the loops. Hence most of the observed Cepheids are in late evolutionary stages. By studying them one may hope to get information about complex aspects of stellar evolution theory.

In the remainder of this chapter we discuss in more detail the evolution through the shell helium-burning phase, for stars of low and moderate mass; the principal feature distinguishing between the two cases is whether or not the star develops a strongly degenerate core. This is based on several different evolution calculations, with codes spanning more than 50 years. Thus, although the general properties are consistent, there are differences between the detailed behaviour, possibly also reflecting differences in the underlying model physics or assumptions.

The evolution of more massive stars, which get into even later nuclear-burning phases, is discussed in Chapter 14.

12.2 Evolution of a moderate-mass star

Early calculations for this case may be exemplified by the evolution of a $5\,{\rm M}_\odot$ star, as shown in Figure 11.5, and in more detail in Figure 12.2.

A notable feature as the star leaves the main sequence is the "hook" in the evolutionary track, towards higher effective temperature. This is a result of the convective cores in moderate- and high-mass stars. As discussed in section 11.3.2, hydrogen is exhausted throughout the core at the same time. This would tend to decrease the energy production, since, at least initially, the temperature outside the core is too low for significant hydrogen shell burning to take place. When the hydrogen abundance gets very low, the star attempts to maintain the energy production by increasing the central temperature. This is achieved through an overall contraction; as usual, the contraction results in a release of gravitational energy, half of which is converted into thermal energy and contributes to the heating of the core. As a result, the direction of evolution turns towards higher effective temperature. Hence in a sense the star reverts to the direction of evolution of its early childhood, but most of the energy production is still provided by the central nuclear burning, with only a relatively modest contribution from the release of gravitational energy. At the same time a hydrogen-burning shell is gradually established. However, only when central hydrogen has virtually disappeared does the shell source become dominant. At that point the shell-burning law takes over, and the core contraction is accompanied by an expansion of the outer parts of the star, leading to evolution towards lower effective temperature. From Figure 11.5 it is evident that stars of mass as low as $1.25\,{\rm M}_\odot$ display a hook; this is consistent with Figure 11.4, which show the presence of a convective core, at least on the zero-age main sequence, in such stars.

It may be shown that, assuming the ideal-gas law, there is an upper limit to the mass of an isothermal core which can be in hydrostatic and thermal equilibrium: the mass fraction

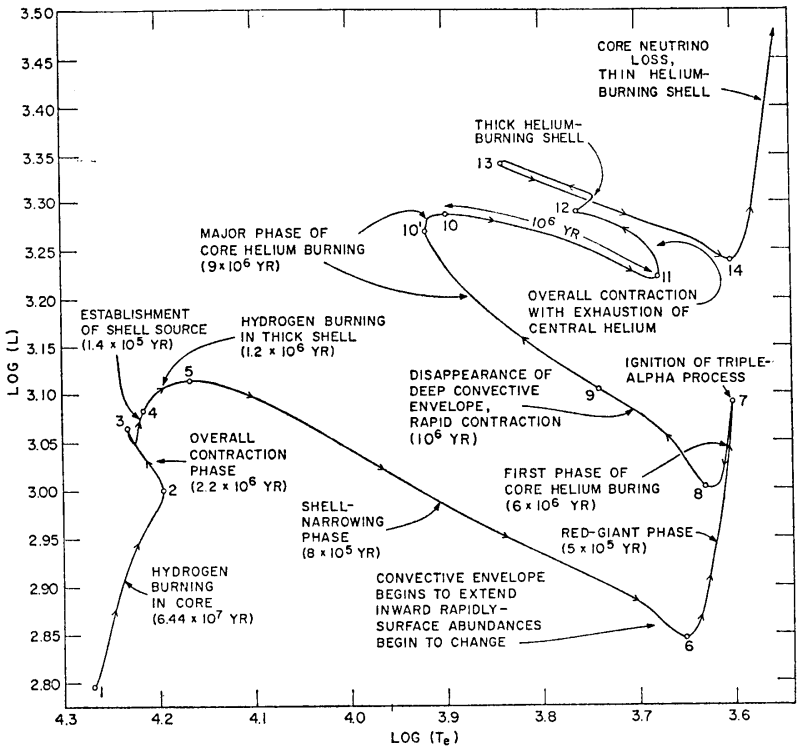

Figure 12.2: Evolutionary track of a Population I star of $5\,M_\odot$ in the Hertzsprung-Russell diagram. The luminosity is given in units of $3.86 \times 10^{33}\,\mathrm{erg\,sec^{-1}}$, and the effective temperature T_e is in K. The evolution time between the labeled points is given in years. (From Iben 1967a.)

$q_\mathrm{c} = m_\mathrm{c}/M$ in the core must be smaller than the so-called *Schönberg-Chandrasekhar limit* $q_\mathrm{SC} \simeq 0.1$ (Schönberg & Chandrasekhar 1942; for a simple discussion of this limit, see Kippenhahn *et al.*, 2012). As the $5\,M_\odot$ star leaves the main sequence, the mass of the helium core, corresponding to the previously convective core, is already very close to this limit (see also Figure 12.3); with the growth of the core during shell burning the limit is quickly exceeded. The core then contracts, essentially on a thermal time scale, and the outer parts of the star expand, moving the star towards and then up the Hayashi track. The comparatively great speed of this phase of evolution is evident in Table 11.1 and in Figure 12.2; observationally it means that the probability of seeing a star during this phase in its evolution is very small, and consequently the corresponding region in the HR diagram, which is known as *Hertzsprung gap*, is sparsely populated with stars.

The changes in the interior of the star are illustrated in Figure 12.3.[4] The format is very similar to Figure 11.4 except that the abscissa is now age, rather than mass;[5] here, however, regions with substantial nuclear energy generation are indicated by heavy hatching, and the regions where composition has been modified are indicated by dots. The figure clearly

[4]Note that this comes from a different evolution calculation from Iben's, which was shown in Figure 12.2, and hence differs from that figure in the details; the overall features are very similar, however.

[5]Both figures can be regarded as cuts through a three-dimensional diagram illustrating structure as a function of stellar mass and age.

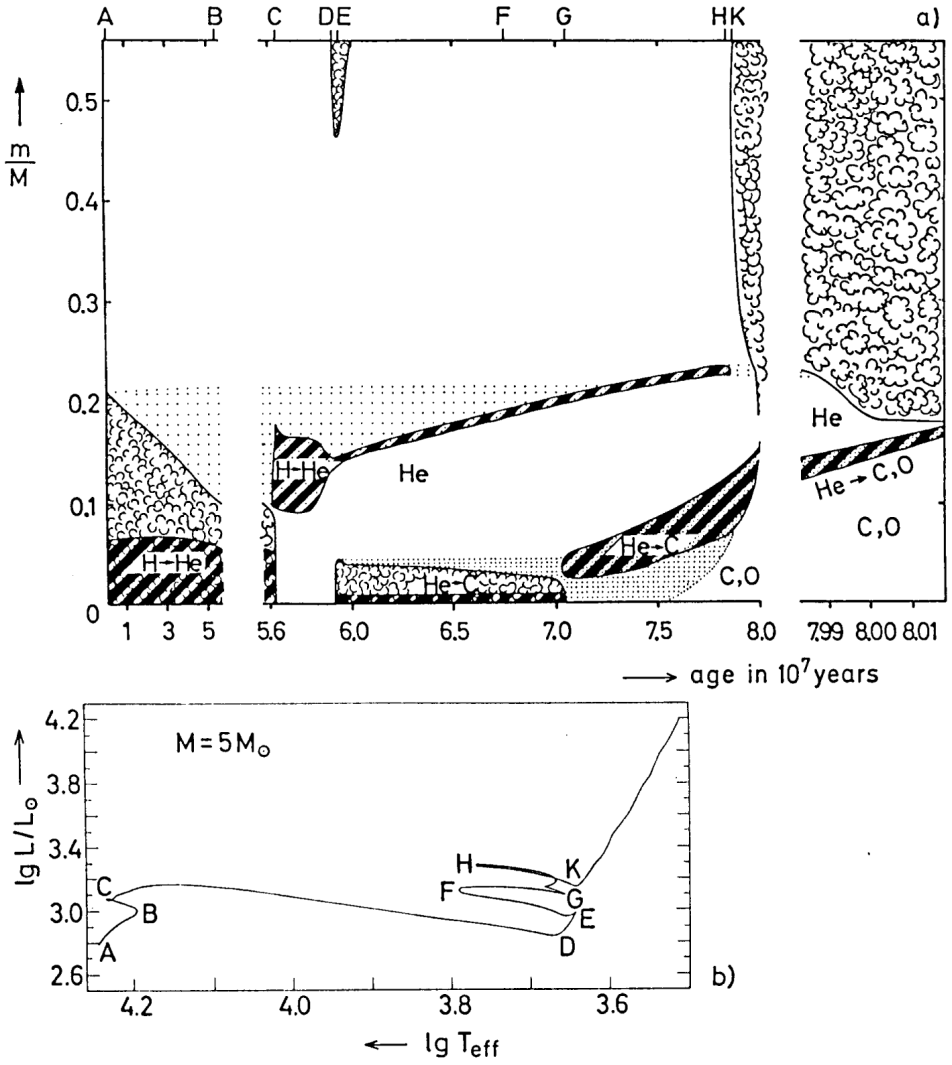

Figure 12.3: Panel a) shows the evolution of the internal structure of a $5\,M_\odot$ star. The format is similar to that used in Figure 11.4: The abscissa is the age of the star (note the change of scale, to resolve the increased speed of evolution, at 5.5×10^7 years and 8×10^7 years). At each point in time the internal structure is represented on the ordinate in terms of the mass fraction m/M; only the inner 60 per cent by mass of the star is included. The "cloudy areas" indicate the extent of the convection zones. Heavily hatched regions indicate where the nuclear energy generation rate ϵ exceeds $10^3\,\mathrm{erg\,g^{-1}\,sec^{-1}}$. Regions of variable chemical composition are dotted. The letters $A \ldots K$ above the upper axis indicate the corresponding points in the evolutionary track, which is shown in panel b) (reproduced from Kippenhahn *et al.*, 2012).

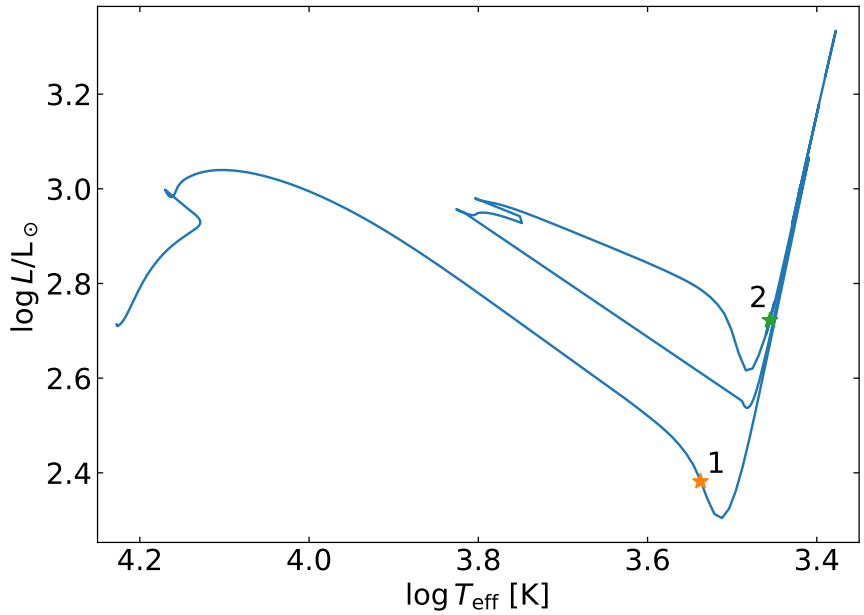

Figure 12.4: Evolution of a $5\,M_\odot$ model, starting from the ZAMS. The model was computed by Mark Lykke Winther using the MESA code (Paxton *et al.*, 2019).

shows the shrinking convective core, which extends beyond the region of nuclear burning, during the main-sequence phase, and the onset of hydrogen shell burning. It should be noted also that just before the onset of core helium burning (discussed further below) the convective envelope extends very deep into the star; this clearly corresponds to the ascent of the star up the Hayashi track.

To illustrate further properties of the evolution we consider yet another model calculation, shown in the HR diagram in Figure 12.4. Some details of the internal structure of the model at the end of the Hertzsprung gap, just before the ascent on the Hayashi track, are shown in Iben diagram in Figure 12.5; here the variables have been scaled to fit within a common range, the actual ranges being given in the figure caption. This model corresponds to point 1 in Figure 12.4. The variation in L is particularly interesting. It is clear that most of the energy is generated in a very thin shell, at $m/M \simeq 0.12$. It should be noted, however, that there is also some increase in luminosity in the core; this is caused by the release of gravitational energy owing to the core contraction. In constrast, the *decrease* in L in the outer parts of the star reflects the relatively rapid expansion: a significant fraction of the energy generated by nuclear reactions is used to work against gravity to expand the star. The variation in the hydrogen abundance reflects the profile left behind by the contracting convective core during the main-sequence phase (*cf.* Figure 11.7), but cut off by the expanding shell source. Finally, because of the generation of energy by the contraction of the core, a temperature gradient is required to transport the energy, and hence the core is no longer isothermal.

The core contraction and expansion of the surface continue with the star moving up the Hayashi track, to the point where core helium burning becomes efficient. The release

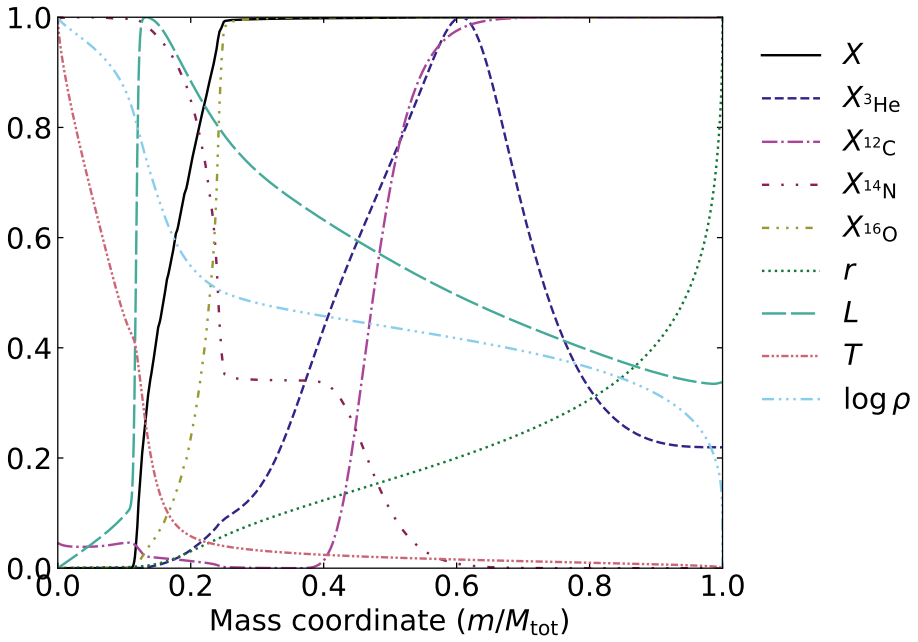

Figure 12.5: The variation with mass fraction of a number of quantities in a $5\,\mathrm{M}_\odot$ model just before the first ascent on the Hayashi track (at point 1 in Figure 12.4). $X_{^3\rm He}$, $X_{^{12}\rm C}$, $X_{^{14}\rm N}$ and $X_{^{16}\rm O}$ indicate the abundances of ^{3}He, ^{12}C, ^{14}N and ^{16}O. The other symbols have their usual meaning. The variables have been rescaled to fit within the same range. The actual ranges are $0 \leq X \leq 0.71$, $0 \leq X_{^3\rm He} \leq 1.3 \times 10^{-4}$, $1.8 \times 10^{-5} \leq X_{^{12}\rm C} \leq 3.4 \times 10^{-3}$, $0 \leq X_{^{14}\rm N} \leq 0.013$, $3.4 \times 10^{-4} \leq X_{^{16}\rm O} \leq 9.4 \times 10^{-3}$, $0 \leq r \leq 43.60\,\mathrm{R}_\odot$, $0 \leq L \leq 710\,\mathrm{L}_\odot$, $3.4 \times 10^3 \leq T \leq 8.1 \times 10^7\,\mathrm{K}$, $-7.57 \leq \log\rho \leq 3.93\,[\mathrm{g\,cm^{-3}}]$. The surface radius of the model is $43.6\,\mathrm{R}_\odot$. (Adapted from Iben 1966.)

of energy in the core causes it to expand. Since the hydrogen shell-burning source is still active, the outer parts of the star contract, in accordance with the shell-burning law. Hence the direction of evolution is reversed; the star moves down the Hayashi track and, when the convective envelope shrinks sufficiently, towards higher effective temperature. Once the star becomes dominated by radiative energy transport, the luminosity is again approximately determined by equation (7.7); hence the evolution occurs along a track which is roughly parallel with that of the contraction before the main sequence, or the expansion during evolution away from the main sequence.

Due to the high temperature sensitivity of the triple-alpha reaction, helium burning occurs in a convective core, as is evident from Figure 12.3.

Once the helium burning is well established, the expansion of the core and the contraction of the surface stops, and the star enters a relatively extended period of core helium burning. Even during this phase, however, the hydrogen shell source contributes a substantial part of the energy. As helium is converted into carbon and oxygen (*cf.* section 8.6), the mean molecular weight of material in the core increases. The effect is the same as during the core hydrogen burning: the core contracts and heats up. Again the shell-burning law operates, causing the envelope to expand and the star to move back towards

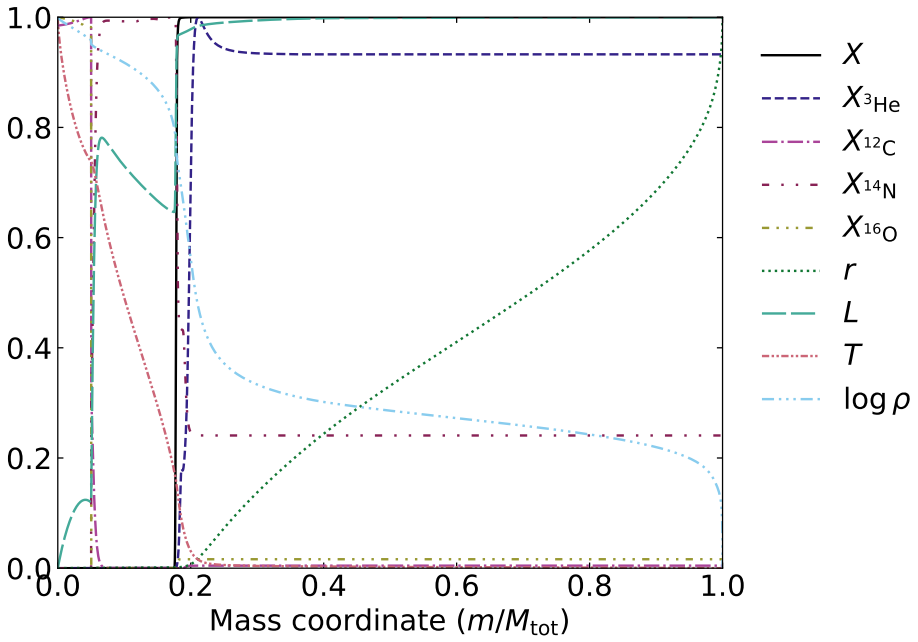

Figure 12.6: The variation with mass fraction of luminosity L, temperature T and distance r from the centre in a $5\,\mathrm{M}_\odot$ model during the double shell-burning phase (at point 2 in Figure 12.4). The variables have been rescaled to fit within the same range. The actual ranges are $0 \leq X \leq 0.69$, $0 \leq X_{^3\mathrm{He}} \leq 6.1 \times 10^{-5}$, $0 \leq X_{^{12}\mathrm{C}} \leq 0.46$, $0 \leq X_{^{14}\mathrm{N}} \leq 0.013$, $0 \leq X_{^{16}\mathrm{O}} \leq 0.52$, $0 \leq r \leq 94.19\,\mathrm{R}_\odot$, $0 \leq L \leq 530\,\mathrm{L}_\odot$, $2.9 \times 10^3 \leq T \leq 1.8 \times 10^8\,\mathrm{K}$, $-8.10 \leq \log\rho \leq 4.47\,[\mathrm{g\,cm^{-3}}]$. (Adapted from Iben 1966.)

the Hayashi track.

When helium is exhausted in the core, helium burning is established in a shell, while the hydrogen shell burning continues; hence the star now has two shell sources (*cf.* Figure 12.3). Just as the exhaustion of hydrogen left a helium core, the exhaustion of helium leaves a core consisting of carbon and oxygen, in which the temperature is too low for the next type of nuclear reaction, *viz.* carbon burning, to take place. The core therefore contracts and heats up, at least initially. But now there are two shell sources. The Iben calculations shown in Figure 12.2 clearly demonstrate the effect of the shell-burning law as applied to the two shell sources. The helium shell source reverses the contraction of the core, and hence leads to an expansion of the region between the two shells; applying again the shell-burning law to the hydrogen shell it then follows that the outer parts of the star contract, and the star yet again moves towards higher effective temperature, again roughly following the relation (7.7) between effective temperature and luminosity. This behaviour is evident in Figure 12.2.

Although this is a beautiful illustration of the operation of the shell-burning law, the recent calculations illustrated in Figure 12.4 show a less clear behaviour. Here the exhaustion of central helium and the establishment of the helium shell burning happen only when the star is near the Hayashi track. Figure 12.6 shows the internal properties of the star during the phase with two shell sources, as obtained from the calculations,

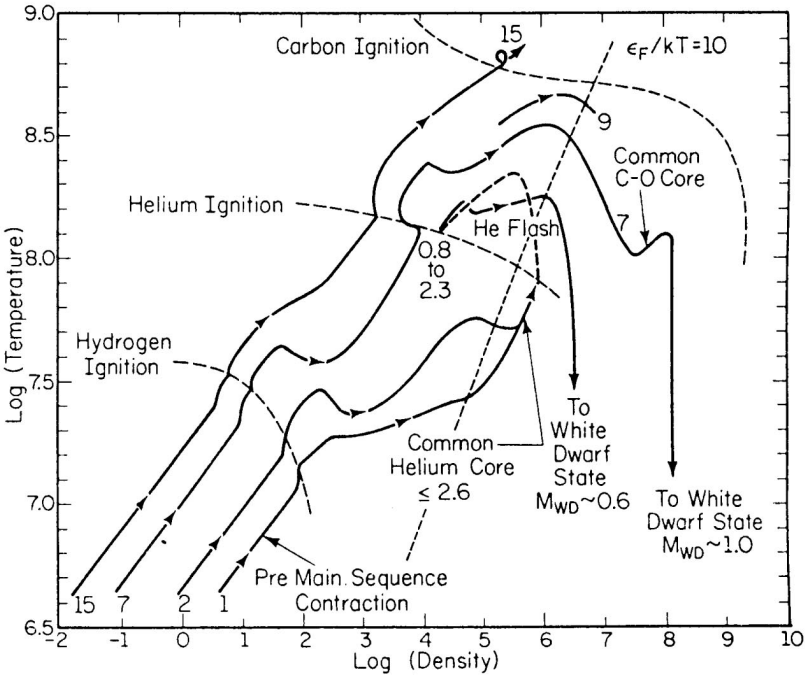

Figure 12.7: Tracks in the density-temperature plane showing the variation with evolution of conditions at the centres of stars of masses 1, 2, 7 and 15 $M_\odot$. The density is in units of $g\,cm^{-3}$, and the temperature is in K. The points where hydrogen, helium and carbon burning are ignited are sketched. Also indicated is the line where the electron Fermi energy equals $10k_BT$; this roughly marks the point where electron degeneracy becomes important. (From Iben 1985.)

corresponding to point 2 in Figure 12.4. The the two shell sources are visible as the sharp jumps in luminosity. The luminosity inside the innermost shell comes exclusively from the gravitational contraction of the core. Between the two shells the luminosity decreases; the expansion of this region requires energy to do work against gravity (compare with the behaviour of L in the outer parts of the model shown in Figure 12.5). In contrast, there is still a modest contraction outside the hydrogen shell, which *releases* gravitational potential energy, thus causing the slight gradual increase in luminosity outside the outermost shell source. During the helium burning the star has had a convective core, which, unlike the situation on the main sequence, has not shrunk during evolution, and consequently the carbon and oxygen produced by helium burning are confined below the helium shell source.

One might now expect a repetition of the story, the core contraction leading to sufficiently high temperatures for carbon burning to set in. However, stars of mass smaller than about $10\,M_\odot$ never get this far. As in the contraction before the main sequence, the problem is degeneracy. The carbon-oxygen core becomes degenerate before the temperature reaches the temperature required for carbon ignition, and at that point the increase in temperature stops. This is illustrated in Figure 12.7, which shows the evolution of stars of various masses in a $(\log \rho_c, \log T_c)$ diagram (the $5\,M_\odot$ star which is discussed here behaves quite similarly to the $7\,M_\odot$ star shown in the figure). Also shown are the temperature-

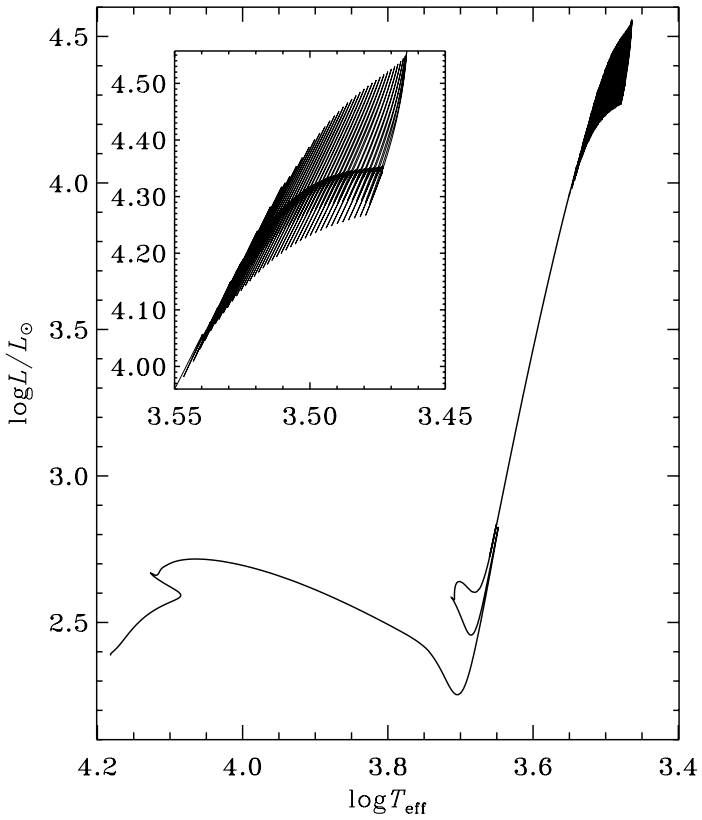

Figure 12.8: Evolution track for a $4\,M_\odot$ model, from the zero-age main sequence to the asymptotic giant branch. As discussed in the text, the behavior in the diagram can be understood in terms of changes in the regions of nuclear energy generation. The insert shows the last phases in more detail, to illustrate the oscillations caused by the thermal instability between the hydrogen and helium shell sources. (Data kindly provided by A. V. Sweigart.)

density lines corresponding to the various stages of nuclear burning, and a line separating the region where degeneracy is important from the region where the ideal-gas law is valid.[6]

In the Iben calculations in Figure 12.2 the direction of evolution is reversed again some time after helium shell-burning has been established, the star moving back towards and up the Hayashi track. The reason for this is that the region between the two shells expands so much that the temperature in the hydrogen-burning shell decreases to the point where the shell is extinguished. The star then has only one shell source; the continuing core contraction therefore leads to expansion of the surface, and hence to the decrease in the effective temperature until the Hayashi track is reached, and then to another ascent of the Hayashi track. A similar behaviour is found in Figure 12.4. This phase of evolution

[6]Returning to pre-main-sequence evolution it should be noted that a star below the minimum mass for hydrogen ignition of about $0.08\,M_\odot$ would have appeared substantially below and to the right of the line for $1\,M_\odot$, crossing into the region of degeneracy and beginning to decrease the central temperature before reaching the conditions required for hydrogen burning. See also Exercise 10.1.

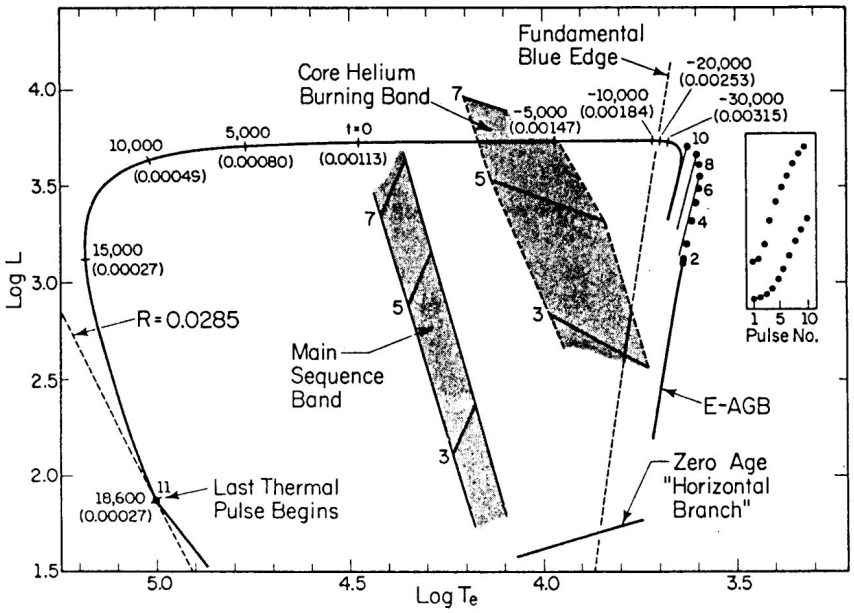

Figure 12.9: The evolution from the Asymptotic Giant Branch towards the white dwarf stage (the figure illustrates the evolution of a $2\,M_\odot$ star, but is also qualitatively correct for the $5\,M_\odot$ star considered here). At the end of the AGB phase, the star undergoes thermal pulses, schematically indicated by points $2 \ldots 10$. The star then suffers strong mass loss, leading to rapid evolution towards higher effective temperature. The evolution times, in years, are indicated relative to a zero-point which has arbitrarily been taken as the point where the star crosses the main sequence. The numbers in brackets indicate the mass left in the hydrogen-rich envelope at that point of evolution. (From Iben 1985.)

is called the *Asymptotic Giant Branch* (or AGB) phase, to distinguish it from the initial ascent of the Hayashi track before helium ignition. As shown in Figure 12.3, the star develops an extremely deep convective envelope during this phase, reaching down well into the layers that have undergone nuclear burning. The resulting mixing (or "dredge-up") to the stellar surface of material that has been processed in nuclear reactions changes the surface composition of the star. The distribution of abundances among the elements, including the ratios between different isotopes, provides very important clues to the nuclear reactions that have occurred in the interior of the star.

The subsequent evolution is complex, as illustrated in Figure 12.8. A thermal instability develops in the helium shell source, causing thermal pulses where the star alternates between having a hydrogen and a helium shell source. As illustrated in the figure (see the insert) the pulses lead to a very large number of excursions in the surface luminosity and temperature; the changes in the structure of the interior, with intermittent convective regions, lead to nuclear reactions producing very heavy elements through neutron capture (see Chapter 15), subsequently brought to the surface by convective mixing and observed in the spectra of these stars. At the same time the luminosity of the star increases greatly, as does its radius. Possibly as a result of the increase in radius and luminosity, the ther-

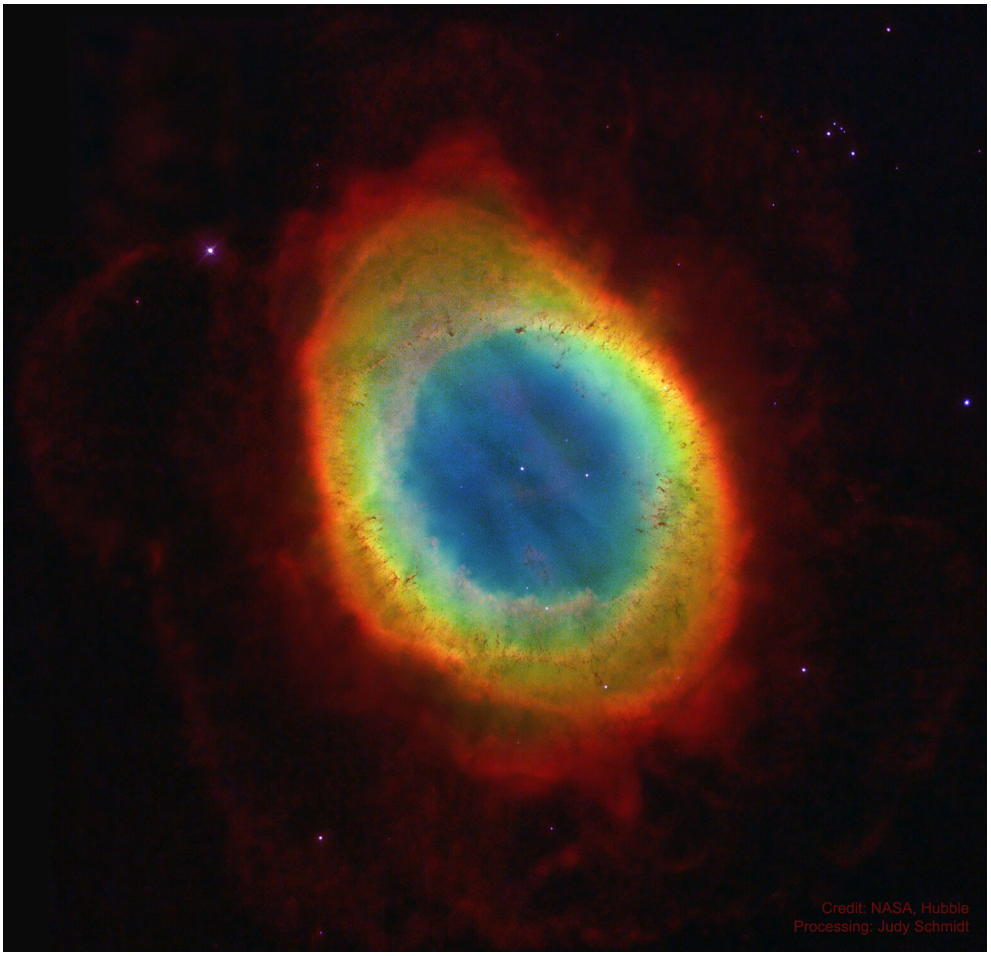

Figure 12.10: The Ring Nebula (M57), an example of a planetary nebula resulting from the late evolution of low- and intermediate-mass stars. The white star in the middle of the ring is the very hot left-over core of the star, which will evolve into a white dwarf.

mal pulses, or instabilities in the outer layers of the star, the star begins to lose mass at a fairly rapid rate.[7] The result appears to be that the star eventually loses essentially all the material outside the degenerate carbon-oxygen core, evolving rapidly across the HR diagram as the envelope extent decreases (*cf.* Fig. 12.9).

The end result is a bare core which is initially extremely hot and hence quite luminous, despite its small size. It illuminates the material which has been lost, and which for a few thousand years forms a fairly well-defined shell around the star, and causes it to shine as a *planetary nebula* (see Fig. 12.10). Subsequently the material is dispersed in the interstellar medium; the degenerate core continues to shine through loss of its thermal energy. It cools gradually, reaching an effective temperature of about 4000 K in about 10^{10} years. Such objects, which are called *white dwarfs*, are discussed in Chapter 16.

[7] In analogy with the observed solar wind, this process has been called a "superwind"; however, the fact that it has been given a name does not mean that the underlying physical mechanism is understood.

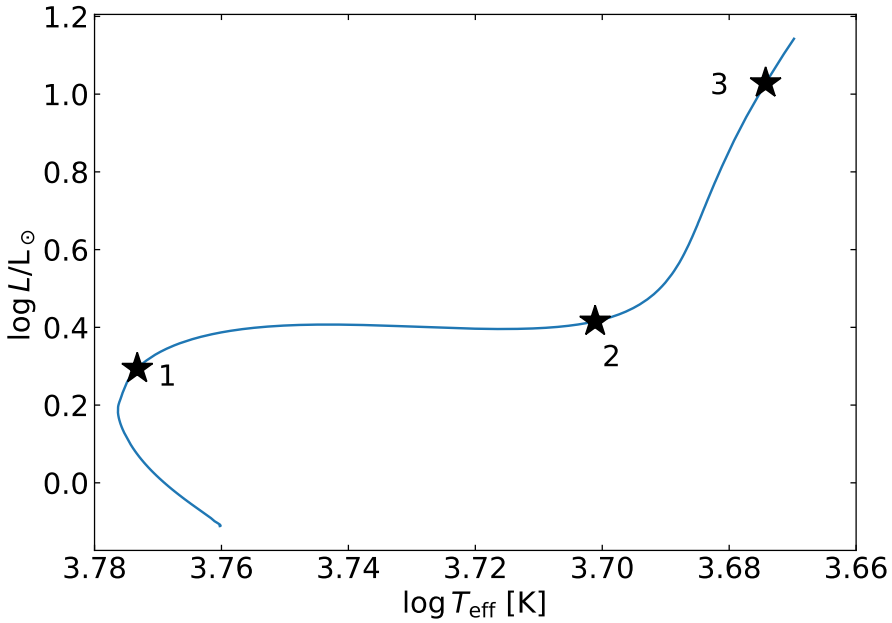

Figure 12.11: Hertzsprung-Russell diagram of the evolution of a $1\,M_\odot$ stellar model, from the ZAMS to the early part of the red-giant phase. The stars mark models for which the internal structure is illustrated in Figs. 12.12 – 12.14. Based on model calculation by Mark Lykke Winther and Jakob Lysgaard Rørsted, using the GARSTEC code (see Weiss & Schlattl, 2008).

12.3 Evolution of a low-mass star

To illustrate the features that distinguish low-mass stellar evolution from the case discussed above, we consider the evolution of a $1\,M_\odot$ stellar model, shown in the HR diagram in Fig. 12.11. A substantial difference is that such a star does not have a convective core during the main-sequence phase. As a result, hydrogen is initially used up only at the centre (*cf.* Figure 11.6), and there is a gradual transition from core hydrogen burning to hydrogen burning in a thick shell, which initially extends almost to the centre. This stage is illustrated in Figure 12.12.

Exercise 12.1:

Explain the curious variation of the ^{14}N abundance with position in Fig. 12.12, on the basis of discussion of the CNO cycles in Section 8.5.2. You may assume that the surface abundances are unchanged since the star was formed.

The helium core grows gradually, as hydrogen is consumed in the shell. Initially the mass of the core is much below the Schönberg-Chandrasekhar limit, and hence the core is stable; therefore the time scale of evolution is determined by the speed of the nuclear burning, unlike the case for the $5\,M_\odot$ star, where the core contraction occurred on a thermal time

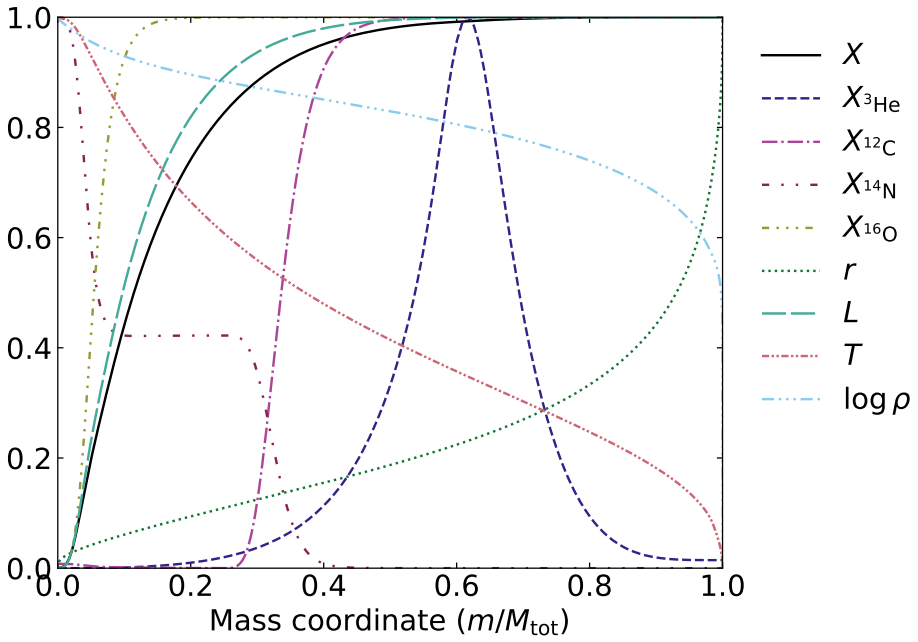

Figure 12.12: The variation with mass fraction of a number of quantities in a $1\,\mathrm{M}_\odot$ model shortly after hydrogen is exhausted at the centre (at point 1 in Figure 12.11). $X_{\rm H}$ gives the hydrogen abundance, whereas $X_{^3\rm He}$, $X_{^{12}\rm C}$, $X_{^{14}\rm N}$ and $X_{^{16}\rm O}$ indicate the abundances of ^{3}He, ^{12}C, ^{14}N and ^{16}O; the curve labelled r shows the variation of the distance r to the centre. The other symbols have their usual meaning. The variables have been rescaled to fit within the same range. The actual ranges are $0 \leq X \leq 0.72$, $1.0 \times 10^{-14} \leq X_{^3\rm He} \leq 4.3 \times 10^{-3}$, $4.2 \times 10^{-6} \leq X_{^{12}\rm C} \leq 2.4 \times 10^{-3}$, $7.0 \times 10^{-4} \leq X_{^{14}\rm N} \leq 7.3 \times 10^{-3}$, $9.6 \times 10^{-4} \leq X_{^{16}\rm O} \leq 5.8 \times 10^{-3}$, $0 \leq r \leq 1.33\,\mathrm{R}_\odot$, $0 \leq L \leq 1.98\,\mathrm{L}_\odot$, $5.9 \times 10^3 \leq T \leq 2.0 \times 10^7\,\mathrm{K}$, $-6.75 \leq \log\rho \leq 2.86\,[\mathrm{g\,cm^{-3}}]$. The surface radius of the model is $1.33\,\mathrm{R}_\odot$. (After Iben 1967b.)

scale as a result of the instability which developed when the core mass exceeded the Schönberg-Chandrasekhar limit. Furthermore, the density of the core is substantially higher than for the $5\,\mathrm{M}_\odot$ star (see Figure 12.7); as a result the core is closer to being degenerate, and hence the Schönberg-Chandrasekhar limit is less sharply defined.

Nevertheless, when the mass of the core exceeds about $0.1\,\mathrm{M}_\odot$, the speed of the contraction increases, and at the same time the thickness of the shell, measured as the range in mass where most of the energy generation takes place, decreases rapidly. This stage is illustrated in Figure 12.13. It is evident that the shell, defined as the region where the luminosity increases, is now quite thin. Furthermore, a slight decrease in luminosity in the outer layers, reflecting the expansion of the envelope, is just visible; although difficult to see, there is also a significant contribution to the luminosity from the release of gravitational energy in the core (this is most visible in the fact that the luminosity requires the temperature gradient to ensure energy transport; hence, unlike in Figure 12.12, the core is not strictly isothermal).

As the core contraction continues, the star moves up the Hayashi track. Also, with

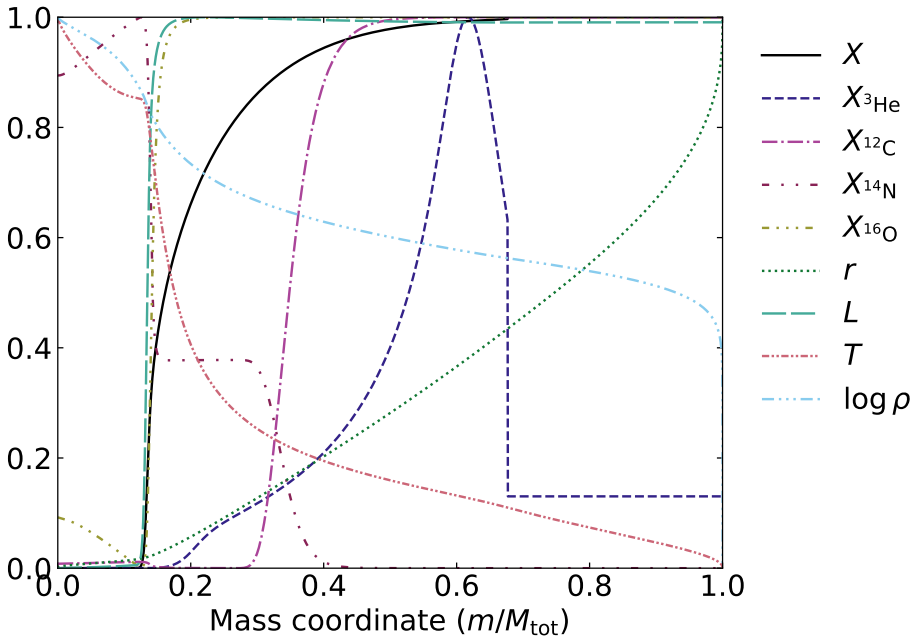

Figure 12.13: The variation with mass fraction of a number of quantities in a $1\,M_\odot$ model after the hydrogen-burning shell has become thin (at point 2 in Figure 12.11). The variables have been rescaled to fit within the same range. The actual ranges are $0 \le X \le 0.72$, $0 \le X_{^3\rm He} \le 4.5 \times 10^{-3}$, $3.9 \times 10^{-6} \le X_{^{12}\rm C} \le 2.4 \times 10^{-3}$, $7.0 \times 10^{-4} \le X_{^{14}\rm N} \le 8.1 \times 10^{-3}$, $4.7 \times 10^{-4} \le X_{^{16}\rm O} \le 5.8 \times 10^{-3}$, $0 \le r \le 2.13\,R_\odot$, $0 \le L \le 2.62\,L_\odot$, $5.0 \times 10^3 \le T \le 2.7 \times 10^7\,$K, $-6.83 \le \log\rho \le 4.34\,[\mathrm{g\,cm^{-3}}]$. The surface radius of the model is $2.13\,R_\odot$. (After Iben 1967b.)

increasing core density matter in the core becomes increasingly degenerate. The innermost third of the model in this phase is shown in Figure 12.14. From the ratio $P_{\rm g}/P$ of the ideal-gas pressure to the actual pressure it is clear that degenerate electrons contribute a large fraction of the pressure at the centre of the model.[8] The star has now developed a convective envelope extending down to $m/M \simeq 0.25$. This is reflected in the sharp change in $X_{\rm H}$ and the abundance $X_{^{14}\rm N}$ of ^{14}N at that point; the convective envelope has reached down into the region where the hydrogen abundance has been changed by nuclear burning on the main sequence, and the resulting mixing has reduced the surface hydrogen abundance from the original value of 0.717 to 0.697.

An interesting feature in Fig. 12.14 (also visible in Fig. 12.13) is the variation of the ^{16}O abundance in the helium core. This reflects the partial conversion of ^{16}O to ^{14}N (see footnote 9 in Chapter 8). This process obviously stops when hydrogen is exhausted and hence proceeds further as the hydrogen shell source moves out through the star, also aided by the increasing temperature in the shell, resulting in the reduction with m/M in $X_{^{16}\rm O}$.

With the onset of degeneracy, the core is no longer heated directly by contraction,

[8] Another consequence of the degeneracy is that the core is again very nearly isothermal; degenerate electrons conduct heat quite efficiently, and hence only a small temperature gradient is required to remove the energy released in the contraction of the core.

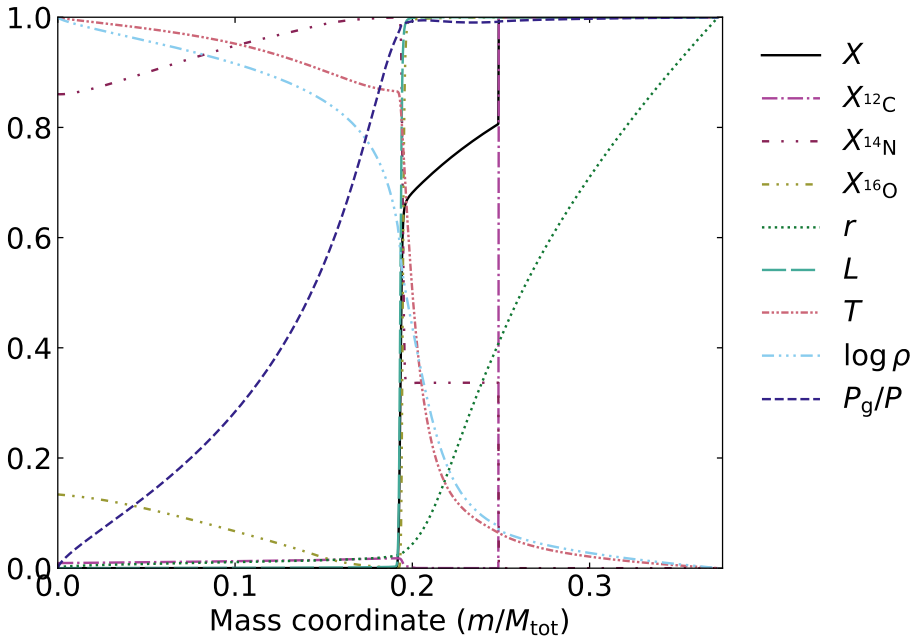

Figure 12.14: The variation with mass fraction of a number of quantities in a $1\,\mathrm{M}_\odot$ model on the Hayashi track (at point 3 in Figure 12.11). $P_{\rm g}/P$ shows the ratio between the pressure computed with the ideal-gas law (equations 3.24 and 3.25) and the actual pressure; the other symbols have the same meaning as in Figure 12.13. The variables have been rescaled to fit within the same range. The actual ranges are $0 \leq X \leq 0.70$, $4.1 \times 10^{-6} \leq X_{^{12}\rm C} \leq 2.0 \times 10^{-3}$, $1.0 \times 10^{-3} \leq X_{^{14}\rm N} \leq 8.3 \times 10^{-3}$, $2.2 \times 10^{-4} \leq X_{^{16}\rm O} \leq 5.8 \times 10^{-3}$, $0 \leq r \leq 1.29\,\mathrm{R}_\odot$, $0 \leq L \leq 10.71\,\mathrm{L}_\odot$, $2.0 \times 10^6 \leq T \leq 3.0 \times 10^7\,\mathrm{K}$, $-1.20 \leq \log\rho \leq 5.01\,[\mathrm{g\,cm^{-3}}]$, $0.26 \leq P_{\rm g}/P \leq 1.0$. The surface radius of the model is $4.89\,\mathrm{R}_\odot$. (After Iben 1967b.)

since the thermal energy of degenerate electrons is independent of temperature. However, the temperature of the hydrogen-burning shell increases as the star moves up the Hayashi track, and this causes an increase in the temperature of the core. When the temperature reaches $10^8\,\mathrm{K}$, helium burning sets in. Unlike the quiet transition to helium burning for the $5\,\mathrm{M}_\odot$ star, this occurs in a thermal run-away, the so-called *helium flash*. The reason is again the degenerate core. In normal (nondegenerate) matter, the release of energy by nuclear burning would cause an increase in the pressure, and hence an expansion and cooling of the matter; in this way equilibrium would be reached between the energy generation and the energy transport. However, in degenerate matter the pressure is essentially independent of temperature; hence when nuclear burning sets in, the temperature of the gas is increased with no change in pressure, and hence no immediate reaction of the core. The increase of the temperature causes a further increase of the energy generation rate, and hence an even stronger increase in the temperature; this leads to a thermal runaway, where the local luminosity in the core increases to of order $10^{11}\,\mathrm{L}_\odot$ during a few hours. This process only stops when the temperature of the core gets so high that degeneracy is lifted [*cf.* the condition (3.61)]. Then the core expands and cools until equilibrium is

reached, and the star enters a phase of quiet core helium burning.

The outer parts of the star cannot react on a time scale shorter than the dynamical time scale, which because of the large radius of the star is of order months. Hence little of the violent activity in the core of the star is visible on the surface. In fact, calculations show that the helium flash only lasts a few hours; the energy it generates is absorbed in work to expand the core and envelope of the star. The detailed changes during the helium flash are still quite uncertain; it is likely that some mass is lost in the process. When equilibrium is restored, the star settles down on the *helium burning main sequence* which observationally corresponds to the horizontal branch, visible in the upper left-hand part of the HR diagram in Figure 2.6a.

Exercise 12.2:

Assume that the helium flash maintains an energy generation corresponding to a local luminosity of $10^{11}\,L_\odot$ for three hours. Compare the total amount of energy liberated with the gravitational binding energy of the core, assumed to have a mass of $0.5\,M_\odot$ and a radius of 10^4 km.

The subsequent evolution of the $1\,M_\odot$ star is probably quite similar to the $5\,M_\odot$ star discussed in section 12.2: after exhaustion of helium in the core the star enters a phase with two shells, finally leading back to the Hayashi track on the Asymptotic Giant Branch, to a phase of thermal instability, to rapid mass loss with the formation of a planetary nebula, and finally to the creation of a white dwarf. This, therefore, is the likely ultimate fate of the Sun. A detailed discussion of the final stages of solar evolution was given by Jørgensen (1991).

Chapter 13

Interpretation of HR diagrams for stellar clusters

13.1 Introduction

All stars in a stellar cluster can be assumed to have formed from the same interstellar gas cloud; hence they presumably have approximately the same age and chemical composition.

Within the simple description of stellar structure that we employ here (neglecting, for example, effects of rotation or a magnetic field), the mass is then the only parameter that distinguishes between the stars in the cluster. Hence the observed properties in a colour-luminosity (or HR) diagram of the cluster are predominantly determined by a single parameter (the mass); we therefore expect the stars to form a single-parameter family of points in the HR diagram, *i.e.*, to fall on a single curve.

This property provides a very valuable test of the theoretical evolution calculations. Furthermore, the results may be used to determine ages and distances to stellar clusters.

13.2 Some properties of isochrones

In Chapters 10 – 12 we presented the results of evolution calculations in terms of *evolutionary tracks* in a $(\log T_{\rm eff}, \log L_{\rm s})$ diagram (see for example Figure 11.5). Here each curve corresponds to models with the same mass but different age. The observed distribution of stars in a stellar cluster, on the other hand, corresponds to stars of the same age but different mass. Such curves can also be plotted in a $(\log T_{\rm eff}, \log L_{\rm s})$ diagram, on the basis of the evolution calculations; they are called *isochrones* (after Greek *iso* = same, *kronos* = time). Figure 13.1 shows examples of computed evolutionary tracks and isochrones.

Since the evolutionary time scale decreases very rapidly with increasing mass, at a given age stars with sufficiently low mass are still in the phase of central hydrogen burning. Therefore all isochrones start out on the main sequence at low masses, and hence low $\log T_{\rm eff}$. A particular isochrone follows the main sequence up to that mass where hydrogen has just been exhausted in the core at the given age. More massive stars at this age are in later evolutionary stages, and hence the isochrones deviate from the main sequence. The mass where the transition away from the main sequence takes place is called the "turn-off" mass $M_{\rm t}$.

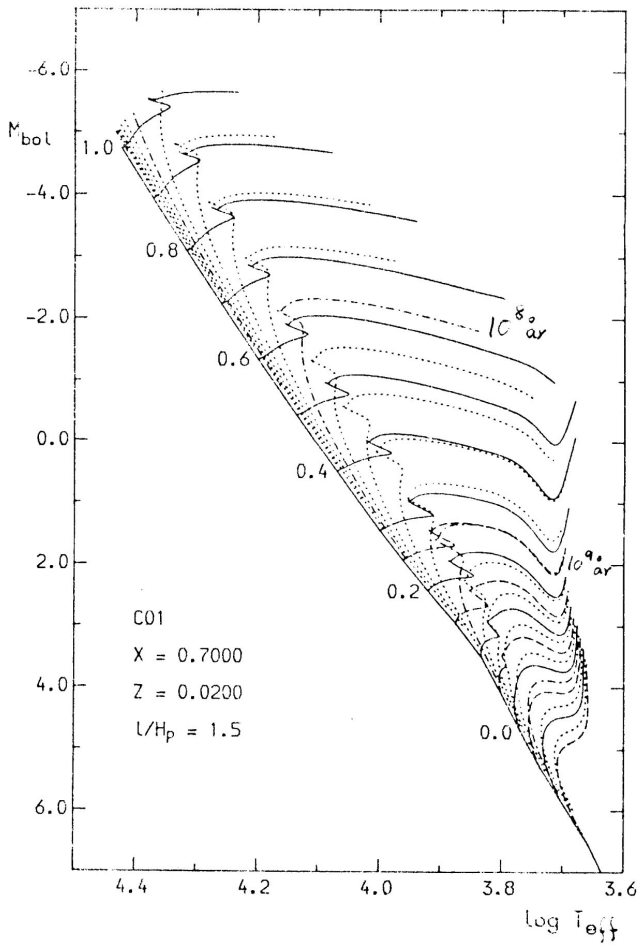

Figure 13.1: Theoretical evolutionary tracks (continuous lines) and isochrones (dashed lines). The ordinate gives the absolute bolometric magnitude $M_{\rm bol}$; it is related to the luminosity $L_{\rm s}$ through $M_{\rm bol} = 4.75 - 2.5\log(L_{\rm s}/\,{\rm L}_\odot)$. On every second evolutionary track $\log(M/\,{\rm M}_\odot)$ is indicated to the left. The isochrones are plotted at ages $t_{\rm i}$ such that the step in $\log t_{\rm i}$ is 0.2; the isochrones for $t_{\rm i} = 10^8$ years and 10^9 years are plotted with a dot-dashed lined, labelled by $t_{\rm i}$. (From Hejlesen 1980).

It is striking that the parts of the isochrones away from the main sequence, corresponding to masses greater than $M_{\rm t}$, are very similar to evolutionary tracks. As a result, a crude test of late stellar evolution can be made simply by comparing the distribution of stars in an observed HR diagram with an appropriate evolutionary track. This property of the isochrones can be understood from the following two results of the evolution calculations (see also Table 11.1):

i) The time the stars spend on the main sequence decreases very rapidly with increasing mass.

ii) The largest fraction of a star's lifetime is spent on the main sequence.

Here i) was discussed in section 11.3.3, where we obtained as an approximation to the main-sequence timescale

$$t_{\rm MS}(M) \sim M^{-(\nu-1)} \ , \tag{13.1}$$

where $\nu = 3$ – 5. After central hydrogen burning the star spends the longest time in the phase of central helium burning. However, the amount of energy available per unit mass from helium burning is considerably smaller than the amount available from hydrogen burning. Furthermore the luminosity of the star is somewhat higher during this phase. As a result the duration of the core helium burning phase is substantially shorter than the duration of the core hydrogen-burning phase. This gives some justification for ii). It follows from the results in Table 11.1 that if $t_{\rm T}(M)$ is the total lifetime of the star, then

$$t_{\rm T}(M) - t_{\rm MS}(M) \lesssim \frac{1}{5} t_{\rm T}(M). \ , \tag{13.2}$$

Hence the situation is roughly as sketched in Figure 13.2.

Exercise 13.1:

Verify the statement made above about the amount of energy available from helium burning, by using the mass defects in Appendix B. Compare the results with the durations of the hydrogen- and helium-burning phases in Table 11.1. If there is a discrepancy, what might be the explanation?

We now consider an isochrone corresponding to the age $t_{\rm i}$. It has the turn-off mass $M_{\rm t}$, determined by $t_{\rm MS}(M_{\rm t}) = t_{\rm i}$. The end point of the isochrone is at the mass $M_{\rm e}$, such that $t_{\rm T}(M_{\rm e}) = t_{\rm i}$. As sketched in Figure 13.3 these two masses are very close. The part of the isochrone departing from the main sequence corresponds to masses between $M_{\rm t}$ and $M_{\rm e}$ and is therefore between the evolutionary tracks for $M_{\rm t}$ and $M_{\rm e}$ (*cf.* Figure 13.3). We can estimate $M_{\rm e} - M_{\rm t}$ from equations (13.1) and (13.2). We have that

$$t_{\rm i} = t_{\rm T}(M_{\rm e}) = t_{\rm MS}(M_{\rm t}) \ , \tag{13.3}$$

or, from equation (13.2)

$$t_{\rm MS}(M_{\rm t}) > t_{\rm MS}(M_{\rm e}) \geq \frac{4}{5} t_{\rm T}(M_{\rm e}) = \frac{4}{5} t_{\rm MS}(M_{\rm t}) \ , \tag{13.4}$$

and hence, from equation (13.1)

$$\ln M_{\rm e} - \ln M_{\rm t} \leq \frac{1}{5} \frac{1}{(\nu - 1)} \leq 0.1 \ , \tag{13.5}$$

if we use that $\nu \geq 3$. Hence the evolutionary track for $M = M_{\rm t}$ gives a reasonable estimate of the run of the isochrone.

This intention of this description is to give an intuitive understanding of the relation between the evolutionary tracks and the isochrones. section 13.5 describes an attempt at a more formal analysis. This shows, as expected, that parts of isochrones corresponding to very rapid phases of evolution lie even closer to evolution tracks. This is particularly the case for the hydrogen shell-burning phase, between hydrogen core exhaustion and the red giant branch, as illustrated in Figure 13.3.

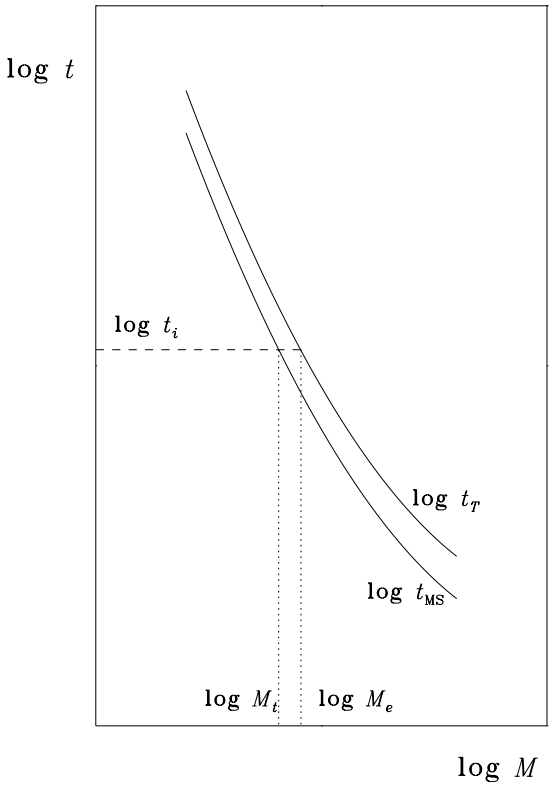

Figure 13.2: Schematic illustration of the dependence of the main-sequence time $t_{\rm MS}$ and the total lifetime $t_{\rm T}$ on the stellar mass. In the figure are indicated the turn-off mass $M_{\rm t}$ and the end-point mass $M_{\rm e}$ for an isochrone corresponding to the age $t_{\rm i}$.

13.3 Interpretation of observed HR diagrams

From the description of the computed isochrones it follows that the lower part of the HR diagram for a stellar cluster consists of stars on the main sequence. Their luminosity $L_{\rm MS}$ is known as a function of the effective temperature, partly from theoretical calculations and partly (mainly) from observations of stars that are so close that their distances, and hence their absolute luminosities, can be determined. By measuring the apparent luminosity of main-sequence stars at a given $T_{\rm eff}$ and using the relation between apparent and absolute luminosity (*cf.* equation [2.8]) it is therefore possible to determine the distance to the cluster. This procedure can be described graphically as sliding the HR diagram for the cluster vertically until the main sequence coincides with the known location of the main sequence; the displacement then determines the distance module $5\log d - 5$, and hence the distance d, to the cluster.

The mass of stars around the point (the turn-off point) where the HR diagram of the cluster starts deviating from the main sequence must correspond to the turn-off mass $M_{\rm t}$ for the isochrone corresponding to the age of the cluster. This mass cannot be observed directly; but on the main sequence there is a relation between on the one hand the mass

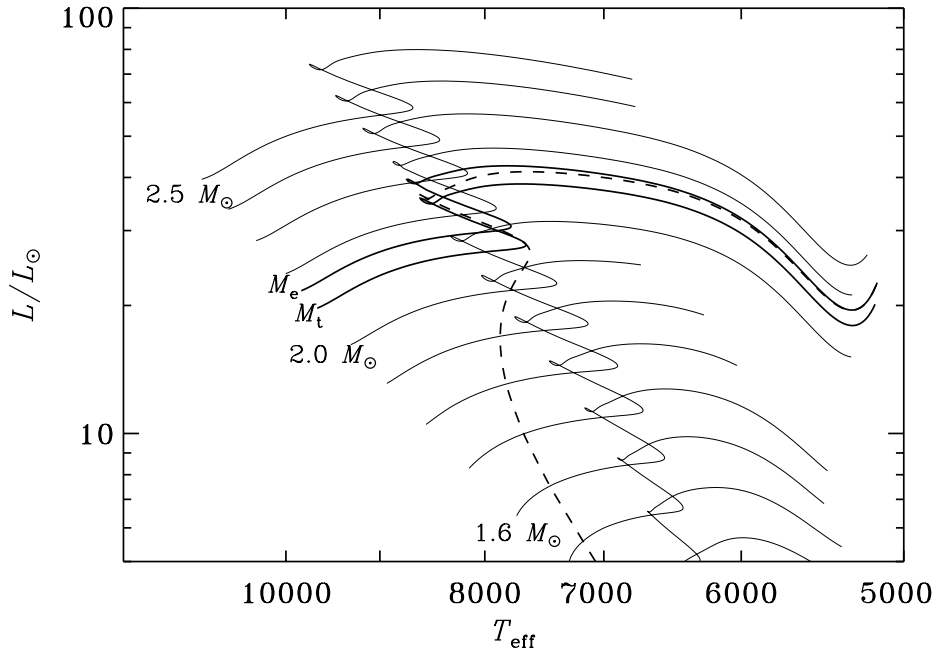

Figure 13.3: An isochrone (dashed line) lies between the evolutionary tracks for the turn-off mass $M_{\rm t}$ and the end-point mass $M_{\rm e}$, indicated by heavy continuous lines; here we only consider evolution to the base of the red giant branch. The age of the isochrone is 8×10^8 years, corresponding to $M_{\rm t} = 2.1\,{\rm M}_\odot$ and $M_{\rm e} = 2.15\,{\rm M}_\odot$. Additional evolutionary tracks are shown with thin continuous lines, for models with a step in mass of $0.1\,{\rm M}_\odot$.

and on the other the luminosity and effective temperature. Hence $M_{\rm t}$, and therefore the age of the cluster, can be determined from $T_{\rm eff}$ and $L_{\rm s}$ at the turn-off point. In Figure 2.7 the ordinate on the right-hand axis is calibrated to age in this manner. A more precise determination of the age is obtained by fitting theoretical isochrones to the observed HR diagram. Such investigations also have to take into account the chemical composition of the stars in the cluster, which affects the location of the isochrones.

An example of such a fit is given in Figure 13.4, from Morgan & Eggleton (1978). The agreement between theory and observation is quite good near the turn-off point but deteriorates somewhat at lower effective temperature, corresponding to higher $({\rm B}-{\rm V})_0$. A possible reason for this discrepancy could be that an inappropriate value has been chosen for the uncertain parameter in the description of convection. The scatter in the observed diagram is only in part caused by observational errors. A more important effect is the presence in the data of unresolved binary stars. Such a system appears with a colour which is an average of the colours of each component but with the combined luminosity, and hence is displaced upwards in the HR diagram relative to the main sequence. Indeed, Morgan & Eggleton demonstrate that with the proper assumption about the distribution of binary stars in the data, a good fit to the observations can be obtained. It should also be noticed that there is a clear gap in the observations just before the turn-off from the main sequence. This evidently corresponds to the hook in the evolutionary tracks and hence in

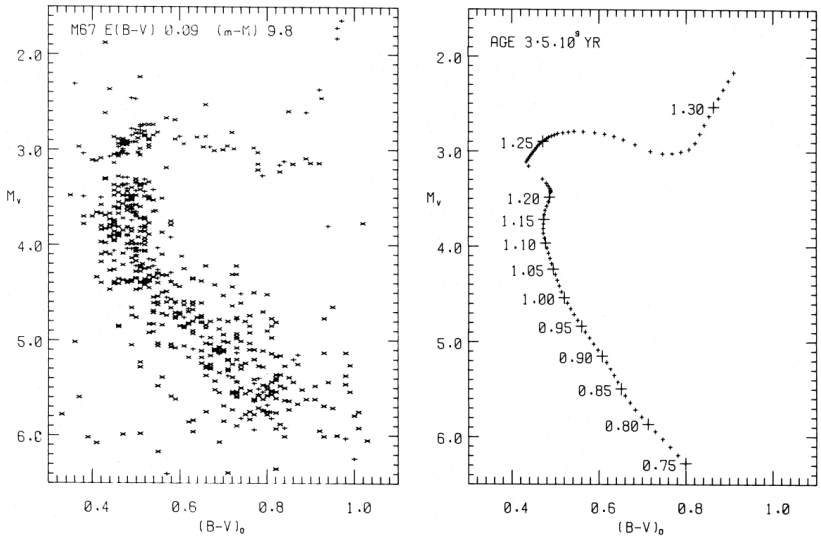

Figure 13.4: Observed HR diagram for the open cluster Messier 67 (left) and theoretical isochrone for an age of 3.5×10^9 years (right); the theoretical values for $T_{\rm eff}$ and $L_{\rm s}$ have been translated into B-V and absolute visual magnitude M_v to allow a direct comparison with the observations. On the isochrone the masses have been indicated in units of the solar mass. In general the agreement between theory and observation is quite good. (From Morgan & Eggleton 1978).

the isochrone, which was caused by the contraction of the core after hydrogen exhaustion and before hydrogen shell burning sets in. Hence the turn-off gap is observational evidence for the presence of a convective core in these stars while they were on the main sequence (*cf.* section 12.2); thus indirectly it reflects a basic physical property of matter, namely the substantial Coulomb barrier between the nuclei in the CNO cycle which leads to the high temperature sensitivity of the energy generation rate.

Exercise 13.2:

Consider a binary system consisting of two identical stars that cannot be resolved observationally. How much is the apparent magnitude of the system decreased relative to the magnitude of each star?

Figure 13.5 gives a qualitative, observational illustration of almost all phases in the evolution of relatively massive stars. By using the correspondence between evolutionary tracks and isochrones it can be compared directly with Figure 12.2. It should be noted in particular that the density of stars in the different parts of the diagram is related to the timescale of the corresponding evolutionary phases. Thus most of the stars are on the main sequence, in the hydrogen core burning phase; but there is also a substantial number

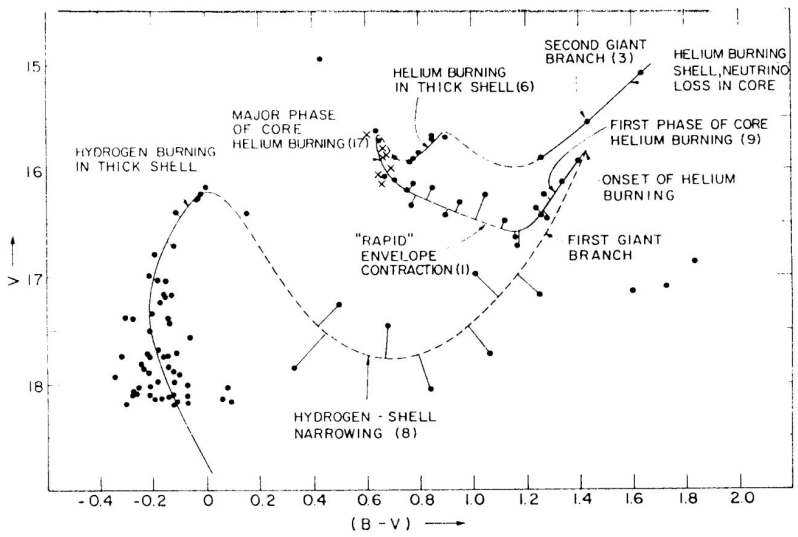

Figure 13.5: Observed HR diagram for a stellar cluster (NGC 1866 in the Large Magellanic Cloud). In the figure are indicated evolutionary phases found by comparing with the theoretical evolution track shown in Figure 12.2. The numbers in brackets indicate the number of stars in each phase of evolution. (From Iben 1985).

of stars in the phase of helium core burning.

13.4 Qualitative analysis of cluster HR diagrams[1]

Already before employing an isochrone, one can identify many specific evolutionary stages and give crude estimates of age and metallicity of a star cluster based just on the appearance in the observed HR diagram.There are about 120 globular star clusters and tens of thousands of open star clusters in the Milky Way. With observations from the *Gaia* mission and *e.g.* the computer program TOPCAT,[2] it has become very easy to produce observed HR diagrams of a large number star clusters, and these are still the basis of age determination based on comparisons with stellar model isochrones.

Figure 13.6 shows a combined HR diagram of three solar-metallicity open clusters, where offsets have been applied in both magnitude and colour for the individual clusters to make their main sequences align. This is needed for a direct comparison to remove the effects of different distances and differences in interstellar reddening and absorption. These relative shifts are non-trivial because they are along both axes, but one is aided by the fact that several features depend on age in a predictive way, because the clusters have the same metallicity (to within a small error-margin). The HR diagram reveals that these clusters have quite different ages; their main-sequences overlap, but their turn-offs are a different magnitudes. The two youngest clusters display a gap close to the very top of the main sequence, at offset G magnitudes of around 14.7 and 13.6, respectively;

[1] This section was kindly provided by Karsten Brogaard.

[2] `http://www.starlink.ac.uk/topcat/`

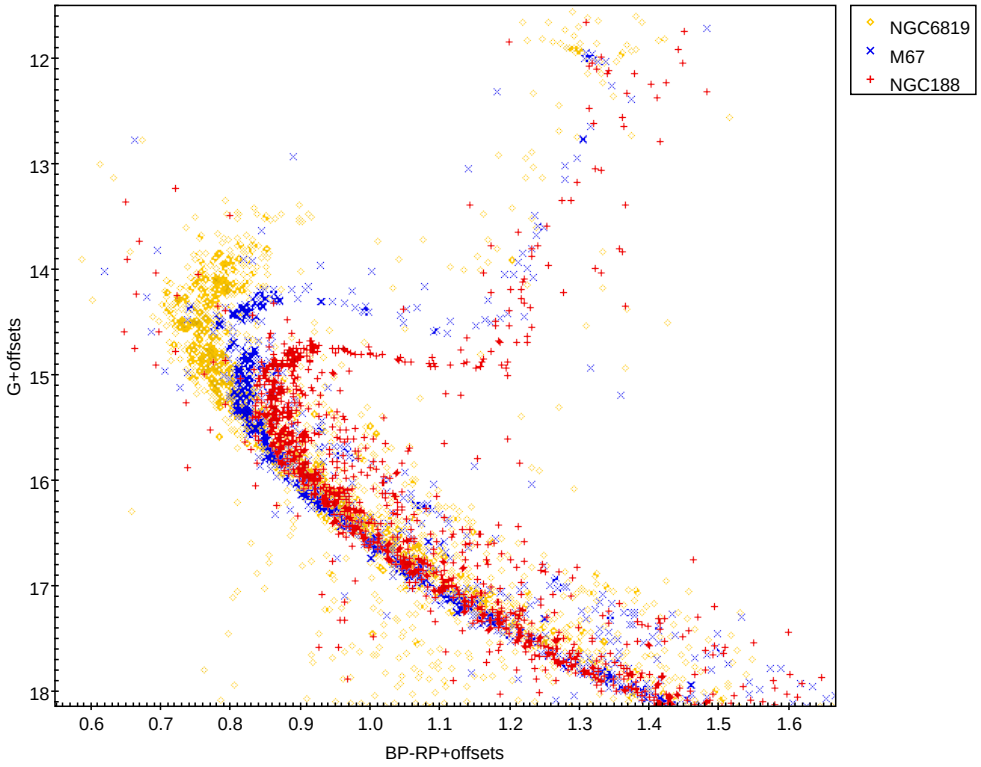

Figure 13.6: Colour-magnitude diagrams for three open clusters, based on *Gaia* data. Here G is the broad-band *Gaia* magnitude, with a passband of 330–1050 nm, whereas colour is based on *Gaia* BP and RP magnitudes, where the blue photometer (BP) covers the short wavelengths in the 330–680 nm range, and the red photometer (RP) covers longer wavelengths in the 640–1050 nm range (see Carrasco *et al.*, 2021).

as mentioned previously, this is due to the fast overall contraction phase that happens at the end of the main sequence for stars with a convective core. There are additional features that support the age difference based on the turn-off magnitudes; the subgiant branch magnitudes follow the same trend, and the faster evolution of the more massive subgiants in the youngest cluster is revealed by the lower number of subgiants. On the red giant branch, the more massive stars are hotter at a given magnitude, and this ordering is consistent with that based on the turn-off and the subgiant branch.

As mentioned in section 13.2, the evolutionary phase with the second-longest lifetime (with the longest lifetime phase being the main sequence) is the central helium-burning phase. This causes an overdensity of stars in that phase in HR diagrams of star clusters. In Figure 13.6, this overdensity can be identified at G close to 12 and BP – RP of about 1.3. As seen, the magnitudes of these stars differ very little, even from cluster to cluster. The very small magnitude offsets that do appear follow the age differences of the clusters, with the youngest cluster showing the brightest magnitudes. This is because younger clusters have higher-mass stars beyond the turn-off, and although stars in all these clusters went through the helium flash, and thus have very nearly the same core mass, they have different envelope masses, and thus the luminosity from the hydrogen shell-burning is

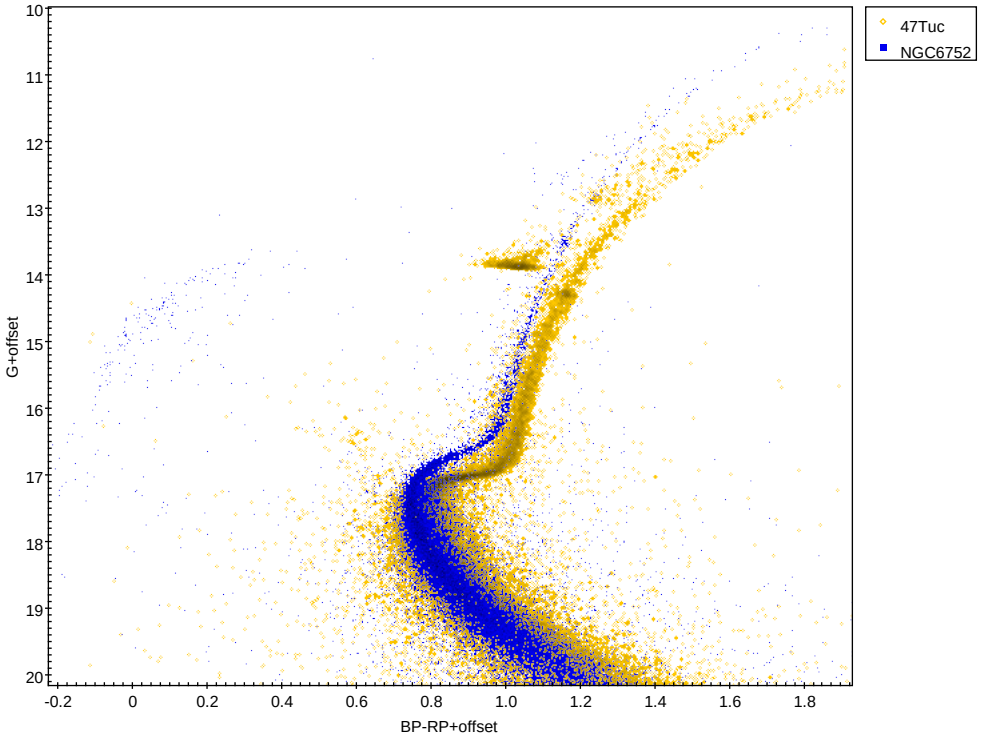

Figure 13.7: Colour-magnitude diagrams for two globular clusters, based on *Gaia* data. See caption to Fig. 13.6.

slightly different. For even younger clusters, with masses of about $2.2\,M_\odot$ or more in the giant phase, the stars do not go through a helium-flash but instead transition stably from the RGB phase to the central helium-burning phase. Therefore, they no longer have similar core-masses to those of lower mass stars, and the absolute magnitude of the over-density of the central helium-burning stars has lost its near-independence of mass. Stars with masses just above the mass corresponding to the transition to quiescent helium ignition have smaller cores and thus lower luminosity than those below the transition, but this quickly changes for stars with increasing masses. At these relatively high masses at ages below 1 Gyr, most Milky Way open clusters have very few stars in the central helium-burning phase. As examples, there are six in NGC 6866 and eight in NGC 6811.

In the literature, very low-mass central helium-burning stars in the globular clusters are called horizontal-branch stars. Stars in the high-metallicity end of the ensemble of globular clusters, which are still metal-poor relative to the Sun, are relatively cool, and thus red, and are called red horisontal branch stars. The higher-mass central helium-burning stars of the open clusters are called red clump stars if they went though a helium flash. Slightly more massive stars that have a helium core mass close to, but different from, that of those that went through a flash are called secondary clump stars, but there is no well-defined upper mass limit to this definition. Stars with masses much larger than $2.2\,M_\odot$ in the central helium-burning phase do not have a specific name, likely because they no longer form an overdensity in the HR diagram.

Figure 13.7 shows a *Gaia* HR diagram of the globular clusters 47 Tuc (also known as NGC 104) and NGC 6752, shifted to common distance and reddening. Because globular

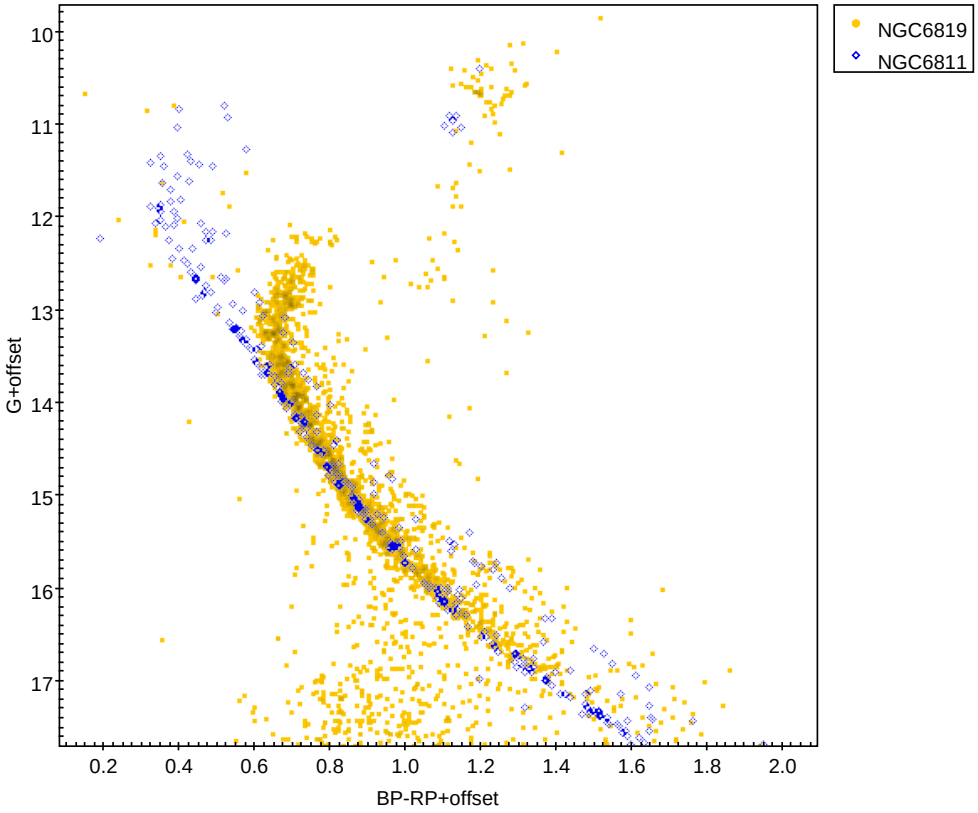

Figure 13.8: Colour-magnitude diagrams for two open clusters, based on *Gaia* data. See caption to Fig. 13.6.

clusters contain many more stars than the open clusters, it is easy to locate the various evolutionary phases; the main sequence, the turn-off, the subgiant branch, the giant branch and the central helium-burning stars (or the horizontal branch). In addition, due to the large number of stars, it is possible to identify more overdensities; the so-called RGB-bump on the RGB of 47 Tuc at G = 14.2, and even AGB stars and the AGB-bump above the red horizontal branch stars and above and to the blue of the RGB at magnitudes just below G = 13 for 47 Tuc. A good reference for obtaining relative and absolute age estimates of globular clusters is VandenBerg *et al.* (2013).

Exercise 13.3:

Use Figure 13.6 to verify the results of your calculation in exercise 13.2 by estimating the magnitude difference from the main sequence to the upper envelope of the main sequence binary stars.

Exercise 13.4:

Order the clusters in Figure 13.6 by age based on turn-off luminosity, subgiant branch

luminosity, RGB colour, and red clump luminosity, respectively. Verify that you get the same ordering from each method.

Exercise 13.5:

Figure 13.8 shows a common HR diagram of the solar-metallicity open clusters NGC 6811 and NGC 6819 shifted to be at a common distance and reddening.

(a) Which is the younger of the two clusters based on the turn-off?

(b) Is this consistent with the luminosity difference between the central helium burning stars in the two clusters? (Hint: secondary clump.)

Exercise 13.6:

Figure 13.7 shows a common HR diagram of the globular clusters 47 Tuc and NGC 6752 using an offset in G-maginitude of +0.11 and an offset in BP–RP of +0.032 for NGC 6752 to account for differences in distance and reddening.

(a) Identify the various evolutionary stages for both clusters.

(b) These clusters have different metallicity. Note how that affects the luminosity of the RGB bump, the colour of the RGB, and the position of the horisontal branch stars.

13.5 Connection between evolution tracks and isochrones

The discussion in section 13.2 was rather inadequate, and only gave an intuitive indication of the reason why isochrones and evolutionary tracks are similar during phases where the evolution is rapid. This section is an attempt to give a slightly more complete description, although proper mathematical precision is certainly not achieved. The basic ideas of the argument are the same as in section 13.2, however.

A star can be described by a point P in the $(\log T_{\rm eff}, \log L_{\rm s})$ plane. P can be regarded as a function of the mass M and age t of the star. Then an evolutionary track is a curve in the plane consisting of a collection of points corresponding to a particular mass but different ages, whereas an isochrone is a collection of points corresponding to the same age but different mass. A difficulty in the presentation is that, as discussed above, the total duration of the evolution of a star depends very strongly on the mass of the star. Thus only a very restricted set of the possible pairs (M, t) corresponds to a star. To obtain a somewhat more homogeneous description we introduce a new time-like parameter τ, which measures the evolutionary state of the star. We leave the definition of τ somewhat imprecise. A reasonable convention would be to let $\tau = 0$ on the zero-age main sequence

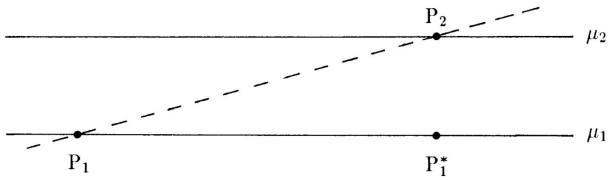

Figure 13.9: Sketch of an isochrone (dashed line) and two corresponding evolution tracks (continuous lines) with mass parameters μ_1 and μ_2. The two points P_1^* and P_2 correspond to the same evolution state.

and $\tau = 1$ at the termination of the evolution of the star. More importantly, we assume that τ can be defined in such a way that a given phase of stellar evolution (*e.g.* the end of central hydrogen burning) corresponds to the same value of τ, regardless of the mass of the star. The most serious lack of precision in the present analysis is probably in the definition of τ; in particular we neglect the problems that would occur at masses where there are drastic changes in the nature of the evolution.[3] On the other hand, this is probably not fatal for the argument.

To work with quantities of order unity we also introduce $\mu \equiv \log(M/\,\mathrm{M}_\odot)$. We now regard the point P as a function $\mathrm{P}(\mu, \tau)$. The definitions of τ and μ have been arranged such that we may assume P to be a "well-behaved" function of μ and τ. We make this assumption more formal by assuming that $\|\partial_\mu \mathrm{P}\|$ and $\|\partial_\tau \mathrm{P}\|$ are of order unity. Here $\partial_\mu \mathrm{P}$ and $\partial_\tau \mathrm{P}$ are the partial derivatives of P with respect to μ and τ, and $\|\cdots\|$ is a suitable norm.

We can now regard the evolution time as a function $t(\mu, \tau)$ of the mass and the evolutionary state. Conversely we can obviously also consider the evolutionary state as a function $\tau(\mu, t)$ of the mass and age of the star.

We now consider an isochrone corresponding to the age $t = t^*$, and regard two points P_1 and P_2 on this isochrone, corresponding to mass parameters μ_1 and μ_2 (*cf.* Figure 13.9). As in section 13.2 the goal is to show that the difference in mass corresponding to the two points, *i.e.*, $|\mu_2 - \mu_1|$, is small compared with the distance between the points; this would show that the isochrone is close to the the evolution tracks corresponding to the two masses.

The two points correspond to evolution states given by the values τ_1 and τ_2 of τ, such that

$$t(\mu_i, \tau_i) = t^* \qquad \text{and} \qquad \mathrm{P}_i = \mathrm{P}(\mu_i, \tau_i), \qquad i = 1, 2\,. \tag{13.6}$$

From a Taylor expansion of the first relation we obtain

$$0 = t(\mu_2, \tau_2) - t(\mu_1, \tau_1) \simeq \left(\frac{\partial t}{\partial \tau}\right)_\mu (\tau_2 - \tau_1) + \left(\frac{\partial t}{\partial \mu}\right)_\tau (\mu_2 - \mu_1)\,, \tag{13.7}$$

[3]Examples would be the transition in behaviour at the end of hydrogen burning between stars with radiative and convective cores; or the difference between stars undergoing, and stars not undergoing, a helium flash at the onset of helium burning.

where, *e.g.*, $(\partial t/\partial\tau)_\mu$ denotes the partial derivative of $t(\mu,\tau)$ with respect to τ at fixed μ. Thus we find that

$$|\mu_2 - \mu_1| \simeq \frac{\left|\left(\frac{\partial t}{\partial \tau}\right)_\mu\right|}{\left|\left(\frac{\partial t}{\partial \mu}\right)_\tau\right|} |\tau_2 - \tau_1| \; . \tag{13.8}$$

In this equation $|(\partial t/\partial\mu)_\tau|$ gives the change with mass in the evolution time required to reach a given evolution state, characterized by the fixed value of τ. As discussed in section 13.2 (*cf.* equation [13.1]) this change is rapid, and hence the derivative is large. Furthermore $|(\partial t/\partial\tau)_\mu|$ measures the time spent during a given change in evolution state, at fixed mass; this is evidently a small quantity during phases of rapid evolution. In such phases it follows from equation (13.8) that

$$|\mu_2 - \mu_1| \ll |\tau_2 - \tau_1| \; , \tag{13.9}$$

and hence that the isochrone is close to the evolutionary tracks with mass parameters μ_1 and μ_2.

We can make this estimate slightly more precise by considering the distance $\|\mathrm{P}_2 - \mathrm{P}_1\|$ between the two points in the $(\log T_{\rm eff}, \log L_{\rm s})$ plane. From a Taylor expansion we obtain

$$\begin{aligned} \|\mathrm{P}_2 - \mathrm{P}_1\| &\simeq \|\partial_\mu \mathrm{P}\,(\mu_2 - \mu_1) + \partial_\tau \mathrm{P}\,(\tau_2 - \tau_1)\| \\ &\geq \|\partial_\tau \mathrm{P}\|\,|\tau_2 - \tau_1| - \|\partial_\mu \mathrm{P}\|\,|\mu_2 - \mu_1| \; . \end{aligned} \tag{13.10}$$

By means of equation (13.8) this gives

$$|\mu_2 - \mu_1| \leq \frac{\left|\left(\frac{\partial t}{\partial \tau}\right)_\mu\right|}{\left|\left(\frac{\partial t}{\partial \mu}\right)_\tau\right| \|\partial_\tau \mathrm{P}\|} \|\mathrm{P}_2 - \mathrm{P}_1\| \left[1 - \frac{\left|\left(\frac{\partial t}{\partial \tau}\right)_\mu\right| \|\partial_\mu \mathrm{P}\|}{\left|\left(\frac{\partial t}{\partial \mu}\right)_\tau\right| \|\partial_\tau \mathrm{P}\|}\right]^{-1} \; . \tag{13.11}$$

To characterize the distance between the evolution tracks we finally introduce the point P_1^* on the track for μ_1 with the same evolution state as P_2, *i.e.*, $\mathrm{P}_1^* = \mathrm{P}(\mu_1, \tau_2)$. Then we find

$$\begin{aligned} \|\mathrm{P}_1^* - \mathrm{P}_2\| &\simeq \|\partial_\mu \mathrm{P}\|\,|\mu_2 - \mu_1| \\ &\leq \frac{\left|\left(\frac{\partial t}{\partial \tau}\right)_\mu\right| \|\partial_\mu \mathrm{P}\|}{\left|\left(\frac{\partial t}{\partial \mu}\right)_\tau\right| \|\partial_\tau \mathrm{P}\|} \|\mathrm{P}_2 - \mathrm{P}_1\| \left[1 - \frac{\left|\left(\frac{\partial t}{\partial \tau}\right)_\mu\right| \|\partial_\mu \mathrm{P}\|}{\left|\left(\frac{\partial t}{\partial \mu}\right)_\tau\right| \|\partial_\tau \mathrm{P}\|}\right]^{-1} \\ &\ll \|\mathrm{P}_2 - \mathrm{P}_1\| \; , \end{aligned} \tag{13.12}$$

since we have assumed that $\|\partial_\mu \mathrm{P}\|$ and $\|\partial_\tau \mathrm{P}\|$ are of order unity. Hence the distance between the two evolution tracks is much smaller than the distance along the isochrones; and the faster the evolution (*i.e.*, the smaller $|(\partial t/\partial\tau)_\mu|$), the closer are the two evolutionary tracks to each other. This was what we set out to demonstrate.

It is obvious that this argument is far from sufficient to hang a man. On the other hand, it does appear (at least to me) reasonably convincing. Suggestions for improvements would be received with gratitude.

Chapter 14

Late evolution of massive stars Element synthesis

14.1 Introduction

In Chapter 12 we discussed the evolution after the main sequence of stars of low and moderate mass. It was found that the evolution proceeded through hydrogen and helium burning, ending with a core consisting of carbon and oxygen, surrounded by helium and/or hydrogen shell-burning sources. Further contraction of the core did not lead to heating, because the core became degenerate; hence the temperature never got high enough to initiate carbon burning. Subsequent instability and mass loss led to the expulsion of essentially the entire envelope outside the core, resulting in the formation of a white dwarf, initially surrounded by a planetary nebula.

With increasing stellar mass the tendency towards degeneracy in the core gets smaller. As illustrated in Figure 12.7, in stars of masses exceeding about $10\,\mathrm{M}_\odot$ the core does not become degenerate before carbon burning starts. The evolution can then proceed through further nuclear burning phases in the core, alternating with gravitational contraction and heating. The result is an onion-like structure of layers of different chemical composition, the heaviest elements being closest to the centre, possibly separated by shell-burning sources.

In the present chapter we analyze these processes in more detail, and discuss the ultimate fate of such a massive star. An important goal here and in the following chapter is to understand the synthesis of elements, and hence the distribution of elements now observed in the Sun and the solar system (*cf.* Figure 14.1). The processes discussed so far account for the production of elements up to oxygen. Heavier elements are produced in the last stages of evolution of massive stars, but it turns out that lower-mass stars also play a crucial role. The discussion provided here is necessarily quite schematic, with little physical or mathematical detail. An excellent exposition of the basic principles of nucleosynthesis was provided by Clayton (1968).

An important feature in understanding nucleosynthesis is the energetics of fusion, as determined by the atomic mass excesses tabulated in Appendix B. A convenient representation of this is in terms of the *mean binding energy per nucleon* $B/\mathcal{A}$, which is illustrated in Figure 14.2. This is determined as the energy released per nucleon in a (fictitious) process where the nucleus is assembled from its constituent nucleons.

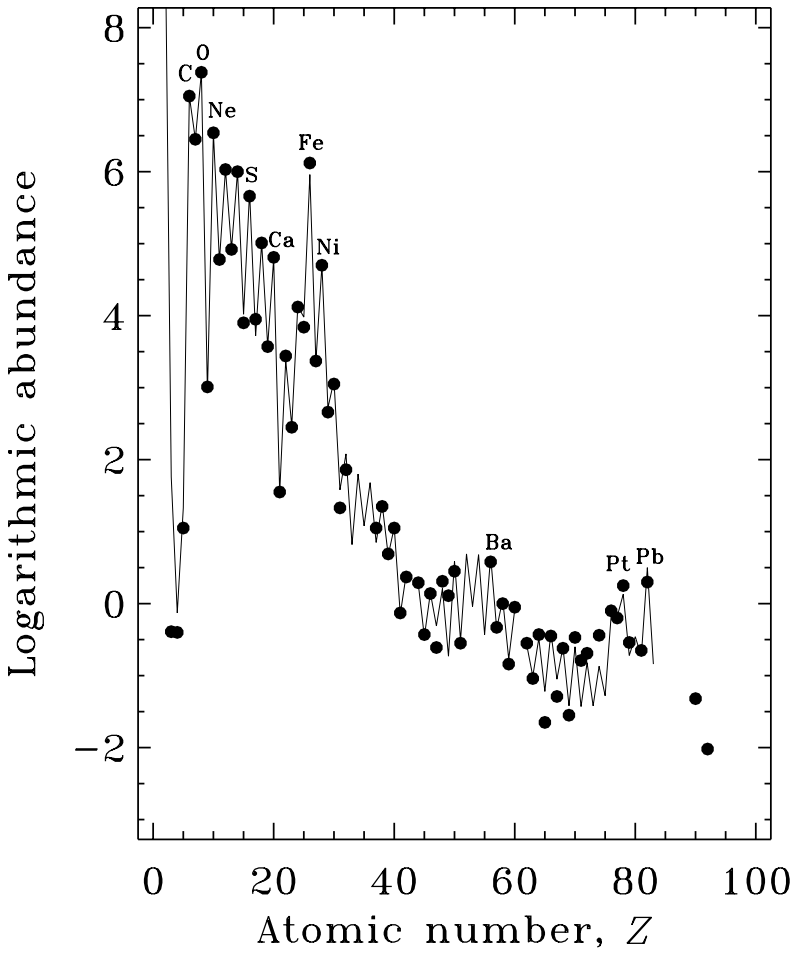

Figure 14.1: Abundances by number of elements in the solar system; the normalization is such that the abundance of Si is 10^6. The dots represent values obtained from spectral analysis for the Sun, whereas the line is based on abundance determinations for meteorites. The abundance data in the figure derive from a compilation by Anders & Grevesse (1989).

Exercise 14.1:

Verify, for a few points, that Figure 14.2 is consistent with the table in Appendix B.

As long as $B/\mathcal{A}$ increases with increasing mass number, fusion between two nuclei is *exothermic*, *i.e.*, releases energy. This is the case for all the reaction we have considered so far. For nuclei of mass exceeding about $60\,m_{\rm u}$, however, $B/\mathcal{A}$ *decreases* with increasing $\mathcal{A}$. Here fusion requires energy input, *i.e.*, is *endothermic*.[1] Thus fusion between heavy

[1] On the other hand, this implies that *fission* of heavy elements is exothermic. This is the reason why nuclear energy can be generated either by fusion of light nuclei or by fission of heavy nuclei.

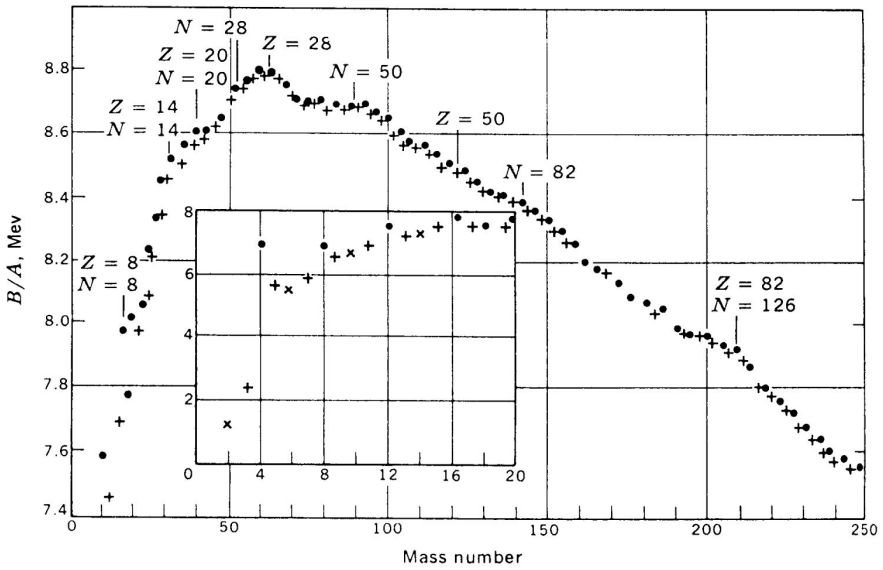

Figure 14.2: The binding energy per nucleon B/A of the most stable nucleus with atomic weight A. The solid circles represent nuclei having an even number of protons and an even number of neutrons, whereas the plusses represent odd-A nuclei; in the insert, the diagonal crosses show odd-odd nuclei. (From Preston 1962.)

nuclei is extremely unlikely; it follows that processes of the nature considered so far cannot produce nuclei heavier than those of the so-called *iron group*, with atomic masses between 50 and 60 $m_{\rm u}$. We return to the question of how to produce even heavier elements in Chapter 15.

14.2 Late evolution stages of massive stars

When the temperature exceeds about 5×10^8 K in the contracting core, carbon burning sets in (*cf.* Figure 12.7). This was discussed briefly in section 8.6; the reaction can result in a number of different end products, as indicated in equation (8.65):

$$ {}^{12}\mathrm{C} + {}^{12}\mathrm{C} \rightarrow \begin{cases} {}^{24}\mathrm{Mg} + \gamma \,, \\ {}^{23}\mathrm{Mg} + n \,, \\ {}^{23}\mathrm{Na} + p \,, \\ {}^{20}\mathrm{Ne} + {}^{4}\mathrm{He} \,, \\ {}^{16}\mathrm{O} + 2\,{}^{4}\mathrm{He} \,. \end{cases} \tag{14.1} $$

Because of the high temperature, the protons and alpha particles that are produced immediately react with other nuclei in the gas, producing additional elements; the neutrons, being neutral, are not affected by the Coulomb barrier, and also react freely. After the ^{12}C exhaustion, further core contraction and heating lead to "Ne burning", through photodisintegration and subsequent α capture of ^{20}Ne [*cf.* equations (8.67) and (8.68)], before

the reactions involving oxygen set in, at around 10^9 K:

$$^{16}\mathrm{O} + {}^{16}\mathrm{O} \rightarrow \begin{cases} {}^{32}\mathrm{S} + \gamma \ , \\ {}^{31}\mathrm{P} + p \ , \\ {}^{31}\mathrm{S} + n \ , \\ {}^{28}\mathrm{Si} + {}^{4}\mathrm{He} \ , \\ {}^{24}\mathrm{Mg} + 2\,{}^{4}\mathrm{He} \ . \end{cases} \tag{14.2}$$

Again reactions involving p, n and ^{4}He lead to the production of additional elements.

After oxygen is exhausted, there is a new phase of contraction and heating. This might be expected to end when fusion of the next major element sets in, possibly ^{24}Mg. Before the temperature gets high enough for this reaction, however, a totally different type reaction becomes dominant. With the increasing temperature, the thermal energy of photons in the gas increases. At 10^9 K a non-negligible fraction of the photons has energies in the MeV range. Such energetic photons can cause photo-dissociation in the nuclei in the gas,[2] such as, for example,

$$^{32}\mathrm{S} + \gamma \rightarrow {}^{28}\mathrm{Si} + {}^{4}\mathrm{He} \ . \tag{14.3}$$

The ^{4}He released in this process may then be captured in other nuclei, including the ^{28}Si. Hence in fact the reaction (14.3) may go both ways, and should therefore be expressed as

$$^{28}\mathrm{Si} + {}^{4}\mathrm{He} \rightleftarrows {}^{32}\mathrm{S} + \gamma \ . \tag{14.4}$$

It follows from Figure 14.2, and is indicated by the location of the γ in equation (14.4), that energy is released in the reaction ^{28}Si + ^{4}He. Thus it is energetically favourable to shift the equilibrium in equation (14.4) towards the right, so that the equation should *really* be written

$$^{28}\mathrm{Si} + {}^{4}\mathrm{He} \rightleftharpoons {}^{32}\mathrm{S} + \gamma \ . \tag{14.5}$$

Furthermore, given the continuing photo-dissociation of the nuclei and hence presence of ^{4}He, there is a possibility of similar reactions involving the subsequent nuclei, such as

$$\begin{aligned} {}^{32}\mathrm{S} + {}^{4}\mathrm{He} &\rightleftharpoons {}^{36}\mathrm{Ar} + \gamma \ , \\ {}^{36}\mathrm{Ar} + {}^{4}\mathrm{He} &\rightleftharpoons {}^{40}\mathrm{Ca} + \gamma \ , \\ &\vdots \\ {}^{52}\mathrm{Fe} + {}^{4}\mathrm{He} &\rightleftharpoons {}^{56}\mathrm{Ni} + \gamma \ . \end{aligned} \tag{14.6}$$

To these reactions must be added similar reversible reactions involving photo-ejection and absorption of protons and neutrons, as well as the decay of unstable nuclei formed in the process. The result is an extremely complex network of reactions, whose evolution must be followed numerically. In general, however, the processes occur almost in equilibrium, with nearly equal numbers of nuclei being dissociated and created. On a slightly longer timescale the equilibrium is shifted towards more tightly bound and hence heavier nuclei. This set of quasi-equilibrium processes is known, somewhat misleadingly, as *silicon burning*.[3]

[2] Much as far less energetic photons cause ionization in atoms.

[3] Strictly speaking, the most tightly bound nucleus is ^{62}Ni which might therefore be expected to be the end product of these reactions; however, there seems to be no efficient reaction path to this nucleus. For a discussion of this issue, see Shurtleff & Derringh (1989).

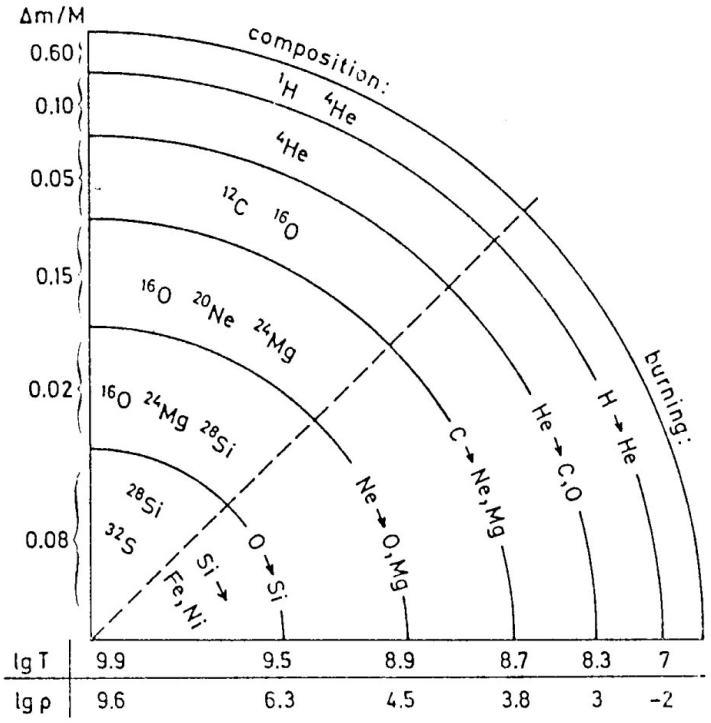

Figure 14.3: Schematic illustration (not to scale) of the "onion-shell" structure in the interior of a highly evolved massive star. Along the vertical radius and below the horizontal radius some typical values of the mass, the temperature (in K) and the density (in $\mathrm{g\,cm^{-3}}$) are indicated. (From Kippenhahn *et al.*, 2012.)

The process has to stop when the iron group is reached, since further addition of ^{4}He requires energy (*cf.* Figure 14.2); the last reaction in the sequence of ^{4}He capture is the last of equations (14.6). Hence there is a tendency to convert the original composition into predominantly ^{56}Ni, although the precise equilibrium composition depends on temperature. How far one gets towards this point depends on the time in which the silicon burning proceeds, as well as on the temperature. Hence, when the central region has been converted to ^{56}Ni, regions further out have not reached that point yet, and still contain a mixture of the elements produced earlier in the quasi-equilibrium. Outside this region, of course, are shells resulting from earlier nuclear-burning stages, and the stellar envelope has more or less the original composition from when the star was formed, apart from the effect of possible dredge-up when the star passed through red-giant phases. The resulting "onion-shell" structure is indicated schematically in Figure 14.3.

It is worth noting that the late stages of stellar evolution are very rapid, compared with the hydrogen- and helium-burning phases. As illustrated in Figure 1.3, oxygen burning only lasts of order 6 months, whereas "silicon burning" is over in about a day. Hence the chances of observing a star while in these evolutionary phases are extremely small.

14.3 Supernova explosion[4]

The end of silicon burning, with the production of nuclei in the iron mass range ($A \sim 60$), leaves the star with a serious problem: it is unable to generate energy in the core from nuclear reaction. Thus only further gravitational contraction remains as a means of providing the energy required from the stellar core. As usual, this leads to a heating up of the core in accordance with the virial theorem.

14.3.1 Physics of the collapse and the explosion

As mentioned above, at the temperatures involved (a few 10^9 K) nuclear reactions, mediated by the strong nuclear force and electromagnetic force, proceed in both directions. In fact, these reactions occur in equilibrium. To describe conditions in the collapsing core, we can approximate the nuclei and nucleons present in the core by an ideal nonrelativistic Maxwell-Boltzmann gas. Furthermore, we assume that the equilibrium is characterized just by conservation of charge and baryon number. Formally, this can be described in terms of two independent chemical potentials, which we chose to be those for protons and neutrons, μ_p and μ_n. Then the chemical potential for a nucleus with charge Z and mass number A can be related to those of the nucleons as

$$\mu(Z,A) = Z\,\mu_\mathrm{p} + (A-Z)\mu_\mathrm{n}\ . \tag{14.7}$$

This is the condition for nuclear statistical equilibrium. Using Maxwell-Boltzmann statistics it allows us to express the number density $n(Z,A)$ of a nucleus in terms of the number densities of free nucleons

$$n(Z,A) = \frac{g(Z,A)A^{3/2}}{2^A}\left(\frac{2\pi\hbar^2}{m_u k_\mathrm{B} T}\right)^{3(A-1)/2} n_\mathrm{p}^Z\, n_\mathrm{n}^{(A-Z)}\, \exp[Q(Z,A)/k_\mathrm{B}T]\ , \tag{14.8}$$

where the nuclear binding energy $Q(Z,A)$ is given by

$$Q(Z,A) = \tilde{c}^2[Zm_\mathrm{p} + (A-Z)m_\mathrm{n} - M(Z,A)]\ , \tag{14.9}$$

and $g(Z,A)$ is the partition function. Here m_p, m_n, $M(Z,A)$ are the masses of the proton, neutron and nucleus, respectively.

As external conditions we have the conservation of baryon number and charge. These can be expressed in terms of n_p, n_n as ($n_i = n(Z_i, A_i)$)

$$\sum_i n_i A_i = \frac{\rho}{m_\mathrm{u}} = n\ , \tag{14.10}$$

$$\sum_i n_i Z_i = n\,Y_\mathrm{e}\ , \tag{14.11}$$

where Y_e defines the number of electrons per baryon.[5]

In the case of nuclear statistical equilibrium, all relevant properties (composition, equation of state, *etc.*) can be determined, once the 3 quantities ρ, T and Y_e are known.

[4] Major parts of this section were kindly contributed by K. Langanke.

[5] Note that Y_e is related to the mean molecular weight μ_e per electron, introduced in section 3.2.2, by $Y_\mathrm{e} = 1/\mu_\mathrm{e}$ In the rest of this chapter, however, μ_e denotes the electron chemical potential.

Under the core conditions, the mass is dominated by nucleons, while the pressure is given by the electrons; these quantities are related by Y_e. The electrons can be described by a degenerate, relativistic Fermi gas. Chandrasekhar showed that the electron degeneracy pressure can only stabilize masses smaller than

$$M_{\rm Ch} \simeq 1.457(2Y_{\rm e})^2[1 + F(T)]\,{\rm M}_\odot \tag{14.12}$$

(see also Chapter 16). This is called the Chandrasekhar limit. The factor $F(T)$ is a finite-temperature correction which for massive stars can correspond to 0.2 – 0.3. Note that for nuclei during silicon burning $Y_{\rm e} \sim 0.5$ [the nuclei involved have (approximately) the same number of protons and neutrons].

To understand the fate of the core we have to consider that the Fermi energy of the electron reaches the level of nuclear energies ($E_{\rm F} \gtrsim 1\,{\rm MeV}$) at densities around $10^7\,{\rm g\,cm^{-3}}$. As the core has a finite temperature (recall that $k_{\rm B}T = 86\,{\rm keV}$ at $T = 10^9\,{\rm K}$), the electrons obey a Fermi-Dirac distribution (see also section 3.5)

$$n(E) \propto \{\exp[(E - \mu_{\rm e})/k_{\rm B}T] + 1\}^{-1}\,, \tag{14.13}$$

characterized by the electron chemical potential $\mu_{\rm e}$, such that $\mu_{\rm e}/k_{\rm B}T$ corresponds to the degeneracy parameter ψ introduced in equation (3.50). In the limit of $T \to 0$, *i.e.*, for complete degeneracy, $\mu_{\rm e} \to E_{\rm F}$, introduced in equation (3.54). For nonrelativistic degeneracy we therefore obtain, using equation (3.55), that $\mu_{\rm e} \simeq 1.2(\rho_7 Y_{\rm e})^{2/3}\,{\rm MeV}$, where $\rho_7 = \rho/(10^7\,{\rm g\,cm^{-3}})$ defines the density in units of $10^7\,{\rm g\,cm^{-3}}$. Thus, the presence of electrons with relatively high energies makes it now energetically favourable to capture electrons by nuclei in processes like

$$(Z, A) + e^- \to (Z - 1, A) + \nu_{\rm e}\,. \tag{14.14}$$

Since this process changes a proton into a neutron (although in a nucleus) one talks about neutronization of the core. Electron capture has two important consequences:

1) It reduces the number of electrons: $Y_{\rm e}$ gets smaller. Thus, the pressure which is available to stabilize the gravitational contraction of the core is reduced. In other words, the Chandrasekhar mass limit decreases as $Y_{\rm e}$ decreases (*cf.* eq. 14.12).

2) The neutrinos produced in the reaction can leave the star. These neutrinos carry kinetic energy (usually of a few MeV) which is lost for the core. In fact, these neutrino losses keep the core at relatively low temperatures.[6]

In summary, the pressure and energy loss due to electron capture accelerates the contraction. It is also important to stress that the relatively low temperatures ensure the presence of a limited number of free protons and neutrons; otherwise the electron capture on free protons would dominate as the energy threshold is smaller than in nuclei. Pre-supernovae simulations estimate the mass fraction of free protons $X_{\rm p} \lesssim 10^{-4}$ at densities $\rho \sim 5 \times 10^9\,{\rm g\,cm^{-3}}$ ($T \simeq 8 \times 10^8\,{\rm K}$). As most nucleons are still bound in nuclei, (*i.e.*, with a large degree of "order"), the collapse proceeds at low entropy. Electron captures

[6] We note that beta decays, in which a neutron is changed into a proton inside a nucleus, can compete with electron capture during certain stages of the final evolution of a massive star. Beta decays cool the star by neutrino emission, but increase the value of $Y_{\rm e}$.

have now reduced the Y_e-value to about 0.44 in the centre of the core and the electron degeneracy pressure is overwhelmed by gravitation leading to an approximately free collapse in the centre. This increases the density and the electron energies enabling further electron captures on the fast collapse time scale. Neutrino losses still cool the star until the core matter reaches densities around $4 \times 10^{11}\,\mathrm{g\,cm^{-3}}$. At such high densities it becomes important to consider the interaction of neutrinos with the surrounding matter. At first, via neutral-weak-current interaction, neutrinos can scatter elastically from nuclei. This randomizes the neutrino path out of the core and the neutrino mean free path is about 8 km at $\rho = 10^{12}\,\mathrm{g\,cm^{-3}}$ during the dynamical collapse time of ~ 1.6 ms. For the same density, the core radius is about $R = 30\,\mathrm{km}$. Thus, neutrinos are unable to diffuse out of the core: they are "trapped".

The neutrinos also scatter inelastically on electrons. In this process, energy is transferred from neutrinos to electrons and the neutrinos are thermalized in about 1/5 of a dynamical time scale. This finally brings also the weak interaction into equilibrium and the inner core where the density exceeds $\sim 10^{12}\,\mathrm{g\,cm^{-3}}$ collapses as a unit (called the homologous core). The mass of the homologous core can be estimated from the appropriate Chandrasekhar mass, taking into account that progressing electron captures have reduced the Y_e-values to about $Y_e \simeq 0.36 - 0.38$, corresponding to $M_{\mathrm{Ch}} \sim 0.7\,\mathrm{M_\odot}$.

The collapse continues until the core reaches nuclear matter densities ($\rho \sim 10^{14}\,\mathrm{g\,cm^{-3}}$). The finite compressibility of nuclear matter brings the collapse to a halt. Note that the sound speed in the homologous core is larger than the infall velocity. In fact, the sonic point, at which these two velocities are equal, is the surface of the homologous core. Thus, the sudden stop of the collapse in the centre creates a shock wave at the surface of the homologous core. This shock wave moves outwards through the rest of the collapsing iron core. The energy available to the shock depends on details of the nuclear equation of state which are still somewhat uncertain. According to current knowledge, the shock energy is of the order 10^{52} erg (or 10 foe, with 1 foe defined as 10 to the power fifty one erg).

The temperature in the shock is very high ($k_B T \sim 10$ MeV). Thus, the matter through which the shock passes will be dissociated, at an energy cost of about 16 foe per $1\,\mathrm{M_\odot}$ matter (the binding energy of Fe is about 8.8 MeV/nucleon). It follows that the success or failure of a prompt explosion, initiated by the shock, depends crucially on the amount of matter it has to traverse, *i.e.*, the mass of the Fe core[7] minus the mass at which the shock starts (homologous core mass). Current estimates put the homologous core mass at $0.7\,\mathrm{M_\odot}$, while the mass of the iron core is about $1.6 - 1.7\,\mathrm{M_\odot}$ for massive stars. Thus, the shock has insufficient energy to explode the star.

The behaviour of the core during the collapse is illustrated in Figure 14.4, which shows the radial motion of various layers, as well as the location of the shock. This shows that the shock stalls at a radius of around 500 km. The figure also indicates that it is revived after about 0.5 sec, finally exploding the star. What has happened?

In the centre of the core, a neutron star is born consisting of the original homologous core and additional mass which has fallen through the shock. This newly-born neutron star attempts to cool as fast as possible. The most effective way is by emission of neutrino pairs (neutrino + anti-neutrino),[8] with a luminosity of up to $5 \times 10^{52}\,\mathrm{erg\,sec^{-1}}$ for each neutrino family, lasting for several seconds. Additionally, there is a very short neutrino

[7] Once the shock reaches the oxygen burning shell, nuclear burning produces energy, helping the explosion.

[8] For example, this may happen through the creation of an electron-positron pair followed by annihila-

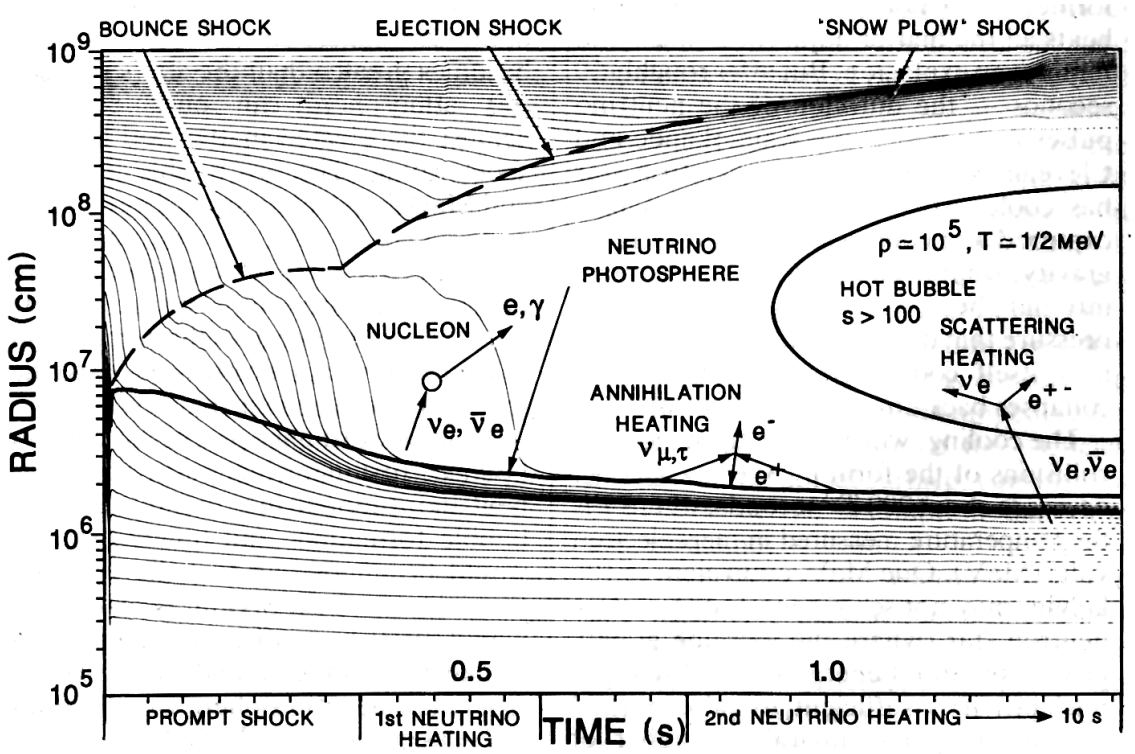

Figure 14.4: The motion in radius of mass shells in a supernova simulation, following the core bounce which happens at time $t = 0$. The shock travels outwards for a short time, gets stalled and is later revived by the neutrinos generated in the cooling of the newborn neutron star. (From Colgate 1989.)

burst just after the bounce when the trapped $\nu_{\rm e}$ neutrinos are released from the core. A detailed review of neutrino processes in supernova explosions was provided by Burrows (1990).

The cross sections for the neutrino absorption on nucleons,

$$\begin{aligned} \nu_{\rm e} + n &\rightarrow p + e^- \,, \\ \bar{\nu}_{\rm e} + p &\rightarrow n + e^+ \,, \end{aligned} \tag{14.16}$$

are tiny, $\sigma \simeq (E_\nu/1\,{\rm MeV})^2 \times 10^{-43}\,{\rm cm}^2$, where E_ν is the neutrino energy ($E_\nu \simeq 15\,{\rm MeV}$ for $\nu_{\rm e}$, $\bar{\nu}_{\rm e}$ neutrinos). Despite the tiny cross section, neutrino-nucleon interaction transfers energy to the matter which has previously been dissociated by the shock. In fact, the matter in the shock is heated within about 0.3 sec to an energy which is larger than the gravitational potential and can therefore be expelled from the star. The explosion mechanism, by which the shock is revived by neutrino heating, is called the delayed supernova mechanism.

---

tion:

$$\gamma + \gamma \rightarrow {\rm e}^- + {\rm e}^+ \rightarrow \nu_{\rm e} + \overline{\nu}_{\rm e} \,, \tag{14.15}$$

where $\overline{\nu}_{\rm e}$ denotes the anti-neutrino.

Exercise 14.2:

Consider a *neutron star* with a mass of $1\,M_\odot$ and a radius of 10^6 cm, assumed to have uniform density. Assuming that the cross section for interaction between a neutrino and a neutron is $10^{-41}\,cm^2$, what is the mean free path of the neutrino within the neutron star?

Exercise 14.3:

Show that a star collapsing without loosing mass will eventually become opaque to neutrinos.

Computer simulations currently strongly favour the delayed mechanism, although even the delayed mechanism does not always generate a successful explosion. The success depends crucially on the effectiveness of the energy transport to the shock region by the neutrinos. Very recent investigations have shown that this energy transport is enhanced by 1) convection, 2) an improved description of the neutrino opacities in dense matter and perhaps 3) by preheating the matter during the early ν_e-neutrino burst. The high-temperature environment related to the shock leads to explosive burning which affects the matter composition up to the oxygen-burning shell. The matter further out is basically unaffected and thus has the same composition as during the hydrostatic burning before the collapse.

A more recent summary of the processes involved in the supernova explosion is shown in Fig. 14.5. This also emphasizes the importance of convective overturning in driving the explosion, now being included in two- and three-dimensional calculations.

The explosion expels the matter outside a certain point at a mass $\sim 1.6\,M_\odot$ (called the mass cut) into the interstellar medium (ISM) where it is mixed with the preexisting matter. The remnant inside the mass cut consists largely of neutrons. Because of the high density, the neutrons are partially degenerate; the degeneracy becomes complete as the core cools, largely through emission of neutrinos, and it settles down as a *neutron star*. These are discussed in more detail in Chapter 16. Observationally, neutron stars have been detected in the form of the *pulsars*, which emit pulses at very regular intervals, with periods between a few milliseconds and a few seconds.

Core-collapse supernovae, as discussed above, are generally known as *Type II supernovae*.[9] We note that only for stars in a certain mass range ($\sim 8 - 30\,M_\odot$ on the main sequence) does the explosion from a core collapse result in the generation of a neutron star. More massive stars also end their lives as core-collapse supernovae, but instead likely generate a black hole in the centre (see also Chapter 16). On the other hand, as discussed in Chapter 12 stars of mass below around $8\,M_\odot$ never reach the latest nuclear burning stages.

[9] In reality the observational classification is more complex: core collapse may also result in supernovae of Type Ib or Ic, characterized by particular features of their spectra (*e.g.* Filippenko 1997). A physically distinct class are the Type Ia supernovae which are caused by the collapse of a white dwarf as a result of mass transfer in a binary system; see Chapter 16.

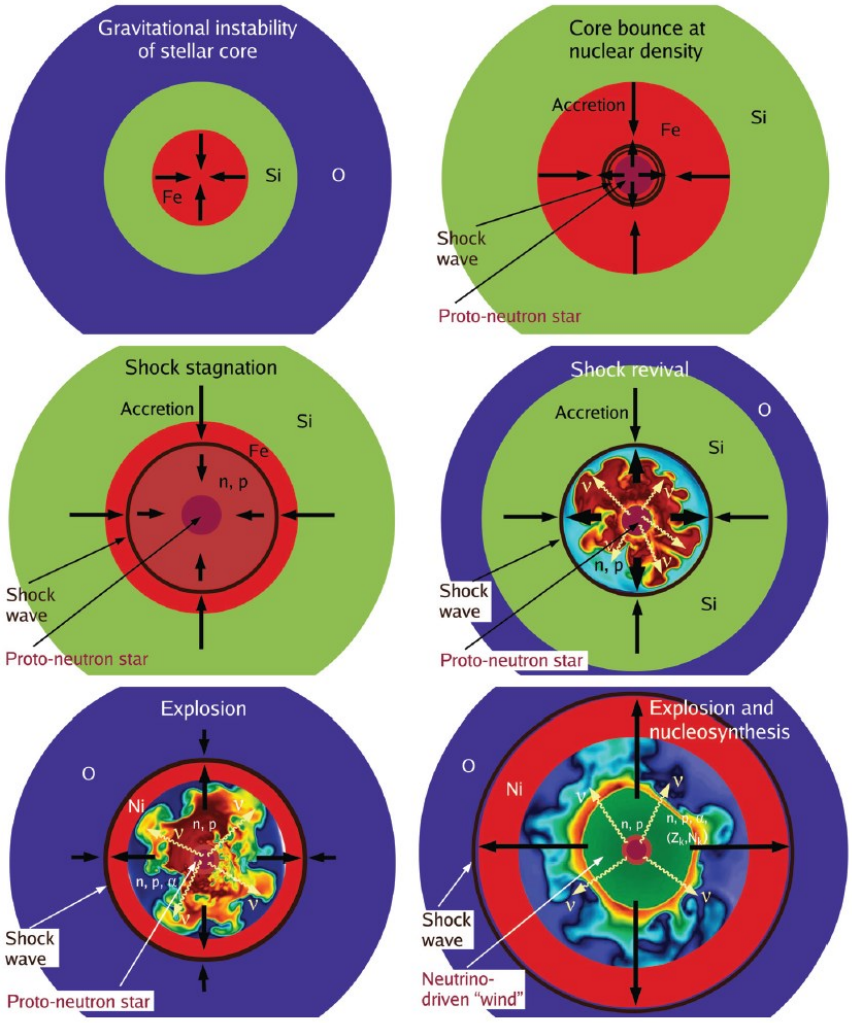

Figure 14.5: Schematic representation of the evolution stages from the onset of stellar core collapse (top left) to the development of a supernova explosion on a scale of several thousand kilometers. The displayed intermediate stages show the moment of core bounce and shock formation (top right), shock stagnation and onset of quasi-stationary accretion (middle left), beginning of the reexpansion of the shock wave ("shock revival", middle right), and acceleration of the explosion (bottom left). Nickel formation is indicated in the matter heated by the outgoing shock, but the rising bubbles of neutrino-heated ejecta and the essentially spherically symmetric neutrino-driven wind (bottom right) are also interesting sites for nucleosynthesis. (From Janka *et al.*, 2012.)

The preceding discussion is obviously only a very rough sketch of the processes that go on in a supernova explosion. However, it is largely supported by detailed numerical calculations; for an excellent, if somewhat outdated, summary of the results of such calculations, see Bethe & Brown (1985). They confirm the role played by both the shock waves and the neutrino absorption in driving the explosion. Indeed, it has been a long-standing problem that even taking into account the combined effects of neutrinos and shocks the energy deposition appeared to be marginally sufficient to drive the explosion. Bethe (1990a) suggested that this problem may be overcome if energy transport by convection is taken into account; some support for this suggestion has come from detailed hydrodynamical simulations, summarized, for example, by Hayes & Burrows (1995), although more recent hydrodynamical calculations have cast doubt on the earlier results. An interesting and very recent suggestion (Burrows *et al.* 2006) is that the generation of acoustic power by turbulence in the accretion onto the core and excitation of oscillations of the core may contribute to driving the explosion. A likely consequence of this is that the explosion looses spherical symmetry, resulting in a kick to the forming neutron star that may give it a large spatial velocity; such high-velocity neutron stars are in fact observed (*e.g.*, Chatterjee *et al.* 2005).

Detailed reviews on the evolution of massive stars and supernovae have been given by Bethe (1990b) and Woosley, Heger & Weaver (2002). We also note the monograph by Arnett (1996) which provides a detailed overview of stellar evolution through to supernova explosions as well as galactic nucleosynthesis.

14.3.2 Observations of supernovae

The energy release in the supernova explosion is enormous. At its maximum, the luminosity may be comparable with the luminosity of an entire galaxy, of order $10^{10}\,\mathrm{L}_\odot$. This lasts for several days, followed by a gradual decay in luminosity over a period of months. Even so, the energy emitted as visible light is only a relatively small fraction of the total amount of energy released, which is of order $10^{53}\,\mathrm{erg}$. Most of the energy is emitted in the form of neutrinos, while sizeable fractions are also used to expel the outer parts of the star with high velocity, or are stored in rotational energy of the remaining core. It is striking that this energy, and the energy required to dissociate the nuclei produced during the preceding nuclear burning, comes entirely from the release of gravitational potential energy of the core.

Exercise 14.4:

Estimate the energy release in gravitational collapse of a core of mass $1\,\mathrm{M}_\odot$, from an initial density of $10^9\,\mathrm{g\,cm^{-3}}$ (typical of the situation during silicon burning) to the nuclear density of $10^{14}\,\mathrm{g\,cm^{-3}}$. Compare with the total rest-mass energy of the core.

Observationally, a supernova explosion is a spectacular phenomenon. Unfortunately[10] they are rare. In our own Galaxy only a few have been recorded, the last in the seventeenth century. An interesting example is the supernova that was recorded by Chinese astronomers in 1054; it is now the site of a interstellar cloud (the *Crab nebula*), containing

[10] Although a nearby supernova might be a little unpleasant.

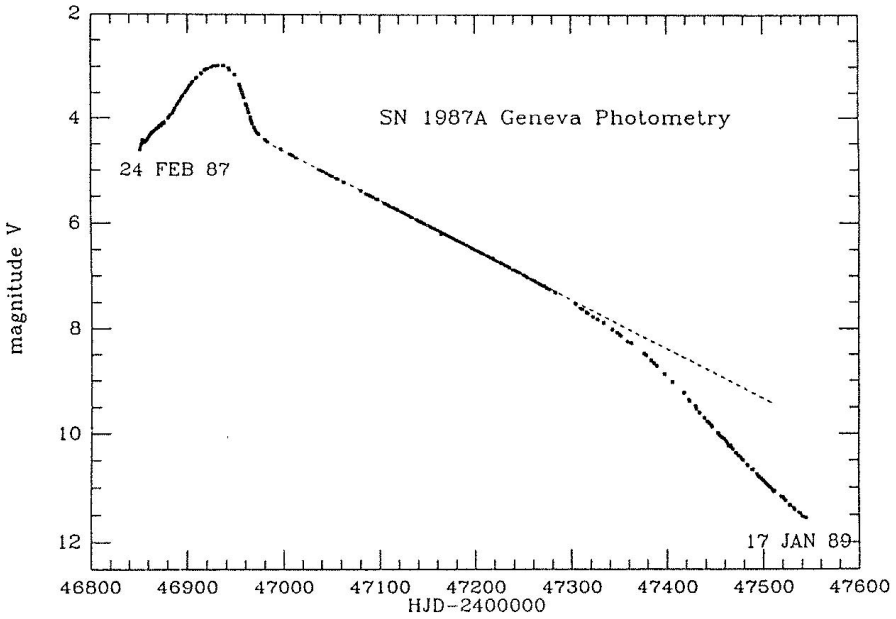

Figure 14.6: Light curve, in V-magnitude, of SN1987A in the Large Magellanic Cloud. The abscissa is days, according to the so-called Julian date. (From Burki *et al.* 1989.)

a pulsar with a period of 0.033 sec, which has been observed in both radio, optical and X-ray emission. Most of our detailed information on supernova explosions is based on supernovae in distant galaxies, and hence difficult to observe. However, in February 1987 a supernova, designated SN1987A, exploded in the Large Magellanic Cloud, a nearby small galaxy. It reached a maximum apparent magnitude of 2.8, and hence was easily visible to the naked eye. More importantly, its relative proximity and brightness permitted very detailed observations. A discussion of the stellar evolution leading up to the explosion, and of the observations, was given by Woosley & Weaver (1989). Chevalier (1992) summarized the first 5 years' investigations of the supernova.

Possibly the most interesting observation was the detection of approximately 20 neutrinos, in two different detectors, from the explosion; the number is in good agreement with the predictions of the supernova models, thus for the first time indicating that the expected nuclear reactions do in fact take place in the core of a supernova. The neutrinos preceded the optical brightening of the star by several hours, in accordance with the response time of the stellar envelope to the energy deposited by the shock and the neutrinos. A summary of the neutrino data and their interpretation was given by Bahcall (1989).

The detailed observations of SN1987A have confirmed the general picture outlined above. The models predict that about $0.15\,M_\odot$ of ^{56}Ni is ejected in a Type II supernova. (Note that this material is not produced in the silicon burning phase, but within the explosion, where nuclear statistical equilibrium for $Y_e = 0.5$ settles predominantly into ^{56}Ni.) ^{56}Ni is unstable towards electron capture and decays in the following sequence to ^{56}Fe:

$$e^- + {}^{56}\mathrm{Ni} \rightarrow {}^{56}\mathrm{Co} + \nu_e \qquad (\text{half life } 6.1 \text{ days}) \,,$$

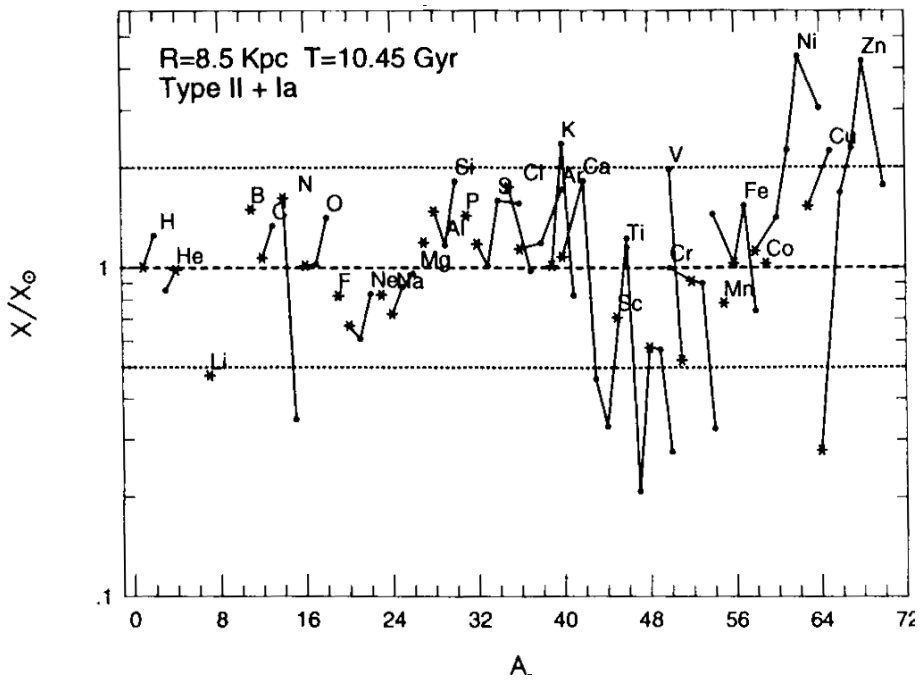

Figure 14.7: Ratio between calculated and observed solar abundances for stable isotopes from hydrogen to zinc. The calculations took into account contributions from Type II and Type Ia supernovae. The dotted lines mark deviations by a factor 2 between calculation and observation. (From Timmes *et al.* 1995.)

$$e^- + {}^{56}\mathrm{Co} \rightarrow {}^{56}\mathrm{Fe} + \nu_\mathrm{e} \qquad (\text{half life 77 days}) \; . \tag{14.17}$$

These radioactive decays provide a major contribution to the energy released by the supernova in the months following the explosion. This happens because the decays go to excited states in the daughter which then deexcites fast by γ emission. The lightcurve of SN1987A, illustrated in Figure 14.6, clearly showed the 77-days half-life decline related to the ^{56}Co decay, which corresponds to the long straight segment of the curve.

Exercise 14.5:

Show that if the energy is provided by radioactive decay, the *magnitude* of the star is a linear function of time. Estimate the half-life of the decay from the slope of the straight segment of the luminosity curve in Figure 14.6, and compare with the half-lives quoted in equation (14.10).

Supernovae also produce other radioactive material, for example about $10^{-4}\,\mathrm{M}_\odot$ of ^{44}Ti. This nucleus has the interesting half-life of 60 years and its decay can be identified by a characteristic 1 MeV γ line. In fact, the COMTEL satellite has observed this line for two historical supernovae from 1680 and 1300. As MeV photons can traverse our Galaxy unhindered, further observations of ^{44}Ti and other γ lines may provide an improved estimate of the supernova rate in our Galaxy (it is currently estimated to be about 2 per century; most of them are optically invisible, as a result of absorption by dust in the

Galaxy). A recent interesting example are observations from the INTEGRAL satellite of a 1.8 MeV line from ^{26}Al which has a half-life of 7.2×10^5 years (Diehl *et al.* 2006); this did indeed lead to an estimate of the core-collapse supernova rate in the Galaxy of 1.9 ± 1.1 events per century.

A major event related to SN1987A, which is eagerly awaited, would be the detection of the neutron star that has probably been formed in the collapse. Clear evidence for the neutron star would be observation of rapid pulses in brightness, corresponding to what is observed from pulsars. So far there have been two false alarms, which were later attributed to instrumental problems; we are still waiting.

A dramatic phenomenon that has recently been associated with supernovae are the *γ-ray bursts* (*e.g.* van Paradijs, Kouveliotou & Wijers 2000; Hurley 2003). These are short bursts of γ rays, lasting from seconds to a few minutes, observed at a rate of about once a day with uniform distribution across the sky. It is now known that they occur at cosmological distances and hence involve huge amounts of energy. It is normally assumed that the energy is beamed in a narrow jet, partly by relativistic effects, so that only those bursts that happen to point towards the Earth are detected. In some cases (see, for example, Hjorth *et al.* 2003) a supernova has been observed that is clearly associated with the burst. A brief discussion of the possible, but still rather uncertain, mechanisms causing the γ-ray bursts was provided by MacFadyen (2004), while Heger *et al.* (2003) discussed the evolution that might lead to a supernova explosion causing a burst.

14.3.3 Effects on the galactic chemical evolution

The nuclear material produced in the supernova explosion is mixed into the interstellar medium and can thus contribute to the initial composition of new generations of stars. Thus, the galactic chemical evolution represents a "cosmic cycle", and modelling the observed solar and stellar abundances requires simulations of the formation of a galaxy and of the stellar mass distribution, birth rates, evolution and lifetimes. A crucial component of the modelling is the calculation of the abundances produced by a star of a given mass and the amount and composition of matter ejected into the ISM by the star's final Type II supernova explosion. Contributions must be added from the Type Ia supernovae; these involve the formation and evolution of binary systems composed of a giant star with a hydrogen envelope and an accreting white dwarf (see also Chapter 16). Finally, recent modelling and observations have shown that colliding neutron stars, resulting from the evolution of binary systems of neutron stars, play an important role (see section 15.3).

Despite its complexity, rather consistent studies of the galactical chemical evolution have been performed (*e.g.* Timmes, Woosley & Weaver 1995); an example is illustrated in Figure 14.7. Although the simulations involve a few model assumptions, excellent agreement is obtained with the solar abundance for isotopes from hydrogen to zinc, when the calculation is sampled at a time 4.55×10^9 y ago, and a distance of 8.5 kpc from the galaxy centre, corresponding to the time and position of the birth of our Sun in the Milky Way Galaxy.

Chapter 15

Nucleosynthesis through neutron capture

15.1 Introduction

The description given in the preceding chapters can account for the production of elements up to the iron group, in relative concentrations approximately corresponding to those observed. However, it is not possible to generate even heavier elements by similar processes. Because of the Coulomb barrier, fusion between charged particles leading to such elements is extremely improbable at moderate temperature; at higher temperature, photo-dissociation gives rise to the quasi-equilibrium processes in the silicon burning, which predominantly generate nuclei around the maximum in the binding energy, *i.e.*, in the iron group. There would appear to be no way to generate even heavier elements.

The solution to this difficulty lies in the observation that neutrons are not affected by the Coulomb barrier. Hence, *if* matter is exposed to a flux of neutrons, heavier elements can be generated through neutron capture, possibly followed by e^- decay converting the neutron into a proton. We postpone the discussion of the source of neutrons, and begin by discussing the likely outcome of such neutron capture.

15.2 Effects of neutron capture

The absorption of a neutron in a nucleus increases its atomic weight without changing the atomic number,

$$(\mathcal{Z}, \mathcal{A}) + n \rightarrow (\mathcal{Z}, \mathcal{A}+1) + \gamma \; . \tag{15.1}$$

However, stable nuclei are concentrated in *the valley of stability* in the $(\mathcal{Z}, \mathcal{A})$ plane, with the number of neutrons being slightly higher than the number of protons. Starting from a nucleus with this property, the reaction (15.1) clearly moves the nucleus away from the valley of stability. If the resulting nucleus is unstable it decays,

$$(\mathcal{Z}, \mathcal{A}+1) \rightarrow (\mathcal{Z}+1, \mathcal{A}+1) + e^- + \overline{\nu}_e \; , \tag{15.2}$$

resulting in the production of the next element. Otherwise the nucleus may capture yet another neutron,

$$(\mathcal{Z}, \mathcal{A}+1) + n \rightarrow (\mathcal{Z}, \mathcal{A}+2) + \gamma \; , \tag{15.3}$$

hence leading to an even heavier isotope of the original element, whose stability must then be tested.

In reality, the situation is more complicated. The beta decay in equation (15.2) is typically a fairly slow process; hence it is possible that even though the nucleus produced in equation (15.1) is unstable, it has time to capture another neutron according to equation (15.3) *before* it decays according to equation (15.2). To describe this, we operate with two different types of neutron capture:

- the *s* process (for slow), where the neutron capture is much slower than the beta decay.
- the *r* process (for rapid), where the neutron capture is much more rapid than the beta decay.

These possibilities are illustrated schematically in Figure 15.1. The s-process path proceeds along the bottom of the stability valley, since it only involves stable nuclei. In particular, it is not possible to produce isotopes which are separated from the stability line by unstable isotopes; hence some isotopes may be identified as being necessarily the result of the r process. On the other hand, the r process produces predominantly neutron-rich nuclei. Hence a stable isotope of a given atomic weight may "shield" an isotope of the same atomic weight, but higher atomic number, from the r process, hence identifying the latter as having been produced by the s process.

The abundances of elements produced by the s process can be estimated reasonably simply. It may be expected that an approximate equilibrium is established, such that equal numbers of a given isotope are produced and destroyed in the process. Consider two nuclei along the s-process path, with atomic weight $\mathcal{A}-1$ and $\mathcal{A}$,[1] let $N_{\mathcal{A}-1}$, $N_{\mathcal{A}}$ be the abundances of these nuclei, and let $\sigma_{\mathcal{A}-1}$, $\sigma_{\mathcal{A}}$ be their average cross sections for neutron capture. The rate of production of nucleus $\mathcal{A}$ from nucleus $\mathcal{A}-1$ is proportional to $\sigma_{\mathcal{A}-1}N_{\mathcal{A}-1}$, and the rate of destruction of nucleus $\mathcal{A}$ is proportional to $\sigma_{\mathcal{A}}N_{\mathcal{A}}$. To maintain equilibrium we therefore expect that, approximately,

$$\sigma_{\mathcal{A}-1}N_{\mathcal{A}-1} \simeq \sigma_{\mathcal{A}}N_{\mathcal{A}} \ , \tag{15.4}$$

i.e., that the product $\sigma_{\mathcal{A}}N_{\mathcal{A}}$ is constant along the s-process path.

The neutron cross section depends strongly on the properties of the nucleus, as illustrated in Figure 15.2. This dependence is linked to the structure of the nuclei. Just as is the case for the electrons in an atom, the nucleons in a nucleus may be regarded as occupying certain shells (with separate sets for the protons and the neutrons), each of which can hold a specific number of nucleons. Furthermore, nucleons enter into the shells in pairs, corresponding to the two directions of the spin. Nuclei where either a neutron shell or a proton shell is filled are particularly stable; if a neutron shell is filled, the nucleus has little incentive to absorb another neutron, and hence the neutron-capture cross section is very low. In contrast, nuclei with an odd number of neutrons, and hence with an incomplete pair, are particularly eager to complete the pair, and hence have very high cross sections. Both effects, the low cross sections at the so-called "magic" neutron numbers (50, 82 and

[1] Note that there is only one isotope at each value of the atomic weight along the s-process path. Hence an s-process nucleus is uniquely characterized by its mass.

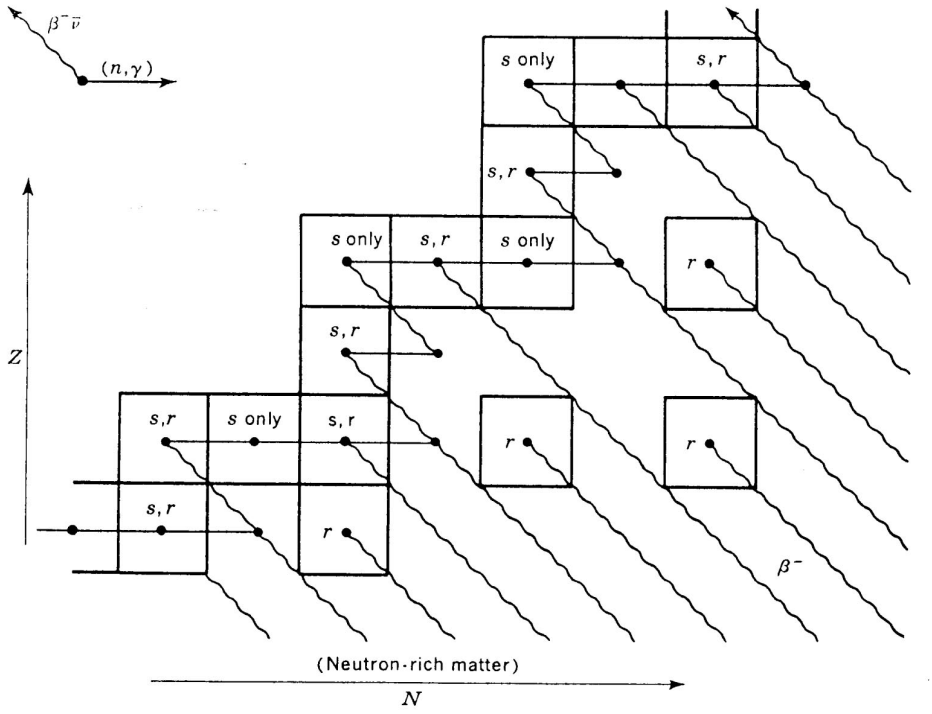

Figure 15.1: Schematic illustration of a portion of the chart of nuclides showing the production of elements by the s and r processes. The s-process path of (n, γ) reactions followed by quick beta decays enters the diagram at the lower left and passes through each nucleus designated by the letter s. Neutron-rich matter produced by rapid neutron capture undergoes a chain of beta decays terminating at the most neutron-rich of the stable isobars (*i.e.*, nuclei with the given atomic weight), which are designated by the letter r. When such a nucleus is separated by an unstable isotope from the nearest isotope with lower mass, the nucleus can only be produced by the r process. Similarly some of the nuclei on the s-process path are shielded from the r process by more neutron-rich isobars, and hence can only be produced by the s process.

126) corresponding to filled shells, and the high cross sections for odd nuclei, are evident in Figure 15.2. Also, it is clear that very roughly the abundances in Figure 14.1 are a mirror image of the cross sections in Figure 15.2, in accordance with the expectation based on equation (15.4) that $N_{\mathcal{A}} \propto \sigma_{\mathcal{A}}^{-1}$.

A more accurate description has to take into account the details of the neutron exposure, and the time dependence of the abundances (*cf.* Clayton 1968). The result is that rather than being constant, $\sigma_{\mathcal{A}} N_{\mathcal{A}}$ is a slowly varying function of $\mathcal{A}$ for nuclei created by the s process. This is illustrated in Figure 15.3.

Estimates of the abundances resulting from r-process neutron capture are more difficult and uncertain; they were discussed also by Clayton (1968). Roughly speaking the result is again a dominance of magic numbers of neutrons in the very neutron-rich nuclei which are created by the neutron exposure. The subsequent beta decays towards the bottom of

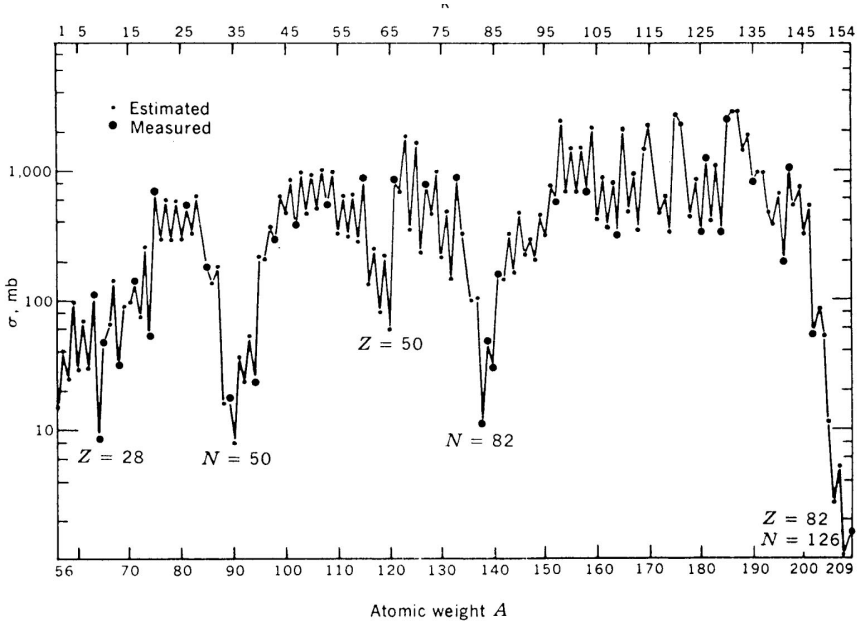

Figure 15.2: Neutron cross sections for nuclei along the s-process path, for a neutron energy around 25 keV. It is obvious that the cross sections are exceptionally low for nuclei with closed shells, at the so-called magic values for the neutron number N (and to a lesser extent the proton number Z). (From Clayton 1968.)

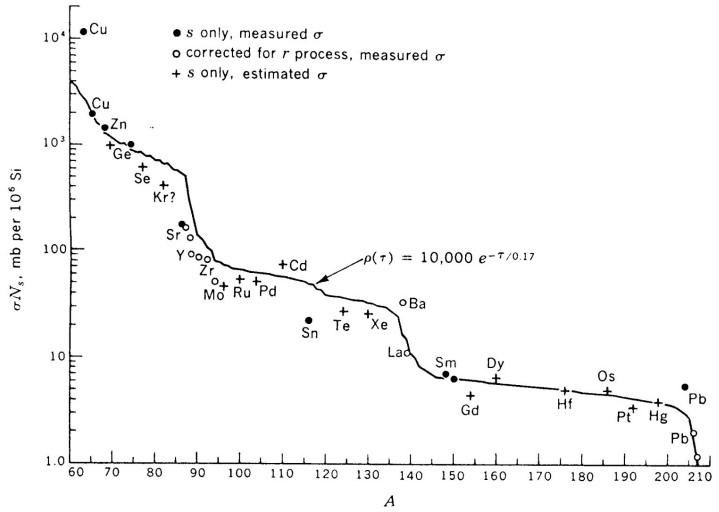

Figure 15.3: The $\sigma_{\mathcal{A}} N_{\mathcal{A}}$ curve for s-process nuclei in the solar system. The product of the neutron-capture cross sections times the nuclide abundance per 10^6 silicon atoms is plotted against atomic weight number A. The curve is the calculated result for a particular model for the neutron exposure. (From Clayton 1968.)

the beta-stability valley then shift the neutron number towards somewhat lower values.

15.3 The sources of neutrons

According to the discussion in Chapter 8, neutrons are not produced by nuclear reactions until carbon burning is reached; at this point the temperature is so high, however, that the neutron capture processes would face impossible competition from photo-dissociation. During silicon burning large numbers of free neutrons are produced also by photo-dissociation, but conditions are clearly even less favourable for neutron reactions to occur on a sufficiently large scale. Hence we need to find other sources for the neutrons.

It appears that nucleosynthesis by the s process occurs in stars on the Asymptotic Giant Branch which are thermally pulsing, alternating between having a hydrogen and a helium shell-burning source. During the pulses matter that has taken part in hydrogen burning (predominantly through the CNO cycle) is mixed from the region where hydrogen burning takes place down into the region of helium burning, where neutron-producing reactions can take place. Two such reactions are commonly considered:

$$^{13}\mathrm{C}(^{4}\mathrm{He}, n)^{16}\mathrm{O} \tag{15.5}$$

(note that ^{13}C is part of the CNO cycle); and a continuation of the reaction in equation (8.64), where ^{14}N undergoes a series of captures of ^{4}He:

$$^{14}\mathrm{N}(^{4}\mathrm{He}, \mathrm{e}^{+}\nu_{\mathrm{e}})\,^{18}\mathrm{O}(^{4}\mathrm{He}, \gamma)\,^{22}\mathrm{Ne}\,(^{4}\mathrm{He}, n)\,^{25}\mathrm{Mg}\ . \tag{15.6}$$

Both reaction sequences lead to the emission of a neutron. Each thermal pulse adds a fresh supply of ^{13}C and ^{14}N and hence gives rise to an episode of neutron capture. It appears that the observed distribution of s-process elements may be understood in terms of such a sequence of neutron exposures. A detailed review of these processes, and the comparison of the outcome with solar-system abundances, was given by Busso, Gallino & Wasserburg (1999).

Evidence that such processes do occur in red giants is provided by the fact that some red giants show very peculiar surface abundances, which may be understood in terms of nucleo-synthesis by the s process. In fact, these stars develop surface convection zones that are sufficiently deep to reach down into the region where the nuclear processes take place (*cf.* Figure 12.3); hence the newly synthesized elements may be brought to the surface. Particularly striking is the presence of technetium in some stars, since all isotopes of technitium are radioactive, with halflives of less than a few million years; technetium is in fact produced as part of the s process. By studying such abundance anomalies we may hope to obtain a detailed test of the model for nucleo-synthesis by slow neutron capture.

The sites of the nuclear r process are still rather uncertain; possible sites were reviewed by Woosley *et al.* (2002). Obviously it requires a location with extreme neutron fluxes. The currently favoured site is the region just above the newly born neutron star in a Type II supernova. This region is called the 'hot neutrino bubble' (see Fig. 14.4). As the $\bar{\nu}_{\mathrm{e}}$ neutrinos, produced by cooling of the neutron star, are on average more energetic than ν_{e} neutrinos, neutrino absorption on nuclei drives the matter just above the neutron star slightly neutronrich (see the cross sections for neutrino absorption following eq. (14.16)). When the matter moves outwards, it cools and protons and neutrons combine into ^{4}He (alpha-particle) and then into heavier nuclei. The excess of neutrons at the beginning

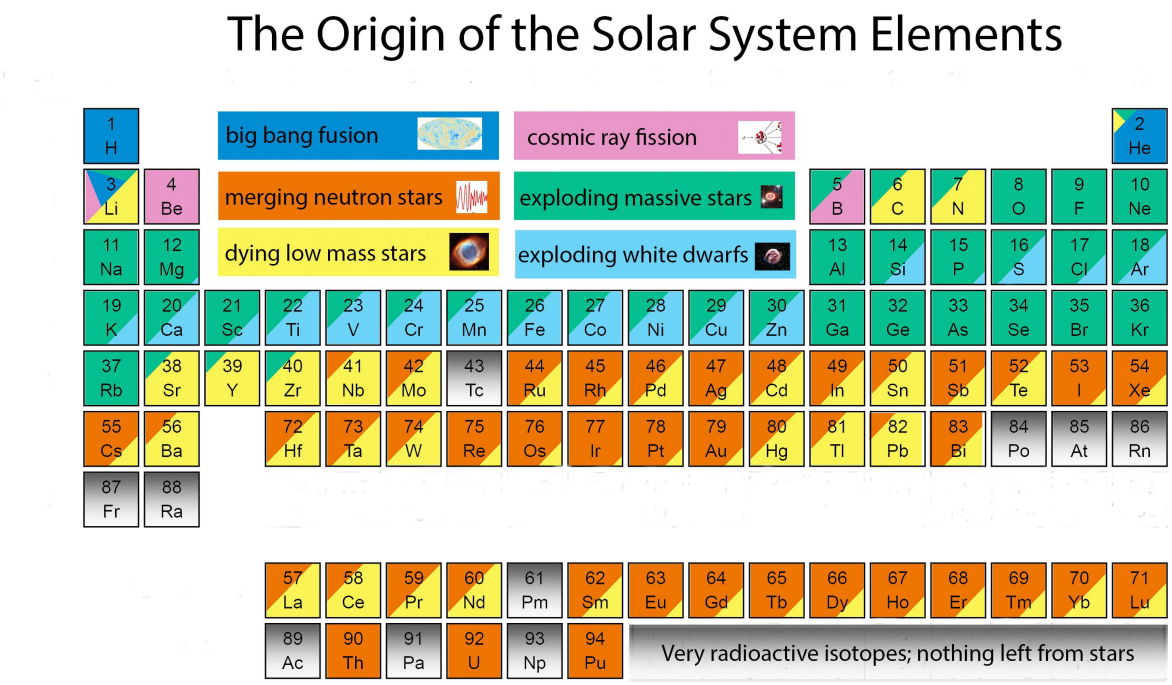

Figure 15.4: Periodic table indicating the likely origins of the different elements (Johnson, 2019; Johnson *et al.* 2020). Figure courtesy Jennifer Johnson.

guarantees that free neutrons are still available which can be captured by the heavy nuclei (around mass 60 – 90) to produce a nuclear r process. Woosley *et al.* (1994) presented a detailed calculation of these processes.

Simulations of the r process within the 'hot neutrino bubble' model is still an ongoing research area and no consistent reproduction of the observed solar r-process abundance has been achieved. Current supernova models appear not to give the right condition to allow for matter flux from the heavy seed nuclei up to the r-process peak around mass $A \sim 200$. This problem might actually be consistent with recent meteoritic data and abundance observations of old stars, which both appear to indicate that two distinct r-process scenarios have contributed to the solar r-process abundance. Possible candidates for the second r-process sites are neutron-star mergers or supermassive stars in the early stage of our galaxy.

The neutron-star-merger hypothesis received a dramatic confirmation with the detection of such a merger in 2017 (Margutti & Chornock, 2021). It was first localized from the observations at three sites of gravitational waves, allowing an optical identification of the source in a relatively nearby galaxy, with a distance of 44 Mpc. The event was also detected as a gamma-ray burst. The subsequent detailed observations showed properties consistent with theoretical modelling, including r-process nucleosynthesis. The extremely high neutron intensity is important for the synthesis of the heaviest elements.

From an observational point of view, extensive data are available from the isotopic composition of solar-system material, particularly as inferred from meteorites, as well as from observations of stellar abundances. Wasserburg, Busso & Gallino (1996) used meteoritic data to discuss the early history of the material that was incorporated in the solar system. Stars of very low heavy-element abundances were considered by Cowan *et al.* (1999); they argued that these stars were formed so early in galactic evolution that little or no s-process nucleosynthesis had yet taken place and therefore assumed that the observed abundances of elements beyond barium corresponded to pure r-process material. The results seemed consistent with the r-processes abundances inferred in the Sun, suggesting uniform conditions for r-process nucleosynthesis in major parts of the history of the Galaxy. Cowan *et al.* also used the observed abundance of the radioactive element thorium, compared with the predicted initial value resulting from r-process nucleosynthesis, to infer the ages of the stars and hence estimate the age of the Galaxy. The results are essentially consistent with those obtained from fitting observed colour-magnitude diagrams of stellar clusters (*cf.* Chapter 13), although still with fairly substantial uncertainties.

Figure 15.4 provides an overview of the sources of the synthesis of the various elements in the periodic table (see also Johnson *et al.*, 2020, for a review). The inferred dominant role of the neutron-star mergers for the heaviest elements is evident.

Chapter 16

Final stages of stellar evolution (Jes Madsen, IFA)

16.1 Introduction

As described earlier in these notes, the final fate of a star depends mainly on its mass. Stars with a mass less than $4 - 8\ M_\odot$ finish the nuclear burning in their centre when the nuclei in the core are carbon or oxygen (the lightest stars perhaps finish with helium and more heavy ones with silicon). Most of their outer mass is ejected in strong stellar wind, leading to the formation of a so-called planetary nebula; the cause of this instability is not well understood, however. The remnant of the star becomes a white dwarf[1] of typically $0.5 - 1.4\ M_\odot$.

As discussed in Chapter 14, stars heavier than $8\ M_\odot$ burn successively heavier nuclei in their centres until their core of about $1.4\ M_\odot$ is made of iron-group isotopes which have the maximum binding energy per nucleon. Then the stellar energy source by fusion terminates, the central pressure drops catastrophically and the star's inner core (of about $1.4\ M_\odot$) collapses in less than a second. If the nuclei in the inner core have reached densities in excess of nuclear matter density (approx. $3 \times 10^{14}\,\mathrm{g\,cm^{-3}}$), the equation of state becomes 'stiff'; *i.e.*, the pressure changes drastically due to, for example, the production of a large number of neutrons by electron captures on nuclei and free protons ($\mathrm{e}^- + p \rightarrow n + \nu_\mathrm{e}$). The neutrons are degenerate at nuclear matter densities which induces a strong pressure (we return to this point later). The increase in pressure stops the collapse of the iron core; it expands slightly (like an elastic ball which has been squeezed together), and sends a shock wave through the outer part of the star. The shock wave and the copious emission of neutrinos from the collapsed core apparently provide enough energy (originating from the released gravitational binding energy) to eject the outer mass of the star ($> 6M_\odot$) in a supernova explosion.[2] In the centre of the star there remains a compact object with $M \sim 1.4M_\odot$, $R \sim 10$ km, mass number $A \sim 2 \times 10^{57}$, neutron number $N \sim 2 \times 10^{57}$ and proton number $Z \sim 10^{54}$. This compact remnant is called a *neutron star*.

If the original star was heavier than about $20\ M_\odot$, its inner core has too much mass

[1] The name is a little misleading. The star has the size of the Earth and is therefore indeed a dwarf; however the description as "white" is only appropriate in the hot initial phase. Later the star cools down and is rather a red dwarf.

[2] However, the models have some difficulty in actually making the star explode.

for the collapse to be stopped by the degeneracy pressure of the neutrons. In this case the collapse continues until a *black hole* is formed.

In the following we discuss briefly the properties of compact objects. In particular, we give a simple derivation of the mass-radius relation for white dwarfs and neutron stars and some arguments why there exists a mass limit for such objects, called the Chandrasekhar mass. Finally we briefly mention some observational consequences.

16.2 Degenerate matter in hydrostatic equilibrium

The properties of white dwarfs and neutron stars are predominantly determined by their content of degenerate electrons and neutrons. The equation of state for degenerate matter has been discussed in section 3.5. Hence it is sufficient to provide a brief summary here.

The number-density distribution of a fermion gas (like neutrons and electrons) can be expressed as

$$n = g_\mathrm{s} \int f(\mathbf{p}) \, \frac{\mathrm{d}^3\mathbf{p}}{h^3} \, , \tag{16.1}$$

where $f(\mathbf{p})$ is a Fermi-Dirac distribution (as a function of momentum), and g_s is a statistical weight ($g_\mathrm{s} = 2$ for electrons and neutrons as there are two possible spin directions). The Fermi-Dirac distribution depends on the temperature T and the chemical potential μ, but the discussion is strongly simplified in the limit $T = 0$, where $f(\mathbf{p})$ becomes a stepfunction:

$$f(\mathbf{p}) = \begin{cases} 1 & \text{for } |\mathbf{p}| \leq p_\mathrm{F} \, , \\ 0 & \text{for } |\mathbf{p}| > p_\mathrm{F} \end{cases} \tag{16.2}$$

(consider that all states in momentum space are occupied up to the Fermi momentum p_F with 2 particles per phase space volume h^3 and that all levels at higher momentum/energy are empty). We shall see below (exercise 16.1) that assuming a $T = 0$ distribution is a reasonable approximation, despite the fact that typical temperatures for neutron stars in the early life are of order $T = 10^{10}$ K, and 10^7 K is a typical temperature during the evolution of a white dwarf.

Using the simplification in equation (16.2), one can calculate the number density and finds $n = g_\mathrm{s} p_\mathrm{F}^3/(6\pi^2\hbar^3)$. The energy density of the gas can be calculated as

$$u = g_\mathrm{s} \int \epsilon(\mathbf{p}) f(\mathbf{p}) \frac{\mathrm{d}^3\mathbf{p}}{h^3} \, , \tag{16.3}$$

where $\epsilon(\mathbf{p}) = (|\mathbf{p}|^2\tilde{c}^2 + m^2\tilde{c}^4)^{1/2}$; similarly the pressure P can also be expressed as an integral. In the following we shall use, however, the general results: $P = 2/3\,u$ for a non-relativistic gas and $P = 1/3\,u$ for an ultra-relativistic gas (*cf.* exercise 3.1).

Table 16.1 summarizes the most important results for a non-relativistic ($\epsilon_\mathrm{F} \ll m\tilde{c}^2$) and ultra-relativistic Fermi ($\epsilon_\mathrm{F} \gg m\tilde{c}^2$) gas at $T = 0$. In Table 16.1 n is the number density, $\epsilon_\mathrm{F} = \epsilon(p_\mathrm{F})$ is the Fermi energy, u is the energy density and P is the pressure.

Note that, even for $T = 0$, the pressure is positive. One finds $P \sim n^{5/3}$ for a non-relativistic degenerate gas and $P \sim n^{4/3}$ for a relativistic degenerate gas.

For a white dwarf in hydrostatic equilibrium the pressure is supplied by the electron degeneracy pressure, while the dominating part of the mass is given by nuclei of a specific type (*e.g.*, ^{12}C) which we can define by their mass and charge numbers (A, Z).[3] Therefore

[3] In general one can replace the ratio A/Z by μ_e in the subsequent equations.

Table 16.1

	NON-REL.	REL.
n	$g_{\rm s}\dfrac{p_{\rm F}^3}{6\pi^2\hbar^3}$	$g_{\rm s}\dfrac{p_{\rm F}^3}{6\pi^2\hbar^3}$
$\epsilon_{\rm F}$	$\dfrac{p_{\rm F}^2}{2m}=\dfrac{1}{2m}\left(\dfrac{6\pi^2\hbar^3 n}{g_{\rm s}}\right)^{2/3}$	$\tilde{c}p_{\rm F}=\tilde{c}\left(\dfrac{6\pi^2\hbar^3 n}{g_{\rm s}}\right)^{1/3}$
u	$\frac{3}{5}n\epsilon_{\rm F}$	$\frac{3}{4}n\epsilon_{\rm F}$
P	$\dfrac{2}{3}u=\dfrac{2}{5}\,\dfrac{1}{2m}\left(\dfrac{6\pi^2\hbar^3}{g_{\rm s}}\right)^{2/3}n^{5/3}$	$\dfrac{1}{3}u=\dfrac{\tilde{c}}{4}\left(\dfrac{6\pi^2\hbar^3}{g_{\rm s}}\right)^{1/3}n^{4/3}$

Properties of non-relativistic and strongly relativistic degenerate matter.

we find for a degenerate electron gas

$$m=m_{\rm e}=511\,{\rm keV}/\tilde{c}^2=9.11\times10^{-28}\,{\rm g}\,, \tag{16.4}$$

$$g_{\rm s}=2\,, \tag{16.5}$$

$$n=n_{\rm e}=n_{\rm p}=\frac{Z}{A}\frac{\rho}{m_H}\simeq\frac{Z}{A}6\times10^{27}\,{\rm cm}^{-3}\left(\frac{\rho}{10^4\,{\rm g\,cm}^{-3}}\right)\,, \tag{16.6}$$

$$\epsilon_{\rm F}=12\,{\rm keV}\left(\frac{\rho}{10^4\,{\rm g\,cm}^{-3}}\right)^{2/3}\left(\frac{Z}{A}\right)^{2/3}\quad(\text{for }\rho\ll2\times10^6\,{\rm g\,cm}^{-3})\,, \tag{16.7}$$

$$\epsilon_{\rm F}=516\,{\rm keV}\left(\frac{\rho}{10^6\,{\rm g\,cm}^{-3}}\right)^{1/3}\left(\frac{Z}{A}\right)^{1/3}\quad(\text{for }\rho\gg2\times10^6\,{\rm g\,cm}^{-3})\,. \tag{16.8}$$

In the expression for n we can use charge neutrality to replace $n_{\rm e}$ by $n_{\rm p}$ ($n_{\rm e}=n_{\rm p}$), where the proton number density $n_{\rm p}$ can be calculated from the mass density ρ of the white dwarf. The reason why there are two expressions for the Fermi energy is the fact that an electron gas becomes relativistic ($\epsilon_{\rm F}>m_{\rm e}\tilde{c}^2$) at $\rho\simeq2\times10^6\,{\rm g\,cm}^{-3}$. (In reality there is, of course, a smooth transition between the two equations of state.)

For a neutron star in equilibrium the pressure is supplied by degenerate neutrons which also contribute most of the mass. Therefore we have

$$m=m_{\rm n}=939.6\,{\rm MeV}/\tilde{c}^2=1.675\times10^{-24}\,, \tag{16.9}$$

$$g_{\rm s}=2\,, \tag{16.10}$$

$$n=n_{\rm n}=\frac{\rho}{m_{\rm n}}\simeq6\times10^{37}\,{\rm cm}^{-3}\left(\frac{\rho}{10^{14}\,{\rm g\,cm}^{-3}}\right)\,, \tag{16.11}$$

$$\epsilon_{\rm F}=30\,{\rm MeV}\left(\frac{\rho}{10^{14}\,{\rm g\,cm}^{-3}}\right)^{2/3}\quad(\text{for }\rho\ll6\times10^{15}\,{\rm g\,cm}^{-3})\,, \tag{16.12}$$

$$\epsilon_{\rm F}=239\,{\rm MeV}\left(\frac{\rho}{10^{14}\,{\rm g\,cm}^{-3}}\right)^{1/3}\quad(\text{for }\rho\gg6\times10^{15}\,{\rm g\,cm}^{-3})\,. \tag{16.13}$$

The central density of a neutron star does not exceed a few times $10^{15}\,{\rm g\,cm}^{-3}$ and we find therefore that the neutron gas is non-relativistic in most neutron stars. As a comparison, the density inside nuclei is about $3\times10^{14}\,{\rm g\,cm}^{-3}$.

Exercise 16.1:

Degeneracy is lifted if the temperature is too large, *i.e.*, if $k_{\rm B}T > \epsilon_{\rm F}$. At which temperatures does this happen in white dwarfs and neutron stars? Assume that $\rho = 10^4\,{\rm g\,cm^{-3}}$ and $10^7\,{\rm g\,cm^{-3}}$ are typical densities for white dwarfs in the non-relativistic and relativistic cases, and that $\rho = 10^{14}\,{\rm g\,cm^{-3}}$ is a typical density for a neutron star.

We now derive a mass-radius relation for white dwarfs and neutron stars. At first we consider the non-relativistic case, *i.e.*, neutron stars and white dwarfs with 'small' number densities. Thus, the pressure is given by $P \sim n_{\rm e}^{5/3}$ (white dwarf) and $P \sim n_{\rm n}^{5/3}$ (neutron star), and since $n_{\rm e} \sim \rho$ (or $n_{\rm n} \sim \rho$) the equation of state has a polytropic form, $P = K\rho^{\Gamma}$ with $\Gamma = 5/3$. For relativistic white dwarfs one finds $P \sim n_{\rm e}^{4/3} \sim \rho^{4/3}$, which again is a polytropic form, now with $\Gamma = 4/3$.

Exercise 16.2:

Using the expressions given in Table 16.1, determine the constant K in the polytrope equation for both white dwarfs and neutron stars. Note that the value of K depends only on natural constants and possibly on Z/A.

We can now apply equation (4.48) to arrive at the following expressions:

$$M = 0.70\left(\frac{10^4\,{\rm km}}{R}\right)^3\left(2\frac{Z}{A}\right)^5 M_\odot \quad \text{(white dwarf, } \Gamma = 5/3)\,, \tag{16.14}$$

$$M = \left(\frac{15.12\,{\rm km}}{R}\right)^3 M_\odot \quad \text{(neutron star, } \Gamma = 5/3)\,, \tag{16.15}$$

$$M = 1.457\left(2\frac{Z}{A}\right)^2 M_\odot = M_{\rm Ch}^{\rm (WD)} \quad \text{(white dwarf, } \Gamma = 4/3)\,, \tag{16.16}$$

$$M = 5.73 M_\odot = M_{\rm Ch}^{\rm (NS)} \quad \text{(neutron star, } \Gamma = 4/3)\,. \tag{16.17}$$

Note that $M \sim R^{-3}$ for non-relativistic systems, but M is independent of R for ultra-relativistic systems. In the last case, is the mass also referred to as the *Chandrasekhar mass* in honour of the Indian astrophysicist who derived this result in 1931 (see Chandrasekhar 1931). Chandrasekhar showed that this is the *maximal* mass which is possible for a white dwarf (naturally neutron stars have been first discussed after Chadwick discovered the neutron in 1932 (Chadwick 1932). For his discovery, Chandrasekhar has been awarded the Nobel Prize in Physics in 1983(!) (Chadwick won his Nobel Prize in 1935.)

We also note that the Chandrasekhar mass is nearly the same for white dwarfs and neutron stars. The reason for this is that the pressure for *relativistic* particles is independent of the particle mass (see Table 16.1), while the density for both white dwarfs and neutron stars are given by the nucleonic contributions. Equation (16.17) follows from equation (16.16) if we replace Z/A by N/A and adopt $N/A = 1$. (There is also a small correction

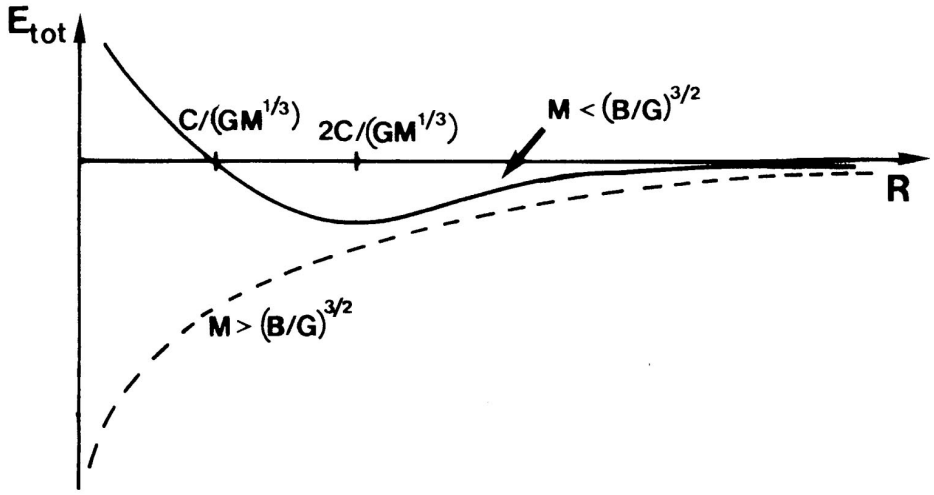

Figure 16.1: The behaviour of the total mass $E_{\rm tot}$ for masses above and below the Chandrasekhar mass. For fixed $M < M_{\rm Ch}$ the energy has a minimum as a function of R, corresponding to a stable equilibrium of the star.

arising from the fact that we have used $m_{\rm n}$ and $m_{\rm u}$, respectively, in the derivation of the two equations.)

We now give a physical argument for the mass-radius relation derived above and for the existence of a mass limit, the Chandrasekhar mass.

The total energy of a compact star can be written in terms of two contributions, $E_{\rm tot} = E_{\rm kin} + E_{\rm pot}$, where $E_{\rm pot} = -M^2G/R$ is the potential energy and $E_{\rm kin} \simeq uR^3$ is the internal (kinetic) energy (we neglect here factors like 2 and π). For a relativistic degenerate gas we have $u = 3n\epsilon_{\rm F}/4 \sim n^{4/3}$ and $n \sim \rho \sim M/R^3$ for the particle number density. Therefore one finds

$$E_{\rm tot,rel} = B\left(\frac{M}{R^3}\right)^{4/3} R^3 - \frac{M^2G}{R} = B\frac{M^{4/3}}{R} - G\frac{M^2}{R}\ , \tag{16.18}$$

where B is a constant.

The total energy is positive if $M < (B/G)^{3/2}$. In this case $E_{\rm tot,rel}$ decreases by increasing the radius, with the consequence that the density and the Fermi energy are reduced and the degenerate gas becomes non-relativistic. When this happens, we have to replace $u \sim n^{4/3}$ by $u \sim n^{5/3}$ in our expression for the kinetic energy and the expression for total energy then reads

$$E_{\rm tot,nonrel} = C\left(\frac{M}{R^3}\right)^{5/3} R^3 - G\frac{M^2}{R} = C\frac{M^{5/3}}{R^2} - G\frac{M^2}{R}\ , \tag{16.19}$$

where C is a constant.

$E_{\rm tot,nonrel}$ becomes negative if $R > C/(GM^{1/3})$, has a minimum at $R = 2C/(GM^{1/3})$ (corresponding to $\mathrm{d}E_{\rm tot,nonrel}/\mathrm{d}R = 0$) and tends to zero for $R \to \infty$ (see Fig. 16.1). The minimum corresponds to a stable equilibrium in the nonrelativistic case and hence to a possible state of the star, with the finite radius $R = (2C/G)M^{-1/3}$. In other words, $M \sim R^{-3}$ as was also found from the polytropic models.

If M is large ($M > (B/G)^{3/2}$) one has $E_{\rm tot,rel} < 0$ and the energy can be decreased without bound by decreasing R. There exists no equilibrium in such a situation.

The Chandrasekhar mass defined the boundary between these two situations. The Chandrasekhar mass corresponds to an unstable equilibrium, defined by $E_{\rm tot,rel} = 0$, as we already know from the virial theorem (section 4.4.3).

The polytropic equations of state which were used in the discussion above are only an approximation. Realistic calculations are more complicated, in particular for neutron stars, for which the equation of state is only insufficiently known, particularly at the high densities in the star's centre. Additional effects arising from general relativity have to be considered in the stability discussion for neutron stars. If these are all taken into account the maximum mass for neutron stars lies between 1.4 and 2.5 $M_\odot$, *i.e.*, it is significantly smaller than the mass limit of 5.73 $M_\odot$ which follows from the simplified discussion given above.

In many white dwarfs the electron gas is relativistic in the central part of the star, but it is non-relativistic further out. This changes the mass-radius relation; but the results derived above give the main features.

With increasing density there can be changes in the relevant physics for white dwarfs which may possibly prevent a collapse. Computer simulations have shown that a white dwarf, which accretes mass from its partner in a binary system and eventually exceeds the Chandrasekhar mass, does not collapse, but explodes in what is called a Type Ia supernova (*e.g.* Kahabka, van den Heuvel & Rappaport 1999). The increased density (and temperature) leads to fast nuclear reactions which change the matter in the central part of the star into ^{56}Ni. The energy production grows explosively: in a degenerate environment the energy set free in nuclear reactions is not used for expansion, but rather for heating which again makes the nuclear reactions proceed even faster; such a process is called a thermonuclear runaway (see also the discussion of the helium flash in section 12.3). Thus the star becomes unstable and finally explodes completely. The subsequent radioactive decay of ^{56}Ni and its daughter ^{56}Co heats the expanding remains of the star and results in nearly identical lightcurves for all Type Ia supernovae. This fact has very important applications in cosmology: it allows Type Ia supernovae to be used as 'standard candles' to probe the geometry of the Universe (*e.g.* Hogan, Kirshner & Suntzeff 1999).

A neutron star which increases its mass by mass accretion from its surroundings finally collapses to a black hole if its mass exceeds the Chandrasekhar mass limit. The same is true if the mass of the collapsing stellar core exceeds the Chandrasekhar mass. The model calculations indicate that this is the case if the mass of original star exceeds about $20\,{\rm M}_\odot$.

A complete description of black holes requires general relativity, and is beyond the scope of these notes. Briefly, the gravitational field in the collapse is so strong that no other physical forces can resist it. As a result, matter is virtually crushed "out of existence": the collapse continues until, at least within the framework of classical physics, a singularity is formed. To make a proper description of this process, quantum-mechanical effects of gravity must be taken into account, and these are currently completely uncertain. These events cannot be observed, however. The gravitational field is so strong that no signal, including light, can escape from the vicinity of the collapsing star. Hence the black hole can only be detected through the effects of the gravitational field surrounding it.[4]

[4] An exception to this statement is the fact that emission of elementary particles may occur near the "surface" of a black hole, through quantum-mechanical fluctuations. For a simple description of this process, see Hawking (1988).

Exercise 16.3:

Consider emission of a photon from the surface of a star of mass M and R. Assume, incorrectly, that the effect of gravity on the photon can be described by assigning a "mass" $h\nu/\tilde{c}^2$ to the photon, where $h\nu$ is the energy of the photon, ν being its frequency, and $\tilde{c}$ is the speed of light. Show that the photon can only escape from the star if the radius is greater than $GM/\tilde{c}^2$. What is the value of this radius for $1\,\mathrm{M}_\odot$? A correct relativistic description shows that the critical radius, the *Schwarzschild radius* R_g, is in fact a factor two larger, *i.e.*,

$$R_g = \frac{2GM}{\tilde{c}^2} \,. \tag{16.20}$$

The sphere with radius R_g around the black hole defines its *event horizon*, from inside which no signal can escape.

16.3 Observations of compact objects

When they are formed white dwarfs and neutron stars are both quite hot (10^7 K and 10^{10} K, respectively, at the centre and somewhat cooler at the surface). Although they do not undergo nuclear reactions, their thermal energy reservoir (in terms of the motion of particles, *i.e.*, nucleons) is large enough to maintain high temperatures for an extended period. This thermal radiation has been studied for a large number of white dwarfs, but it has not been definitely confirmed for neutron stars as here the luminosity is too small.

Exercise 16.4:

Estimate the luminosity of a typical white dwarf with surface temperature 10^5 K (shortly after its formation) and 10^4 K (after cooling over some 100 million years). Give a similar estimate for a neutron star with surface temperature 5×10^6 K (after cooling for a few years). In which part of the spectrum must one look for such objects? Can one perform the searches from the surface of the Earth?

By now white dwarfs, and particularly their thermal radiation, have been extensively studied, and their mass-radius relation has been confirmed. An important technique for investigating the structure of white dwarfs is to analyse the frequencies of their pulsations.

To study neutron stars one has to adopt indirect methods. Fortunately neutron stars can be identified in two ways: as pulsars and as X-ray sources.

The first pulsar was discovered in 1967[5] (Hewish *et al.* 1968). By now more than 1200 pulsars are known. It is characteristic for these objects that they emit periodic signals, *pulses*; they were initially, and are still predominantly, detected in the radiowave frequency range, but later also in the optical, UV and X-ray frequency bands. These pulses

[5]The supervisor of the PhD student who discovered the pulsars won the Nobel Prize for the discovery in 1974.

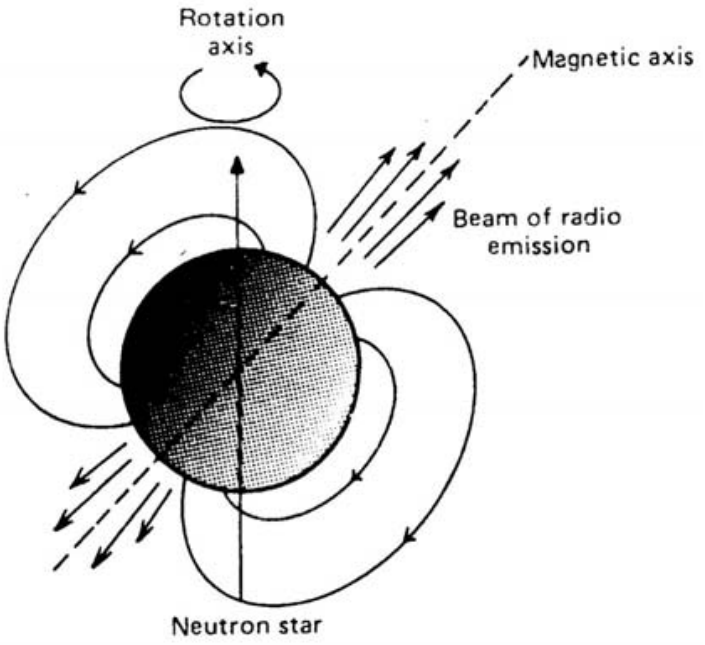

Figure 16.2: Schematic model of a pulsar. From Longair (1981).

are extraordinarily precise, with periods between 1.55 ms and a few seconds. For some pulsars the period has been determined with an accuracy of up to 13 digits; therefore pulsars are amongst the most precise clocks known.[6] Before the grandfather clock is replaced by a radio telescope, however, it should be kept in mind that the period of most pulsars slowly increases (this can be modelled) and that some pulsars show so-called glitches, in which their period suddenly decreases by a few parts in 10 000.

These changes in the period are connected with the physical mechanism behind pulsars (see also Fig. 16.2): a rotating neutron star with a strong magnetic field ($10^8 - 10^{13}$ Gauss; the strongest magnetic fields in the laboratory are of order $10^5 - 10^6$ Gauss; the Earth's magnetic field is about 0.5 Gauss). The dipole axis of the magnetic field forms a constant angle with the star's rotational axis. The strong magnetic field induces electric fields which pull charged particles (in particular positrons) from the star's surface. The particles spiral out along the magnetic fieldlines with velocities close to the speed of light and emit well-collimated and forward-directed synchroton radiation which, as in a lighthouse beam, sweeps around due to the star's rotation. If we happen to look inside this beam we see the pulsar blinking once per rotation.

The strong magnetic fields can be explained by the freeze-in of the magnetic flux, *i.e.*, by the conservation of the magnetic fieldlines during the collapse of the parent star on its way to become a neutron star. As a result, the field strength varies as $B \sim R^{-2}$, strongly

[6] In the binary system PSR $1913+16$ one such perfect clock orbits another neutron star in a very tight orbit (Hulse & Taylor 1975). In this case one can determine the orbital motion extremely precisely and in this way obtain the masses of the stars as $(1.4411 \pm 0.0007) M_\odot$ and $(1.3873 \pm 0.0007) M_\odot$. Furthermore, the observed orbit only fits the model if the emission of gravitational waves is taken into account. This was the first detection of this phenomenon, predicted by Einstein's general theory of relativity. Hulse and Taylor deservedly got the Nobel price in physics in 1993 for their discovery of this interesting system (Hulse 1994; Taylor 1994).

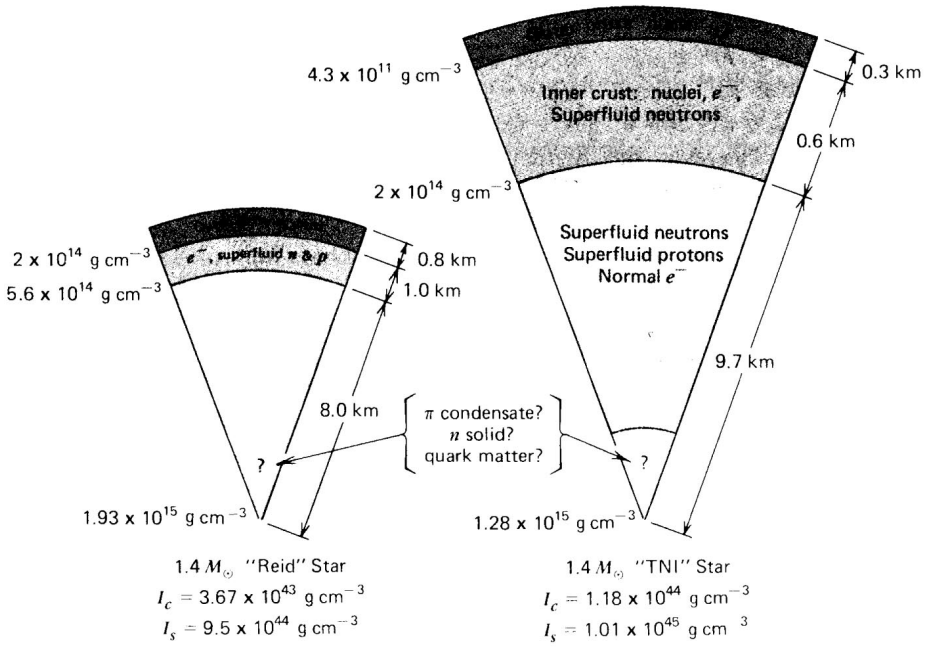

Figure 16.3: Cross sections of two $1.4M_\odot$ neutron stars with different equations of states, and hence different internal structure. In the outermost part (the "outer crust") the atomic nuclei are in an ordered crystal structure. The composition of the central parts is unknown. From Shapiro & Teukolsky (1983).

increasing the field of the original star. The very rapid rotation (for milli-second pulsars the rotational velocity corresponds to a large fraction of the speed of light and approaches the limit at which the star is ripped apart) is explained by the conservation of angular momentum during the collapse ($V_{\rm rot} \sim R^{-1}$). For the fastest pulsars gas accretion from a partner star in a binary system is also important to explain the angular momentum.

The pulsar periods increase slowly as the available rotational energy decreases (in the first year perhaps by gravitational wave radiation, later by magnetic dipole radiation). The star then adopts a more spherical and less oblate shape. As the outer layers consist of a solid shell (crust) – an ionic crystal structure as sketched in Fig. 16.3 – these changes in shape occur in sudden cracks induced by the stress in the outer crust, as in a neutron-star quake. The related changes in the moment of inertia results in small, sudden changes in the period which, for example, have been observed for several years in the pulsar in the Crab Nebula (the pulsar and the nebula were created by a supernova explosion observed by Chinese astronomers in 1054.)

Although pulsars can be explained as rotating neutron stars, and confirm therefore the existence of neutron stars, we emphasize that many details are not yet well understood, since neutron stars involve matter densities and magnetic fields with values which are much larger than can be produced in laboratories. However, this also implies that the study of neutron stars allows us to learn more about the properties of nuclear matter at

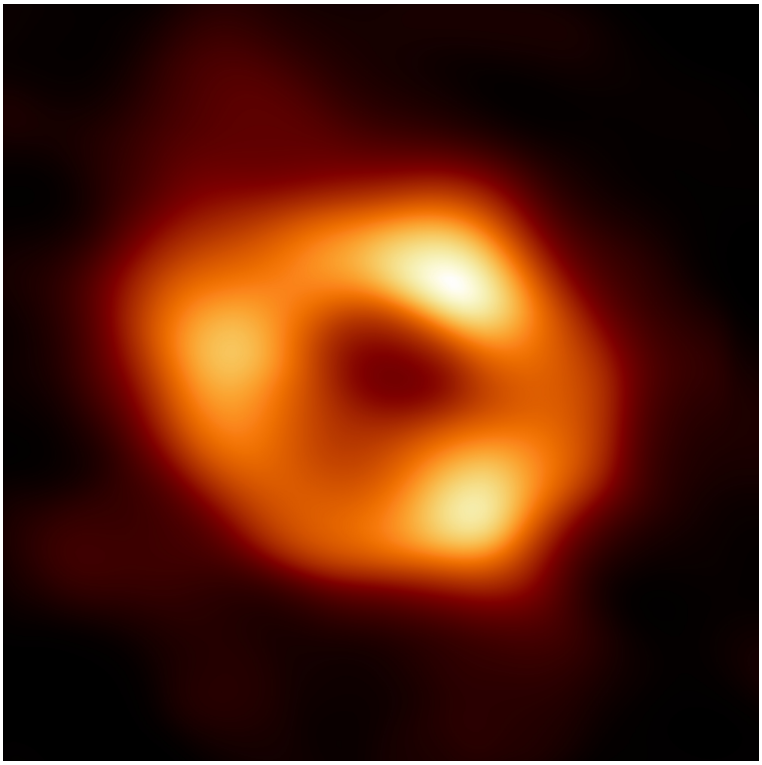

Figure 16.4: Image of the black hole at the centre of the Galaxy, obtained from a global network, the so-called Event Horizon Telescope (EHT), of mm-wavelength radio telescopes. Data released in May 2022. (Credit: EHT Collaboration.)

high densities and thus about the strong interaction.

Neutron stars have also been identified as X-ray sources in binaries. These are systems in which the neutron star is so close to its partner star that it pulls matter gravitationally from the partner. This matter is accreted (including its angular momentum) in a disc around the neutron star, is heated and slowly falls onto the star, accompanied by the emission of X-rays. It is thought that some of the fastest-spinning pulsars have obtained their angular momentum in this way.

Such binary X-ray sources are also the main candidates for black-hole searches. As the name indicates, black holes do not emit light themselves. However, if matter falls towards a black hole from a neighbouring star intense X-ray radiation may result; the infalling matter typically forms an accretion disk around the black hole and is heated to very high temperatures by the release of gravitational energy, resulting in the emission of X rays.

Here is a method to detect black holes: Find a binary X-ray source. Convince yourself that the energy emission indicates a strong gravitational field and that the time variation of the signal is so short that the source has to be of very small dimensions. This can then only be a neutron star or a black hole. Determine the mass of the compact object by applying Kepler's law for its orbital motion. If the mass is larger than the maximum mass for a neutron star, the object has to be a black hole. A discussion of such observations was provided recently by Lasota (1999). In reality, this is not quite as simple as one has to know precisely the maximum mass for neutron stars. But one has by now identified a dozen candidates (including Cygnus X-1, A0620-00, LMC X-3) whose masses are so large

that they are very probably black holes (the mass of Cygnus X-1 is definitely larger than $3.3\,M_\odot$, very likely even in the range $9 - 15\,M_\odot$).

Compelling evidence for very massive black holes has been found from observations of the motion of stars near the centres of galaxies, including our own (*e.g.* Eckart & Genzel 1999; for an overview, discussing also activity in galactic nuclei associated with black holes, see Blandford & Gehrels 1999). In particular, Schödel *et al.* (2002) observed a star in a highly eccentric orbit around the centre of the Milkey Way Galaxy, with a period of 15.2 years; from this they estimated the mass of the central object of the Galaxy to be $2.6 \times 10^6\,\mathrm{M}_\odot$, within a such a small region that the only realistic possibility is a black hole. These observations have subsequently been refined through observations of stars passing very close to the central compact object, where effects of general relativity have become apparent, removing any doubt about the nature of the central object as a black hole. A further remarkable confirmation came from radio observations that directly showed the emission from the disk around the black hole being shadowed by the event horizon (see Fig. 16.4.

References

Abdurashitov, J. N., Bowles, T. J., Cherry, M. L., *et al.*, 1999. [Measurement of the solar neutrino capture rate by Sage and implications for neutrino oscillations in vacuum]. *Phys. Rev. Lett.*, **83**, 4686 – 4689.

Abell, G., 1964. *Exploring the Universe*, Holt, Rinehart and Winston, Inc., New York.

Adelberger, E. G., Austin, S. M., Bahcall, J. N., *et al.*, 1998. [Solar fusion cross sections]. *Rev. Mod. Phys.*, **70**, 1265 – 1291.

Aerts, C., Christensen-Dalsgaard, J. & Kurtz, D. W., 2010. *Asteroseismology*, Springer, Heidelberg.

Agostini, M., *et al.*, The Borexino Collaboration, 2020. [Experimental evidence of neutrinos produced in the CNO fusion cycle in the Sun]. *Nature*, **587**, 577 – 582.

Ahmad, Q. R., Allen, R. C., Andersen, T. C., *et al.*, 2001. [Measurement of the rate of $\nu_e + d \rightarrow p + p + e^-$ interactions produced by ^{8}B solar neutrinos at the Sudbury Neutrino Observatory]. *Phys. Rev. Lett.*, **87**, 071301(1-6).

Ahmad, Q. R., Allen, R. C., Andersen, T. C., *et al.*, 2002. [Direct evidence for neutrino flavor transformation from neutral-current interactions in the Sudbury Neutrino Observatory]. *Phys. Rev. Lett.*, **89**, 011301-(1 – 6).

ALMA Partnership, Brogan, C. L., *et al.*, 2015. [The 2014 ALMA Long Baseline Campaign: First results from high angular resolution observations toward the HL Tau Region]. *Astrophys. J.*, **808**, L3-(1–10).

Anders, E. & Grevesse, N., 1989. [Abundances of the elements: meteoritic and solar]. *Geochim. Cosmochim. Acta*, **53**, 197 – 214.

Andersen, A. C., Jørgensen, U. G., Nicolaisen, F. M., Sørensen, P. G. & Glejbøl, K., 1998. [Spectral features of presolar diamonds in the laboratory and in carbon star atmospheres]. *Astron. Astrophys.*, **330**, 1080 – 1090.

Angulo, C., Arnould, M., Rayet, M., *et al.*, 1999. [A compilation of charged-particle induced thermonuclear reaction rates]. *Nucl. Phys. A*, **656**, 3 – 183.

Anselmann, P., Hampel, W., Heusser, G., *et al.*, 1995. [GALLEX solar neutrino observations: complete results for GALLEX II]. *Phys. Lett. B*, **357**, 237 – 247.

Appel, S., Bagdasarian, Z., Basiloco, D., *et al.*, The Borexino Collaboration, 2022. [Improved measurement of solar neutrinos from Carbon-Nitrogen-Oxygen cycle by Borexino and its implications for the standard solar model]. *Phys. Rev. Lett.*, **129**, 252701-(1 – 10).

Arnett, D., 1996. *Supernovae and nucleosynthesis. An investigation of the history of matter, from the Big Bang to the present*, Princeton University Press, Princeton, N.J.

Asplund, M., Grevesse, N., Sauval, A. J. & Scott, P., 2009. [The chemical composition of the Sun]. *Annu. Rev. Astron. Astrophys.*, **47**, 481–522.

Bahash, L., 1989. [The Age-of-the-Earth Debate]. *Scientific American*, **261** (August) p. 78 – 83 (US p. 90 – 96)[7].

Bahcall, J. N., 1989. *Neutrino astrophysics*, Cambridge University Press, Cambridge.

Bahcall, J. N., 1990. [The solar-neutrino problem]. *Scientific American*, **262** (May), p. 26 – 33.

Bahcall, J. N., 1996. [Solar neutrinos: Where we are, where we are going]. *Astrophys. J.*, **467**, 475 – 484.

Bahcall, J. N. & Pinsonneault, M. H., 1995. (With an appendix by G. J. Wasserburg). [Solar models with helium and heavy-element diffusion]. *Rev. Mod. Phys.*, **67**, 781 – 808.

Bahcall, J. N., Krastev, P. I. & Smirnov, A. Yu., 1998. [Where do we stand with neutrino oscillations?]. *Phys. Rev. D*, **59**, 096016-(1-22).

Bahcall, J. N., Lande, K., Lanou Jr, R. E., Learned, J. G., Hamish Robertson, R. G. & Wolfenstein, L., 1995. [Progress and prospects in neutrino astrophysics]. *Nature*, **375**, 29 – 34.

Bahcall, J. N., Pinsonneault, M. H., Basu, S. & Christensen-Dalsgaard, J., 1997. [Are standard solar models reliable?]. *Phys. Rev. Lett.*, **78**, 171 – 174.

Baraffe, I., Chabrier, G. & Gallardo, J., 2009. [Episodic accretion at early stages of evolution of low-mass stars and brown dwarfs: a solution for the observed luminosity spread in H-R diagrams?]. *Astrophys. J.*, **702**, L27–L31.

Basri, G., 2000a. [The discovery of brown dwarfs]. *Scientific American*, **282** (April), 56 – 63.

Basri, G., 2000b. [Observations of brown dwarfs]. *Annu. Rev. Astron. Astrophys.*, **38**, 485 – 519.

Basu, S. & Antia, H. M., 2008. [Helioseismology and solar abundances]. *Phys. Rep.*, **457**, 217–283.

Bethe, H. A., 1990a. [Supernovae]. *Phys. Today*, **43** (September), p. 24 – 27.

Bethe, H. A., 1990b. [Supernova mechanisms]. *Rev. Mod. Phys.*, **62**, 801 – 866.

Bethe, H. A. & Brown, G., 1985. [How a supernova explodes]. *Scientific American*, **252** (May), p. 40 – 48 (US p. 60 – 68).

Blandford, R. & Gehrels, N., 1999. [Revisiting the black hole]. *Physics Today*, **52**, No. 6 (June), 40 – 46.

Boger, J., Hahn, R. L., Rowley, J. K., *et al.* (the SNO collaboration), 2000. [The Sudbury Neutrino Observatory]. *Nucl. Inst. Meth.*, **A449**, 172 – 207.

Boss, A. P., 1985. [Collapse and formation of stars]. *Scientific American*, **252** (January), p. 28 – 33 (US p. 40 – 45).

Bradbury, R., 1953. [The Golden Apples of the Sun]. In *The Golden Apples of the Sun*, Rupert Hart-Davis, London.

Brown, A. G. A., 2021. [Microarcsecond astrometry: Science highlights from *Gaia*]. *Annu. Rev. Astron. Astrophys.*, **59**, 59 – 115.

Burki, G., Cramer, N., Burnet, M., Rufener, F., Pernier, B. & Richard, C., 1989. [The Geneva photometric monitoring of SN 1987A]. *ESO Messenger*, No. 55, 51.

Burrows, A., 1990. [Neutrinos from supernova explosions]. *Ann. Rev. Nucl. Part. Sci.*, **40**, 181 – 212.

[7]Unfortunately, in *Scientific American* the page numbers do not agree between the American and the European editions. Here page numbers in the European edition are given by default, in most cases in addition with the US page numbers in brackets.

Burrows, A., Hubbard, W. B., Lunine, J. I. & Liebert, J., 2001. [The theory of brown dwarfs and extrasolar giant planets]. *Rev. Mod. Phys.*, **73**, 719 – 765.

Burrows, A., Livne, E., Dessart, L., Ott, C. D. & Murphy, J., 2006. [A new mechanism for core-collapse supernova explosions]. *Astrophys. J.*, **640**, 878 – 890.

Busso, M., Gallino, R. & Wasserburg, G. J., 1999. [Nucleosynthesis in Asymptotic Giant Branch stars: Relevance for Galactic enrichment and Solar System formation]. *Ann. Rev. Astron. Astrophys.*, **37**, 239 – 309.

Calder, N., 1997. *The manic Sun*, Pilkington Press.

Carrasco, J. M., Weiler, M., Jordi, C., Fabricius, C., De Angeli, F., Ewans, D. W., van Leeuwen, F., Riello, M. & Montegriffo, P., 2021. [Internal calibration of *Gaia* BP/RP low-resolution spectra]. *Astron. Astrophys.*, **652**, A86-(1–20).

Castellani, V., Degl'Innocenti, S., Fiorentini, G., Lissia, M. & Ricci, B., 1997. [Solar neutrinos: Beyond standard solar models]. *Phys. Rep.*, **281**, 309 – 398.

Caughlan, G. R. & Fowler, W. A., 1988. [Thermonuclear reaction rates V]. *Atomic data and nuclear data tables*, **40**, 283 - 334.

Chadwick, J., 1932. [Possible existence of a neutron]. *Nature*, **129**, 312.

Chandrasekhar, S., 1931. [The maximum mass of ideal white dwarfs]. *Astrophys. J.*, **74**, 81 – 82.

Chandrasekhar, S., 1939. *An introduction to the study of stellar structure*, University of Chicago Press, Chicago (reissued 1957, by Dover Publ.)

Chaplin, W. J. & Miglio, A., 2013. [Asteroseismology of solar-type and red-giant stars]. *Annu. Rev. Astron. Astrophys.*, **51**, 353 – 392.

Chatterjee, S., Vlemmings, W. H. T., Brisken, W. F., Lazio, T. J. W., Cordes, J. M., Goss, W. M., Thorsett, S. E., Fomalont, E. B., Lyne, A. G. & Kramer, M., 2005. [Getting its kicks: a VLBA parallax for the hyperfast pulsar B1508+55]. *Astrophys. J.*, **630**, L61 – L64.

Christensen-Dalsgaard, J., 1995. [Effects of opacity on stellar oscillations]. In *Frontiers of Astrophysics, Proceedings of the Rosseland Centenary Symposium*, eds Lilje, P. B. & Maltby, P., 161 – 180 (Institute of Theoretical Astrophysics, Oslo).

Christensen-Dalsgaard, J., 2002. [Helioseismology]. *Rev. Mod. Phys.*, **74**, 1073 – 1129.

Christensen-Dalsgaard, 2021. [Solar structure and evolution]. *Living Rev. Solar Phys.*, **18**, 2-(1–189).

Christensen-Dalsgaard, J., Däppen, W., Ajukov, S. V., Anderson, E. R., Antia, H. M., Basu, S., Baturin, V. A., Berthomieu, G., Chaboyer, B., Chitre, S. M., Cox, A. N., Demarque, P., Donatowicz, J., Dziembowski, W. A., Gabriel, M., Gough, D. O., Guenther, D. B., Guzik, J. A., Harvey, J. W., Hill, F., Houdek, G., Iglesias, C. A., Kosovichev, A. G., Leibacher, J. W., Morel, P., Proffitt, C. R., Provost, J., Reiter, J., Rhodes Jr., E. J., Rogers, F. J., Roxburgh, I. W., Thompson, M. J., Ulrich, R. K., 1996. [The current state of solar modeling]. *Science*, **272**, 1286 – 1292.

Christensen-Dalsgaard, J., Däppen, W., Dziembowski, W. A. & Guzik, J. A., 2000. [An introduction to helioseismology]. In *Variable Stars as Essential Astrophysical Tools*, ed. C. İbanoğlu, Kluwer Academic Publishers, p. 59 – 167.

Clayton, D. D., 1968. *Principles of Stellar Evolution and Nucleosynthesis*, McGraw-Hill, New York.

Cleveland, B. T., Daily, T., Davis Jr, R., Distel, J. R., Lande, K., Lee, C. K., Wildenhain, P. S. & Ullman, J., 1998. [Measurement of the solar electron neutrino flux with the Homestake chlorine detector]. *Astrophys. J.*, **496**, 505 – 526.

Cohen, E. R. & Taylor, B. N., 1987. [The 1986 adjustment of the fundamental physical constants]. *Rev. Mod. Phys.*, **59**, 1121 – 1148.

Colgate, S. A., 1989. [Hot bubbles drive explosions]. *Nature*, **341**, 489 – 490.

Cowan, J. J., Pfeiffer, B., Kratz, K.-L., Thielemann, F.-K., Sneden, C., Burles, S., Tytler, D. & Beers, T. C., 1999. [r-process abundances and chronometers in metal-poor stars]. *Astrophys. J.*, **521**, 194 – 205.

Cox, J. P. & Giuli, R. T., 1968. *Principles of Stellar Structure*, Gordon and Breach, New York.

D'Antona, F. & Mazzitelli, I., 1985. [Evolution of very low mass stars and brown dwarfs. I. The minimum main-sequence mass and luminosity]. *Astrophys. J.*, **296**, 502 – 513.

Däppen, W. & Guzik, J. A., 2000. [Astrophysical equation of state and opacity]. In *Variable Stars as Essential Astrophysical Tools*, ed. C. İbanoğlu, Kluwer Academic Publishers, p. 177 – 212.

Davis, R., 2003. [Nobel lecture: A half-century with solar neutrinos]. *Rev. Mod. Phys.*, **75**, 985–994.

Decin, L., 2021. [Evolution and mass loss of cool aging stars: a Daedalean story]. *Annu. Rev. Astron. Astrophys.*, **59**, 337 – 389.

Diehl, R., Halloin, H., Kretschmer, K., Lichti, G. G., Schönfelder, V., Strong, A. W., von Kienlin, A., Wang, W., Jean, P., Knödlseder, J., Roques, J.-P., Weidenspointner, G., Schanne, S., Hartmann, D. H., Winkler, C. & Wunderer, C., 2006. [Radioactive ^{26}Al from massive stars in the Galaxy]. *Nature*, **439**, 45 – 47.

Eckart, A. & Genzel, R., 1999. [The massive black hole at the Galactic Center]. *J. Astrophys. Astron.*, **20**, 187 – 196.

Eddington, A. S., 1930. *The internal constitution of the stars*, Cambridge University Press, Cambridge.

Eggleton, P. E. & Faulkner, J., 1981. [Why do stars become red giants?] In *Physical Processes in Red Giants*, p. 179 – 182, eds Iben, I. & Renzini, A., Reidel, Dordrecht.

Eguchi, K., Enomoto, S., Furuno, K., *et al.*, 2002. [First results from KamLAND: Evidence for reactor antineutrino disappearance]. *Phys. Rev. Lett.*, **90**, 021802-(1–6).

Elsworth, Y., Howe, R., Isaak, G. R., McLeod, C. P. & New, R., 1990. [Evidence from solar seismology against non-standard solar-core models]. *Nature*, **347**, 536 – 539.

Elsworth, Y., Howe, R., Isaak, G. R., McLeod, C. P., Miller, B. A., Wheeler, S. J. & New, R., 1995. [Fine spacing of the $l = 0$, $l = 2$ acoustic eigenmodes and the solar neutrino problem: particle physics and cosmological implications]. In *Proc. GONG'94: Helio- and Astero-seismology from Earth and Space*, eds Ulrich, R. K., Rhodes Jr, E. J. & Däppen, W., Astronomical Society of the Pacific Conference Series, vol. 76, San Francisco, **76**, 51 – 54.

Emden, R., 1907. *Gaskugeln*, B. G. Teubner, Leibzig.

Filippenko, A. V., 1997. [Optical spectra of supernovae]. *Annu. Rev. Astron. Astrophys.*, **35**, 309 – 355.

Friis-Christensen, E. & Lassen, K., 1991. [Length of the solar cycle: an indicator of solar activity closely associated with climate]. *Science*, **254**, 698 – 700.

Fukuda, S., Fukuda, Y., Ishitsuka, M., *et al.*, 2001. [Solar ^{8}B and hep neutrino measurements from 1258 days of Super-Kamiokande data]. *Phys. Rev. Lett.*, **86**, 5651 – 5655.

Fukuda, Y., Hayakawa, T., Ichihara, E., *et al.*, 1998a. [Measurements of the solar neutrino flux from Super-Kamiokande's first 300 days]. *Phys. Rev. Lett.*, **81**, 1158 – 1162.

Fukuda, Y., Hayakawa, T., Ichihara, E., *et al.*, 1998b. [Measurement of a small atmospheric ν_μ/ν_e ratio]. *Phys. Lett. B*, **433**, 9 – 18.

Geiss, J., Eberhardt, P., Büchler, F, Meister, J. & Signer, P., 1970. [Apollo 11 and 12 solar wind composition experiments: Fluxes of He and He isotopes]. *J. Geophys. Res.*, **75**, 5972 - 5979.

Gough, D. O. & Toomre, J., 1991. [Seismic observations of the solar interior]. *Ann. Rev. Astron. Astrophys.*, **29**, 627 – 685.

Gough, D. O. & Weiss, N. O., 1976. [The calibration of stellar convection theories]. *Mon. Not. R. astr. Soc.*, **176**, 589 - 607.

Gribov, V. & Pontecorvo, B., 1969. [Neutrino astronomy and lepton charge]. *Phys. Lett. B*, **28**, 493–496.

Grundahl, F., 1999. [Globular cluster ages and Strömgren CCD photometry]. In *Spectrophotometric Dating of Stars and Galaxies*, eds I. Hubeny, S. Heap & R. Cornett, ASP Conf. Ser. Vol. **192**, p. 223 – 230.

Höppner, W. & Weigert, A., 1973. [Central gravitational field of stars and evolution to red giants]. *Astron. Astrophys.*, **25**, 99 – 103.

Harrington, R. S., Dahn, C. C., Kallarakal, V. V., Guetter, H. H., Riepe, B. Y., Walker, R. L., Pier, J. R., Vrba, F. J., Luginbuhl, C. B., Harris, H. C. & Ables, H. D., 1993. [U. S. Naval Observatory photographic parallaxes. List IX]. *Astron. J.*, **105**, 1571 – 1580.

Harvey, J., 1995. [Helioseismology]. *Physics Today*, **48**, No. 10 (Oct.), 32 – 38.

Hawking, S. W., 1988. *A brief history of time*, Bantam Books, New York.

Haxton, W. C., Hamish-Robertson, R. G. & Serenelli, A. M., 2013. [Solar neutrinos: status and prospects]. *Annu. Rev. Astron. Astrophys.*, **51**, 21 – 61.

Hayashi, C., Hoshi, R. & Sugimoto, D., 1962. [Evolution of the stars]. *Progr. Theor. Phys.*, Suppl. No. 22, pp. 1 – 183.

Hayes, J. C. & Burrows, A., 1995. [A new dimension to supernovae]. *Sky and Telescope*, **90**, 30 – 33 (July).

Hearnshaw, J. B., 1992. [Origins of the stellar magnitude scale]. *Sky and Telescope*, **84**, 494 – 499 (November).

Heber, V. S., McKeegan, K. D., Steele, R. C. J., Jurewicz. A. J. G., Rieck, K. D., Guan, Y., Wieler, R., & Burnett, D. S., 2021. [Elemental abundances of major elements in the solar wind as measured in genesis targets and implications on solar wind fractionation]. *Astrophys. J.*, **907**, 15-(1 – 16).

Heger, A., Fryer, C. L., Woosley, S. E., Langer, N. & Hartmann, D. H., 2003. [How massive single stars end their life]. *Astrophys. J.*, **591**, 288 – 300.

Hejlesen, P. M., 1980. [Studies in stellar evolution II: Age and mass calibrations for hydrogen burning evolutionary stages]. *Astron. Astrophys. Suppl.*, **39**, 347 - 377.

Henyey, L. G., LeLevier, R. & Lev'ee, R. D., 1955. [The early phases of stellar evolution]. *Publ. Astron. Soc. Pacific*, **67**, 154–160.

Hewish, A., Bell, S. J., Pilkington, J. D. H., Scott, P. F. & Collins, R. A., 1968. [Observation of a rapidly pulsating radio source]. *Nature*, **217**, 709 – 713.

Hjorth, J., Sollerman, J., Møller, P., Fynbo, J. P. U., Woosley, S. E., Kouveliotou, C., Tanvir, N. R., Greiner, J., Andersen, M. I., Castro-Tirado, A. J., Castro Cerón, J. M., Fruchter, A. S., Gorosabel, J., Jakobsson, P., Kaper, L., Klose, S., Masetti, N., Pedersen, H., Pedersen, K., Pian, E., Palazzi, E., Rhoads, J. E., Rol, E., van den Heuvel, E. P. J., Vreeswijk, P. M., Watson, D. & Wijers, R. A. M. J., 2003. [A very

energetic supernova associated with the γ-ray burst of 29 March 2003]. *Nature*, **423**, 847 – 850.

Hoffman, P. F. & Schrag, D. P., 2000. [Snowball Earth]. *Scientific American*, **282** (January), 50 – 57.

Hogan, C. J., Kirshner, R. P. & Suntzeff, N. B., 1999. [Surveying space-time with supernovae]. *Scientific American*, **280** (January), 28 – 33.

Hotta, H., Kusano, K. & Shimada, R., 2022. [Generation of solar-like differential rotation]. *Astrophys. J.*, **933**, 1999-(1 – 30).

Hulse, R. A., 1994. [The discovery of the binary pulsar]. *Rev. Mod. Phys.*, **66**, 699 – 710.

Hulse, R. A. & Taylor, J. H., 1975. [Discovery of a pulsar in a binary system]. *Astrophys. J.*, **195**, L51 – L53.

Hurley, K., 2003. [Observational properties of cosmic γ-ray bursts]. In *Supernovae and Gamma-Ray Bursters*, *Lecture Notes in Physics*, vol. **598**, ed. K. Weiler, Springer, Berlin, p. 301 – 316.

Iben, I., 1965. [Stellar evolution. I. The approach to the main sequence]. *Astrophys. J.*, **141**, 993 – 1018.

Iben, I., 1966. [Stellar evolution. III. The evolution of a $5\,M_\odot$ star from the main sequence through core helium burning]. *Astrophys. J.*, **143**, 483 – 504.

Iben, I., 1967a. [Stellar evolution within and off the main sequence]. *Ann. Rev. Astron. Astrophys.*, **5**, 571 – 626.

Iben, I., 1967b. [Stellar evolution. VI. Evolution from the main sequence to the red-giant branch for stars of mass $1\,M_\odot$, $1.25\,M_\odot$ and $1.5\,M_\odot$]. *Astrophys. J.*, **147**, 624 – 663.

Iben, I., 1985. [The life and times of an intermediate mass star – in isolation/in a close binary]. *Ql. J. Roy. astr. Soc.*, **26**, 1 – 39.

Iben, I., 1991. [Single and binary star evolution]. *Astrophys. J. Suppl.*, **76**, 55 – 114.

Iben, I. & Renzini, A., 1984. [Single star evolution I. Massive stars and early evolution of low and intermediate mass stars]. *Phys. Rep.*, **105**, 329 – 406.

Iglesias, C. A., Rogers, F. J. & Wilson, B. G., 1992. [Spin-orbit interaction effects on the Rosseland mean opacity]. *Astrophys. J.*, **397**, 717 – 728.

Janka, H.-T., Hanke, F., Hüdepohl, L., Marek, A., Müller, B. & Obergaulinger, M., 2012. [Core-collapse supernovae: Reflections and directions]. *Prog. Theor. Exp. Phys.*, 01A309, p. 1 – 33.

Jayawardhana, R., 2004. [Unravelling brown dwarf origins]. *Science*, **303**, 322 – 323.

Johnson, J. A., 2019. [Populating the periodic table]. *Science*, **363**, 474 – 478.

Johnson, J. A., Fields, B. D. & Thompson, T. A., 2020. [The origin of the elements: a century of progress]. *Phil. Trans. R. Soc. A*, **378**, 20190301-(1 – 28).

Jørgensen, U. G., 1991. [Advanced stages in the evolution of the Sun]. *Astron. Astrophys.*, **246**, 118 – 136.

Kahabka, P., van den Heuvel, E. P. J. & Rappaport, S. A., 1999. [Supersoft X-ray stars and supernovae]. *Scientific American*, **280** (February), 28 – 35.

Kasting, J. F., Toon, O. B. & Pollack, J. B., 1988. [How climate evolved on the terrestrial planets]. *Scientific American*, **258** (February), p. 46 – 53 (US p. 90 – 97).

Kearns, E., Kajita, T. & Totsuka, Y., 1999. [Detecting massive neutrinos]. *Scientific American*, **281** (August), 48 – 55.

Kippenhahn, R. & Weigert, A., 1990. *Stellar structure and evolution*, Springer-Verlag, Berlin.

Kippenhahn, R., Weigert, A. & Weiss, A., 2012. *Stellar structure and evolution, Second Edition*, Springer-Verlag, Berlin.

Kirsten, A., 1999. [Solar neutrino experiments: results and implications]. *Rev. Mod. Phys.*, **71**, 1213 – 1232.

Koshiba, M., 2003. [Nobel lecture: Birth of neutrino astrophysics]. *Rev. Mod. Phys.*, **75**, 1011–1020.

Kovalevsky, J., 1998. [First results from Hipparcos]. *Ann. Rev. Astron. Astrophys.*, **36**, 99 – 129.

Krane, K. S., 1988. *Introductory nuclear physics*, John Wiley & Sons, New York.

Kurtz, D. W., 2022. [Asteroseismology across the Hertzsprung-Russell diagram]. *Annu. Rev. Astron. Astrophys.*, **60**, in the print.

Labitzke, K. & van Loon, H., 1993. [Some recent studies of probable connections between solar and atmospheric variability]. *Ann. Geophys.*, **11**, 1084 – 1094.

Lasota, J.-P., 1999. [Unmasking black holes]. *Scientific American*, **280** (May), 30 – 37.

Lebreton, Y., 2000. [Stellar structure and evolution: deductions from Hipparcos]. *Ann. Rev. Astron. Astrophys.*, **38**, 35 – 77.

Leibacher, J. W., Noyes, R. W., Toomre, J. & Ulrich, R. K., 1985. [Helioseismology]. *Scientific American*, **253**, (September) p. 34 – 43 (US p. 48 – 57).

Libbrecht, K. G., 1988. [Solar and stellar seismology]. *Space Science Rev.*, **47**, 275 – 301.

Libbrecht, K. G. & Woodard, M. F., 1991. [Advances in helioseismology]. *Science*, **253**, 152 – 157.

Longair, M. S., 1981. *High energy astrophysics*, Cambridge University Press.

Lovelock, J. E. & Whitfield, M., 1982. [Life span of the biosphere]. *Nature*, **296**, 561 – 563.

McDonald, A. B., 2016. [Nobel lecture: The Sudbury Neutrino Observatory: Observation of flavor change for solar neutrinos]. *Rev. Mod. Phys.*, **88**, 030502-(1–9).

MacFadyen, A., 2004. [Long gamma-ray bursts]. *Science*, **303**, 45 – 46.

Maeder, A., 1977. [Four basic solar and stellar tests of cosmologies with variable past G and macroscopic masses]. *Astron. Astrophys.*, **56**, 359 – 367.

Magic, Z., Collet, R., Asplund, M., Trampedach, R., Hayek, W., Chiavassa, A., Stein, R. F. & Nordlund, Å, 2013. [The STAGGER-grid: A grid of 3D stellar atmosphere models. I. Methods and general properties]. *Astron. Astrophys.*, **557**, A26-(1 – 30).

Margutti, R. & Chornock, R., 2021. [First multimessenger observations of a neutron star merger]. *Annu. Rev. Astron. Astrophys.*, **59**, 155 – 202.

Mattauch, J. H. E., Thiele, W. & Wapstra, A. H., 1965. [1964 Atomic Mass Table]. *Nucl. Phys.*, **67**, 1 – 31.

Miesch, M. S., Brun, A. S., DeRosa, M. L. & Toomre, J., 2008. [Structure and evolution of giant cells in global models of solar convection]. *Astrophys. J.*, **673**, 557 – 575.

Mihalas, D., 1978. *Stellar Atmospheres*, 2nd ed., W. H. Freeman, San Francisco.

Mikheyev, S. P. & Smirnov, A. Yu., 1985. [Resonance enhancement of oscillations in matter and solar neutrino spectroscopy]. *Yad. Fiz.*, **42**, 1441–1448 (English translation: *Sov. J. Nucl. Phys.*, **42**, 913–917).

Miller Bertolami, M. M., 2022. [A red giants' toy story]. *Astrophys. J.*, **941**, 149-(1 – 21).

Morgan, J. G. & Eggleton, P. P., 1978. [A reappraisal of the gap in the HR diagram of M67]. *Mon. Not. R. astr. Soc.*, **182**, 219 - 231.

Mosumgaard, J. R., Jørgensen, A. C. S., Weiss, A., Silva Aguirre, V. & Christensen-Dalsgaard, J., 2020. [Coupling 1D stellar evolution with 3D-hydrodynamical simula-

tions on-the-fly II: Stellar evolution and asteroseismic applications]. *Mon. Not. R. astr. Soc.*, **491**, 1160 – 1173.

Mužić, K., Schödel, R., Scholz, A., Geers, V. C., Jayawardhana, R., Ascenso, J. & Cierza, L. A., 2017. [The low-mass content of the massive young cluster RCW 38]. *Mon. Not. R. Astr. Soc.*, **471**, 3699 – 3712.

Nittler, L. R., 2004. [Nuclear fossils in stardust]. *Science*, **303**, 636 – 637.

Novotny, E., 1973. *Introduction to stellar atmospheres and interiors*, Oxford University Press, New York.

Palla, F. & Stahler, S. W., 1999. [Star formation in the Orion Nebula cluster]. *Astrophys. J.*, **525**, 772 – 783.

Parker, P. D. & Rolfs, C. E., 1991. [Nuclear energy generation in the solar interior]. In *Solar interior and atmosphere*, eds Cox, A. N., Livingston, W. C. & Matthews, M., Space Science Series, University of Arizona Press, p. 31 – 50.

Paxton, B. Smolec, R., Schwab, J., Gautschy, A., Bildsten, L., Cantiello, M., Dotter, A., Farmer, R., Goldberg, J. A., Jermyn, A. S., Kanbur, S. M., Marchant, P., Thoul, A., Townsend, R. H. D., Wolf, W. M., Zhang, M. & Timmes, F. X. , 2019. [Modules for Experiments in Stellar Astrophysics (MESA): Pulsating variable stars, rotation, convective boundaries, and energy conservation]. *Astrophys. J. Suppl.*, **243**, 10-(1 – 44).

Pedersen, B. B., VandenBerg, D. A. & Irwin, A. W., 1990. [The prediction of stellar effective temperatures from the mixing-length theory of convection]. *Astrophys. J.*, **352**, 279 - 290.

Popovas, A, Nordlund, Å & Szydlarski, M., 2023. [Glol MHD simulations of the colar convective zone using a volleyball mesh decomposition. I. Pilot]. Submitted to *Astron. Astrophys.* `[arXiv:2211.09564 [astro-ph.SR]]`

Preston, M. A., 1962. *Physics of the nucleus.* Addison-Wesley Publishing Company, Reading, Massachusetts.

Ray, T. P., 2000. [Fountains of youth: early days in the life of a star]. *Scientific American*, **283** (August), 30 – 35.

Reid, I. N., 1999. [The HR diagram and the galactic distance scale after Hipparcos]. *Ann. Rev. Astron. Astrophys.*, **37**, 191 – 237.

Reipurth, B. & Bally, J., 2001. [Herbig-Haro flows: probes of early stellar evolution]. *Annu. Rev. Astron. Astrophys.*, **39**, 403–455.

Sackmann, I.-J. & Boothroyd, A. I., 2003. [Our Sun. V. A bright young Sun consistent with helioseismology and warm temperatures on ancient Earth and Mars]. *Astrophys. J.*, **583**, 1024 – 1039.

Sandage, A., 1957. [Observational approach to evolution. II. A computed luminosity function for K0 – K2 stars from $M_v = +5$ to $M_v = -4.5$]. *Astrophys. J.*, **125**, 435 - 444.

Schneider, S. H., 1989. [The changing climate]. *Scientific American*, **261** (September), p. 38 – 46 (US p. 70 – 78).

Schödel, R., Ott., T., Genzel, R., Hofmann, R., Lehnert, M., Eckart, A., Mouawad, N., Alexander, T., Reid, M. J., Lenzen, R., Hartung, M., Lacombe, F., Rouan, D., Gendron, E., Rousset, G., Lagrange, A.-M., Brandner, W., Ageorges, N., Lidman, C., Moorwood, A. F. M., Spyromilio, J., Hubin, N. & Menten, K. M., 2002. [A star in a 15.2-year orbit around the supermassive black hole at the centre of the Milky Way]. *Nature*, **419**, 694 – 696.

Schönberg, M. & Chandrasekhar, S., 1942. [On the evolution of the main-sequence stars]. *Astrophys. J.*, **96**, 161 – 172.

Schwarzschild, M., 1958. *Structure and evolution of the stars*, Princeton University Press, Princeton, New Jersey.

Seaton, M. J., Yan, Y., Mihalas, D. & Pradhan, A. K., 1994. [Opacities for stellar envelopes]. *Mon. Not. R. astr. Soc.*, **266**, 805 – 828.

Shapiro, S. L. & Teukolsky, S. A., 1983. *Black holes, white dwarfs, and neutron stars*, Wiley-Interscience.

Shurtleff, R. & Derringh, E., 1989. [The most tightly bound nucleus]. *Am. J. Phys.*, **57**, 552.

Stahler, S. W., 1991. [The early life of stars]. *Scientific American*, **265** (July), p. 28 – 35.

Stahler, S. W., 1994. [Early stellar evolution]. *Pub. Astron. Soc. Pacific*, **106**, 337 – 343.

Stein, R. F. & Nordlund, Å., 1989. [Topology of convection beneath the solar surface], *Astrophys. J.*, **342**, L95 - L98.

Stein, R. F. & Nordlund, Å., 1998. [Simulations of solar granulation. I. General properties]. *Astrophys. J.*, **499**, 914 – 933.

Steindl, T., Zwintz, K. & Vorobyov, E., 2022. [The imprint of star formation on stellar pulsations]. *Nature Comm.*, **13**, 5355-(1 – 12).

Svensmark, H., 1998. [Influence of cosmic rays on Earth's climate]. *Phys. Rev. Lett.*, **81**, 5027 – 5030.

Svensmark, H. & Friis-Christensen, E., 1997. [Variation of cosmic ray flux and global cloud coverage—a missing link in solar-climate relationships]. *J. Atmos. Solar-Terr. Phys.*, **59**, 1225 – 1232.

Trampedach, R., Asplund, M., Collet, R., Nordlund, Å. & Stein, R. F., 2013. [A grid of three-dimensional stellar atmosphere models of solar metallicity. I. General properties, granulation, and atmospheric expansion]. *Astrophys. J.*, **769**, 18-(1 – 15).

Trampedach, R., Stein, R., Christensen-Dalsgaard, J., Nordlund, Å & Asplund, M., 2014. [Improvements to stellar structure models, based on a grid of 3D convection simulations – II. Calibrating the mixing-length formulation]. *Mon. Not. R. astr. Soc.*, **445**, 4366 – 4384.

Tayler, R. J., 1988. [What makes red giants?]. *Nature*, **335**, 14 – 15 (News and Views).

Taylor, J. H., 1994. [Binary pulsars and relativistic gravity]. *Rev. Mod. Phys.*, **66**, 711 – 719.

Timmes, F. X., Woosley, S. E. & Weaver, T. A., 1995. [Galactic chemical evolution: hydrogen through zinc]. *Astrophys. J. Suppl.*, **98**, 617 – 658.

van Leeuwen, F., 1997. [The HIPPARCOS mission]. *Space Science Rev.*, **81**, 201 – 409.

van Paradijs, J., Kouveliotou, C. & Wijers, R. A. M., 2000. [Gamma-ray burst afterglows]. *Annu. Rev. Astron. Astrophys.*, **38**, 379 – 425.

VandenBerg, D. A., Brogaard, K., Leaman, R. & Casagrande, L., 2013. [The ages of 55 globular clusters as determined using an improved $\Delta V_{\rm TO}^{\rm HB}$ method along with color-magnitude constraints and their implications for broader issues]. *Astrophys. J.*, **775**, 134-(1 – 47).

Wasserburg, G. J., Busso, M. & Ballino, R., 1996. [Abundances of actenides and short-lived nonactenides in the interstellar medium: diverse supernova sources for the *r*-processes]. *Astrophys. J.*, **466**, L109 – L113.

Weiss, A., 1989. [Investigation of a criterion for the evolution to red giants]. *Astron. Astrophys.*, **209**, 135 – 140.

Weiss, A. & Schlattl, H., 2008. [GARSTEC—the Garching Stellar Evolution Code. The direct descendant of the legendary Kippenhahn code]. *Astrophys. Space Sci*, **316**, 99 – 106.

Whitworth, A. P., 1989. [Why red giants are giant]. *Mon. Not. R. astr. Soc.*, **236**, 505 – 544.

Williams, J. P. & Cieza, L. A., 2011. [Protoplanetary disks and their evolution]. *Annu. Rev. Astron. Astrophys.*, **49**, 67–117.

Wilson, O. C., Vaughan, A. H. & Mihalas, D., 1981. [The activity cycles of stars]. *Scientific American*, **244** (February), p. 82 – 91 (US p. 104 – 119).

Winn, J. N. & Fabrycky, D. C., 2015. [The occurrence and architecture of exoplanetary systems]. *Annu. Rev. Astron. Astrophys.*, **53**, 409–447.

Wolfenstein, L., 1978. [Neutrino oscillations in matter]. *Phys. Rev. D*, **17**, 2369–2374.

Woosley, S. E., Heger, A. & Weaver, T. A., 2002. [The evolution and explosion of massive stars]. *Rev. Mod. Phys.*, **74**, 1015 – 1071.

Woosley, S. E., Wilson, J. R., Mathews, G. J., Hoffman, R. D. & Meyer, B. S., 1994. [The r-process and neutrino-heated supernova ejecta]. *Astrophys. J.*, **433**, 229 – 246.

Woosley, S. & Weaver, T., 1989. [The great supernova of 1987]. *Scientific American*, **261** (August) p. 24 – 32 (US p. 32 – 40).

Youssef, N. H., 1986. [A search for gold in the Sun]. *Astron. Astrophys.*, **164**, 395 – 396.

Appendix A

Some useful constants

Speed of light	$\tilde{c}$	$2.99792458\times10^{10}\,\mathrm{cm\,sec^{-1}}$
Gravitational constant	G	$6.672320\times10^{-8}\,\mathrm{dyn\,cm^2\,g^{-2}}$
Atomic mass unit	m_u	$1.6605402\times10^{-24}\,\mathrm{g}$
Electron mass	m_e	$9.1093897\times10^{-28}\,\mathrm{g}$
Electron charge	e	1.60217733×10^{-19} C
		4.80320680×10^{-10} ESU
Planck's constant	h	$6.6260755\times10^{-27}\,\mathrm{erg\,sec}$
Boltzmann's constant	k_B	$1.380658\times10^{-16}\,\mathrm{erg\,K^{-1}}$
		$8.6173857\times10^{-5}\,\mathrm{eV\,K^{-1}}$
Radiation density constant	a	$7.565914\times10^{-15}\,\mathrm{erg\,cm^{-3}\,K^{-4}}$
Stefan-Boltzmann constant	σ	$5.67051\times10^{-5}\,\mathrm{erg\,cm^{-2}\,sec^{-1}\,K^{-4}}$
Atomic weight of hydrogen	A_H	1.007825
Atomic weight of helium	A_{He}	4.002603
Ionization potential for hydrogen	χ_H	13.595 eV
First ionization potential for helium	χ_{He}	24.580 eV
Second ionization potential for helium	χ_{He^+}	54.403 eV

Conversions:

From Ångstrom to cm:	1 Å =	$10^{-8}\,\mathrm{cm}$
From barn to cm^2:	1 barn =	$10^{-24}\,\mathrm{cm^2}$
From N to dyn:	1 N =	$10^5\,\mathrm{dyn}$
From J to erg:	1 J =	$10^7\,\mathrm{erg}$
From eV to erg:	1 eV =	$1.60217733\times10^{-12}\,\mathrm{erg}$
From atmosphere to $\mathrm{dyn\,cm^{-2}}$:	1 atm =	$1.01325\times10^6\,\mathrm{dyn\,cm^{-2}}$
Year:	1 year =	$3.155815\times10^7\,\mathrm{sec}$
Astronomical unit:	1 A.U. =	$1.49598\times10^{13}\,\mathrm{cm}$
Parsec:	1 pc =	$3.08568\times10^{18}\,\mathrm{cm}$
Lightyear:	1 ly =	$9.46053\times10^{17}\,\mathrm{cm}$
	=	0.3066 pc

Astronomical constants:

Solar radius	$\mathrm{R}_\odot$	$6.9599 \times 10^{10}\,\mathrm{cm}$
Solar mass	$\mathrm{M}_\odot$	$1.989 \times 10^{33}\,\mathrm{g}$
Solar luminosity	$\mathrm{L}_\odot$	$3.846 \times 10^{33}\,\mathrm{erg\,sec^{-1}}$
Solar effective temperature	$T_{\mathrm{eff},\odot}$	$5778\,\mathrm{K}$
Solar apparent magnitudes:		
	V	-26.74
	B	-26.09
	U	-25.96
	m_{bol}	-26.82
Solar absolute magnitudes:		
	M_V	4.83
	M_B	5.48
	M_U	5.61
	M_{bol}	4.75
Solar spectral type:		G2V

Notes:

With the exception of G, discussed below, the values of the fundamental constants are taken from the 1986 CODATA list (*cf.* Cohen & Taylor 1987).

i) The CODATA value of the gravitational constant is $G = (6.67259 \pm 0.00085) \times 10^{-8}\,\mathrm{dyn\,cm^2\,g^{-2}}$. G and $\mathrm{M}_\odot$ are connected by

$$G\,\mathrm{M}_\odot = 1.32712438 \times 10^{26}\,\mathrm{dyn\,cm^2\,g^{-1}}\,, \tag{A.1}$$

from solar system dynamics. Thus the CODATA value of G corresponds to $\mathrm{M}_\odot = 1.988919 \times 10^{33}\,\mathrm{g}$. However the value $\mathrm{M}_\odot = 1.989 \times 10^{33}$, which is commonly used, corresponds to $G = 6.672320 \times 10^{-8}\,\mathrm{dyn\,cm^2\,g^{-2}}$, which is well within the error bars of the CODATA value. Thus I use this value for G, and the "usual" value for $\mathrm{M}_\odot$.

ii) Of the values given above, a and σ are not fundamental, in the sense that they are given directly in terms of the remaining constants as

$$a = \frac{8\pi^5 k_B^4}{15\tilde{c}^3 h^3}\,, \tag{A.2}$$

$$\sigma = \frac{a\tilde{c}}{4}\,. \tag{A.3}$$

Their values are included here for convenience.

Appendix B

Atomic mass excesses

Atomic mass excesses, for computation of the energy liberated in nuclear reactions (*cf.* equations [8.15] and [8.16]). Based on the scale $^{12}C \equiv 0$; 1 amu = 931.478 MeV. The data are largely derived from the review by Mattauch, Thiele & Wapstra (1965). Terminal zeros are generally not significant digits. (From Clayton 1968).

Z	Element	A	M − A, Mev
0	n	1	8.07144
1	H	1	7.28899
	D	2	13.13591
	T	3	14.94995
	H	4	28.22000
		5	31.09000
2	He	3	14.93134
		4	2.42475
		5	11.45400
		6	17.59820
		7	26.03000
		8	32.00000
3	Li	5	11.67900
		6	14.08840
		7	14.90730
		8	20.94620
		9	24.96500
4	Be	6	18.37560
		7	15.76890
		8	4.94420
		9	11.35050
		10	12.60700
		11	20.18100
5	B	7	27.99000
		8	22.92310
		9	12.41860
		10	12.05220
		11	8.66768
		12	13.37020
		13	16.56160
6	C	9	28.99000
		10	15.65800
		11	10.64840
		12	0
		13	3.12460
		14	3.01982
		15	9.87320
7	N	12	17.36400
		13	5.34520
		14	2.86373
		15	0.10040
		16	5.68510
		17	7.87100
8	O	14	8.00800
		15	2.85990
		16	−4.73655
		17	−0.80770
		18	−0.78243
		19	3.33270
		20	3.79900
9	F	16	10.90400
		17	1.95190
		18	0.87240
		19	−1.48600
		20	−0.01190
		21	−0.04600
10	Ne	18	5.31930
		19	1.75200
		20	−7.04150
		21	−5.72990
		22	−8.02490
		23	−5.14830
		24	−5.94900
11	Na	20	8.28000
		21	−2.18500
		22	−5.18220
		23	−9.52830
		24	−8.41840
		25	−9.35600
		26	−7.69000
12	Mg	22	−0.14000
		23	−5.47240
		24	−13.93330
		25	−13.19070
		26	−16.21420
		27	−14.58260
		28	−15.02000
13	Al	24	0.1000
		25	−8.9310
		26	−12.2108
		27	−17.1961
		28	−16.8554
		29	−18.2180
		30	−17.1500
14	Si	26	−7.1320
		27	−12.3860
		28	−21.4899
		29	−21.8936
		30	−24.4394
		31	−22.9620
		32	−24.2000
15	P	28	−7.6600
		29	−16.9450
		30	−20.1970
		31	−24.4376
		32	−24.3027

Z	Element	A	M − A, Mev
15	P	33	−26.3346
		34	−24.8300
16	S	30	−14.0900
		31	−18.9920
		32	−26.0127
		33	−26.5826
		34	−29.9335
		35	−28.8471
		36	−30.6550
		37	−27.0000
		38	−26.8000
17	Cl	32	−12.8100
		33	−21.0140
		34	−24.4510
		35	−29.0145
		36	−29.5196
		37	−31.7648
		38	−29.8030
		39	−29.8000
		40	−27.5000
18	Ar	34	−18.3940
		35	−23.0510
		36	−30.2316
		37	−30.9509
		38	−34.7182
		39	−33.2380
		40	−35.0383
		41	−33.0674
		42	−34.4200
19	K	36	−16.7300
		37	−24.8100
		38	−28.7860
		39	−33.8033
		40	−33.5333
		41	−35.5524
		42	−35.0180
		43	−36.5790
		44	−35.3600
		45	−36.6300
		46	−35.3400
		47	−36.2500
20	Ca	38	−21.6900
		39	−27.3000
		40	−34.8476
		41	−35.1400
		42	−38.5397
		43	−38.3959
		44	−41.4596
		45	−40.8085
		46	−43.1380
		47	−42.3470
		48	−44.2160
		49	−41.2880
21	Sc	40	−20.9000
		41	−28.6450
		42	−32.1410
		43	−36.1740
		44	−37.8130
		45	−41.0606
		46	−41.7557
		47	−44.3263
		48	−44.5050
		49	−46.5490
		50	−44.9600
22	Ti	42	−25.1230
		43	−29.3400
		44	−37.6580
		45	−39.0020
		46	−44.1226
		47	−44.9266
		48	−48.4831
		49	−48.5577
		50	−51.4307
		51	−49.7380
		52	−49.5400
23	V	46	−37.0600
		47	−42.0100
		48	−44.4700
		49	−47.9502
		50	−49.2158
		51	−52.1989
		52	−51.4360
		53	−52.1800
		54	−49.6300
24	Cr	48	−42.8130
		49	−45.3900
		50	−50.2490
		51	−51.4472
		52	−55.4107
		53	−55.2807
		54	−56.9305
		55	−55.1130
		56	−55.2900
25	Mn	50	−42.6480
		51	−48.2600
		52	−50.7020

Z	Element	A	M − A, Mev
25	Mn	53	−54.6820
		54	−55.5520
		55	−57.7048
		56	−56.9038
		57	−57.4800
		58	−55.6500
26	Fe	52	−48.3280
		53	−50.6930
		54	−56.2455
		55	−57.4735
		56	−60.6054
		57	−60.1755
		58	−62.1465
		59	−60.6599
		60	−61.5110
		61	−59.1300
27	Co	54	−47.9940
		55	−54.0140
		56	−56.0310
		57	−59.3389
		58	−59.8380
		59	−62.2327
		60	−61.6513
		61	−62.9300
		62	−61.5280
		63	−61.9200
28	Ni	56	−53.8990
		57	−56.1040
		58	−60.2280
		59	−61.1587
		60	−64.4707
		61	−64.2200
		62	−66.7480
		63	−65.5160
		64	−67.1060
		65	−65.1370
		66	−66.0550
29	Cu	58	−51.6590
		59	−56.3590
		60	−58.3460
		61	−61.9840
		62	−62.8130
		63	−65.5831
		64	−65.4276
		65	−67.2660
		66	−66.2550
		67	−67.2910
		68	−65.4100
30	Zn	60	−54.1860
		61	−56.5800
		62	−61.1230
		63	−62.2170
		64	−66.0003
		65	−65.9170
		66	−68.8810
		67	−67.8630
		68	−69.9940
		69	−68.4250
		70	−69.5500
		71	−67.5200
		72	−68.1440
31	Ga	63	−56.7200
		64	−58.9280
		65	−62.6580
		66	−63.7060
		67	−66.8650
		68	−67.0740
		69	−69.3262
		70	−68.8970

Index